

Proton Coupled Electron Transfer at Heavy Metal Sites

DISSERTATION

FOR THE AWARD OF THE DEGREE

“DOCTOR RERUM NATURALIUM”

OF THE GEORG-AUGUST-UNIVERSITÄT GÖTTINGEN

WITHIN THE DOCTORAL CHEMISTRY PROGRAM OF THE GEORG-AUGUST UNIVERSITY SCHOOL OF
SCIENCE (GAUSS) IN THE GRADUATE SCHOOL BENCH

SUBMITTED BY

DANIEL DELONY, M. SC.

FROM CELLE, GERMANY

GÖTTINGEN, 2020

Thesis Committee

Prof. Dr. Sven Schneider

Institut für Anorganische Chemie, Georg-August Universität Göttingen

Prof. Dr. Franc Meyer

Institut für Anorganische Chemie, Georg-August Universität Göttingen

Prof. Dr. Max. C. Holthausen

Institut für Anorganische und Analytische Chemie, Johann Wolfgang Goethe-Universität Frankfurt am Main

Members of the Examination Board

- | | |
|---|--|
| 1. Reviewer | Prof. Dr. Sven Schneider
Institut für Anorganische Chemie, Georg-August Universität Göttingen |
| 1. Reviewer | Prof. Dr. Franc Meyer
Institut für Anorganische Chemie, Georg-August Universität Göttingen |
| | Prof. Dr. Max. C. Holthausen
Institut für Anorganische und Analytische Chemie, Goethe-Universität Frankfurt am Main |
| Further members
of the
examination
board | Prof. Dr. Ricardo Mata
Institut für Physikalische Chemie, Georg-August Universität Göttingen |
| | Dr. Michael John
Institut für Organische und Biomolekulare Chemie, Georg-August Universität Göttingen |
| | Dr. Christian Sindlinger
Institut für Anorganische Chemie, Georg-August Universität Göttingen |

Date of oral examination: 10.12.2020

Für Katharina und Theo

Mein besonderer Dank gilt:

meinem Betreuer Prof. Dr. Sven Schneider, für die interessanten wissenschaftlichen Fragestellungen und die große Freiheit mit der ich an die Themen herangehen durfte. Sven, dein ständiges Hinterfragen von Ergebnissen hat meinen Sinn für sauberes Arbeiten weiter geschärft.

Meinem Zweitbetreuer Prof. Dr. Franc Meyer, für die Übernahme der Zweitkorrektur und die anregenden Gespräche.

Prof. Dr. Max. C. Holthausen, für die unglaublich herzliche Aufnahme in deinen Arbeitskreis und die Übernahme der Drittkorrektur und natürlich für die erfolgreichen Kooperationen.

Dr. Martin Diefenbach, für das begeisterte Unterrichten der Quantenchemie. Ohne dich hätte ich in so kurzer Zeit niemals so viel lernen können.

Dem AK Holthausen, dafür dass ich mich selten so willkommen gefühlt habe wie bei euch.

My collaboration partners, for the successful collaborations and their scientific contribution to this thesis: Dr. Christian Würtele (X-Ray, many good conversations), Dr. Serhiy Demeshko (SQUID), Dr. Milan Orlita (magnetic IR), Dr. A. Claudia Stückl (EPR), Prof. Dr. Bas de Bruin (EPR) and Gannon Connor, Prof. Patrick L. Holland and Prof. James M. Mayer (NH₃ oxidation collaboration).

Dem AK Schneider, für die schöne und prägende Zeit in der Gruppe. Mein Dank gilt hier auch insbesondere Dr. Markus van Alten, Dr. Josh Abbenseth und Dr. Florian Wätjen für die gemeinsamen Projekte und Gespräche. Bei Isa, Markus, Josh und Sarah möchte ich mich des Weiteren für die Vernichtung zahlreicher Tonnen an Kaffeebohnen und die dabei verbrachte Zeit bedanken.

Meinen Korrekturlesern, Dr. Bastian Schluschaß, Richt van Alten und Jascha Lau. Vielen Dank für die vielen hilfreichen Anmerkungen und die gute Zeit während der Promotion.

Dem Graduiertenkolleg BENCH, für die Erweiterung meines Horizonts auf die Quantenchemie und die Ermöglichung meines Austausches in Frankfurt.

Zuletzt möchte ich mich aus tiefstem Herzen bei meiner Familie bedanken:

Meinen Eltern, dafür dass ihr immer an mich geglaubt habt und mich bereits in jungen Jahren bedingungslos unterstützt habt meinen Weg zu gehen. Ohne euch hätte ich nicht einmal Abitur machen können, da ein Kind aus einer Arbeiterfamilie ja „nichts auf dem Gymnasium zu suchen hat“....

Meiner Frau Katharina, dafür dass du seit mittlerweile sieben Jahren geduldig darauf wartest, dass ich mit meiner „Ausbildung“ abschließe. Vielen Dank auch für die jahrelange Unterstützung, Beratung und Ermöglichung eines Soziallebens. Mein Leben wurde durch dich bunter und vollkommener.

Meinem Sohn Theo, mein letzter Dank geht an dich. Du weißt es zwar nicht, aber du hast entscheidend dazu beigetragen, dass diese Arbeit schneller fertiggestellt wurde. Du hast mich zum einen zusätzlich motiviert fertig zu werden und warst zum anderen seit deiner Geburt das liebste Kind der Welt. Du hast mich nachts schlafen lassen und mir tagsüber den Freiraum gegeben zu schreiben.

Table of Contents

Table of Contents	1
I. INTRODUCTION	6
1. Oxygen and Oxygenation chemistry	1
1.1 Oxygenation Chemistry in Nature	1
1.2 Terminal Oxo Complexes	3
2. Proton-Coupled Electron Transfer	8
2.1 General Aspects in PCET Chemistry	8
2.2 PCET Thermochemistry	9
3. Computational Thermochemistry	12
3.1. Computational Methods	12
3.2. Relativistic Effects on Thermochemistry	16
4. Outline	18
4.1 Outline of Chapter II	18
4.2 Outline of Chapter III	19
4.3 Outline of Chapter IV	20
II. A TERMINAL IRIIDIUM OXO COMPLEX WITH A TRIPLET GROUND STATE	22
1. Synthesis of Terminal Iridium Hydroxo Complexes	23
2. Synthesis and Characterisation of a Terminal Iridium Oxo Complex	27
3. Reactivity of the Terminal Iridium Oxo Complex	35
3.1. Oxygen Atom Transfer and Philicity Derivation	35
3.2. BD(F)E determination of the hydroxo/oxo couple 2/4	40
3.3. C-H bond Activation Chemistry of 4	44
4. Summary of Chapter II	50
III. EXCURSUSES	52
1. Excursus 1: Interconversion of Phosphinyl Radical and Phosphinidene Complexes by Proton Coupled Electron Transfer	53

2. Excursus 2: Facile Conversion of Ammonia to a Nitride in a Rhenium System that Cleaves Dinitrogen	56
IV. ON THE EFFECT OF SPIN-ORBIT COUPLING IN SOLUTION THERMOCHEMISTRY	58
1. Characterisation of the rhenium(III/IV) amine complexes 23, 25 and of rhenium(IV) amide 24	60
1.1 Characterisation of rhenium(III) amine complex 23	60
1.2 Characterisation of the Rhenium(IV) Amide Complex 24	63
1.3 Characterisation of cationic rhenium(IV) amine complex 25	64
2. Computational Rationalisation of the Spectroscopic and Magnetic Features	66
2.1. Computational Rationalisation of rhenium(III) amine complex 23	66
2.2. Computational Rationalisation of rhenium(IV) amide complex 24	70
2.3. Computational Rationalisation of rhenium(IV) amine complex 25	73
3. (Free) Reaction Enthalpy Determination	75
3.1. Experimental (Free) Reaction Enthalpy Determination	75
3.2. Computational (Free) Enthalpy Determination	78
4. Summary of Chapter IV	81
V. CONCLUSION AND OUTLOOK	84
VI. EXPERIMENTAL DETAILS	90
1. Materials and Methods	91
1.1 General remarks	91
1.2 Analytical Methods	92
2. Synthesis	95
2.1. Improved synthesis for [(PNP)IrOH] 2	95
2.2. Synthesis of [Na(thf)(PNP)IrOH] ₂ 1	96
2.3. Improved synthesis of [(PNP)IrOH][PF ₆] 3	97
2.4. Synthesis of [(PNP)IrO] 4	98
2.5. Synthesis of [(PNP)IrCO ₃] 8	99
2.6. Synthesis of [(PNP)IrPMe ₃] 10	100
2.7. Reactivity of 4 towards H ₂	101
2.8. Reactivity of 4 towards CO	101
2.9. Synthesis of [(PNP)IrO(C ₁₂ H ₈ O)] "Xanthenolate" 11	101
2.10. Synthesis of [(PNP)IrO(C ₁₃ H ₉)] "Fluorenoate" 12	101
2.11. Reactivity of 4 towards benzaldehydes (X ^{para} = H, Me, OMe, F)	101

2.12.	General synthesis of [(PNP)IrO ₂ CPh-X] 14-X with X ^{para} = F, OMe, Me, H)	102
2.13.	Synthesis of [(PNP)Ir(H)(Cl)] 15	104
2.14.	Synthesis of [(ⁱ PrP ^H NP)ReCl ₃][BarF ₂₄] 25	105
2.15.	Deprotonation of [(ⁱ PrP ^H NP)ReCl ₃][BarF ₂₄] 25	105
2.16.	N-H/D exchange of 23	105
2.17.	Reevaluation of the 23/25 redox potential	106
3.	Isothermal Titration Calorimetry	107
3.1	BD(F)E determination of 4	107
3.2	BDE determination of 23	108
3.2.1	Enthalpy determination of the PCET reaction in THF	108
3.2.2	Enthalpy determination of the PCET reaction in DCM	111
3.3	pK _A value determination of 25	114
3.4	pK _A value determination of Mes*OH	116
3.5	P-H BDE value determination of 17	118
3.6	Mean BDE determination of [(PNP)Re(Cl)(NH ₂)] 20	121
4.	Computational Details	124
4.1.	General Remarks	124
4.2.	A Terminal Iridium Oxo with a Triplet Ground State	126
4.2.1.	Molecular Geometries	126
4.2.1.	Spin State and Reaction Energetics	127
4.2.2.	Total Energies	128
4.2.3.	State-Averaged CASSCF computations	129
4.3.	On the Spin-Orbit Coupling influence in solution thermochemistry	133
4.3.1.	Molecular Geometries	133
4.3.1.	State Averaged CASSCF Computations	134
4.3.2.	CASSCF/NEVPT2 State Composition and QDPT Eigenvectors	136
4.3.3.	Comparison of Magnetic Properties Theory vs. Experiment	137
4.3.4.	Spin State and Reactions Energetics	138
4.3.5.	Total Energies	141
4.4	Interconversion of Phosphenyl Radical and Phosphenidene Complexes by Proton Coupled Electron Transfer	143
5.	Benchmarked Experimental Results	144
6.	LITERATURE	148
7.	APPENDIX	158

A. Crystal Structures	159
A.1. X-Ray Single-Crystal Analysis of 1	159
A.2. X-Ray Single-Crystal Analysis of 3	161
A.3. X-Ray Single-Crystal Analysis of 4	163
A.4. X-Ray Single-Crystal Analysis of 8	165
A.5. X-Ray Single-Crystal Analysis of 10	167
A.6. X-Ray Single-Crystal Analysis of 14-H	169
A.7. X-Ray Single-Crystal Analysis of 14-F	171
A.8. X-Ray Single-Crystal Analysis of 14-OMe	173
A.9. X-Ray Single-Crystal Analysis of 11	175
A.10. X-Ray Single-Crystal Analysis of 12	177
A.11. X-Ray Single-Crystal Analysis of 15	179
A.12. X-Ray Single-Crystal Analysis of 25	181
B. List of Chemical Compounds	183
C. Independent PCET Model	184
C.1. Derivation of the fitting function	184
C.2. Incooperation into Visual Basics	185
D. Cartesian Coordinates of Computed Structures	186
E. List of abbreviations	206
F. Curriculum Vitae	208

Chapter I

I. Introduction

1. Oxygen and Oxygenation chemistry

“Oxygen: An essential toxin”

I. C. Gunsalus, 1973^[1]

1.1 Oxygenation Chemistry in Nature

Oxygen is the most abundant element in the Earth crust and after iron the most abundant element on Earth in general.^[2] The dioxygen essential to respiration was nevertheless not always part of the Earth atmosphere. Only since the first cyanobacteria started to produce dioxygen as a waste product of photosynthesis, the oxygen amount started to rise slowly to the present value of 21 %. On the way there, oxygen was responsible for the first mass extinction in Earth history, known as the great oxygenation event (GOE).^[3] This catastrophe can be seen as the first indication of the high reactivity of dioxygen. Life had to adapt to the new atmosphere and overcame it utilizing the former poison as an energy supply. An evolutionary stroke of genius, since the aerobic respiration had a significantly higher energy potential than former anaerobic processes, thus making the way free for higher life forms.^[4] The biological oxygen fixation takes place in the coordination sphere of base metals with either copper (hemocyanin) or iron (haemoglobin) in the centre of attraction for invertebrates and vertebrates, respectively.^[5] The latter has an iron(II)-high spin (hs) metal centre coordinated to a porphyrin ring in the active site of the protein (**I**), which loses its paramagnetic ground state upon coordination of O₂ and yields a diamagnetic oxyhaemoglobin species (**II**) (Figure i1, a).^[6]

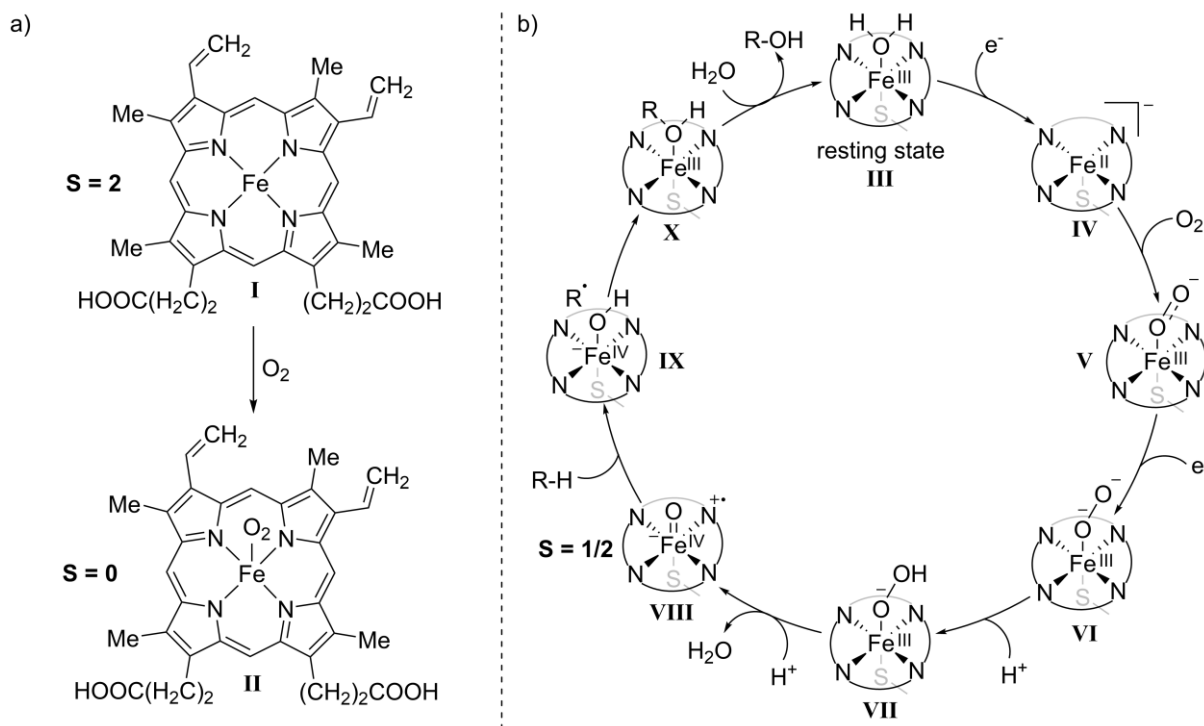


Figure i1: a) Chemical structure of the heme-b unit of haemoglobin and cytochrome P450 (top) and schematic end-on oxygen binding to haemoglobin (bottom). b) Catalytic oxygenation cycle of cytochrome P450.^[1,7]

This finding in 1936 started an intense and still ongoing discussion about the nature of the Fe-O₂ binding, including a low-spin (ls) Fe(II, ls)-O₂(singlet) interaction (Pauling model), an Fe(III, ls)-O₂⁻ interaction, in which the superoxo ligand is antiferromagnetically coupling to the iron centre (Weiss model) and an antiferromagnetically coupled intermediate-spin model (is) Fe(II, is)-O₂(triplet) (McClure, Harcourt, Goddard model).^[8] All these models agree in some aspects with the performed experiments and are among the first examples of oxygen metal binding interactions discussed in the literature. The same structural motif as for haemoglobin can be found in cytochrome proteins which are responsible for biological electron transfer and oxygenation chemistry.^[9] Here, the ubiquitous class of cytochrome P450 enzymes is of special interest, since these enzymes play a vital role in the metabolism of xenobiotics¹ and in the synthesis of critical signal molecules.^[1] In contrast to haemoglobin, the iron is in the ferric iron(III) oxidation state (**III**). Dioxygen binds after reduction of **III** and is further activated by an electron-proton-proton transfer cascade (ET-PT-PT)² (**IV-VII**), yielding a terminal iron(IV) oxo complex (**VIII**) as the key intermediate for the oxygenation of unactivated hydrocarbons (Figure i1, b).^[1,7] The crucial reaction step of the catalytic cycle is the hydrogen atom transfer (HAT) from the hydrocarbon substrate to **VIII** followed by the radical rebound of the carbo-radical to **IX**, which yields the desired alcohol product complex **X**.^[10] Such iron oxo moieties play a vital role for many biological enzyme families like cyclooxygenases and peroxidases and are proposed key intermediates in many different reaction types like (cis)-hydroxylation, oxidative ligand transfer, desaturation/cyclisation by HAT and electrophilic aromatic substitution.^[11-13] Another important field of biochemistry in which a terminal oxo species is discussed is the oxygen evolving complex (OEC) in the heart of photosystem(II) (PSII) (Figure i2).^[14]

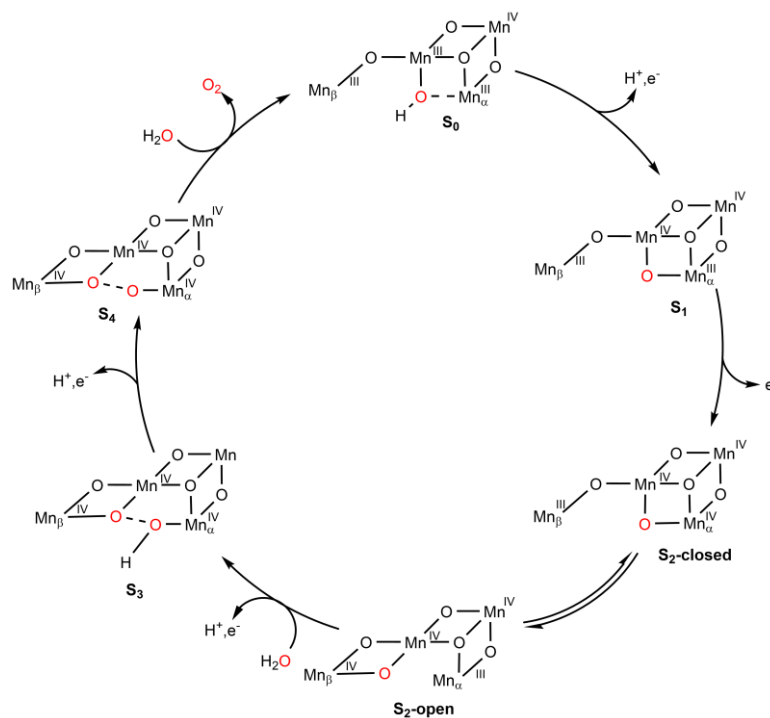


Figure i2: Schematic catalytic cycle of the oxygen evolving complex (OEC) according to Cox et al.^[14], structures of S₀ and S₁ in analogy to Pal et al.^[15]

¹ Xenobiotics are compounds which are not naturally part of the organism.

² For a detailed discussion of ETPT/HAT/PCET chemistry see Section 2.

The manganese-calcium Mn_4O_5Ca cofactor in the active centre of PSII is activated by a proton-coupled electron transfer (PCET)³ step from the **S₀** to the **S₁** state, which is further oxidized to the **S₂** state. Here, the cubic form of **S₂-closed** is in equilibrium with an open form, **S₂-open**, in which the Mn_α now has a vacant coordination site to coordinate a second water molecule yielding **S₃** after PCET (Figure i2). For **S₃** an oxygen-oxygen interaction between $Mn_\alpha-O- -O-Mn_\beta$ is already predicted. The O-O bond is formed upon a last PCET step (**S₄**), leading to the rapid release of dioxygen upon coordination of a water molecule.^[14,15] These reaction types of transition metal oxo complexes, which nature performs with ease, are essential for the synthesis of fine chemicals from unactivated, fossil hydrocarbons as well as for future sustainable fuel cells and will be one of the main topics discussed in Chapter II of this thesis.^[16,17]

1.2 Terminal Oxo Complexes

“The Oxo Wall stands”

Craig L. Hill in correspondence with Harry B. Gray^[18]

Thousands of terminal transition metal oxo complexes are reported in the literature, but they are not evenly distributed over the d-block.^[17] Most transition metal oxo complexes are found for the early transition metals in high oxidation states bearing a low d-electron count. This finding was rationalized by Ballhausen and Gray in 1962 by the consideration of the molecular frontier orbitals (MO) of the vanadyl oxo ion complex $[(H_2O)_5V(IV)O]^{2+}$ **XI** (Figure i3).^[19] **XI** is in tetragonal (C_{4v}) coordination with four equivalent water ligands in equatorial position and one water ligand and the oxo ligand in opposite axial positions. Considering the 3d, 4s and 4p metal orbitals, a MO scheme with 17 orbitals arises which excellently reproduces the spectroscopic and magnetic data of **XI**.^[19] Additionally, a simplified MO scheme for near octahedral oxo complexes can be deduced from their elaborate approach which explains why only few examples of late transition metal oxo complexes exist (Figure i3, right). Together with the metal-oxo π -bonding interaction, a strong M-O triple bond can be formed for low electron counts d^{0-2} , since only the non-bonding d_{xy} will be populated. For higher d-electron counts the π^* -orbitals of the M-O unit will be populated and thus lead to a weakening of the M-O moiety. The vanadyl(IV) oxo complex **XI** exhibits with a d^1 -configuration a M-O triple bond, with one electron in the non-bonding d_{xy} , while the iron(IV) oxo **VIII** (d^4) (see Figure i1) bears two electrons in the π^* -orbitals and therefore only exhibits a M-O double bond. This finding does not only explain the high reactivity of **VIII**, as discussed in Section 1.1, but also explains the spin state of the system. For the observed doublet ground state of **VIII**, a triplet configuration at the iron centre is needed that couples antiferromagnetically with the heme radical cation. This triplet configuration of the metal centre is predicted in the MO scheme due to the degeneracy of the π^* -orbitals.

The population of more than 5 d-electrons leads to a break down of the M-O π -bonding interaction, resulting in a basic oxo ligand which is e.g. not stable towards protonation. These findings led to the definition of the “Oxo-

³ For a detailed discussion of PCET chemistry see Section 2.

Wall¹⁹: There is no stable terminal transition metal oxo complex in a tetragonal coordination sphere with d-electron counts higher than d^5 . Since oxidation states are limited for the late transition metals, and very high oxidation states would favour the extrusion of O_2 or the oxidation of the environment, the oxo wall is placed between group 8 and 9 of the periodic system.^[20]

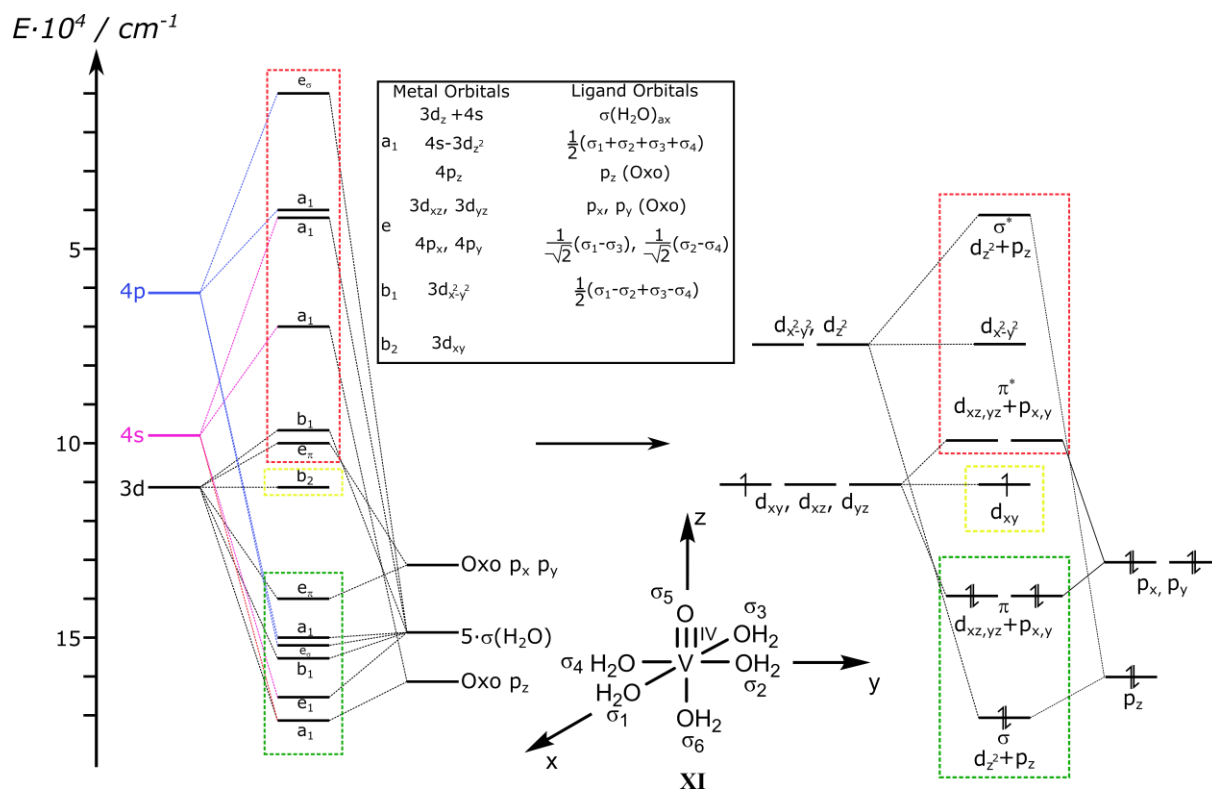


Figure 13: Full frontier orbital MO scheme of the vanadium(IV) oxo complex **XI** after Ballhausen and Gray with bonding orbitals (green) non-bonding orbital (yellow) and anti-bonding orbitals (red) (left)^[19] and simplified deduced MO scheme of a metal ion in near octahedral coordination sphere with an oxo ligand (right).

Late transition metals often favour lower coordination numbers than the (pseudo)octahedral coordination discussed above, but the lower coordination numbers change the d-orbital splitting in e.g. tetrahedral and square-planar complexes and thus the starting point of the metal oxo bonding discussion changes. The t_2 orbital set in tetrahedral coordination interacts with the oxo ligand, forming the σ - and π -bonding interactions, while the former e orbital set remains unchanged, thus forming two non-bonding orbitals (Figure i4, left).⁴ A similar situation arises for a square-planar oxo complex. Here, the d_{z^2} and d_{yz} orbitals do not interact with the oxo moiety and are therefore non-bonding orbitals. The only difference to the (pseudo)tetrahedral coordination is that the non-bonding orbitals are not degenerate as for the trigonal coordination (Figure i4, right). With the two non-bonding orbitals in (pseudo)tetrahedral and (pseudo)square-planar geometry, the formal oxo wall in these coordination environments is shifted from a d^5/d^6 to a d^7/d^8 configuration. The oxo wall in these coordination spheres is therefore formally between group 10 and 11, and up to date, there is no isolated transition oxo complex that violates the oxo wall.^[18]

⁴Please note, that here the z-axis in tetrahedral coordination is ligand centred for clarity.

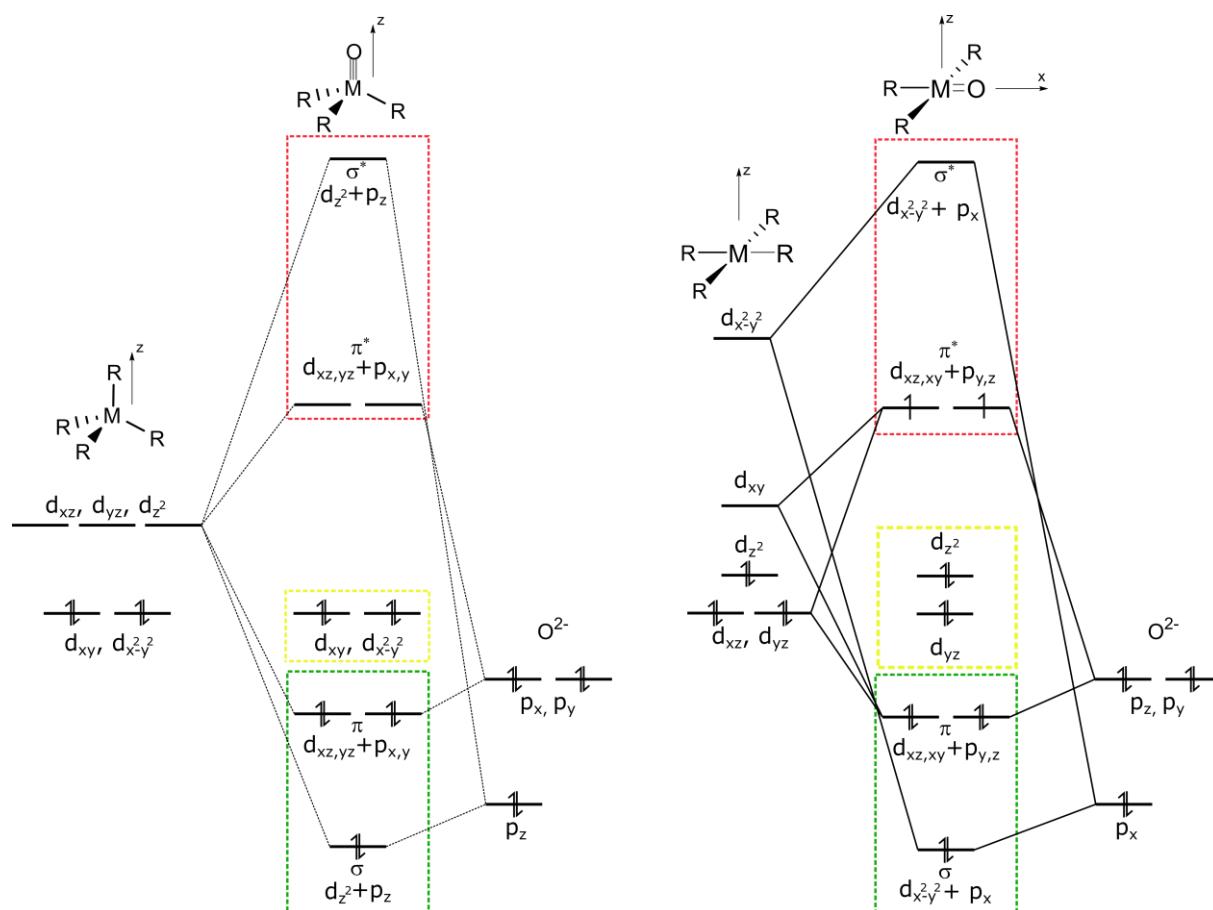


Figure i4: Schematic MO scheme for a terminal oxo complex in trigonal coordination sphere depicted exemplarily for a d^4 metal ion (left). Schematic MO scheme for a terminal oxo complex in C_{2v} symmetry depicted exemplarily for a d^6 metal ion (right)

The M-O π^* population of late, electron rich, group 9 transition metals (Rh, Ir) explains their prevalence in synthetic hydroxylation, water oxidation and related (isoelectronic) nitrene transfer chemistry.^[21–26] The isolation of the reactive late transition metal oxo/nitrene intermediates is therefore important for a detailed understanding of their reactivity. The few reported examples of this complex class in group 9 are dominated by pseudo(tetrahedral) geometries and terminal imido complexes are by far more common than terminal oxo complexes which most likely can be attributed to their higher steric protection from the N-R group (Figure i5).^{[27–33][34][35–37]} Only two terminal oxo complexes of group 9 are reported, both are closed-shell and in (pseudo)-tetrahedral coordination. The oxotrimethyliridium complex **XXI** by Wilkinson is in the iridium(V) oxidation state and thus exhibits a triple bond, while the thermolabile cobalt oxo complex **XVII** reported by Anderson is in the cobalt(III) oxidation state and thus exhibits double bond character.^{[33,36].5} The lower bond order of **XVII** is reflected by its higher reactivity compared to **XXI**. While **XXI** is mostly inert and can only oxygenate phosphines,^[38] cobalt oxo **XVII** additionally is a strong hydrogen atom abstractor with an estimated bond dissociation free energy (BDFE) of 85 kcal mol^{-1} .

⁵ Anderson et al. discuss a triple bond in their paper even though the electron count $[\text{Co(III)}, d^6]$ formally forbids a triple bond in this geometry. Additionally, their own DFT computations have the Co-O σ^* -orbital as the HOMO thus reducing the bond order to two. For this reason, complex **XVII** is discussed to obtain double character, to stay consistent with the oxo-wall discussion above.

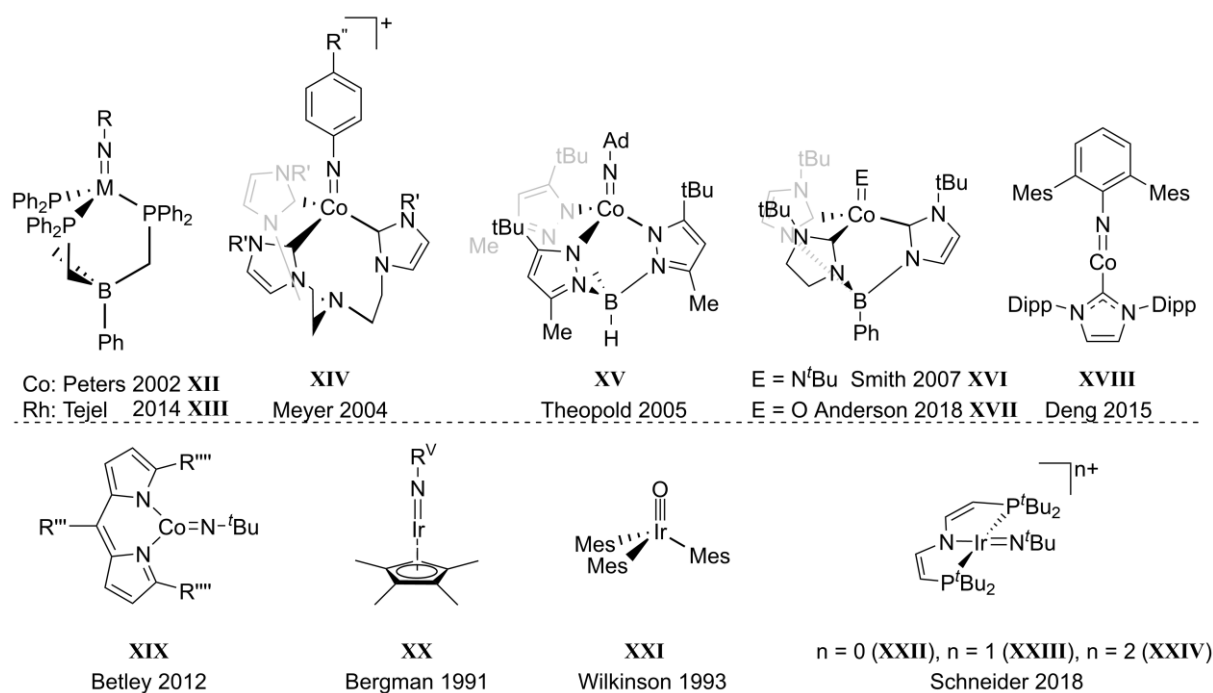


Figure i5: Literature reported isolated group 9 terminal imido and oxo complexes of cobalt^[27–33], rhodium^[34] and iridium^[35–37]. R(Peters) = Tol, R(Tejel) = Ad, Dipp, C₆F₅; R' = H, Me; R'' = OMe, Me; R''' = 3,5-bis(trifluoromethyl)phenyl; R'''' = 2,6-bis(diphenylmethyl)-4-methylphenyl R^v = ^tBu, SiMe₂^tBu, 2,6-dimethylphenyl, Dipp.

The reported group 9 oxo/imido complexes have a diamagnetic ground state, but catalytic nitrene and oxygenation transfer is often associated to proceed via radical pathways and therefore accessible open-shell states are discussed for the intermediates.^[39,40] The only exceptions here are the two-coordinate cobalt(II) imido complex **XVIII** of Deng et al. and the square-planar iridium(III/IV/V) imido redox series **XXII-XXIV** by Schneider et al (Figure i6).^[31,37] Iridium imide **XXII** represents an unprecedented iridium complex with a triplet ground state, which is strongly stabilised by spin-orbit coupling as shown by SQUID magnetometry and computational analysis. Substantial N-radical “imidyl” character of **XXII** with a $(\pi_1^*/\pi_2^*)^2$ configuration is predicted by computations, in perfect agreement with the MO scheme depicted in Figure i4, resulting in ambiphilic nitrene transfer reactivity with CO₂, PMe₃ and H₂. On the other hand, the cationic imido species **XXIII** does not show reactivity with selected nucleo- and electrophiles, which is attributed to spin-delocalisation by spin-orbit coupling and is also in line with the formally higher Ir-N bond order. Reactivity studies of the dicationic complex **XXIV** were hampered by its thermally instability forming the cationic nitride complex **XXVI** and isobutene.^[37]

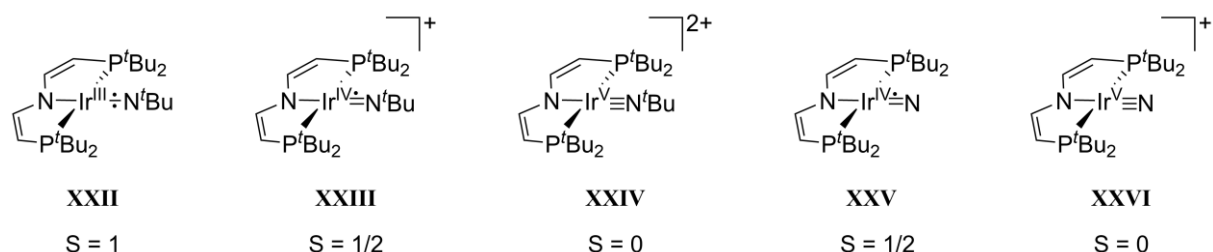
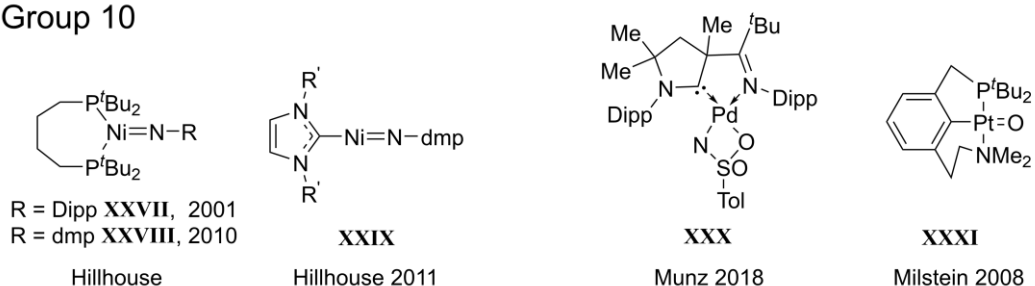


Figure i6: Square-planar terminal imido and nitride complexes with their formal oxidation states reported by Schneider et al.^[37,41]

Examples of terminal imido/oxo complexes beyond group 9 are even scarcer.^{[42–44][45][46]} Here, a series of nickel imides **XXVII-XXIX** by Hillhouse et al., a palladium imide **XXX** by Munz and co-workers, a platinum(IV) oxo **XXXI** by Milstein et al, and very recently a copper(I) supported open-shell nitrene complex **XXXI** by Betley and co-workers were reported (Figure i7).^[42–47] The platinum oxo complex **XXXI** of Milstein is a thermolabile

compound which inserts the oxygen atom into the Pt-P bond when heated to room temperature. **XXXI** has diverse oxygenation chemistry with several substrates like carbon monoxide, phosphines, dihydrogen, hydrides and water.^[47] With an electron count of d^6 , **XXXI** exhibits a Pt-O double bond but is significantly more reactive than the cobalt oxo **XVII**, thus highlighting the importance of the accessibility of the metal oxidation state on the stability/reactivity of the formed oxo complex. Very recently, a copper supported triplet nitrene complex **XXXII** was isolated by Betley and co-workers which shows diverse nitrene transfer chemistry.^[46] Even though the short Cu-N bond distance (1.75 Å) suggests multi-bonding character, XAS studies derived a copper(I) oxidation state which was further refined by SORCI-CAS⁶ computations. Here, the copper(I)-triplet (d^{10}) nitrene configuration dominates the ground state (58%), while the copper(II) doublet imidyl configuration only sums up to 25%. These results suggest, that **XXXII** can be considered as the only stable imido complex beyond the oxo wall, stabilized by the enormous steric bulk around the reactive centre. As discussed in this Section, isolated terminal oxo complexes beyond group 8 are rare complexes and especially only closed-shell species have been published until now. In Chapter II of this thesis the isolation and characterisation of a new terminal iridium oxo complex with a triplet ground state will be discussed.

a) Group 10



b) Group 11

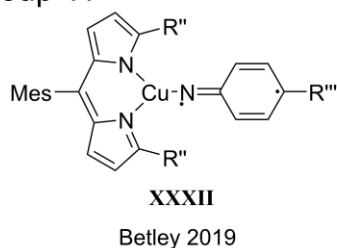


Figure i7: a) Literature reported terminal imido and oxo complexes of group 10 of nickel^[43,44], palladium^[45], platinum^[47]; R' = 1,1,7,7-tetraethyl-1,2,3,5,6,7-hexahydro-3,3,5,5-tetramethyl-s-indacene; b) Only literature reported terminal imido complex of copper^[46]. R'' = 3,5-bis(trifluoromethyl)phenyl R''' = O^tBu, ^tBu.

⁶ Spectroscopy-oriented con

figuration interaction complete active space

2. Proton-Coupled Electron Transfer

“Among the most elementary and significant of all reactions is the transfer of a hydrogen atom...”

Ahmed H. Zewail, Nobel Laureate 1999^[48]

2.1 General Aspects in PCET Chemistry

This Section will describe and define the terms proton-coupled electron transfer (PCET), hydrogen atom transfer (HAT) or stepwise proton-electron steps (PTET/ETPT), which are relevant to the chemistry of terminal oxo complexes. Transfer of electrons and protons is ubiquitous in bioenergetic processes in nature (e.g. Cytochrome P450, OER in photosynthesis, nitrogen fixation)^[7,49,50], synthesis (e.g. Hydroxylations, Hydroaminations, Haber-Bosch process)^[50,51] and artificial energy conversions (e.g. fuel cells, combustion)^[52], just to name a few, and many excellent reviews^[53,54] and books^[48] have been published on the topic. Meyer et al. introduced the term Proton-coupled electron transfer (PCET) first in 1981 for concerted transfer of one proton and one electron, but the term is nowadays used more broadly for the general transfer of (multiple) protons and electrons even from different reaction sites.^[55] Many sub-terms have been introduced in the literature to differentiate between the various expressions and mechanisms of PCET chemistry (Figure i8, a).

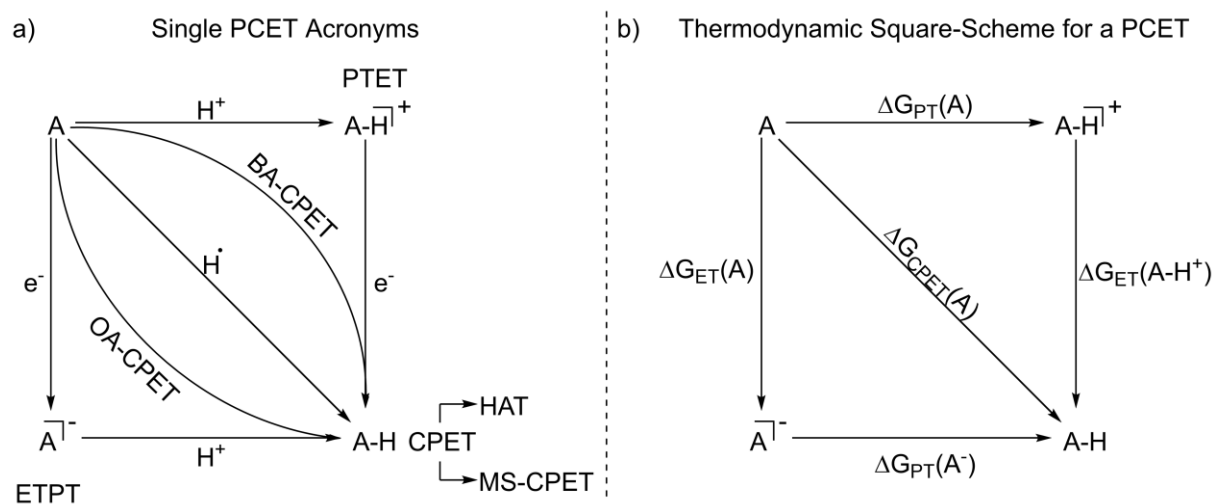


Figure i8: a) Acronyms for single-proton single-electron PCET transformations of an acceptor molecule A. PTET = Proton-transfer electron-transfer; CPET = Concerted proton-electron Transfer; ETPT = Electron-transfer proton-transfer; BA-CPET⁷ = Basic asynchronous concerted proton-electron transfer; OA-CPET = Oxidative Asynchronous CPET; MS-CPET = Multiple-site CPET; HAT = Hydrogen Atom Transfer. b) Thermodynamic square-scheme for a PCET. ΔG_{ET} = Free enthalpy of electron transfer, ΔG_{PT} = Free enthalpy of proton transfer, ΔG_{CPET} = Free enthalpy of concerted proton-electron transfer

The original definition of the PCET term by Meyer et al. is best described as a concerted proton-electron transfer (CPET) as first discussed by Savéant et al.^[56], while reactions with subsequent proton/electron transfer are referred to as PTET or ETPT processes, respectively.^[53] For a CPET processes in which the formal hydrogen atom comes from multiple reaction sites (e.g. proton from the ligand, electron from the metal) the term multi-centre (MS)-CPET is commonly used in the literature, while a process in which the hydrogen atom is transferred from one

⁷ The abbreviations BA- and OA-CPET were introduced in this thesis for space reasons and are written out in their original publication by Anderson et al.

reaction site is called hydrogen atom transfer (HAT).^[53] Recently the group of Anderson gave experimental proof for another nuance in PCET chemistry, an asynchronously concerted pathway, which is computationally predicted to proceed via lower activation barriers than the fully synchronous transfer (Figure i8, a, bend arrows). Here, the transition state is closer to either an oxidative (OA-CPET) or to a basic (BA-CPET) transfer character.^[57,58] The distinction between the different mechanistic models is often ambiguous. This can be visualised on the example of the crucial reaction step of cytochrome P450 (see Section 1.1, Figure i1). Here, the Fe(IV) oxo moiety reacts with an unactivated hydrocarbon in which the proton and the electron both arise from one C-H bond rendering this reaction as a HAT, but on the acceptor site the proton binds to the oxygen and the electron quenches the radical cation in the porphyrin unit rendering it as a MS-CPET.

2.2 PCET Thermochemistry

“Not radical character but driving force quantifies PCET chemistry”

Key message of James M. Mayer, 1998^[59]

The (free) enthalpy of a formal hydrogen atom transfer can be split, following Hess' law, into the sum of enthalpies of proton transfer and subsequent electron transfer (Figure i8, b, eq.i1).^[60] The pK_A value of a substance is derived as the decadic logarithm of the proton transfer equilibrium constant with a reference base (eq.i2)^[61], thus the free enthalpy of proton transfer ΔG_{PT} is derived for standard conditions via eq.i3. The free energy of electron transfer can be derived analogously from the difference of the redox potentials between two reactants following eq.i4. With these equations at hand, the reaction free enthalpy of a CPET step is obtained from eq.i5.



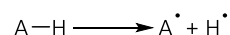
$$\Delta G_{CPET} = \Delta G_{PT} + \Delta G_{ET} \quad \text{eq.i1}$$

$$\Delta pK_A = \log_{10} \Delta K_{eq} \quad \text{eq.i2}$$

$$\Delta G_{PT} = RT \ln K_{eq} = RT \ln 10 \Delta pK_A = 5.70 \Delta pK_A \quad \text{eq.i3}$$

$$\Delta G_{ET} = zF\Delta E^0 = 96.5\Delta E^0 \quad \text{eq.i4}$$

$$\Delta G_{CPET} = 5.70 \Delta pK_A + 96.5\Delta E^0 \quad \text{eq.i5}$$



$$BDFE(A-H) = 5.70 pK_A + 96.5E^0 - 96.5E^0(H^+/H_{2, solv}) + \Delta G_{solv}^0(H^\bullet) + \Delta G_f^0(H^\bullet) \quad \text{eq.i6}$$

$$\rightarrow BDFE(A-H) = 5.70 pK_A + 96.5E^0 + C_G \quad \text{eq.i7}$$

$$C_H = C_G - T[S_f^0(H^\bullet) + \Delta S_{solv}^0(H^\bullet)], \text{ for } \Delta S_{solv}^0(A-H) \approx \Delta S_{solv}^0(A^\bullet) \quad \text{eq.i8}$$

Figure i9: Thermodynamic equations (in kJ mol^{-1}) based on the square scheme Figure i8,b for a CPET reaction between an acceptor molecule A' and a donor molecule D-H (top) and derivation of the absolute bond dissociation (free) energy equation in analogy to Bordwell and Tilset.^[62,63]

Absolute bond dissociation (free) energies BD(F)E's are commonly used in PCET literature to simplify the comparison between different substrates. To convert the relative reaction free enthalpy of eq.i5 into a BDFE value, the enthalpy of the formally released "free hydrogen atom" must be considered. Here, three terms are important:

1) The standard reduction potential of the H[·]/H⁺ couple in the respective solvent⁸, 2) The free enthalpy of solvation $\Delta G_{\text{solv}}^0(\text{H}^{\cdot})$ and 3) The free enthalpy of formation $\Delta G_{\text{f}}^0(\text{H}^{\cdot})$ of the hydrogen atom (eq.i6).^[63] The enthalpy of solvation for a hydrogen atom is commonly approximated by the solvation enthalpy of argon, while in older literature the solvation enthalpy of H₂ was used.^[64] The three terms are commonly abbreviated in the literature with the solvent depended term C_G yielding Bordwell's equation (eq.i7).^[62] Especially in organic literature, the enthalpic term bond dissociation energy (BDE) is commonly used. For the derivation of a BDE the C_G term has to be replaced by the term C_H, in which the entropic contribution of the hydrogen atom formation is subtracted from C_G (eq.i8), under the assumption that the solvation entropy difference between A-H and A[·] is negligible.^[65] This assumption holds true for most organic PCET reagents, but cannot generally be applied to transition metal complexes, since a PCET from the latter may lead to electronic rearrangement and thus results in significant changes in the solvation entropy.^[66] Here, equilibration techniques and calorimetric measurements, as described in the main part of this thesis, enable the direct measurement of the CPET reaction enthalpy for transition metal complexes.

A long-standing discussion in PCET chemistry was the necessity of radical character for hydrogen atom transfer. Organic HAT transformations generally do involve radicals (RO[·], Cl[·]), while the oxidation of hydrocarbons with chromates or permanganates start from diamagnetic species.^[59] Radical intermediates are discussed in the literature to be part of the mechanism of permanganate oxidation reactions.^[67,68] First hints, that the radical character is not rendering the HAT reactivity of transition metal compounds gave the analysis of the rhenium(II) oxo [(bis-acetylene)Re(II)O]⁻ anion **XXXIII** by Mayer et al. **XXXIII** exhibits significant Re=O π^{*}-character and yields upon one-electron oxidation the rhenium(III) oxo **XXXIV** which indeed shows radical reactivity but not arising from the oxo ligand. Instead of the expected formation of an hydroxo ligand, the metal centre is the reactive site, yielding the dimerization of **XXXV** to **XXXVI** or, in low yields, hydrogen atom abstraction from tributyltin hydride, to the rhenium hydride complex **XXXVI** (Figure i10).^[69] This finding lead to the detailed kinetic investigation of the oxidation of hydrocarbons with closed-shell CrO₂Cl₂, in which the bimolecular attack of CrO₂Cl₂ was found to be the rate determining step.^[70,71] Furthermore, a positive linear correlation between the activation enthalpy and the reaction enthalpy is found, supporting the formation of carboradicals over carbocations. Additionally for substrate oxidation with closed-shell MnO₄⁻, a linear free energy relationship between the bond strength and rate constant is found, which leads to the key message: Not radical character but the driving force of the reaction is rendering a proton-coupled electron transfer.^[59]

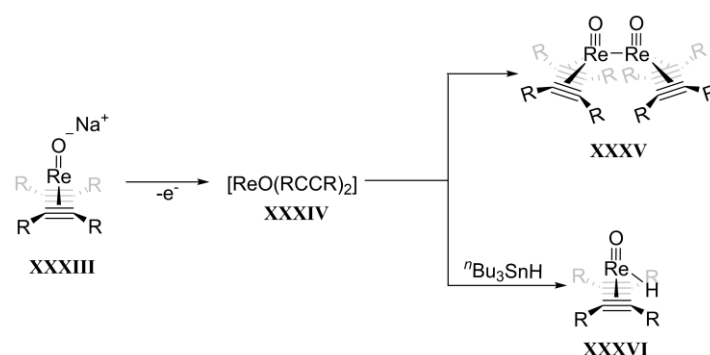


Figure i10: Radical reactivity of rhenium(II) oxo complex **XXXV** reported by Mayer et al.

⁸ Potentials referenced vs. the ferrocene/ferrocenium couple in organic media.

The PCET chemistry of transition and f-block metals is generally of interest, since the weakest found Element-Hydrogen bonds are found in this field. One important reagent here is samarium diiodide.^[72] The oxophilic Sm^{2+} ion weakens the O-H bonds of alcohols and water by up to 280 kJ mol^{-1} through coordination to the oxygen atom and thus enables the hydrogen atom transfer from the O-H group to a substrate.^[73,74] Also simple transition metal hydrides ($\text{BDFE}[\text{CpCr}(\text{CO})_3\text{-H}] = 240 \text{ kJ mol}^{-1}$; $\text{BDFE}[\text{CpFe}(\text{CO})_2\text{H}] = 210 \text{ kJ mol}^{-1}$) are commonly used in catalysis and can possess BDFE values close to the limit ($\text{BDFE}(\text{H}_2, \text{gas})/2 = 203 \text{ kJ mol}^{-1}$) of thermodynamic favourable dihydrogen gas formation.^[53] Transition metal ion PCET chemistry is long known to be critically pH dependent, which was first rationalized by Pourbaix in 1945.^{[75],9} Here, the chemistry of transition metal oxo species was of special interest, since these species were important in biochemical (see Section 1.1) and organic oxidation reactions.^[76,77] One of the best analysed examples in the field is the aquo-hydroxo-oxo complex series $[\text{cis}(\text{bpy})_2(\text{py})\text{RuOH}_x]^{y+}$,¹⁰ **XXXVII(x,y)** whose ET, PT, PCET, hydride transfer and hydrocarbon oxidation chemistry was investigated in detail (Figure i11, a).^[53,78,79]

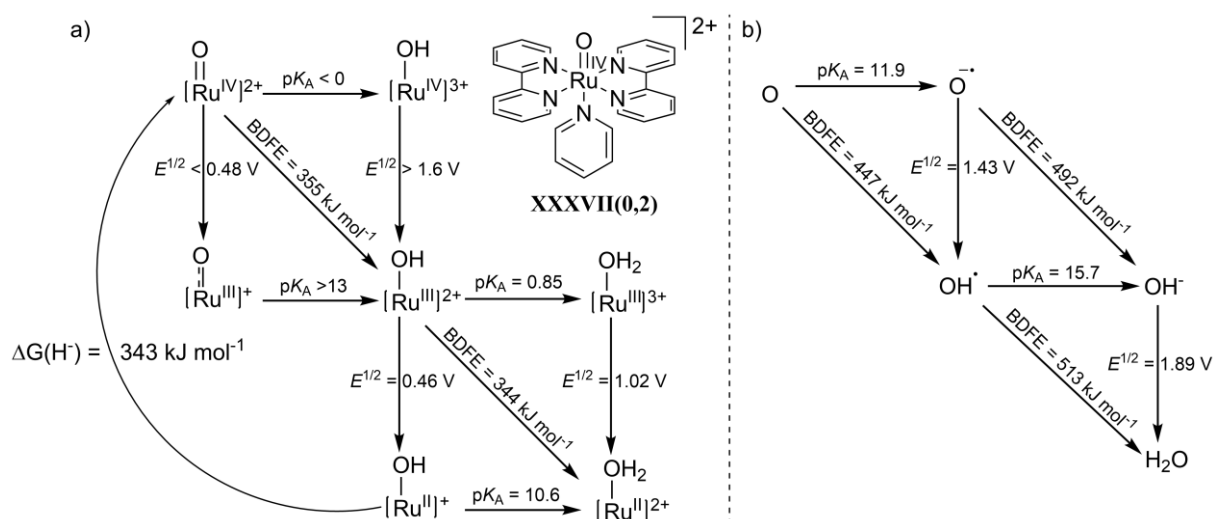


Figure i11: a) Thermodynamic data of the PCET chemistry of **XXXVII** in aqueous solution. Potentials are given vs. NHE. Values without an equal sign are upper limits. ^[53,78,79] b) Thermodynamic data of the PCET chemistry of water. Potentials are given vs. NHE. ^[53,80]

The most interesting finding in these studies, expressed in the poorly defined pK_A and $E^{1/2}$ values between **XXXVII(0,2)** and **XXXVII(1,2)**, is the strong preference of **XXXVII(0,2)** to undergo a CPET step over a stepwise proton/electron transfer. The O-H BDFE of water strongly decreases by 160 kJ mol^{-1} (Figure i11, b) upon coordination to **XXXVII**, but still yields high BDFE values of 355 kJ mol^{-1} and 344 kJ mol^{-1} for **XXXVII(0,2)** and **XXXVII(1,2)**, respectively. This rationalizes the high hydrocarbon oxidation capability of **XXXVII** and related systems.^[81] This thesis will in the following Chapters focus on the investigation of PCET chemistry of heavy metal complexes.

⁹ In the preface of this book it is mentioned that the first version of the atlas is published in the dissertation of M. Pourbaix in 1945.

¹⁰ bpy = bipyridine; py= pyridine

3. Computational Thermochemistry

The main Chapters II and IV include the computational rationalisation of a spin-orbit coupling effect (SOC) on PCET solution thermochemistry. The following Section will therefore give a brief introduction to the performed computational methods and to the treatment of relativistic effects. Since this is no pure theoretical work, this Section is meant as a brief introduction for the interested reader and to find orientation in the performed methods and corresponding literature.

3.1. Computational Methods

“I think I can safely say that nobody understands quantum mechanics”

Richard P. Feynman, 1964¹¹

Two main methods are frequently used for the computation of thermochemical data. Density functional theory (DFT) and wavefunction theory (WFT) based *ab initio* (from first principle) methods with the Hartree-Fock (HF) theory at the fundament.^[82] On the one hand, modern DFT methods are indispensable tools for the fast, cost efficient computation of ground- and excited-state structures and many more properties, but on the other hand they lack a systematic improvement towards the “real” state of the analysed system.^{[82-84],12} The solution of the time-dependent Schrödinger equation (eq.i9) can yield the desired “real” properties of a molecule, but only for non-trivial systems like H_2^+ etc. a strategy for its exact solution is known.^[84]

$$\hat{H}\Psi = E\Psi \quad \text{eq.i9}$$

$$\hat{H} = \hat{T} + \hat{V}_{Ne} + \hat{V}_{ee} \quad \text{eq.i10}$$

A systematic approach towards the exact solution of eq.i9, and therefore towards a better understanding of the errors of the computations, can be achieved by *ab initio* techniques.^[85] The Hartree-Fock method is based on a mean-field approach, in which electron n only experiences the mean electric field of the other $n-1$ electrons of the molecule. This non-interacting electrons approach thus only represents a rough estimate of the electronic situation in the molecule.^[86,87] Electrons as charged particles experience coulombic interactions with other electrons in the molecule and their movement must therefore be correlated. This can be systematically treated by post Hartree-Fock methods by introducing the correlation energy E_c as the difference between the HF energy E_{HF} to the (unknown) exact energy E_{exact} of the system (eq.i11).^[87,88] The correlation energy is, due to the variational principle, always a negative quantity and “stabilises” the system.

$$E_C = E_{exact} - E_{HF} \quad \text{eq.i11}$$

¹¹ Richard P. Feynman on his Messenger Lecture at Cornell University. I am deeply sorry for all the footnotes in this Section.

¹² For time reasons, DFT is not discussed in detail. An excellent book for a chemist’s introduction to DFT by Koch and Holthausen can be found in the quotation.

¹³ Electronic Hamiltonian \hat{T} = electron kinetic energy, \hat{V}_{Ne} = potential nucleus/e⁻ energy \hat{V}_{ee} = potential e⁻/e⁻ energy.

The correlation treatment is encountered by “opening” the unoccupied orbitals for the electrons through an excitation operator. A straightforward approach for the excitation treatment is called configuration interaction (CI) in which e.g. electron i from orbital Φ_i is excited into the unoccupied orbital Φ_a for a single excitation, electrons i and j from the orbital Φ_i and Φ_j are excited into unoccupied Φ_a and Φ_b for a double excitation etc. The specific method is then named after the performed excitations (e.g. CISDT = CI with single, double and triple excitations). Full configuration interaction (FCI) is reached for n -fold excitations and here the only difference to the exact solution of the Schrödinger equation is due to the use of finite basis sets.^{[87],14}

$$\Psi_{\text{CI}} = \Phi_0 + \sum_{i,a} C_i^a \Phi_i^a + \sum_{\substack{i<j \\ a<b}} C_{ij}^{ab} \Phi_{ij}^{ab} + \dots \quad \text{eq.i12}$$

Unfortunately, an FCI treatment of the correlation problem scales with the number of electrons n of the system with basis functions N to N^n , thus the computational costs for the description of a 5d metal complex system with $n > 100$ electrons are elusive.^[87] Therefore, the excitations need to be treated in a more cost-efficient manner. The modern “gold standard” of computational chemistry is the coupled-cluster (CC) approach with single, double and perturbative triple excitations CCSD(T).^{[89],15} Here, the excitations are treated within an exponential operator \hat{T} (eq.i13), which is expanded by a Taylor series (eq.i14). The higher excitation amplitudes are now expressed as products of the single and double excitations (for CCSD), which is drastically reducing the computational costs by maintaining high predictive power.^[87]

$$\Psi_{\text{CC}} = \exp(\hat{T}) \Psi_{\text{HF}} \quad \text{eq.i13}$$

$$\exp(\hat{T}) = 1 + \hat{T} + \frac{1}{2!} \hat{T} \hat{T} + \frac{1}{3!} \hat{T} \hat{T} \hat{T} + \dots, \text{ with } \hat{T} = \hat{T}_1 + \hat{T}_2 \text{ for CCSD} \quad \text{eq.i14}$$

For comparison, the computational error of CCSD(T) for small molecules (BH, HF, H₂O), compared to a FCI computation, is ~ 16 times smaller than for a CISDT computation, while the formal excitation level is the same.^[87] Even though the computational demand of the CCSD(T) method is drastically reduced compared to CI methods, it nevertheless scales with N^7 .^[90] Therefore, the computation of medium-sized or larger transition metal complex systems is currently prohibitive, even on modern computer clusters. This issue can be addressed by several methods such as partitioning or localization schemes.^[91-96] An “our own n -layered integrated molecular orbital and molecular mechanics” (ONIOM) approach is partitioning the molecule in different “onion like” layers, in which the correlation problem is then treated on the inner layer at the high CCSD(T) level of theory, while the outer layer(s) are computed with cheaper methods e.g. DFT and Molecular Mechanics (MM) (Figure i12).^{[96-98],16} A possible truncation of the haemoglobin molecule from Section 1.1 could therewith include the iron and its direct coordination environment in the inner layer (Figure i12, green), the porphyrin ring in the medium layer (Figure i12, orange) and the protein chain in the outer layer (Figure i12, red). The ONIOM3 (three layers) energy is then derived via eq.i15. ONIOM methods perform excellently in several benchmarks and are therefore a good method for the computation of accurate energies for metal complex systems.^[96]

¹⁴ The term basis set will be briefly introduced later.

¹⁵ In conjunction with a complete basis set extrapolation

¹⁶ Please note that the outer layers are composed of the inner layer plus additional parts, e.g. the intermediate layer of Figure i12 also includes the iron centre.

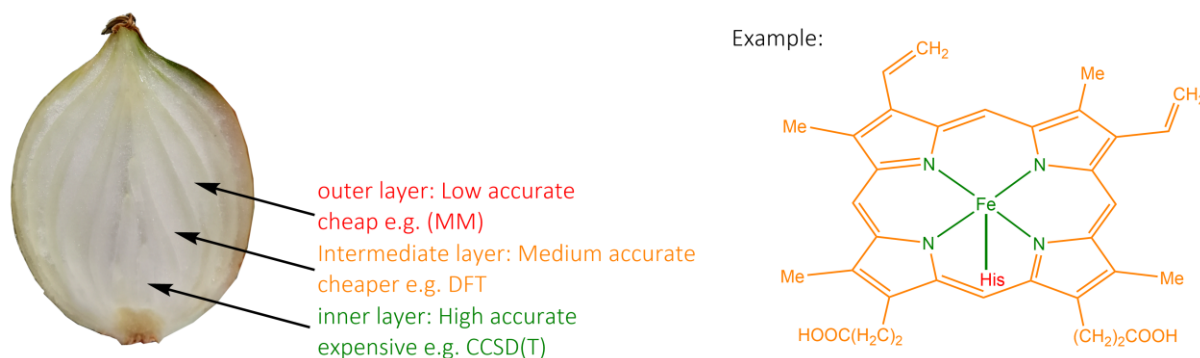


Figure i12: Illustration of the ONIOM approach based on Svenson et al.^[98]

$$E^{ONIOM3} = E_{Inner\ layer}^{High} + E_{Intermediate\ Layer}^{Medium} - E_{Inner\ Layer}^{Medium} + E_{Outer\ Layer}^{Low} - E_{Intermediate\ Layer}^{Low} \quad \text{eq.i15}$$

A second method, which does not rely on the truncation of the molecule into different layers but on the localisation of the correlation problem, is the domain-based local pairs of natural orbitals CCSD(T) (DLPNO-CCSD(T)) approach of the Neese group.^[94] Here, pairs of natural orbitals (PNOs)^[99,100] are constructed from a set of projected atomic orbitals (PAOs) which are assigned to a given electron pair specific local domain. This enables the localised treatment of the correlation problem or simply speaking: Electron i on one end of the molecule is not correlated with electron j on the opposite edge. The computational costs of the DLPNO method scale almost linearly with the system size, while 99.9% of the CCSD(T) correlation energy can be recovered, rendering DLPNO-CCSD(T) as a very cost efficient and precise method for accurate thermochemistry.^[95]

Besides the dynamical correlation mentioned above, the “static correlation” as a second contribution to the correlation energy must be mentioned. Static correlation describes the situation, in which the electronic ground state cannot be described with a single Slater determinant e.g. the ground state of a molecule is not a singlet or a triplet but a combination of both.^[87] Multiconfigurational character can already be observed for small molecules of the type XH_2 . While for water ($X = O$, $\sigma = 104.5^\circ$)^[101] the $3a_1$ orbital lies well below the $1b_1$ orbital (one Slater determinant is sufficient) the orbitals are close for methylene ($X = C$, $\sigma = 134^\circ$)^[102] and thus the singlet and triplet state are close in energy.^[103,104]

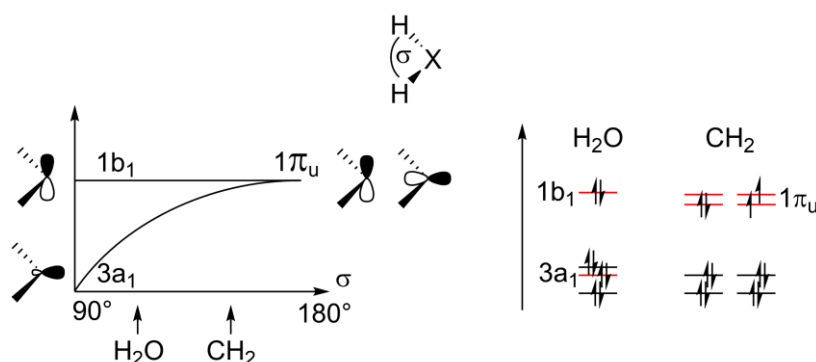


Figure i13: Walsh type diagram of the active orbitals for a XH_2 molecule (left)^[103] and simplified molecular orbital scheme for water and methylene deduced from the Walsh diagram. 1s electrons are omitted for clarity (right).

Multireference character is commonly addressed by a complete active space self consistent field (CASSCF) treatment. Here, the valence orbitals of a molecule are defined as active orbitals in which an FCI treatment is performed.^[105–108] Additionally, the MO coefficients of the active orbitals are optimised for a better description of the electronic, multireference ground state. On the example of Figure i13, the methylene molecule has **two**

electrons in the two active orbitals leading to a 2,2 CAS expansion. Several methods are known for the (expensive) combination of static and dynamic correlation and an excellent review on this topic is written by Shepard et al.^[109]

One particular method applicable to larger molecules is the *n*-electron valence perturbation theory of second order from the Cimraglia group (NEVPT2).^[110–112] NEVPT2 has two main advantages compared to the also common complete active space perturbation theory of second order (CASPT2).^[113,114] NEVPT2 exhibits exact size consistency^[115] and lacks of intruder states.^{[116],17}

The predictive power of any computation is always determined by the methods level of theory and equally important by the applied basis set. An excellent book Chapter by Jensen et al. is written on this topic.^[117] A given basis set is a set of functions for the atomic orbitals (AO) of the atoms in the molecule, which are then yielding the molecular orbitals (MO) in the computation as linear combinations (LCAO approach).¹⁸ The simplest basis set of single-zeta (SZ) type only has functions for the occupied AOs (e.g. *s*- and *p*-type functions for Li-Ar) and thus has no flexibility to describe bonding interactions. A double-zeta (DZ) type basis adds functions with one higher angular momentum than the occupied AOs (e.g. *d*-orbitals for *p*-block elements) etc. Additionally, polarisation and augmentation functions can be added to a given basis to further enhance its flexibility for chemical bonding.^[117] While general chemical trends can already be described on low level basis sets (e.g. double zeta), accurate thermochemistry needs computations close to the complete basis set (CBS) limit. The Karlsruhe basis sets denoted e.g. def2-TZVP (second generation-triple zeta valence + polarisation) have been shown to be close to the DFT CBS limit with rational computational costs and are thus frequently used in the literature.^[118] For *ab initio* methods the correlation consistent Dunning basis sets (cc-VnZ, correlation consistent-*n*-zeta valence) are of particular interest, since they are designed in “shells”¹⁹ in which each shell captures a similar amount of correlation energy, thus enabling an accurate extrapolation to the CBS.^[119,120] The extrapolations are however only most accurate when large basis sets (*n* = Q, 5) are used.^[121] Here, explicitly correlated F12 extensions to the Dunning basis sets perform excellently and converge faster and closer to the CBS even when a double zeta basis is used. They rely on R12 methods (interelectronic distance) with non-linear terms and density fitting (RI) for faster convergence and are used in conjunction with explicitly correlated F12 coupled cluster expansions.^[122–127]

For this reason, this thesis will feature the ONIOM approach mentioned above, including CCSD(T)-F12/VTZ computations, and the DLPNO-CCSD(T) method for the accurate computation of 5d metal complex systems.

¹⁷ The cited papers show that CASPT2 is not generally fulfilling these criteria. For NEVPT2 the size consistency and the lack of intruder states are shown in the original publications.

¹⁸ Plane wave basis sets for surface chemistry are not discussed.

¹⁹ A shell refers to the cardinal number of the basis set e.g. First shell no correlation (HF), cc-VDZ = Second shell , cc-VTZ = third shell etc.

3.2. Relativistic Effects on Thermochemistry

“I know that Einsteins theory of special relativity is correct because every weekend goes by twice as normal”

Anonymous

The special theory of relativity was introduced by Albert Einstein in his 1905 publication “Zur Elektrodynamik bewegter Körper” and is based on one fundamental assumption: Light is moving at a constant, universal speed in vacuum.^[128] Many important quantities can be deduced from this elemental assumption, but for chemists the most important consequence is the acceleration of the inner electrons of heavy elements, which leads to the relativistic contraction and stabilisation of the s- and p-electrons, while the d- and f-electrons are destabilised.^[129] Several basic phenomena are attributed to this scalar relativistic effect such as the yellow colour of gold, the “inert-pair” effect in main group chemistry or the tendency for higher oxidation states of 5d metals compared to their 4d analogues.^[130] For valence electrons the relativistic effect scales with $\sim Z^2$.^[131] A second important relativistic effect, which also scales with $\sim Z^2$,^[132] is the coupling of the spin- and angular momentum of the electron, termed spin-orbit coupling (SOC). Even though SOC also scales with $\sim Z^2$ for valence orbitals, it already has a non negligible effects on the F + H₂ reaction cross section.^[133] Furthermore, the enhanced reactivity of 5d metals in gas phase methane activation, compared to their 4d analogues, can be explained by high relativistic stabilisation and significant SOC contributions on the formed carbene complexes.^[134] The scalar relativistic effects are routinely incorporated in general quantum chemistry, while SOC effects are mostly neglected, since they are assumed to be “quenched by the ligand field”.^[135–139] Contrary to the theory Kývála and Rulišek reported in 2008 on the computational prediction of M^{3+/2+} (M = Ru, Os) reduction potentials of twelve different complexes by multireference methods. Here, the inclusion of SOC was indispensable for the agreement with the experiment, resulting in an average potential shift of –70 mV and –300 mV for ruthenium and osmium, respectively.^[140] A vivid review on relativistic effects in chemistry is given by Pyykkö.^[141]

Relativistic effects are included in the time-dependent Schrödinger equation. An approach for its solution is the Dirac-Fock (DF) method, which uses a four-component Hamiltonian with time as a variable. For the majority of molecules with >2 atoms this approach is elusive, since the DF method has high computational costs and also suffers from negative energy solutions.^[142] Additionally, dynamic correlation is not included in the classic DF method resulting in a good description of relativistic effects on cost of the description of correlation effects. For this reason, several empirical approaches have been developed to add relativity to non-relativistic methods. For heavy metals the electrons are often divided into valence and core electrons (for correlated methods) in which the latter are then described with a scalar-relativistic electron core potentials (ECP), but also all-electron scalar relativistic basis sets (SARC) are known.^[143,144] ECPs are derived from a relativistic all electron treatment of the corresponding atom and have shown to sufficiently describe the electronic situation of heavy metals. Additionally, they remove a significant number of electrons from the explicit treatment in the computation and are therefore crucial for the computation of big to medium sized 5d metal complex systems, e.g. the relativistic “Stuttgart” ECP on iridium^[145] removes 60 electrons from the explicit treatment. A comprehensive book Chapter on this topic is written by Dolg.^[146] One approach to reduce the four-component Hamiltonian of the time-dependent Schrödinger

equation to a two-component Hamiltonian is called zeroth order regular approximation (ZORA).^{[142,147–152],20} ZORA is e.g. the recommended method of choice for relativistic DFT computations in the ADF program packages (also including a spin-orbit coupling ZORA method) and is as well implemented in the ORCA program package.^[153,154] SOC can also be introduced to a non-relativistic, correlated computation by applying a spin-orbit mean field (SOMF) operator, which is reproducing the full relativistic²¹ SOC stabilisations of e.g. Pd, PdCl and Pd₂⁺ within a few wavenumbers.^[155] Further development of this methodology led to the inclusion of the SOMF operator into CASSCF.^[156] In the following chapters the SOC effect on 5d metal pincer PCET chemistry will be analysed by CASSCF-NEVPT2-QDPT computations, where QDPT is the quasi-degenerate perturbation theory. By QDPT a SOMF is applied on the CASSCF-NEVPT2 wavefunction for the explicit treatment of SOC.

²⁰ Two-component: Neglecting the positronic solutions and thus also the problems of the negative solutions. A book chapter by M. Barysz is given in the quotation.

²¹ Full Breit-Pauli Operator

4. Outline

4.1 Outline of Chapter II

The synthesis and characterisation of late transition metal oxo complexes is, as discussed in Chapter 1, an active field of chemistry, with only two reported examples in group 9.^[33,36] Here, open-shell systems are of special interest, since they are frequently suggested as key intermediates in oxygenation chemistry and in related nitrene transfer catalysis.^[39,40] The group of Schneider recently presented the successful isolation of a terminal iridium imido complex series [(PNP)IrN^tBu]ⁿ⁺ (n = 0,1,2) **XXII-XXIV** featuring the first iridium complex (**XXII**) with a triplet ground state.^[37] This is rendering the PNP pincer platform as an ideal ligand for the stabilisation of an isoelectronic terminal iridium oxo complex. Additionally, the open-shell ground state of **XXII** hints towards an open-shell character of the desired oxo species (Figure i14).

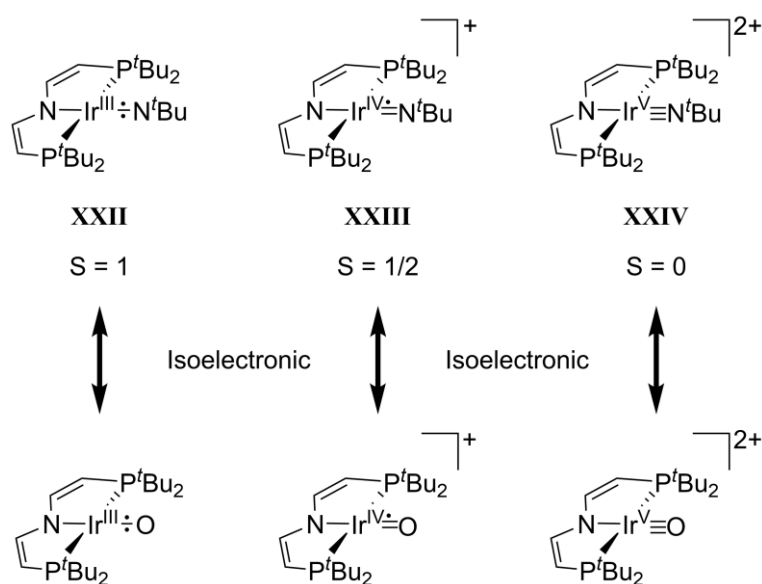


Figure i14: Potential isoelectronic terminal iridium oxo complexes to the terminal iridium imido complexes reported by Schneider et al.

In Section 1 of the upcoming Chapter, the synthesis and characterisation of an iridium(I,II,III) hydroxo complex redox series will be covered, including improved synthetic routes compared to the published ones in the Ph.D. thesis of *Dr. Markus van Alten born Kinauer*. In Section 2 the synthetic pathways towards the terminal iridium(III) oxo complex **4** and its full spectroscopic and magnetic characterisation will be discussed, including rationalisation by high level *ab initio* computations of the electronic structure of **4** and on the PCET thermochemistry of the O-H bond cleavage from **2** to **4**. The reactivity of **4** will be analysed in Section 3, including the determination of its philicity by reaction with selected small molecules, the derivation of the O-H bond strength (BD(F)E) of **2** by isothermal titration calorimetry and the comparison to the theoretically predicted value. The Section ends with the C-H bond oxygenation reactivity of **4**, including thermal reactivity and reactivity under irradiation. At the end a summary of the Chapter can be found in Section 4.

4.2 Outline of Chapter III

In the excurses Chapter III, results are discussed which arose from collaborations within our group with *Dr. Josh Abbenseth* (Section 1) and with the external collaboration partners from the Yale University *Prof. James Mayer* and *Prof Patrick Holland* and *Gannon Connor* as their Ph.D. student (Section 2).

Excursus 1: Interconversion of Phosphinyl Radical and Phosphinidene Complexes by Proton Coupled Electron Transfer discusses the calorimetric P-H BDE determination of a [(PNP)Os(H)(PHMes*)] phosphinyl radical complex **17** which forms the phosphinidene [(PNP)Os(H)(PMes*)] complex **19** upon PCET. Additionally, the derivation of the pK_A value of the cationic phosphide complex [(PNP)Os(H)(PHMes*)]⁺ **18** will be reported (Figure i15).

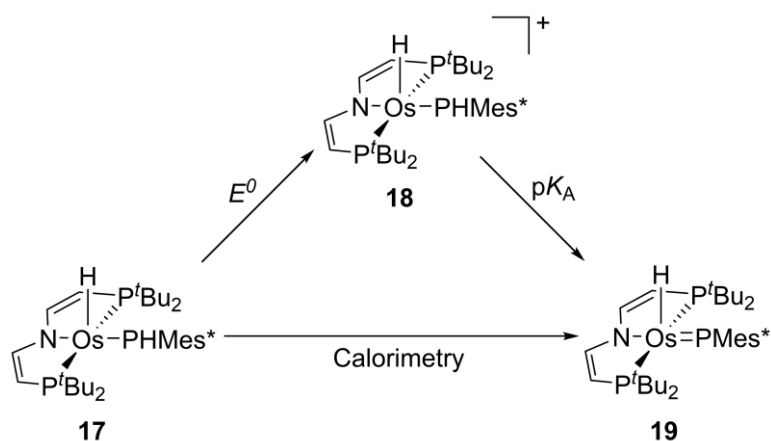


Figure i15: Thermodynamically examined PCET chemistry of the osmium phosphanyl radical/phosphinidene complex couple.

Excursus 2: is about the thermodynamic analysis of a rhenium(III) amide [(PNP)Re(Cl)(NH₂)], rhenium(V) nitride [(PNP)Re(Cl)(N)], complex couple **20/22** relevant for ammonia oxidation. Here, the N-H BDE of the double PCET step is determined by isothermal titration calorimetry (Figure i16).

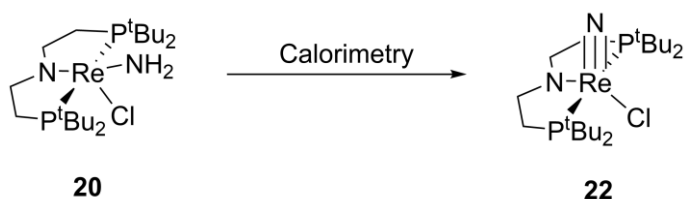


Figure i16: Investigation of the mean BDE of the double PCET step from **13** to **12** by isothermal titration calorimetry.

4.3 Outline of Chapter IV

In Chapter II, the O-H bond of the terminal iridium(II) hydroxo/iridium(III) oxo couple **2/4** was found to be stabilised by 2.9 kJ mol^{-1} as a reason of spin-orbit coupling (SOC).^[157] The small SOC effect on the O-H BDE was attributed to the negligible spin-change at the heavy metal centre upon PCET, resulting in similar SOC stabilisations for **2** and **4**, respectively. In Chapter IV the SOC effect on the PCET chemistry at heavy metal sites will be further analysed. Here, the rhenium(III) amine complex $[(P^HNP)Re(III)Cl_3]$ **23**, which has been shown to be a good starting platform for the incorporation of N_2 into benzonitrile, is chosen as a platform. **23** exhibits an extraordinary shift of its ^{31}P -NMR signal to $\delta_{31P} = -1526 \text{ ppm}$, which was assigned to high temperature independent paramagnetism (TIP) as a result of strong SOC. This finding is rendering this platform as an ideal candidate for the investigation of a high SOC effect on its PCET thermochemistry, especially since the corresponding product of HAT the rhenium(IV) amide $[(PNP)Re(IV)Cl_3]$ **24** is as well accessible.^[158] In chapter IV the PCET process from **23** to **24** will be thermochemically analysed via direct calorimetric measurement or via oxidation to the rhenium(IV) amine complex $[(P^HNP)Re(IV)Cl_3]^+$ **25** and subsequent deprotonation (Figure i17). On the computational site, the reaction thermochemistry will be computed “spin-free” via the ONIOM and DLPNO method (see Chapter I Section 3.1), while SOC is introduced by CASSCF-NEVPT2-QDPT computations (see Chapter I Section 3.2).

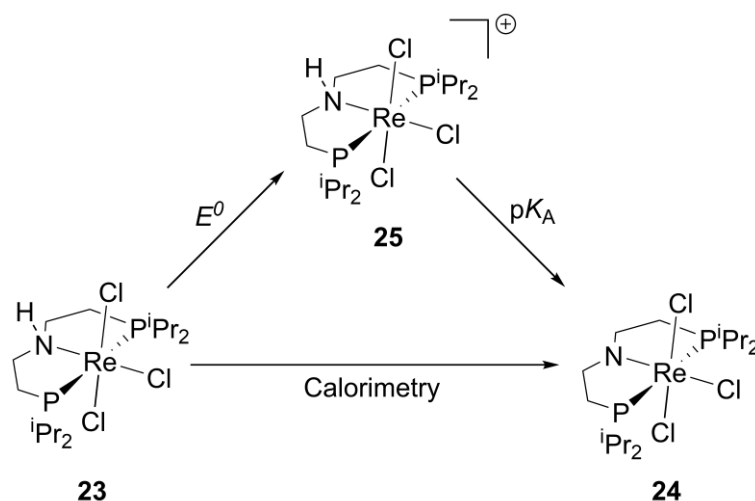


Figure i17: Examination scheme for the N-H BD(F)E of **15** by direct HAT (calorimetry) or oxidation and subsequent deprotonation (square scheme).

In Section 1, the structural, spectroscopic and magnetic properties of the rhenium(III) amine **23** (Section 1.1) and rhenium(IV) amide complex **24** (Section 1.2) are discussed, extended by the characterisation of the cationic rhenium(IV) amine complex **25** $[(P^HNP)Re(IV)(Cl)_3][BARF_{24}]$ (Section 1.3).

In Section 2, the *ab initio* computational rationalization of the spectroscopic and magnetic features of the complexes **23** (Section 2.1), **24** (Section 2.2) and **24** (Section 2.3) are presented by means of complete active space self consistent field (CASSCF) computations extend by n-electron valence perturbation theory of second order (NEVPT2) followed by quasi-degenerate perturbation theory (QDPT) to include spin-orbit coupling effects.

In Section 3, the (free) reaction enthalpy of the PCET reaction is measured experimentally (Section 3.1) and compared to the predicted value by the *ab initio* techniques DLPNO and ONIOM(CCSD(T)-f12/DFT) (Section 3.2).

At the end in Section 4, a summary of the Chapter can be found.

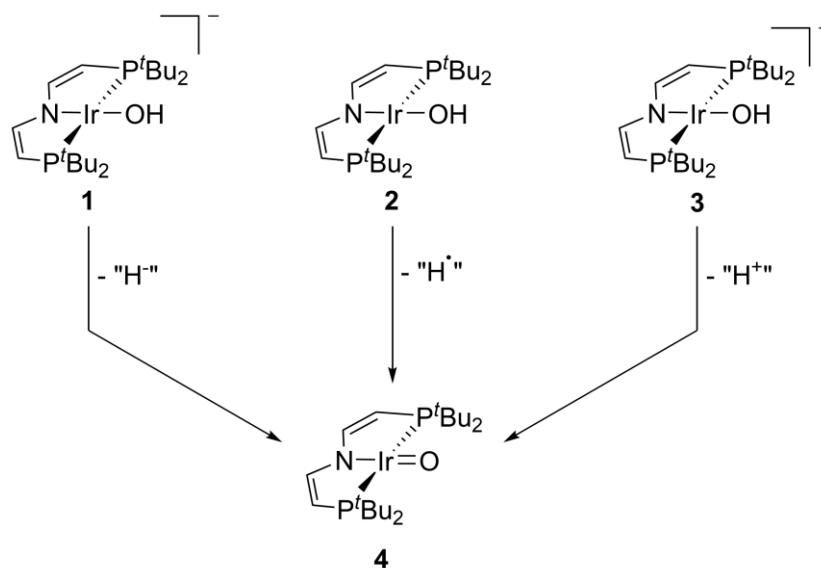
Chapter II

II. A Terminal Iridium Oxo Complex with a Triplet Ground State

1. Synthesis of Terminal Iridium Hydroxo Complexes

Parts of this Chapter have been published in: D. Delony, M. Kinauer, M. Diefenbach, S. Demeshko, C. Würtele, M. C. Holthausen, S. Schneider, Angew. Chem. Int. Ed. 2019 58, 10971-10974. "A Terminal Iridium Oxo Complex with a Triplet Ground State. The initial synthesis of the neutral Ir(II) hydroxo complex 2 as well as the cationic Ir(III) hydroxo complex 3 and their analysis, as well as first attempts towards the iridium oxo complex were performed by Dr. Markus Van Alten born Van Alten born Kinauer and will be briefly discussed here.

Towards the synthesis of a terminal oxo complex of iridium a suitable precursor platform must be found. Possible pathways would be (1) Oxygen Atom Transfer (OAT) with reagents like pyridine-N-oxide or trimethylamine-N-oxide with a low valent iridium platform or (2) Hydrogen Atom Transfer (HAT) from terminal hydroxo complexes. Both pathways are literature known. The only known terminal oxo complex of iridium by Wilkinson et al.^[36] (see Chapter I in Section 1.2) was synthesized by treatment of Ir(Mes)₃ with trimethylamine-N-oxide, while for the isoelectronic terminal imido complexes, the HAT route was utilized for the synthesis of [(PNP)IrNR]ⁿ⁺ (R = ^tBu, Ph, n= 0, 1, 2) **XXII-XXIV**.^[37,159] Due to the structural similarity of the latter to the pincer platform utilized in this thesis, the HAT route is followed here. Therefore, the synthesis of terminal hydroxo complexes of the type (PNP)Ir-OH is required as a starting platform towards the synthesis of a terminal oxo complex. Of course, HAT is not the only possible route to transform a terminal hydroxo complex into a terminal oxo complex. Depending on the metal oxidation state, also hydride transfer and deprotonation should be considered (Scheme 1).



Scheme 1: Possible Pathways from terminal iridium hydroxo platforms bearing a PNP pincer ligand towards a terminal oxo. Hydride Transfer (left), Hydrogen Atom Transfer (HAT, middle) and deprotonation (right).

As a starting platform for this project, the well established square planar iridium chloro pincer complex [(PNP)Ir(Cl)] **5** was chosen,^[160] which has proven to be a versatile precursor for formally isoelectronic complexes to a terminal oxo, like terminal nitrides and imido complexes.^[37,41] Salt metathesis with NaOH in a mixture of THF and water (7:1) is yielding the desired Ir(II) hydroxo complex **2** [(PNP)Ir(OH)] in very good yields (>90%) (Figure 1a). Only a careful exclusion of O₂ in the synthesis leads to high yields, due to the inherently higher instability of **2** towards dioxygen compared to **5**.

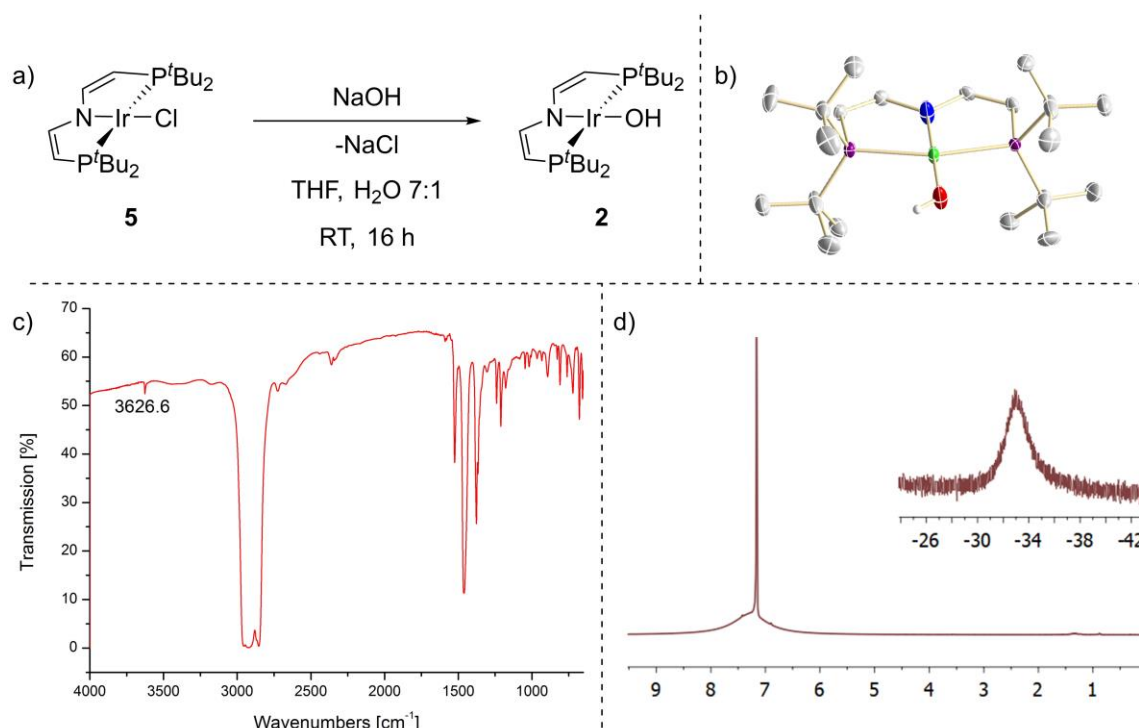


Figure 1: a) Improved synthetic route from **5** to **2** by salt metathesis with NaOH. b) Molecular structure in the solid state of **2** obtained by X-ray single crystal diffraction. The ORTEP plot shown with anisotropic displacement parameters at 50 %. All C-H hydrogen atoms as well as the disorder of the molecule are omitted for clarity. Selected parameters: Ir-N/O: 1.988(3) Å, Ir-P: 2.3172(10) Å, C=C: 1.340(6) Å N-Ir-O: 180°, P-Ir-P: 161.64(5)°. c) IR(Nujol) spectrum of **2**. d) ^1H (para)-NMR spectrum of **2** in benzene at 25 °C.

Structural confirmation for **2** was obtained by single crystal X-ray diffraction, which shows the expected square planar coordination mode (angle sum around Ir = 360°).²² The molecule is heavily disordered in the solid state with the oxygen and nitrogen atoms on opposite positions, thus the distinction between the Ir-N and Ir-O bond length is impossible ($d_{\text{Ir-N/O}} = 1.988 \text{ \AA}$) (Figure 1b). The O-H stretch in the infrared spectrum of **2** appears as a weak transmission at $\nu_{\text{O-H}} = 3627 \text{ cm}^{-1}$ (Figure 1c) in line with other literature known square planar iridium hydroxo complexes like the complexes reported by Werner et al.^[161,162] [$\text{trans-Ir(OH)(C}_2\text{H}_4\text{)(P}^i\text{Pr}_3\text{)}_2$] ($\nu_{\text{O-H}} = 3652 \text{ cm}^{-1}$) and [$\text{trans-Ir(OH)(=C=C=CPh}_2\text{)(P}^i\text{Pr}_3\text{)}_2$] ($\nu_{\text{O-H}} = 3643 \text{ cm}^{-1}$) or the pincer complexes by Parvez et al.^[163] [$\text{PCP}^R\text{Ir(OH)}$]²³ ($\nu^{R=tBu}_{\text{O-H}} = 3642 \text{ cm}^{-1}$, $\nu^{R=iPr}_{\text{O-H}} = 3625 \text{ cm}^{-1}$) and Burger et al.^[164] [(PDI)Ir(OH)]²⁴ ($\nu_{\text{O-H}} = 3561 \text{ cm}^{-1}$). The hydroxo complex **2** has a paramagnetic ground state with broadened signals ($\delta = 7.2 \text{ ppm}$ and $\delta = -33 \text{ ppm}$) in the ^1H (para)-NMR spectrum (Figure 1d). It is noteworthy that **2** is therefore representing the only literature reported paramagnetic iridium hydroxo complex. The electrochemistry of **2** was investigated by cyclic voltammetry (CV) to analyse the accessibility of the anionic and cationic hydroxo complexes **1** and **3**. On first glance, both redox events ($E^0(\text{Red}) = -2.12 \text{ V}$; $E^0(\text{Ox}) = -0.37 \text{ V}$) seem to be reversible, which indicates that hydroxo complex **1** and **3** are both stable and isolatable (Figure 2). A more detailed analysis by the *Randles-Sevcik* equation (see Chapter III, Section 1.2.1) gives a reversible electrochemical process with fast electron transfer to freely diffusing ions (Figure 2a), but the analysis of the scan rate depended peak ratio (forward vs. backward peak) reveals for the

²² Crystal grown by Dr. Markus van Alten, born Kinauer, crystal structure solved by Dr. Christian Würtele.

²³ PCP = Bis(2-diisopropylphosphaneyl)phenyl)carbene

²⁴ PDI = Pyridine-diimine

reduction, a moderate decrease of the peak ratio at higher scan rates, indicating a quasi-reversible process with a slowly equilibrating chemical reaction after the electrochemical step (EC mechanism) (Figure 2c, left).

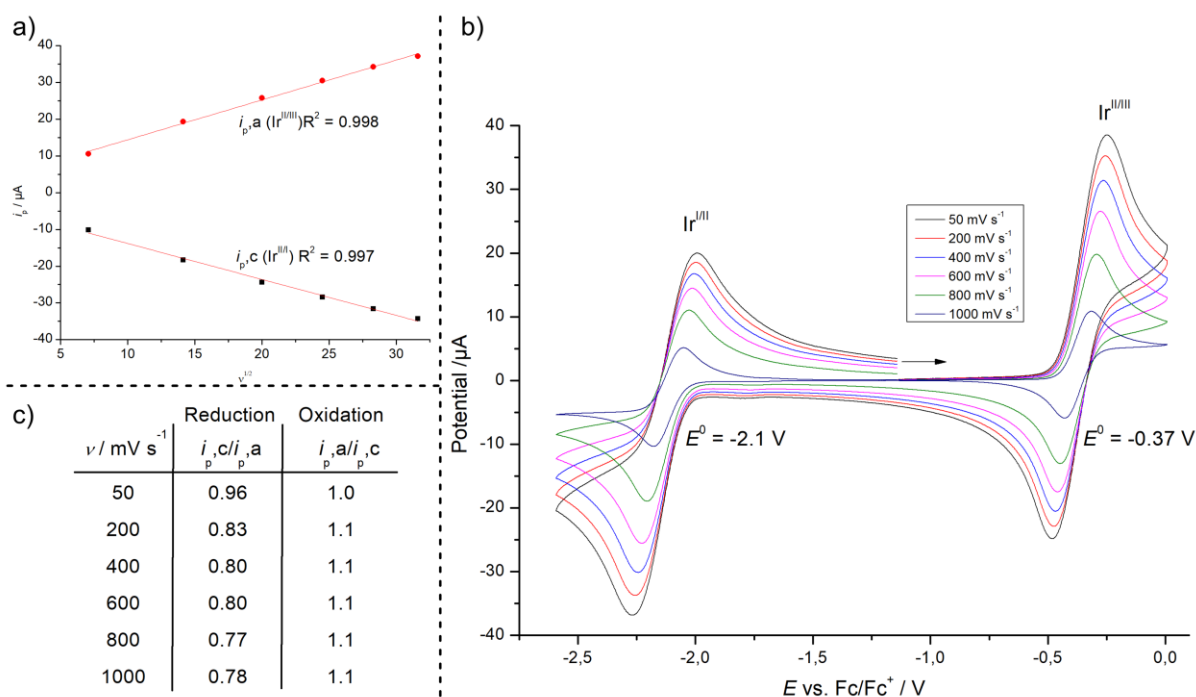


Figure 2: a) Linear regression of i_p vs. $\nu^{1/2}$ ($i_{p,c}$ for the reduction iridium (II/I) couple and $i_{p,a}$ for the iridium (II/III) couple) for the oxidation. b) Cyclic Voltammogram of **2** (1 mM) at different scan rates in THF with NBu_4PF_6 (0.1 M) as the conducting salt. Shown is the first cycle. c) Scan rate dependent peak ratio of the forward and backward peak for the reduction as well as for the oxidation.

A possible explanation for the chemical irreversibility is the dimerization of the formed iridium(I) hydroxo species which is a literature known process.^[161,165] On the oxidative site the i_p ratio is, at any scan rate close to unity and supports a reversible process. Indeed the oxidation of **2** with AgPF_6 as the oxidizing agent in DCM yields selectively (isolated yield: 92%) the desired cationic hydroxo species **3** $[(\text{PNP})\text{Ir}(\text{OH})][\text{PF}_6]$ (Figure 3a and d). The cationic hydroxo species could be confirmed by XRD analysis (Figure 3b).²⁵ Again, the angle sum around iridium sums up to 360° , but no disorder of the molecule in the N-Ir-O plane is observed as for **2**. The Ir-O bond length is significantly shortened by 0.05 \AA to $d_{\text{Ir-O}} = 1.935 \text{ \AA}$, which indicates an increase in bond strength and represents the by far shortest Ir-OH bond reported in literature.^{26,[166–174]} Also, the N-Ir-O angle is slightly deviating from 180° (N-Ir-O = 177°) and hints towards a minor amount of π -backdonation from the pincer nitrogen, however it could as well arise from packing effects in the crystal. IR spectroscopy yields a decrease of the O-H stretching frequency ($\nu_{\text{O-H}} = 3577 \text{ cm}^{-1}$) by 50 wavenumbers compared to **2**, which supports a higher degree of activation of the O-H bond of **3** (Figure 3c). **3** exhibits a C_{2v} symmetric signal set with four signals in the $^1\text{H-NMR}$ spectrum ($\delta = 14.6 \text{ ppm}$, $\delta = 7.1 \text{ ppm}$, $\delta = 5.2 \text{ ppm}$ and $\delta = 1.8 \text{ ppm}$)^{and} one signal for the pincer phosphorous atoms in the $^{31}\text{P-NMR}$ spectrum ($\delta = 41.3 \text{ ppm}$). The O-H group of **3** is remarkably deshielded with a proton shift to $\delta_{\text{O-H}} = 14.6 \text{ ppm}$, which hints towards an acidification of the O-H group (Figure 3d).

²⁵ Crystal grown by Dr. Markus Van Alten born Kinauer, crystal structure solved by Dr. Christian Würtele.

²⁶ Scifinder© and Google Scholar© search on „iridium hydroxide“ on 20.04.2020 and additional tracing of cross references.

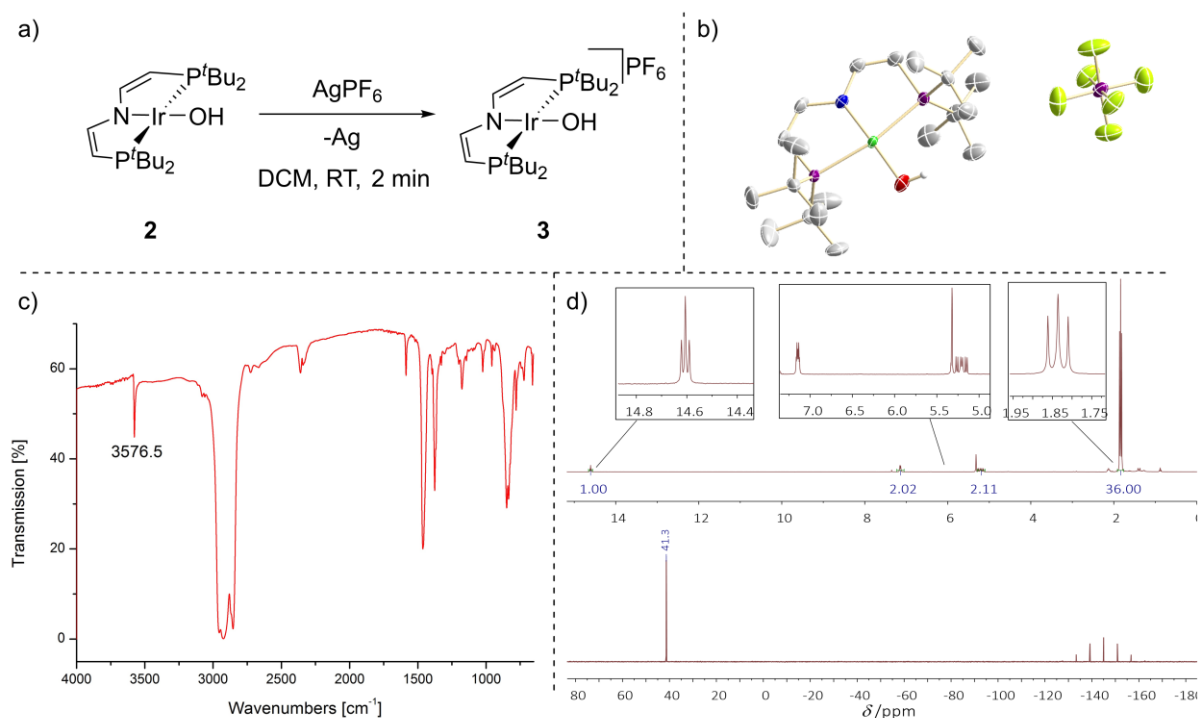


Figure 3: a) Improved synthetic route to the cationic hydroxo species **3** by oxidation of **2** with AgPF_6 . b) Molecular structure in the solid state of **3** obtained by X-ray single crystal diffraction. The ORTEP plot shown with anisotropic displacement parameters at 50 %. All C-H hydrogen atoms and disorder omitted for clarity. Selected parameters: Ir-O: 1.935(3) Å, Ir-N: 1.900(4) Å, Ir-P: 2.3348(12) Å, C=C: 1.326(8) Å N-Ir-O: 177.35(18)°, P-Ir-P: 167.39(4)°. c) IR spectrum of **3** in Nujol. d) ^1H -NMR spectrum (top) and $^{31}\text{P}\{^1\text{H}\}$ -NMR spectrum (bottom) of **3** in DCM-d_2 at 25 °C.

The reduction towards an anionic iridium(I) hydroxo complex can be achieved by treatment of **2** with 1 M Na/Hg as the reducing agent in few THF, yielding an orange product (Figure 4a). The solution needs to be cooled immediately to $-40\text{ }^\circ\text{C}$ because the product is temperature sensitive and decomposes to several species at prolonged times, at room temperature as well as in the solid state. The molecular structure of the reduction product was determined by XRD analysis. Complex **1** is not monomeric but a dimer of the iridium(I) hydroxo species $[(\text{PNP})\text{Ir}(\text{NaOH})(\text{thf})_2]_2$ with bridging sodium atoms, which confirms the hypothesis regarding the chemically non-reversible behaviour in the cyclic voltammogram of **2** (Figure 4b).²⁷ The metal centre is coordinated in a square-planar fashion with only weak distortion from the ideal 360° (Angle sum around iridium = 358°) and the Ir-O bond is drastically elongated to $d_{\text{Ir-O}} = 2.134\text{ \AA}$ and therefore reflects the high electron count. The O-H hydrogen atoms could be found in the electronic density map and isotopically refined, giving an O-H bond length of $d_{\text{O-H}} = 0.79\text{ \AA}$, which is already close to the O-H bond length in pure $\text{NaOH}\cdot\text{H}_2\text{O}$ $d_{\text{O-H}} = 0.74\text{ \AA}$.^[175] A C_{2v} symmetric signal set is found for **1** with four signals in the ^1H -NMR spectrum ($\delta = 6.89\text{ ppm}$, $\delta = 4.02\text{ ppm}$ and $\delta = 1.35\text{ ppm}$, $\delta = -2.1\text{ ppm}$) and one signal in the $^{31}\text{P}\{^1\text{H}\}$ -NMR spectrum ($\delta = 57.2\text{ ppm}$). The dimeric nature of **1** could be observed as well in solution by the broadened NMR-signals, due to hindered rotation (Figure 4c). The O-H protons of **1** are shifted to $\delta_{\text{O-H}} = -2.1\text{ ppm}$ which hints towards some hydridic character.

²⁷ Crystal structure solved by Dr. Christian Würtele. The same structure was previously reported by Dr. Markus van Alten born Kinauer.

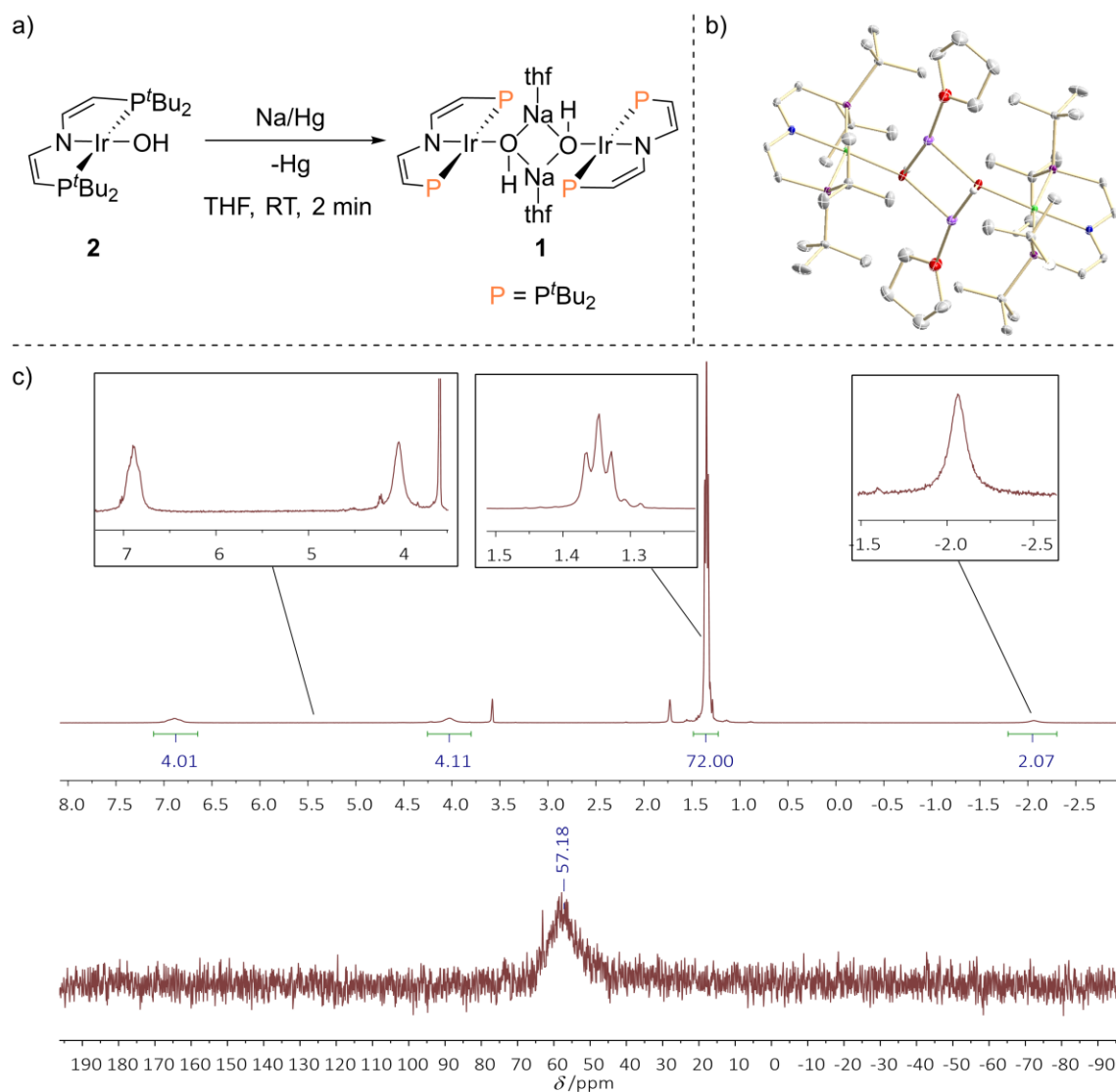


Figure 4: a) Synthetic route towards the iridium(I) hydroxo species **1** from **2** by reduction with sodium amalgam in THF. b) Molecular structure in the solid state of **1** obtained by X-ray single crystal diffraction. The ORTEP plot shown with anisotropic displacement parameters at 50 %. All C-H hydrogen atoms, disorder and a cocrystallised THF molecule omitted for clarity. Selected parameters: Ir-O: 2.1341(13) Å, Ir-N: 2.0352(19) Å, Ir-P1: 2.2889(6) Å, Ir-P1: 2.2914(6) Å, C1=C2: 1.349(3), C11=C12: 1.345(3), Na1-O1: 2.235(2), O1-Na1-O1#: 91.60(7)°, N-Ir-O: 176.53(7)°, P-Ir-P: 163.26(2)°. c) ^1H -NMR (top) and $^{31}\text{P}\{^1\text{H}\}$ -NMR (bottom) of **1** in $\text{THF-}d_8$ at 25 °C.

2. Synthesis and Characterisation of a Terminal Iridium Oxo Complex

The inherent thermal instability of **1** prevents its use as a synthetic starting platform, therefore only the hydroxo complexes **2** and **3** were probed as precursors towards the terminal iridium oxo complex. Addition of KO^tBu in THF to **3** leads to a direct colour change from red-violet to purple. Washing with pentane and crystallisation from toluene leads to the isolation of the desired terminal oxo complex **4** [(PNP)Ir(O)] in moderate yields as confirmed by single crystal X-ray analysis (Figure 5, b). It must be noted, that absolutely pure and Na/K dried toluene must be used, since otherwise exclusively the hydroxo complex **2** will be obtained (Figure 5a). Even with sublimed KO^tBu the yield of **4** does not exceed 60% and green, pentane soluble side products are formed. A second route towards **4** is the HAT reaction from **2**, therefore the strong hydrogen atom abstracting reagent 2,4,6-tris-*tert*-butylphenoxy]

(Mes*O) was added to **2**. Performing this reaction in polar solvents like THF will only lead to a 50:50 mixture of **4** and **2**, indicating a very low driving force for the reaction, however in contrast to the deprotonation route from **3** no side products are observed. The equilibrium can be shifted exclusively to the product site by usage of an unpolar solvent like hexamethyldisiloxane (HMDSO) or pentane. Here, the additional driving force arises from the precipitation of **4**, while the starting materials as well as the second product 2,4,6-tris-*tert*-butylphenol (Mes*OH) are all soluble. Filtration of the reaction mixture, washing with pentane and crystallisation from toluene yields the terminal oxo complex **4** pure in high isolated yields (80%) (Figure 5a).

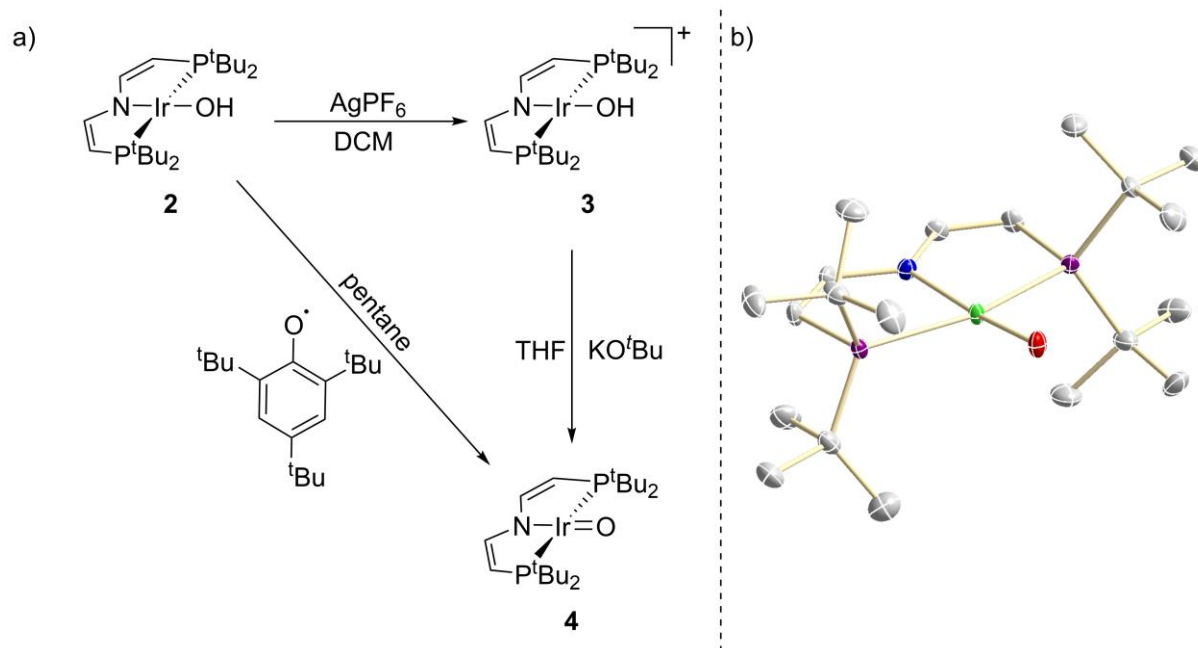


Figure 5: a) Synthetic routes towards **4** by oxidation of **2** with AgPF_6 to **3** and subsequent deprotonation with KO^tBu in THF or HAT from **2** with Mes*O in pentane. b) Molecular structure in the solid state of **4** obtained by X-ray single crystal diffraction. The ORTEP plot shown with anisotropic displacement parameters at 50 %. All C-H hydrogen atoms and disorder are omitted for clarity. Selected parameters: Ir-O: 1.827(4) Å, Ir-N: 2.040(4) Å, Ir-P1: 2.3296(9) Å, Ir-P2: 2.3296(9) Å, C1=C2: 1.344(4), N-Ir-O: 173.6(6)°, P-Ir-P: 163.16(4)°.

XRD analysis of **4** reveals a square-planar coordinated iridium metal centre (angle sum around Ir = 360°),²⁸ with a drastically reduced Ir-O bond length ($d_{\text{Ir-O}} = 1.827(4)$ Å) compared to the hydroxo species **1-3**, which indicates multibonding character within the Ir-O moiety (Figure 5b). This is also reflected by the N-Ir-O angle of 174° , which speaks for the avoidance of π -back donation from the pincer nitrogen. For the isoelectronic iridium imido complex **XXII** [(PNP)Ir(N^tBu)] a longer Ir-N bond length was reported ($d_{\text{Ir-N}} = 1.868(2)$ Å). This reflects the high steric shielding of the N-^tBu group.^[37] The Ir-O bond of **4** is significantly elongated ($\Delta = 0.1$ Å), compared to the only other reported iridium oxo complex by Wilkinson et al^[36] **XXI** ($d_{\text{Ir-O}} = 1.73$ Å) (Figure 6a, left). This can be explained by a simple molecular orbital (MO) scheme of the Ir-O bonding for both species. The terminal oxo by Wilkinson is in trigonal coordination with a formal iridium(V) oxidation state. The d_{z^2} orbital is forming the σ -bonding interaction between iridium and oxygen and the d_{yz} and d_{xz} orbitals the π -bonding interactions, while the $d_{x^2-y^2}$ and d_{xy} orbitals stay non-bonding. With the six electrons from the formal O^{2-} ligand and the four electrons from the iridium(V) metal centre only bonding and non-bonding orbitals are occupied, resulting in an Ir-O triple bond (Figure 6a, left). The terminal oxo **4** is in a square planar coordination mode with a formal iridium(III) metal centre. Here,

²⁸ Crystal structure solved by Dr. Christian Würtele.

the $d_{x^2-y^2}$ is forming the σ -bonding interaction and the d_{xz} and d_{xy} orbitals the π -bonding interactions, while the d_z^2 and d_{yz} orbitals remain non-bonding. The two additional electrons from the formal iridium(III) oxidation state result in the population of antibonding π^* orbitals which reduces the bond order of **4** to an Ir-O double bond (Figure 6a, left).

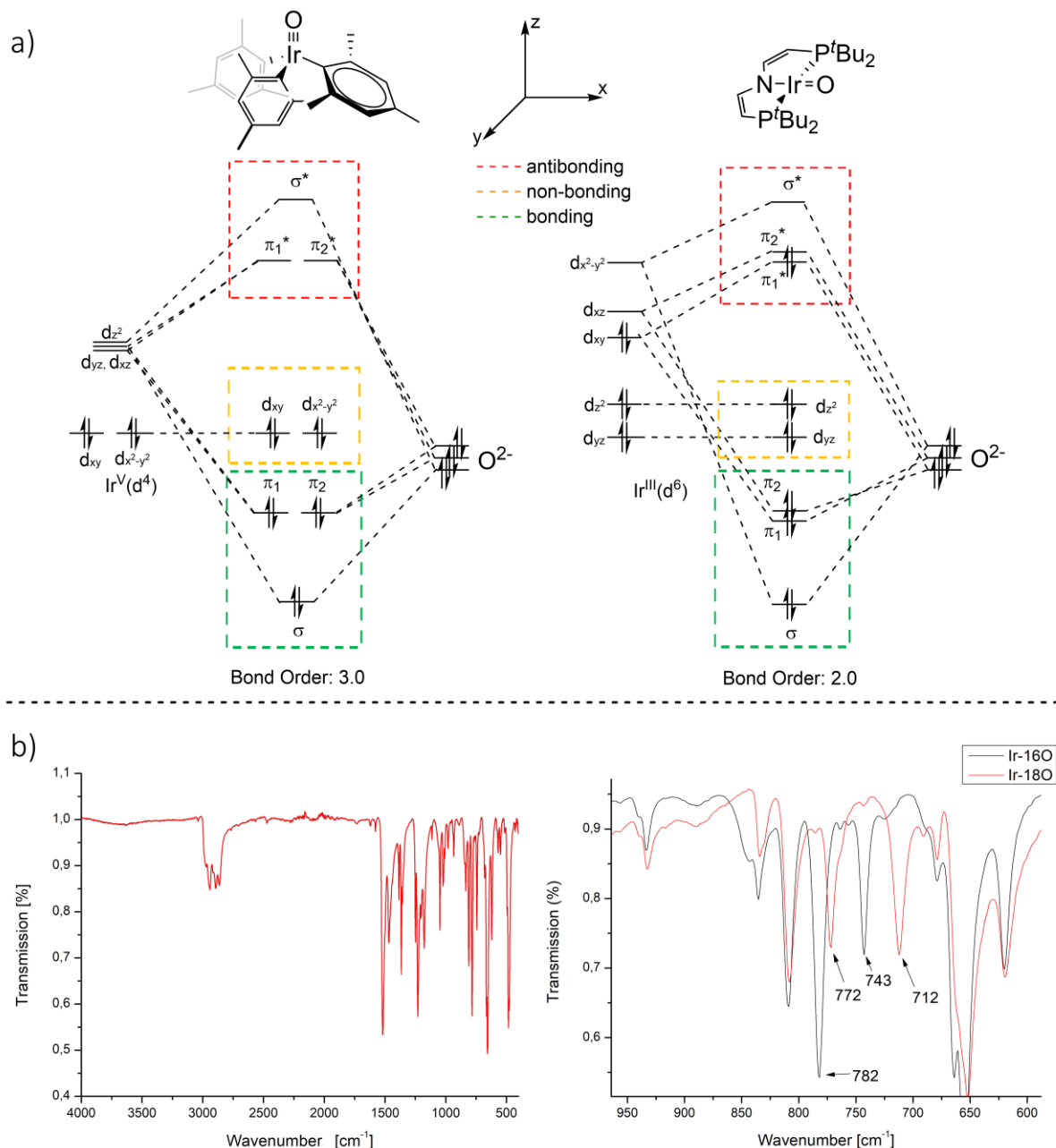


Figure 6: a) MO-scheme of the Ir-O bond for **4** (right) and the Wilkinson oxo complex **XXI** (left). b) IR(ATR) spectrum of **4** (left) and overlay of the IR(ATR) spectrum of **4** and its ^{18}O isotopologue.

The IR (ATR²⁹) of **4** is silent in the region of around 3500 cm^{-1} where O-H stretches would be expected, which supports the formation of a terminal oxo complex (Figure 6a). For further bonding analysis the ^{18}O -isotopologue of **4** was synthesised. The Ir-O stretching frequency was thereby assigned to $\nu_{\text{Ir-O}} = 743\text{ cm}^{-1}$, while the Ir- ^{18}O stretching frequency of $\nu_{\text{Ir-O}} = 712\text{ cm}^{-1}$ is in good agreement to the expected value of the harmonic oscillator

²⁹ ATR = Attenuated total reflection

approximation ($\nu_{\text{Ir-O}}(\text{HO}) = 701 \text{ cm}^{-1}$). The other visible deviations in the ^{18}O -isotopologue spectrum at e.g. $\nu = 772 \text{ cm}^{-1}$ can tentatively be assigned to Fermi resonances in the ^{16}O isotopologue which cancel upon labelling (Figure 6b, right). A comparison of the Ir-O frequencies of **4** and **XXI** ($\nu_{\text{Ir-O}} = 802 \text{ cm}^{-1}$)^[36] supports the stronger bond for the latter, confirming the picture of a double bond for **4** and a triple bond for **XXI**.

The electrochemistry of **4** was analysed by cyclic voltammetry, revealing two redox events at $E_{1/2} = -1.95 \text{ V}$ and $E_{1/2} = -0.13 \text{ V}$ vs. Fc/Fc^+ (Figure 7a)³⁰. The reductive wave is quasi-reversible, which can be rationalized by the higher electron count of the formal anionic oxo species **4**⁻ and thus less stabilizing π -bonding character within the Ir-O unit. In analogy to the MO-scheme of Figure 6a the Ir-O bond of the anionic terminal oxo **4**⁻ is further activated (the bond order drops to 1.5) and thus the complex is destabilized. The oxidative event is at a very mild potential for a formal $\text{Ir}^{\text{III}}/\text{Ir}^{\text{IV}}$ oxidation^[176] reflecting the high covalency in the Ir-O unit and therefore the low validity of the concept of oxidation numbers for very covalent complexes in general.

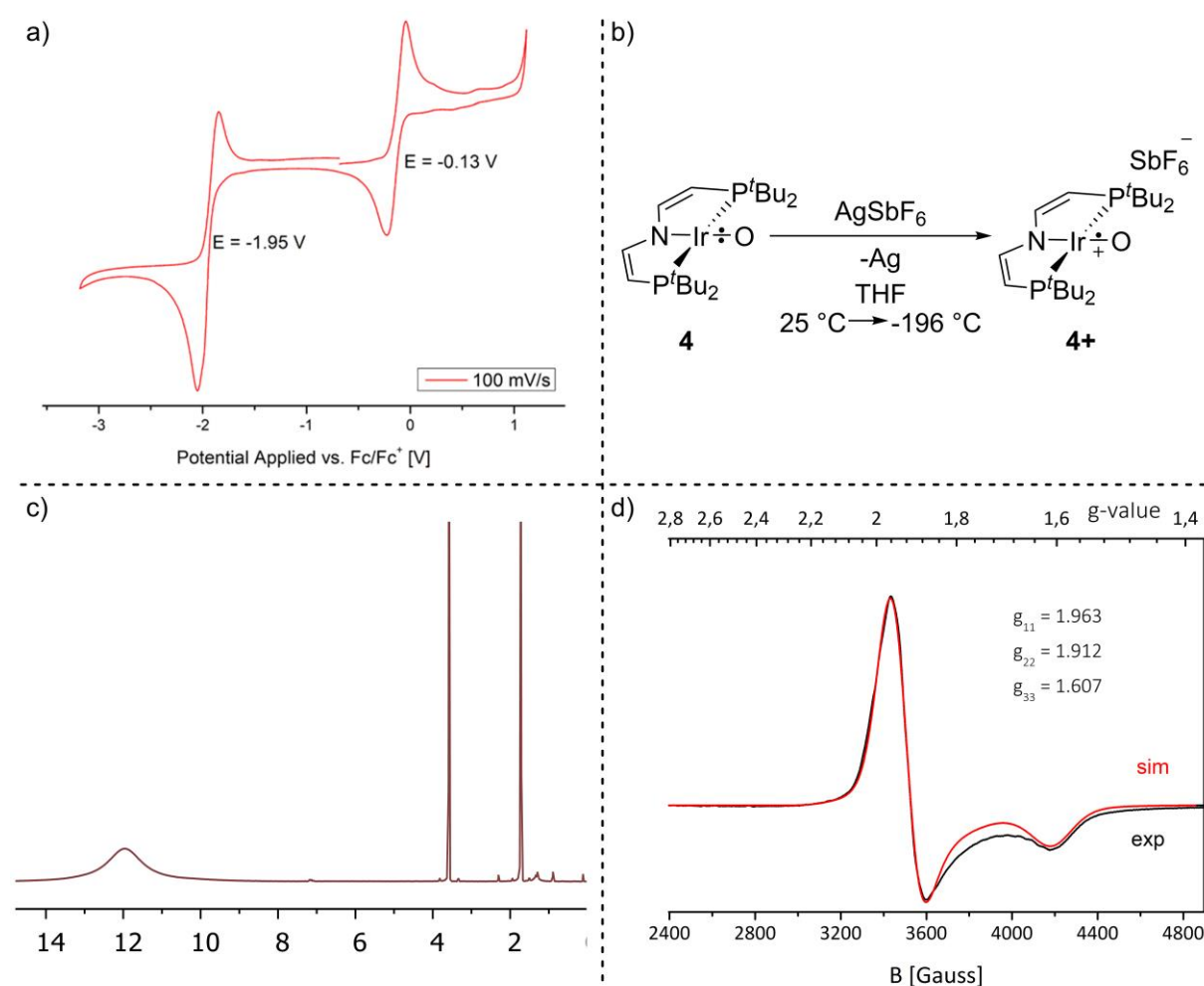


Figure 7: a) Cyclic Voltammogram of **4** (1.0 mM) in THF with 0.1 M NBu_4PF_6 . Shown is the 2nd cycle. b) Oxidation of **4** with AgSbF_6 in THF at room temperature and trapping of the formed species **4**⁺ with liquid nitrogen. c) ^1H (para)-NMR spectrum of the reaction after filtration. d) X-Band EPR spectrum at 143 K obtained by oxidation of **4** with AgSbF_6 in THF.³¹

³⁰ Cyclic voltammogram recorded by Niklas Welker.

³¹ Simulation of the EPR spectrum by Prof. Dr. Bas de Bruin University of Amsterdam.

The electrochemistry of **4** seems very promising for the synthesis of a cationic terminal oxo, thus the chemical oxidation with AgSbF_6 in PhCl was probed (Figure 7b). An instant colour change from the reddish purple of **4** to a blue violet is observed. Keeping this solution at ambient temperature will lead to the decomposition of the species, in which the cationic hydroxo **3** could be observed as the main decomposition product. Directly cooling with liquid nitrogen after the reaction enables the spectroscopic characterisation of **4+** $[(\text{PNP})\text{Ir}(\text{O})][\text{SbF}_6]$. The ^1H (para)-NMR of **4+** speaks for a C_{2v} symmetric complex with only one main signal at $\delta = 11.9$ ppm, which indicates that **4+** is also a terminal oxo complex, since a decomposition pathway by insertion into the metal phosphorous bond, as observed for the platinum oxo by Milstein,^[47] would reduce the product symmetry to C_1 (Figure 7c). Transient **4+** was further analysed by EPR spectroscopy where an almost axial spectrum with a very low g -anisotropy for a 5d metal compound ($g_{11} = 1.96$, $g_{22} = 1.91$ and $g_{33} = 1.61$) can be observed.³² A comparison to the formally isoelectronic iridium(IV) nitride complex **XXV** $[(\text{PNP})\text{Ir}(\text{N})]$ and the iridium(IV) imido complex **XXIII** $[(\text{PNP})\text{Ir}(\text{NtBu})^+]$ highlights the special electronic structure of **4+**.^[37,41] For **XXV** ($g_{11} = 1.86$, $g_{22} = 1.58$, $g_{33} = 1.32$) and **XXIII** ($g_{11} = 1.71$, $g_{22} = 1.63$, $g_{33} = 1.33$) the g -anisotropy is much more distinct and the values are less deviating from the value of the free electron $g_e = 2.002$.³³ This supports a ligand centred oxyl radical character for **4+**. Further insight into the electronic structure of **4+** was obtained by computational analysis on the PBE0-D3/def2TZVP level of theory.³⁴ The cationic oxo **4+** is computed to be in square planar coordination geometry (angle around iridium = 360°) with a significantly shortened Ir-O bond ($d_{\text{Ir-O}} = 1.75 \text{ \AA}$) compared to the crystal structure of **4** and additionally a lower N-Ir-O angle (169.7°). This nicely reflects the trend of rising bond order and thus shorter Ir-O bond length due to less electrons in antibonding π^* -orbitals. Additionally, the rare oxyl radical character of **4+** is confirmed by the Mulliken spin density analysis (O: 75 %).

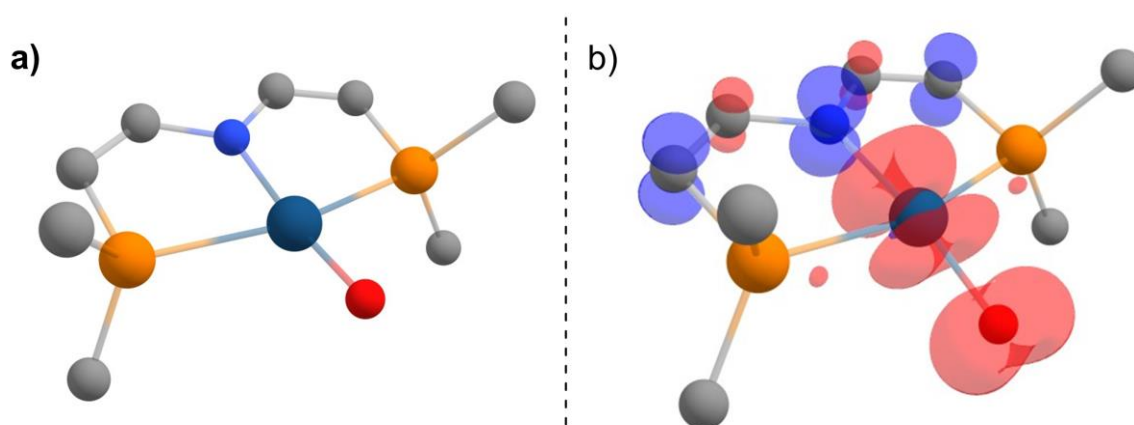


Figure 8: a) Structure of **4+** on the PBE0-D3/def2TZVP level of theory. b) Mulliken spin density plot at isovalue 0.0075 a_0^{-3} computed at the PBE0-D3/def2TZVP level of theory. Ir: 42% O: 75% N: -18%

³² The fitting of the EPR spectrum was performed by Prof. Dr. Bas de Bruin, University of Amsterdam.

³³ https://physics.nist.gov/cgi-bin/cuu/Value?gem|search_for=all free electron g factor

³⁴ For more details see Section 4.2 of Chapter VI.

The three sharp and strongly paramagnetically shifted signals in the $^1\text{H}\{\text{para}\}$ -NMR spectrum of **4** ($\delta_{\text{tBu}} = +21$ ppm, $\delta_{2\text{xCH}} = -62$ ppm, $\delta_{2\text{xCH}} = -76$ ppm) support a C_{2v} symmetric structure on the NMR timescale (Figure 9a). The signals are almost temperature invariant over a wide range (-75 to $+65$ °C) besides the third signal ($\delta_{2\text{xCH}} = -76$ ppm), which exhibits approximately Curie dependence above ~ 250 K, which indicates accessible thermally excited states (Figure 9b). Such spectroscopic behaviour was also found for the isoelectronic $[(\text{PNP})\text{Ir}=\text{N}^t\text{Bu}]$ complex **XXII** and was rationalized by *ab initio* computations. Imido complex **XXII** has a triplet ground state which is strongly stabilised by spin-orbit coupling (SOC). This causes a non-magnetic ground state that mixes due to temperature independent paramagnetism (TIP) with the open-shell excited states.^[37] This explains the sharp signals NMR signals and their paramagnetic shift in contrast to the broadened signals expected for a classic, paramagnetic compound.

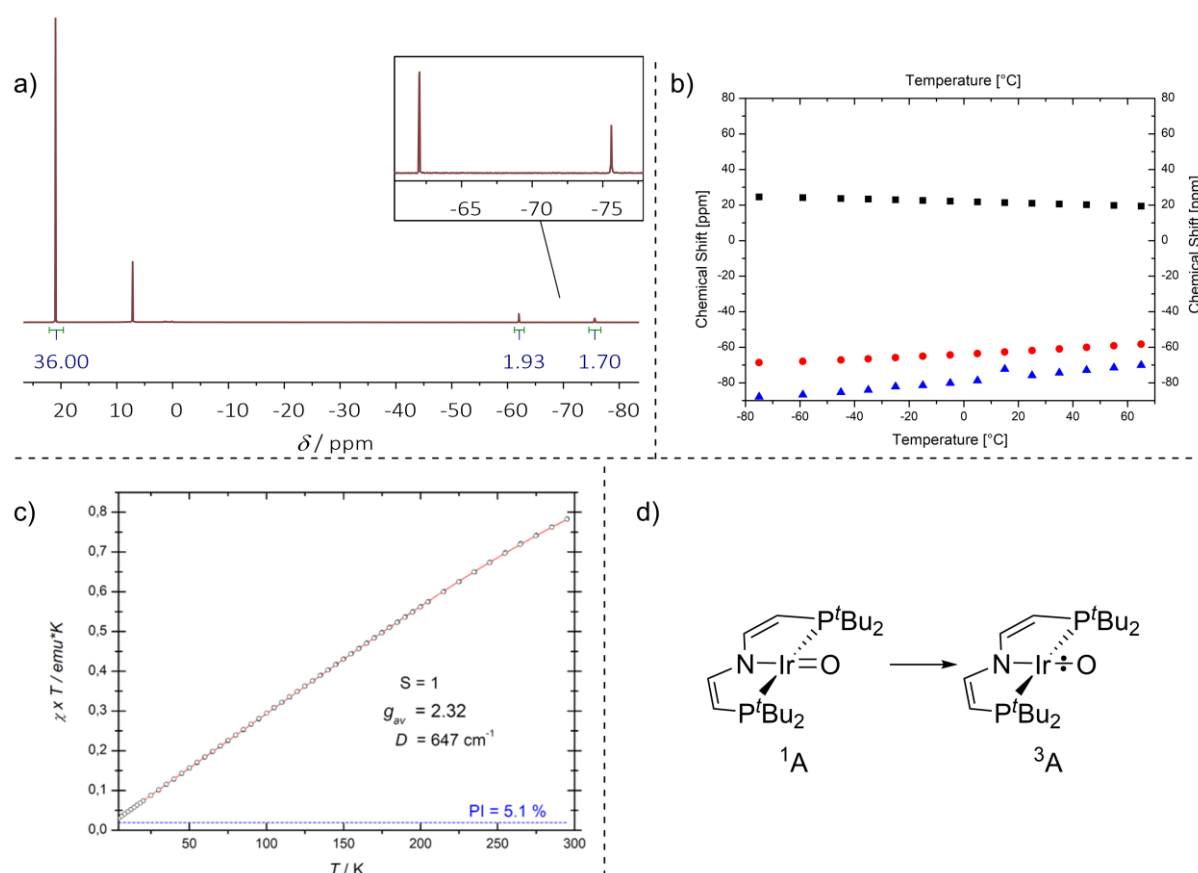


Figure 9: a) $^1\text{H}\{\text{para}\}$ -NMR of **4** in C_6D_6 at 25 °C. b) VT-NMR of **4** from -75 °C to $+65$ °C. c) Temperature dependent magnetic susceptibility measurement by SQUID magnetometry. d) Revision of the Lewis-structure of **4** reflecting the triplet ground state.

Accordingly, the $\chi_M T$ vs. T curve of a powder sample of **4**, obtained by SQUID magnetometry features temperature independent paramagnetism up to around 250 K and shows slight bending of the curve at higher temperatures which arises from the partial population of excited states (Figure 9c).³⁵ The data can be fitted with a spin Hamiltonian for a triplet state ($S = 1$, $g_{\text{av}} = 2.32$) with a large zero-field splitting ($D = 647$ cm^{-1}) which is 181 cm^{-1} higher compared to imido complex **XXII**. This can be attributed within a simple ligand-field picture to reduced covalent bonding of **4** in the $\text{Ir}=\text{E}$ ($\text{E} = \text{ER}, \text{O}$) moiety, which leads to a smaller relativistic nephelauxetic effect for **4**

³⁵ SQUID magnetometric measurements performed by Dr. Serhiy Demeshko.

and therefore to a higher effective spin-orbit coupling parameter ζ_{eff} .³⁶ With these spectroscopic and magnetic data at hand, the Lewis-structure of **4** should be revised in analogy to Figure 9d as a biradical species.

The spectroscopic and magnetic description of **4** is corroborated by high level (*ab initio*) computations.³⁷ The structures are optimized by DFT on the B3LYP(V)-(D3)/def2TZVP level of theory and reproduce the short Ir-O bond $d_{\text{Ir-O}}^{\text{DFT}} = 1.80 \text{ \AA}$ and the near linearity of the N-Ir-O moiety (179.0°) for the $^3A''$ state (Figure 10a). In contrast, the lowest singlet state ($^1A'$) of **4** exhibits a high deviation from linearity (157.0°) as also found computationally for the isoelectronic platinum(IV) pincer (PCN) oxo complex **XXXI** by Milstein et al. (Triplet state: C-Pt-O = 175.4° ; Singlet state: C-Pt-O = 138.2°).^[47,177] The adiabatic triplet-singlet gap of **4** is significantly higher with $\Delta E(T/S) = 41 \text{ kJ mol}^{-1}$ compared to the computational value of **XXXI** which vanishes on high level *ab initio* computations resulting in virtually isoenergetic states of **XXXI**.^[177]

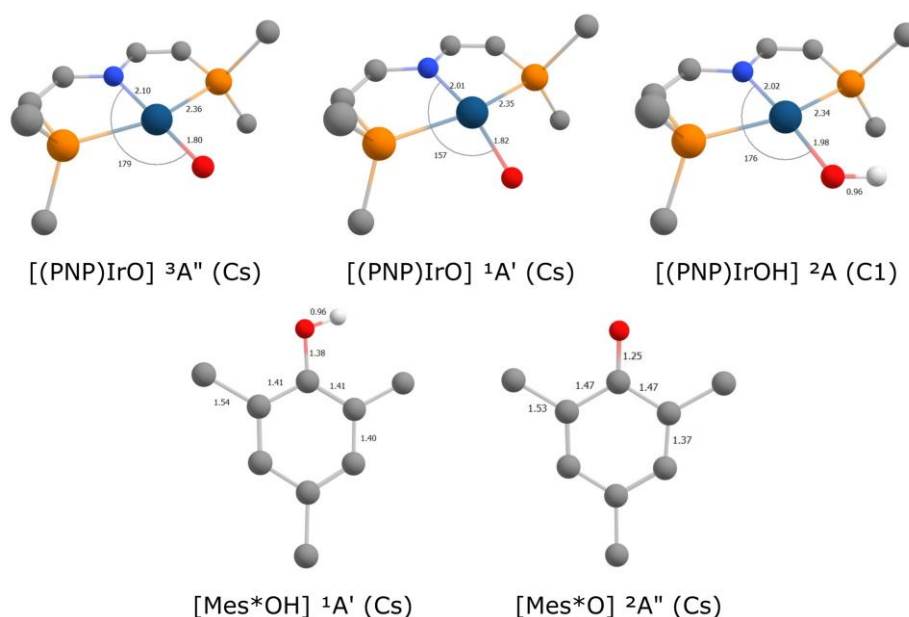


Figure 10: a) Computed structures for **4** ($^3A''$, $^1A'$), **2** (2A) as well as for Mes*OH and Mes*O on the B3LYP(V)-D3/def2TZVP level of theory. Selected parameters: **4**($^3A''$): Ir-O: 1.80 Å, Ir-N: 2.10 Å, Ir-P: 2.36 Å, N-Ir-O: 179° ; **4**($^1A'$): Ir-O: 1.82 Å, Ir-N: 2.01 Å, Ir-P: 2.35 Å, N-Ir-O: 157° ; **2**(2A): Ir-O: 1.98 Å, Ir-N: 2.02 Å, Ir-P: 2.34 Å, O-H: 0.96 Å, N-Ir-O: 176° . Mes*OH($^1A'$): C=C(O): 1.41 Å, C-C(Bu): 1.54 Å, C-O: 1.38 Å, O-H: 0.96 Å; Mes*O($^2A''$): C=C(O): 1.47 Å, C-C(Bu): 1.53 Å, C-O: 1.25 Å.

For a more detailed insight into the electronic structure and the influence of spin-orbit coupling (SOC) in **4** and **2**, state averaged multireference computations on the CASSCF/NEVPT2 level of theory, extended by quasi-degenerate perturbation theory (QDPT), were performed. The active spaces were constructed to reflect the bonding situation around the iridium metal centre. In addition to the 5d orbitals of iridium the σ - and π -bonding interaction of the oxo moiety, the σ -bonding interaction of the phosphorous atoms and the π -bonding interaction of the pincer-nitrogen atom were considered leading to a (16,10) CAS extension for **4** and to a (17,11) CAS extension for **2**, where the O-H σ -bonding interaction is additionally considered. In analogy to the DFT computations, the CASSCF wavefunction also predicts a triplet ground state for **4** $\Delta E_{T/S} = 52 \text{ kJ mol}^{-1}$ with a Ir-O

³⁶ The spin-Hamiltonian formally loses its physical meaning in cases of strong spin-orbit coupling, making "spin" a bad quantum number. It is, nevertheless, easier to capture. For further information please see reference [258].

³⁷ The computations of this chapter, except for the computations for **4**, were performed by Dr. Martin Diefenbach. A comprehensive discussion of the computations performed for this Section can be also found in Section 4.2 of chapter VI.

$(\pi_1^* \pi_2^*)^2$ configuration and a doublet ground state $\Delta E(D/Q) = 388 \text{ kJ mol}^{-1}$ for **2** (Figure 11). Upon treatment of spin-orbit coupling (SOC) by QDPT the triplet ground state of **4** is strongly stabilised ($\Delta E(\text{SOC}) = -23.5 \text{ kJ mol}^{-1}$) and splits into its $m_s = 0, \pm 1$ microstates, resulting in an isolated “non-magnetic” ground state.

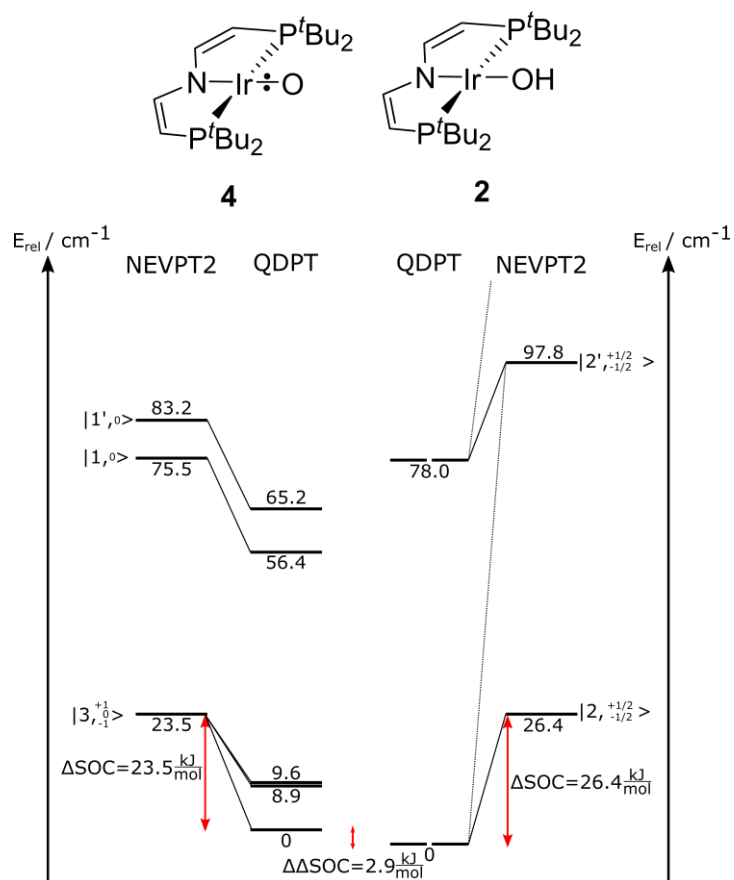


Figure 11: CASSCF state correlation on the NEVPT2 level of theory and with spin-orbit coupling (SOC) treatment by QDPT for **4** (16,10) (left) and **2** (17,11) (right) based on state averaged CASSCF wavefunctions over all roots which arise from excitations within the 5d shell of the metal centre **4** (50 singlet, 45 triplet, and 5 quintet states), **2** (40 doublet, 10 quartet states)

The zero-field splitting to the excited states was computed to $D_{\text{QDPT}} = 775 \text{ cm}^{-1}$, which very nicely reflects the experimental value of 647 cm^{-1} . The same picture was derived for the imido complex **XXII**, even though the computed and experimentally found zero-field splitting was significantly lower ($D_{\text{QDPT}} = 450 \text{ cm}^{-1}$).^[37] Conclusively, imido complex **XXII** and oxo complex **4** have both a spin-orbit stabilized triplet ground state, but **4** experiences a higher SOC stabilisation due to the reduced covalency of the Ir-E (E = N/O) unit. The doublet ground state of **2** has contributions from the first excited doublet root and is even exhibiting a higher stabilisation by SOC than **4** ($\Delta E(\text{SOC}) = -26.4 \text{ kJ mol}^{-1}$) resulting in a differential SOC effect of -2.9 kJ mol^{-1} which formally describes a strengthening of the O-H bond by SOC (Figure 11).

3. Reactivity of the Terminal Iridium Oxo Complex

3.1. Oxygen Atom Transfer and Philicity Derivation

With the terminal oxo complex **4** at hand, its reactivity towards oxygen atom transfer (OAT), including the derivation of its philicity, was probed with selected reagents. Hydrogenolysis of **4** with 1 bar H₂ at ambient temperature in benzene leads to a direct colour change from purple to green (Figure 12a). **4** is already after 5 min fully converted as seen by the immediate measurement of ¹H-NMR after the addition of dihydrogen (Figure 12b, top). A broad signal at $\delta = 7$ ppm indicates the formation of **2** and of a second, C_{2v} symmetric product, with broadened signals ($\delta_{2\times CH} = 7.16$ ppm, $\delta_{2\times CH} = 4.49$ ppm, $\delta_{4\times C(CH_3)_3} = 1.32$ ppm) accompanied by the formation of H₂O at $\delta \sim 0$ ppm. **2** is fully converted after one hour reaction time and yields a new orange product (Figure 12b, bottom).

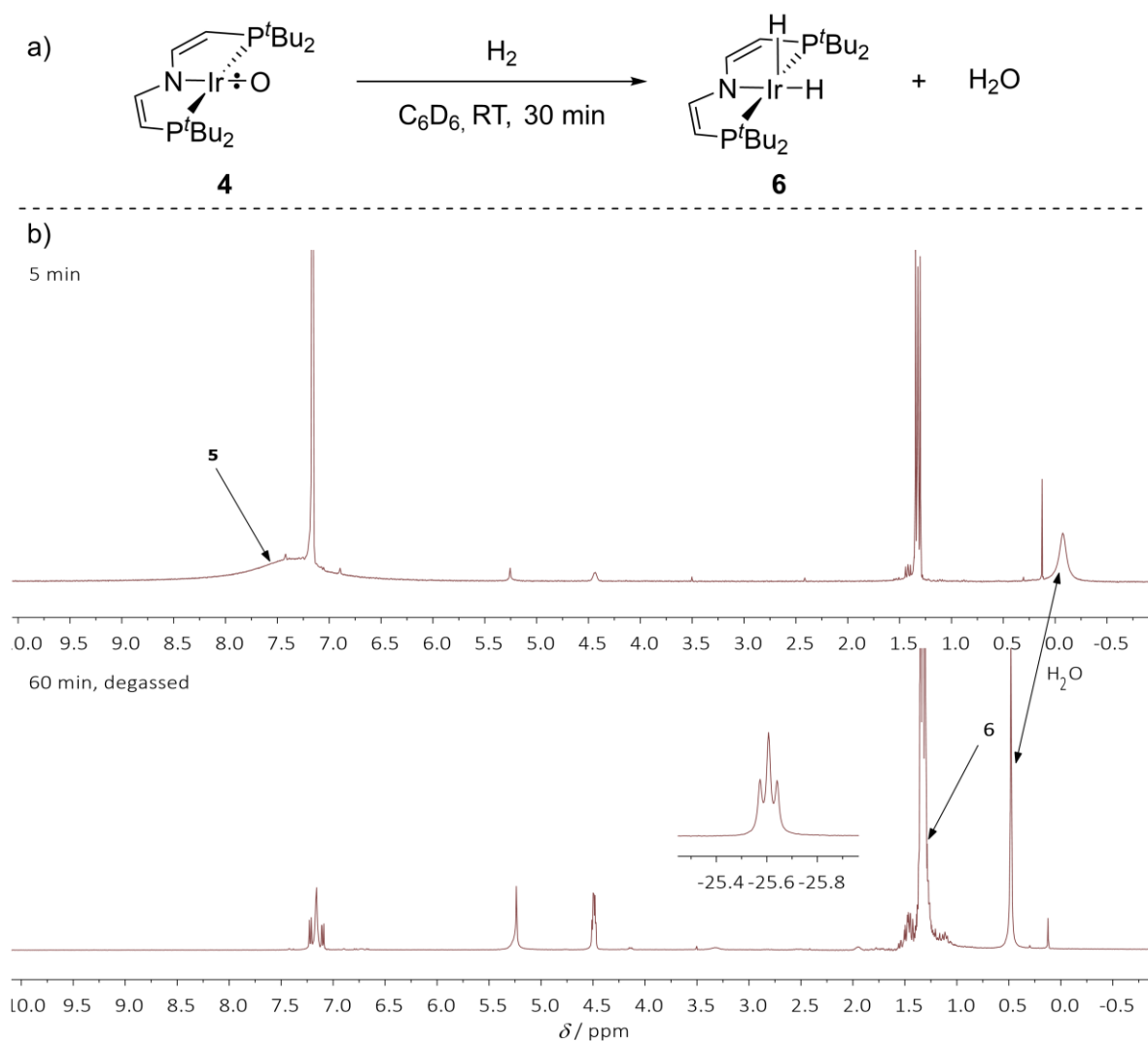


Figure 12: a) Hydrogenolysis of **4** with 1 bar H₂ at ambient temperature in benzene to **6** and water. b) ¹H-NMR of the reaction mixture under 1 bar of H₂ gas 5 min after the addition. c) ¹H(para)-NMR of the reaction mixture 1 h after the addition after degassing and addition of Ar.

The signals of the new product are broadened in the presence of H₂ which speaks for chemical exchange. The H₂O signal shifts (concentration depended) to $\delta \sim 0.4$ ppm after freeze-pump-thaw degassing the mixture, which resembles the literature known shift in C₆D₆ (Figure 12, c).^[178] Additionally a new signal at $\delta = -26$ ppm can be observed, integrating to two protons, thus the NMR signals can be assigned to the dihydride complex **6** [(PNP)Ir(H)₂] previously reported by Schneider et al.^[37] Here, hydrogenolysis of **XXII** also led to the formation of **6** and ^tBuNH₂ as the second product and again reflects the chemical relationship between **4** and **XXII**.

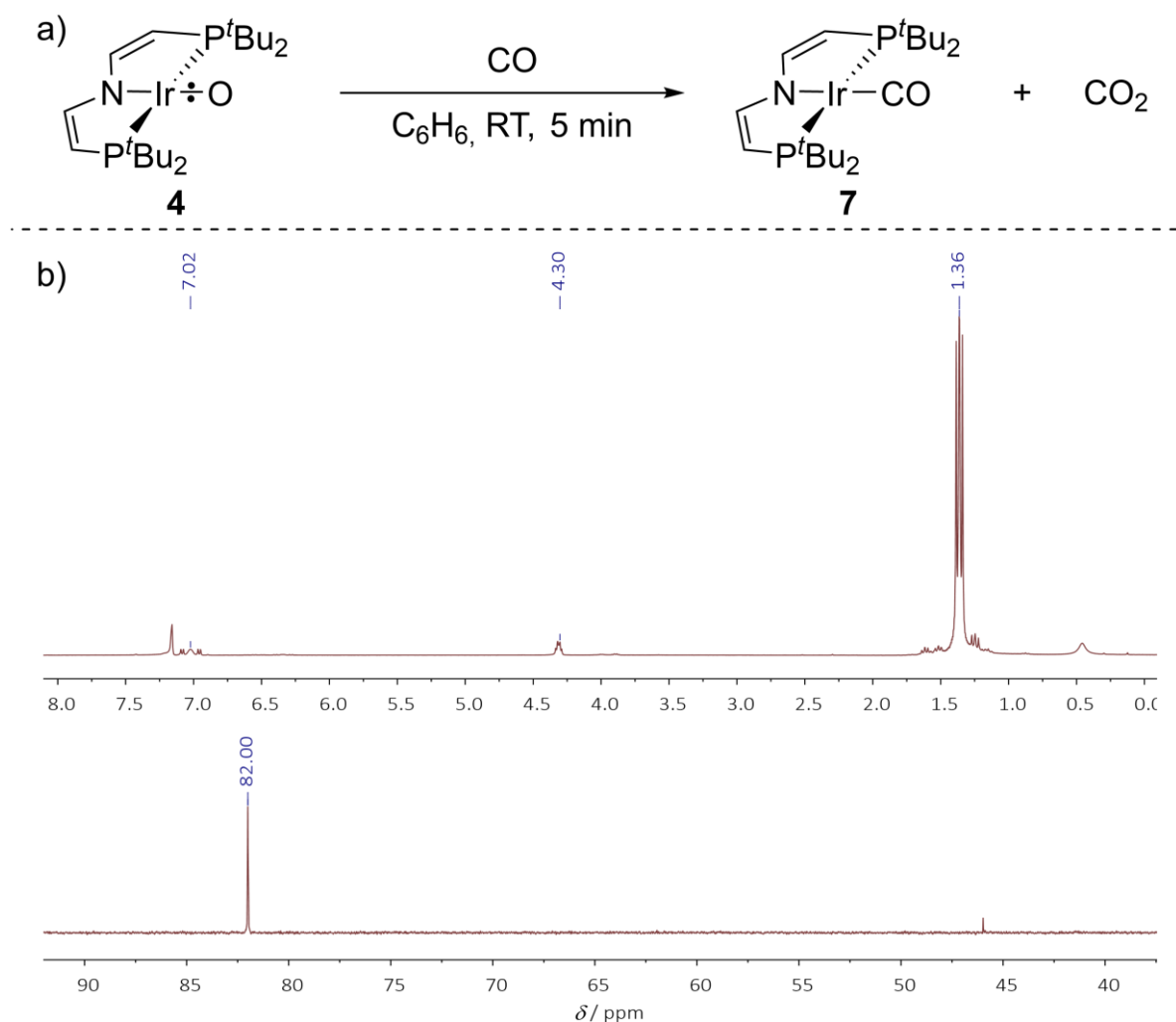


Figure 13: a) Carbonylation of **4** in benzene at ambient temperature yielding **7** and CO₂. b) ¹H-NMR spectrum of the reaction mixture. c) ³¹P-NMR spectrum of the reaction mixture. d) Headspace analysis plot of the reaction mixture.

The reaction of **4** with CO gas (1 bar) in benzene at ambient temperature gives an immediate colour change to pale yellow (Figure 13a). The ¹H-NMR spectrum of the reaction mixture shows the formation of one, C_{2v} symmetric, main product with three distinct signals in the spectrum ($\delta_{2xCH} = 7.02$ ppm, $\delta_{2xCH} = 4.30$ ppm, $\delta_{4x(CH_3)} = 1.36$ ppm) and one signal in the ³¹P-NMR spectrum ($\delta = 82$ ppm) which confirms the synthesis of the previously reported [(PNP)IrCO] carbonyl complex **7** (Figure 13b).^[179] Thus, in analogy to Milstein's platinum oxo **XXXI** [(PCN)Pt(O)][BF₄]³⁸, the second product must be CO₂, which could be confirmed by headspace analysis.^{[47],39} The

³⁸ PCN = C₆H₃[CH₂P(^tBu)₂](CH₂)₂N(CH₃)₂

³⁹ Head space analysis performed by M.Sc. Marcus Thater

reaction of CO₂ with iridium hydroxo- and imido complexes forming the (hydrogen)carbonate analogous is literature reported and speaks for a nucleophilic oxo moiety.^[35,37,168,172] In the ³¹P-NMR spectrum of the carbonylation reaction of **4**, also a second species at $\delta = 46$ ppm can be found, which might arise from the reaction of **4** with the formed CO₂.

To test the hypothesis, that the side product in the carbonylation reaction of **4** arises from reactivity with the second product CO₂, **4** was directly reacted with carbon dioxide. The addition of CO₂ to a degassed THF solution of **4** at ambient temperature leads to an instant colour change to deep red (Figure 14a). The ¹H-NMR spectrum of the reaction exhibits no paramagnetic species but three distinct signals ($\delta_{2xCH} = 6.40$ ppm, $\delta_{2xCH} = 5.45$ ppm, $\delta_{4xC(CH_3)_3} = 1.47$ ppm) which belong to one species by integration. The ³¹P-NMR spectrum exhibits one signal at $\delta = 46$ ppm, which is identical to the second product in the carbonylation of **4** (Figure 14b and c) and thus supports the aforementioned hypothesis. A potential candidate for the quaternary carbonyl C atom is found at $\delta = 174$ ppm in the ¹³C-NMR spectrum, which exhibits no coupling to the phosphorous atoms (Figure 14d).

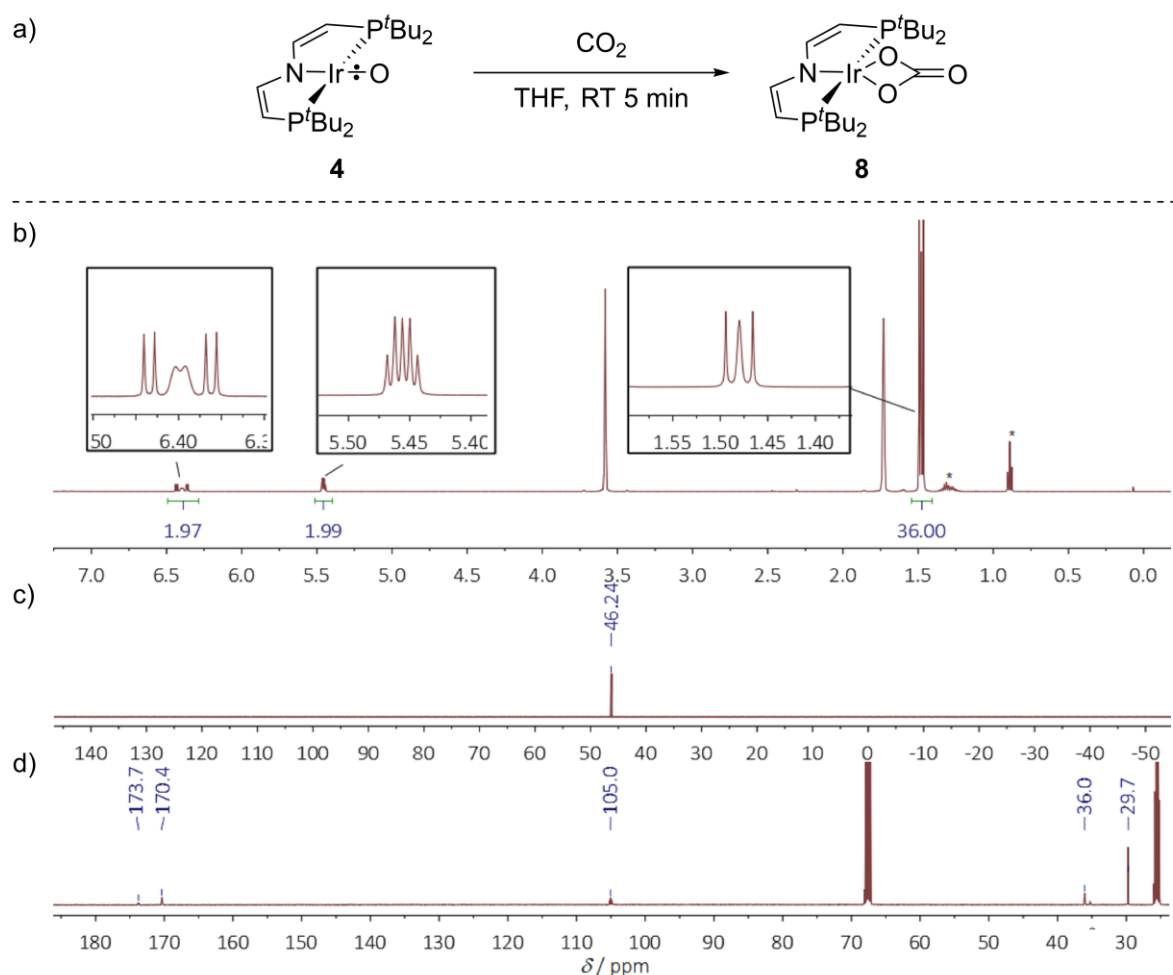


Figure 14: a) Synthesis scheme for the reaction of **4** with CO₂ in THF at ambient temperature yielding the carbonate complex **5**. b) ¹H-NMR spectrum of **5** in THF-d₈ at ambient temperature. Signals marked with * arise from *n*-pentane. c) ³¹P-NMR spectrum of **8** in THF-d₈ at ambient temperature. d) ¹³C-NMR spectrum of **5** at ambient temperature. Signals marked with * arise from *n*-pentane.

The IR(ATR) spectrum exhibits three distinct sharp signals in the “carbonyl region” at $\nu = 1663$ cm⁻¹, 1625 cm⁻¹ and 1553 cm⁻¹, which as well supports the formation of a carbonate complex (Figure 15a). Crystallisation from few toluene at -40 °C yields crystals suitable for XRD analysis and finally confirms the successful isolation of the

iridium(III) carbonate complex [(PNP)Ir(CO₃)] **8**.⁴⁰ The metal centre in **8** is in square planar coordination (angle sum around Ir = 360°)⁴¹ with two oxygen atoms of the carbonate unit coordinated to the metal centre at angles of N-Ir-O₁ = 151° and N-Ir-O₂ = 146°. The Ir-O bonds are elongated compared to **4** ($d_{\text{Ir-O}_1}$ = 2.06 Å and $d_{\text{Ir-O}_2}$ = 2.07 Å) resembling their single bond character. The carbonyl atom has two different sets of C-O bonds. The C-O bond to the uncoordinated oxygen is significantly shortened ($d_{\text{C-O}_3}$ = 1.224(4) Å) which indicates double bond character, while the bonds to the coordinating oxygen atoms are elongated ($d_{\text{C-O}_1}$ = 1.32 Å and $d_{\text{C-O}_2}$ = 1.31 Å) compared to “free” carbonate (Figure 15, b).^[180]

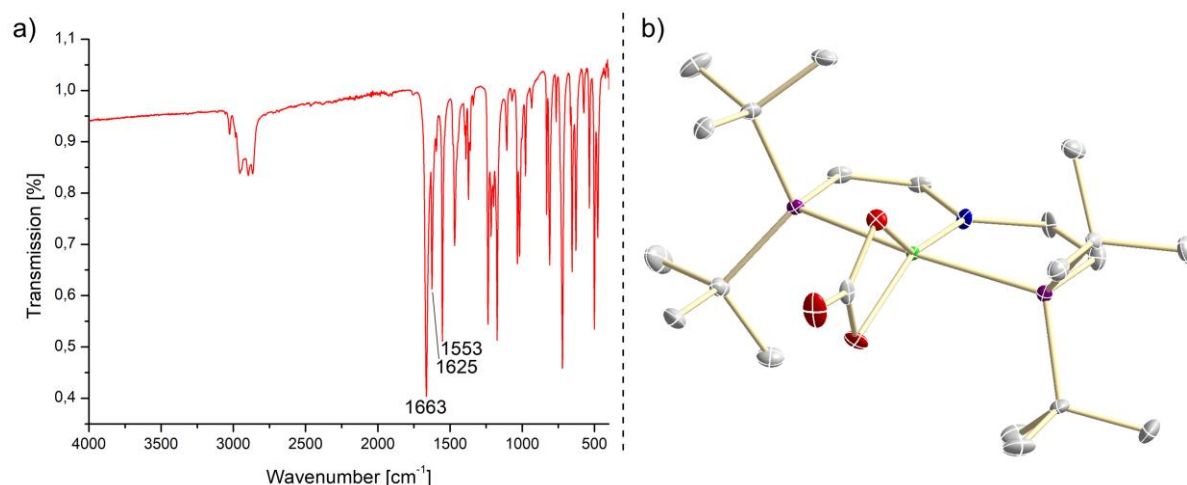


Figure 15: a) IR(ATR) spectrum of **8** b) Molecular structure in the solid state of **8** obtained by X-ray single crystal diffraction. The ORTEP plot shown with anisotropic displacement parameters at 50 %. All C-H hydrogen atoms, disorder and a cocrystallised toluene molecule omitted for clarity. Selected parameters: Ir-O₁: 2.061(2) Å, Ir-O₂: 2.068(2) Å, Ir-N: 1.928(3) Å, Ir-P1: 2.3374(8) Å, Ir-P2: 2.3383(8) Å, C1=C2: 1.326(4), O₁-C₂₁: 1.317(4), O₂-C₂₁: 1.313(4), O₃-C₂₁: 1.224(4), N-Ir-O₁: 151.47(10)°, N-Ir-O₂: 146.35(10)°, P-Ir-P: 163.75(3)° N-Ir-C₂₁: 177.38(12)°.

The philicity of **4** was further analysed with trimethyl phosphine as an ambiphilic reagent.^[37,181,182] While the addition of 1 eq. PMe₃ to a suspension of **4** in pentane at ambient temperature only results in partial conversion, the addition of 2 eq. leads to full conversion of the starting materials accompanied by the formation of a new complex and OPMe₃^[183] as determined by ³¹P-NMR spectroscopy (Figure 16a and c).⁴² Besides the main signal in the ³¹P-NMR at δ = 61.5 ppm, a second signal at δ = 61.3 ppm can be observed, which is assigned to the hydrido phenyl complex **9** [(PNP)Ir(H)(Ph)], this indicates an oxidative addition of the NMR solvent to an intermediately formed iridium(I) species.^[179] The NMR solvent was changed to cyclohexane-d₁₂ in which side reactivity only played a very minor role. The OPMe₃ can be removed by washing with hexamethyldisiloxane (HMDSO) and crystallisation at -40 °C yields material pure enough for further analysis. In the ³¹P-NMR spectrum, two sets of signals were found at $\delta_{\text{P}} = 61.75$ ppm, $\delta_{\text{P}} = -52.6$ ppm which integrate in a 2:1 ratio and exhibit P-P coupling ($J_{\text{P-P}} = 16.9$ Hz) and thus support the coordination of a second equivalent PMe₃ to the iridium(I) complex intermediate, which is left after the oxygenation of the first equivalent of PMe₃ (Figure 16e).⁴³

⁴⁰ Picking and measurement of the crystal by Dr. Sebastian Forrest, solving of the crystal structure by Dr. Christian Würtele.

⁴¹ Angle sum computed with the carbonyl C atom as the 4th substituent.

⁴² The solvent is changed to the more unreactive pentane, compared to the published route, to encounter the reactivity of **10** the reaction time could drastically be reduced.

⁴³ Please note, that for a reliable integration of ³¹P-NMR spectra the T_2 time needs to be adjusted, which was not done here. Therefore, the integrated values can only be estimates.

In analogy, the $^1\text{H-NMR}$ spectrum exhibits a C_{2v} symmetric species with four sets of signals ($\delta_{2xCH} = 7.00$ ppm, $\delta_{2xCH} = 4.19$ ppm, $\delta_{P(CH_3)_3} = 1.82$ ppm and $\delta_{4x(C_6H_5)} = 1.31$ ppm) which integrate to 2:2:9:36. This further supports the coordination of PMe_3 (Figure 16d).⁴⁴ XRD analysis finally confirms the coordination of PMe_3 to the formed iridium(I) fragment (Figure 16b). The iridium(I) PMe_3 complex $[(\text{PNP})\text{Ir}(\text{PMe}_3)]$ **10** is in square planar coordination environment (angle sum around iridium = 360.0°) with one PMe_3 ligand coordinating. The Ir-N bond length is, due to the *trans*-effect of the strongly σ -donating phosphine, elongated compared to the other complexes reported in this thesis. From this reactivity the philicity of **4** can be attributed to be of nucleo- to ambiphilic character.

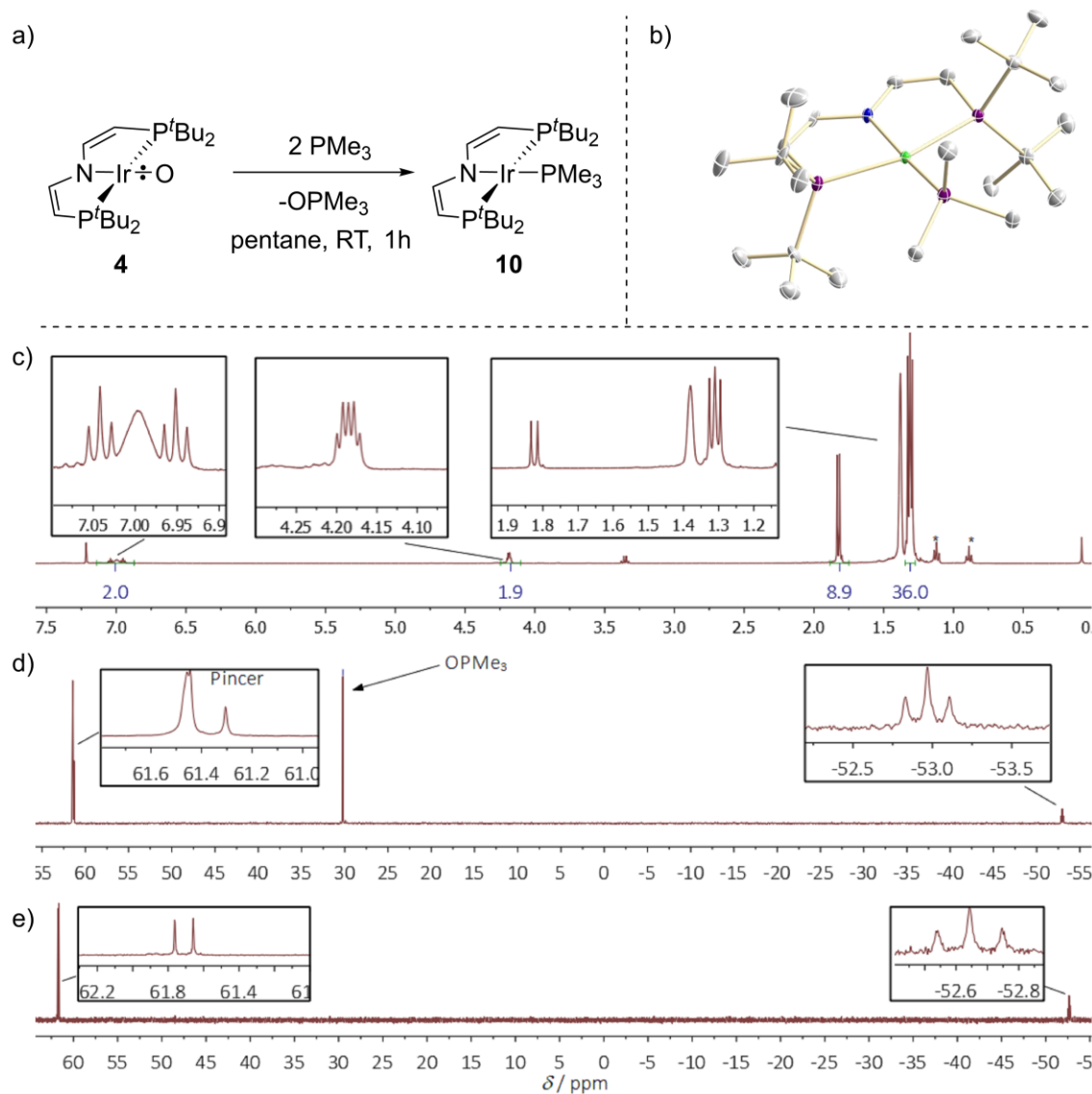
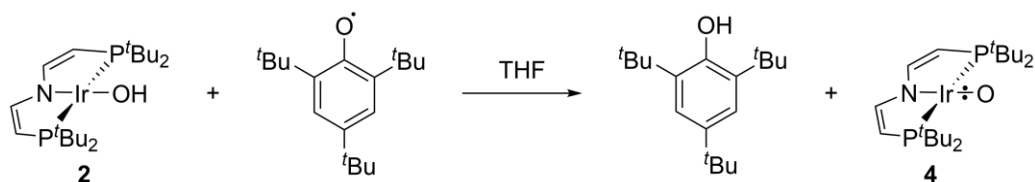


Figure 16: a) Synthetic scheme for the reaction of **4** with 2 eq. PMe_3 to **10** and OPMe_3 in THF at ambient temperature. b) Molecular structure in the solid state of **10** obtained by X-ray single crystal diffraction. The ORTEP plot shown with anisotropic displacement parameters at 50 %. All C-H hydrogen atoms are omitted for clarity. Selected parameters: Ir-P₃: 2.2418(13) Å, Ir-N: 2.092(4) Å, Ir-P1: 2.3361(13) Å, Ir-P2: 2.3594(14) Å, C1=C2: 1.326(7), P1-C₂₁: 1.843(5) Å, N-Ir-P₃: 174.03(12)°, P-Ir-P: 160.37(4)°. c) $^{31}\text{P-NMR}$ spectrum of the reaction mixture in C_6D_6 (reaction also carried out in C_6D_6). d) $^1\text{H-NMR}$ spectrum of the **10** in cyclohexane- d_{12} at ambient temperature. e) $^{31}\text{P-NMR}$ spectrum of **10** in cyclohexane- d_{12} . Signals marked with an asterisk belong to pentane.

⁴⁴ This special solvent was chosen to partially overcome the thermal instability of **10**.

3.2. BD(F)E determination of the hydroxo/oxo couple 2/4

An important measure for the ability of terminal oxo complexes to activate and oxygenate C-H bonds, is the bond dissociation (free) energy (BD(F)E) of the formed O-H bond upon hydrogen atom transfer. Thus the O-H bond strength of the hydroxo/oxo couple **2/4** in THF was determined by isothermal titration calorimetry (ITC).⁴⁵ Therefore, the strong hydrogen atom transfer (HAT) reagent Mes*O with a reported $BDE_{Mes^*OH}^{THF}$ of 354 kJ mol^{-1} was chosen as a titrant to **2** (Figure 18a).^[184]



Scheme 2: Reaction analysed by isothermal titration calorimetry.

The reaction is only slightly exothermic with a maximum heat rate of $16 \mu\text{J s}^{-1}$ and has no s-shaped character of the titration curve, which implies an equilibrium constant close to unity (Figure 18b). The background corrected integrated thermogram is fitted with an independent PCET model (for more information of this model see Section C in Chapter 7) and yields indeed a low reaction enthalpy of $\Delta H_r = -3.8 \text{ kJ mol}^{-1}$ and an even slightly endergonic equilibrium constant $K = 0.993$. Appealingly, the stoichiometry factor $n = 0.998$ is very close to the ideal value of unity for an $A+B \rightarrow C+D$ reaction and indicates the clean conversion of **2** to **4** without severe weighting errors or impurities of the compounds (Figure 18c and d). The low driving force is not unexpected, since in Section 2 the synthetic hydrogen atom transfer (HAT) from **2** with Mes*O in THF also does not lead to full conversion but runs into an equilibrium. The driving force for the synthesis of **4** was here enhanced by an unpolar solvent to enable precipitation of **4**. With the literature known BDE value of Mes*O an experimental value for the O-H bond of **2** can be calculated to $BDE_{2O-H}^{THF} = 350 \pm 2 \text{ kJ mol}^{-1}$. For the determination of the BDFE of **2**, the BDFE of Mes*O in THF had to be determined first via a solvent transfer (MeCN \rightarrow THF) utilizing the Abrahams solvation model as described by Mayer et al. (eq. 1).^{[53,185,186],46}

a)	α	β	b)	
THF	0	0.51	$BDFE_{R-H}^{THF} = BDFE_{R-H}^{MeCN} + \Delta\Delta G_{solv}(H) + [\Delta\Delta G_{solv}(R) - \Delta\Delta G_{solv}(R-H)]$ eq. 1 $[\Delta\Delta G_{solv}(R) - \Delta\Delta G_{solv}(R-H)] = -41.92[\alpha_{Mes^*OH}\beta_{MeCN} - \alpha_{Mes^*OH}\beta_{THF}] = 0.63 \text{ kJ mol}^{-1}$ eq. 2 $BDFE_{R-H}^{THF} = (323 + 1.03 + 0.63) \text{ kJ mol}^{-1} = 325 \text{ kJ mol}^{-1}$	
MeCN	0	0.22		
Mes*OH	0.22	---		

Figure 17: a) Abrahams model parameters for the solvation transfer of Mes*OH from MeCN to THF.^[185,186] **b) eq. 1:** Bond dissociation free energy of R-H in THF or MeCN ($BDFE_{Mes^*OH}^{MeCN} = 323 \text{ kJ mol}^{-1}$) respectively.^[53] $\Delta\Delta G_{solv}(H)$ differential free energy of solvation between MeCN and THF of a hydrogen atom $\Delta G_{THF}^{298.15 K}(H_2) = -20.38 \text{ kJ mol}^{-1}$ and $\Delta G_{MeCN}^{298.15 K}(H_2) = -21.41 \text{ kJ mol}^{-1} \rightarrow \Delta\Delta G_{solv}(H) = 1.03 \text{ kJ mol}^{-1}$.^[53] $\Delta\Delta G_{solv}(R)$ differential free energy of solvation between MeCN and THF of the residual radical. $\Delta\Delta G_{solv}(R-H)$, the differential free energy of solvation between MeCN and THF of the HAT reagent. **eq. 2:** Calculation of the differential free energy of solvation between the solvents with the Abrahams parameters.

The free energy of solvation of the hydrogen atom was approximated by the free energy of solvation of H_2 and the solvation difference of the residual radical Mes*O and Mes*OH were obtained with the Abrahams parameters in eq. 2. The BDFE for Mes*OH in THF is calculated to 325 kJ mol^{-1} and therewith the BDFE of **2** is determined with

⁴⁵ A comprehensive description of the experiment can be found in Section 3.1 of chapter VI.

⁴⁶ Please note, that after this work a new reference value for Mes*O was published: $BDFE = 311 \text{ kJ mol}^{-1}$.^[259] Based on this value the BDE of Mes*O can be calculated (Approximating $TS^{\circ}(H) \approx TS^{\circ}(H_2) = 27 \text{ kJ mol}^{-1}$)^[260] to $BDE = 338 \text{ kJ mol}^{-1}$. Therefore, the values of **2** change to $BDFE = 311 \text{ kJ mol}^{-1}$ / $BDE = 334 \text{ kJ mol}^{-1}$.

the experimental value of $\Delta G_r = 0$ to 325 ± 6 kJ mol⁻¹. Additionally, via a square scheme approach, the pK_A value of the cationic hydroxo complex **3** can be calculated with the reported^[187] C_H value of 66 kcal mol⁻¹ in THF to pK_A^{3^{O-H}} = 19.

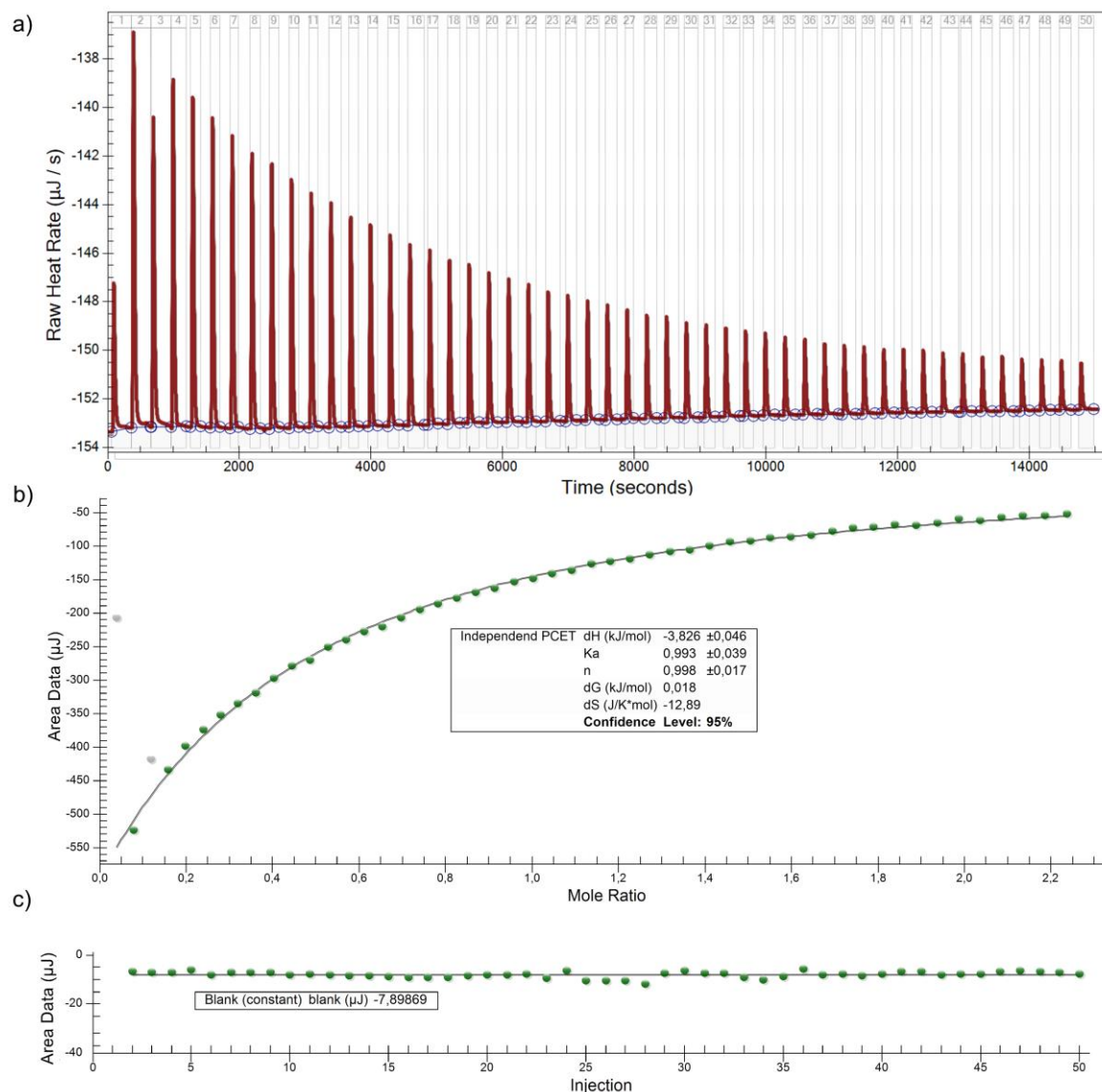


Figure 18: a) Raw heat curve of the titration of **2** (2.0 mM, 950 μL) with Mes*O (15.3 mM, 250 μL) in THF at 25 °C with fifty 5 μL injection steps. b) Background corrected integrated thermogram fitted with an independent PCET model. c) Background of the titration, the first point was out of range and it not shown here.

The PCET reaction was additionally analysed by computational means with the high level *ab initio* techniques ONIOM(CCSD(T)-F12b/DFT⁴⁷) and DLPNO,^{[95,97,98],48} where the ONIOM energy is computed via eq. 3.

$$E_{\text{ONIOM}} = E(\text{Truncation})_{\text{CCSD(T)-F12b}} - E(\text{Truncation})_{\text{DFT}} + E(\text{Fullsystem})_{\text{DFT}} \quad \text{eq. 3}$$

Truncation: Referring to truncated model systems; Fullsystem: Referring to the untruncated systems.

Two different truncation levels were probed for the ONIOM approach, “H-truncation” where hydrogen atoms replace the *tert*-butyl groups on the complexes **2** and **4** and Mes*OH and Mes*O, respectively and “Me-

⁴⁷ DFT: B3LYP(V)-D3/def2TZVP + Solvation Correction (SMD:THF) on the converged structures.

⁴⁸ Computations performed by Dr. Martin Diefenbach. A comprehensive computational analysis of the thermochemistry can be found in Section 4.2 of chapter VI.

truncation" where methyl groups replace *tert*-butyl groups. The *ab initio* methods also assign the triplet electromer of **4** as the ground state, but with a smaller triplet/singlet gap is smaller ($\Delta E(T/S)^{ab\text{ }initio} = 37\text{--}41\text{ kJ mol}^{-1}$) compared to the value of the DFT computation ($\Delta E(T/S)^{DFT} = 74\text{ kJ mol}^{-1}$). The DFT level of theory places the simple HAT reaction (Figure 19i and Table 1) of the complexes **4** and **2**, forming a free hydrogen atom, at 322 kJ mol^{-1} , whereas the *ab initio* techniques converge at much higher values. The DLPNO approach predicts for this reaction step a BDE of 349 kJ mol^{-1} , while all ONIOM approaches converge at 339 kJ mol^{-1} . The computation of the Mes*OH/Mes*O couple (Figure 19ii) is resulting in a BDE of 308 kJ mol^{-1} on the DFT level and a BDE of 335 kJ mol^{-1} at the DLPNO level of theory, while the results are more differing between the ONIOM approaches (Table 1). Here, the Mes*O-H bond is predicted to be stronger, the higher the level of theory. While the H-truncation on double-zeta basis is resulting in an BDE of 326 kJ mol^{-1} the Me-truncation triple-zeta basis computation results in a BDE of 331 kJ mol^{-1} . All computational approaches predict an endergonic reaction enthalpy for reaction iii), while experimentally a slightly exothermic reaction was observed (Table 1). A possible explanation is the higher uncertainty on the Mes*OH/Mes*O couple for all computational methods, while the computation of the "pure" BDE of the **2/4** couple (reaction i) yields comparable values to the experimental BDE of 350 kJ mol^{-1} .

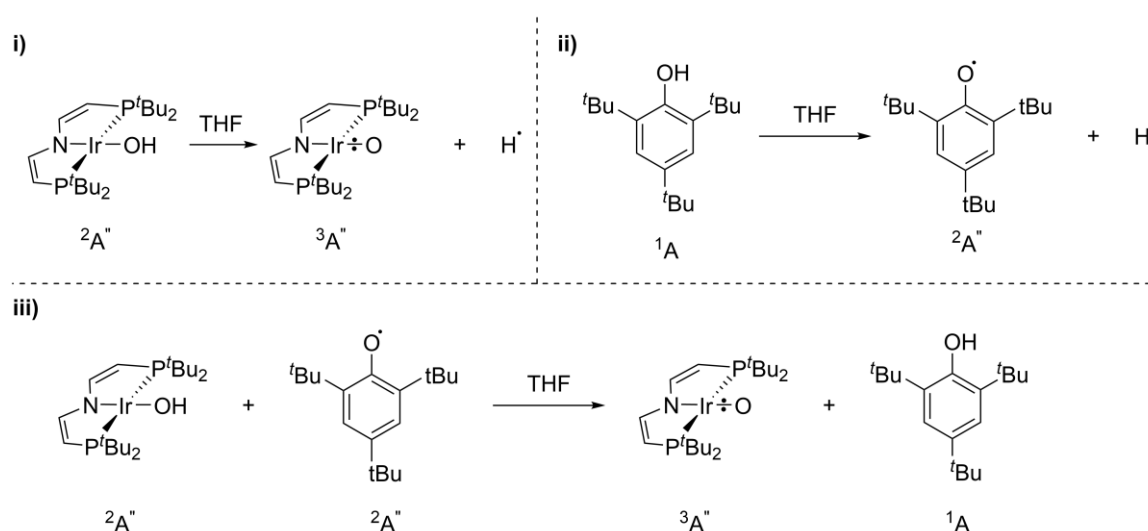


Figure 19: i) HAT reaction between **2** and **4** forming a free hydrogen atom. ii) HAT reaction between Mes*OH and Mes*O forming a free hydrogen atom. iii) PCET reaction between **2** and Mes*O forming iroxo and Mes*OH.

Table 1: Summary table of the thermochemical computations a) All structures computed at the DFT(B3LYP(V)-D3/def2TZVP) level of theory values given in kJ mol^{-1} . b) Triplet/Singlet gap on different levels of theory, Excitation energy at 0 K from the $3A$ (C_2) to the lowest energy $1A$ (C_2) electromer. c) Reaction enthalpy at 298 K of reaction **i**) including solvation in THF. d) Reaction enthalpy at 298 K of reaction **i**) including solvation in THF and spin-orbit coupling derived by CASSCF-NEVP2/QDPT $\Delta\Delta E_{SOC} = -2.9\text{ kJ mol}^{-1}$. e) Reaction enthalpy at 298 K of reaction **ii**) including solvation in THF. f) Reaction enthalpy at 298 K of reaction **iii**) including solvation in THF. g) Reaction enthalpy at 298 K of reaction **iii**) including solvation in THF and spin-orbit coupling derived by CASSCF-NEVP2/QDPT $\Delta\Delta E_{SOC} = -2.9\text{ kJ mol}^{-1}$. f) h) B3LYP(V)-D3/def2TZVP i) DLPNO-CCSD(T)/CBS(T,Q) level of theory. j) ONIOM(CCSD(T*)-VDZ-F12:DFT)(H:Bu) k) ONIOM(CCSD(T*)-VDZ-F12:DFT) (Me:Bu) l) ONIOM(CCSD(T*)-VTZ-F12:DFT)(H:Bu) m) ONIOM(CCSD(T*)-VTZ-F12:DFT) (Me:Bu).

Method ^a / kJ mol^{-1}	$\Delta E(T/S)^b$	ΔH_{solv}^c i)	$\Delta H_{solv}(SOC)^d$ i)	ΔH_{solv}^e ii)	ΔH_{solv}^f iii)	$\Delta H_{solv}(SOC)^g$ iii)
DFT ^h)	74.0	321.8	324.7	308.3	16.4	13.5
DLPNO ⁱ)	41.1	349.1	352.1	335.1	17.0	14.1
ONIOM(H:VDZ-F12b) ^j)	36.7	338.6	341.5	326.4	15.1	12.2
ONIOM(Me:VDZ-F12b) ^k)	36.9	339.0	342.2	327.6	14.5	11.6
ONIOM(H:VTZ-F12b) ^l)	39.9	339.3	341.9	329.2	12.7	9.8
ONIOM(Me:VTZ-F12b) ^m)	40.5	339.4	342.3	330.6	11.7	8.8

The spin-orbit coupling effect determined by multi-reference treatment of **2** and **4** in Section 2 (Figure 11, $\Delta\Delta E_{\text{SOC}} = -2.9 \text{ kJ mol}^{-1}$) is almost closing the gap between experiment and theory. The rather small value of the SOC effect was however unexpected. In a simple picture, **2** with its doublet ground state, only has one electron on the heavy nucleus which experiences spin-orbit coupling, while **4** is in a triplet ground state with two unpaired electrons which can be influenced by SOC. In this simple picture, **4** should be more stabilized by SOC than **2**. A possible explanation for the small SOC effect comes from the computed spin-density plots of **2** and **4** on the DFT and NBO-NPA level of theory (Figure 20). While the SOMOs of **4** predominantly exhibit Ir-O π^* -character, which results in an equal spin-density distribution over iridium and oxygen, the spin-density of **2** is mainly focused on the metal centre. The experimental and computational analysis of **4** is therewith representing an unprecedented iridium oxo biradical with strong oxyl radical character. The overall spin density at the iridium metal centre of **4** therefore does not change significantly compared to **2** upon PCET, which results in similar SOC stabilisations and thus no substantial overall SOC effect on the thermochemistry. This is a contrary situation as the quenching of the SOC effect by the ligand field commonly proposed in the literature.^[134,136–138]

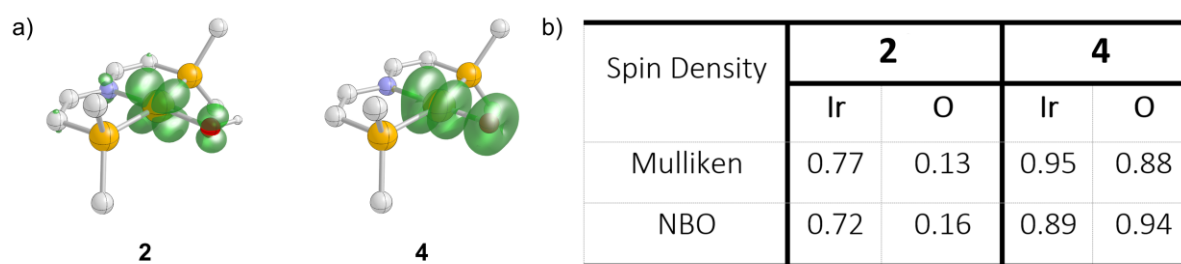


Figure 20: a) B3LYP(V)-D3/def2TZVP spin-density plots for the triplet ground state of **4** ($^3A''$) (top) and the doublet ground state of **2** ($^2A''$) (bottom) shown at isovalue $0.0075 a_0^{-3}$. b) Mulliken and NBO/NPA analysis of the spin density of **2** and **4**.

With all these thermodynamic parameters at hand, a full square scheme for all discussed oxo species can be formulated (Figure 21). The pK_A value of 19 of **3** is much more acidic than for **2** ($pK_A = 46$) but still in the medium range in THF, thus **4** is stabilized as a weak base. The irreversible reduction in the cyclic voltammogram of **4** can be easily explained by the super base character of the formed anionic oxo **4⁻** which might even be capable of deprotonating the solvent THF itself. The O-H bond strength rises within the hydroxo redox series. The anionic hydroxo complex **1** has the lowest BDE with 336 kJ mol^{-1} , therefore the anionic oxo complex **4⁻** will favour deprotonation over hydrogen atom abstraction. The BDE of neutral oxo complex **4** lies directly in the middle and is with a BDE value of 350 kJ mol^{-1} strong enough for the activation of weak C-H bonds but is not sufficient for the cleavage of the strong C-H bonds of most solvents. The same picture arises for the pK_A value of **4** and thus explains why **4** is stable in the first place. The cationic hydroxo complex **3** is bearing the strongest O-H bond with 372 kJ mol^{-1} . A comparison of the spin densities at the oxygen atom of **4** (O: 95%) and **4⁺** (O: 75%) reveals, that the more reactive cationic oxo **4⁺** has less radical character, which supports the statement of James Mayer that “Not radical character but bond strength is defining radical reactivity”.^[25]

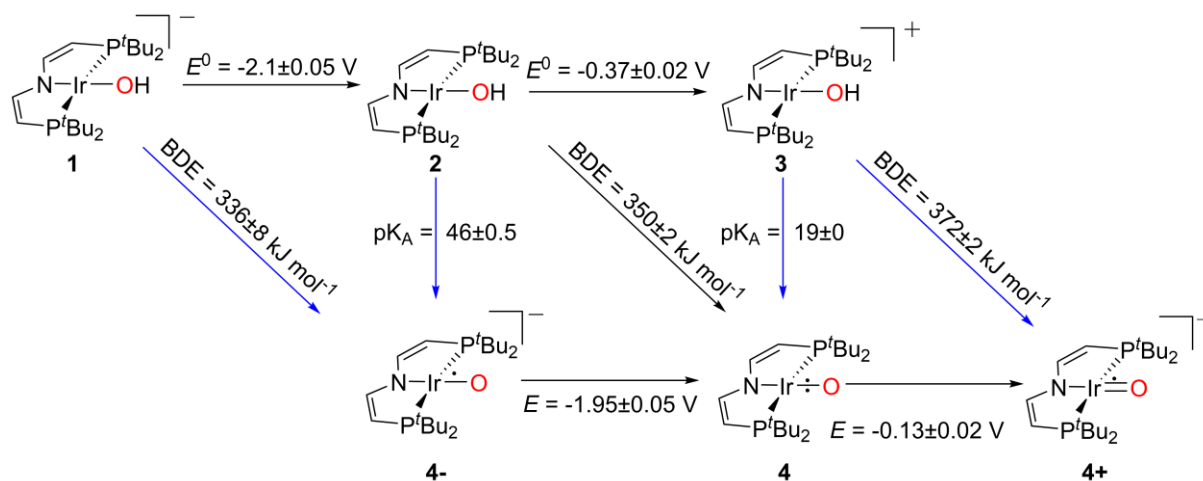


Figure 21: Thermodynamic parameters of **4⁻**, **4** and **4⁺** with a square scheme approach: Blue = calculated values via $BDE^{THF} = 23.06E^0 + 1.37pK_A + 66$ ^[187]. The errors for the cyclic voltammograms are taken from upper limits standard errors of the technique. For the irreversible processes the error is assumed to be higher. Please note, that for reliable data only electrochemically reversible signals should be considered, thus the values shown here give a qualitative picture.

3.3. C-H bond Activation Chemistry of **4**

With the O-H bond strength of **2** at hand ($BDE = 350$ kJ mol⁻¹, $BDFE = 325$ kJ mol⁻¹), the C-H bond activation capability of **4** is analysed. C-H bonds belong to the strongest bonds in nature with BDE values up to 558 kJ mol⁻¹ (HC=C-H, gas), 472 kJ mol⁻¹ (C₆H₆, gas) or 439 kJ mol⁻¹ (CH₄, gas), and can surpass elemental hydrogen gas (436 kJ mol⁻¹).^[53] The C-H bond strength decreases when the formed carboradicals can be stabilized by delocalisation over larger π -systems or when aromaticity can be reached upon HAT (Figure 22).

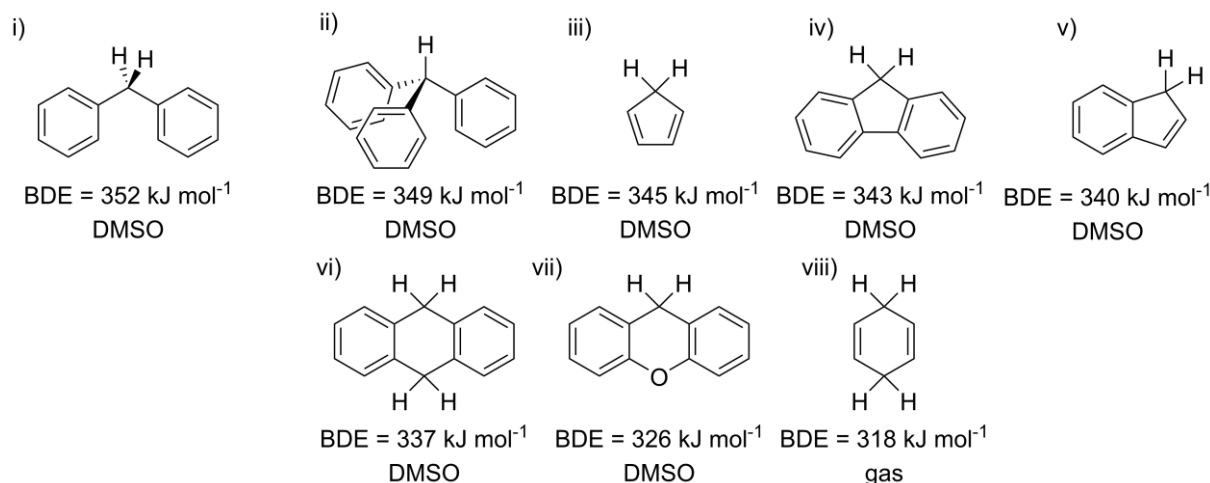


Figure 22: Selection of C-H bond strength in the range of **4** sorted by BDE. The weak C-H bonds are depicted for clarity. For 1,4-cyclohexadiene (viii) no value in DMSO was found.^[53]

The selective oxygenation of C-H bonds is a fundamental process in nature and an active field in chemical research, thus the most desired reactivity of **4** would be the formation of C-O bonds after the initial HAT reaction.^[188,189] For HAT reagents with two active HAT sites like cyclohexadiene or dihydroanthracene (Figure 22vi and viii, respectively) the driving force towards the aromatic products benzene and anthracene will most likely be higher than towards the formation of an alkoxide complex (Figure 23a). On the other hand, reagents with only one active hydrogen atom can form an intermediate carboradical which can further react with a second equivalent of **4** to form a C-O bond (Figure 23b).

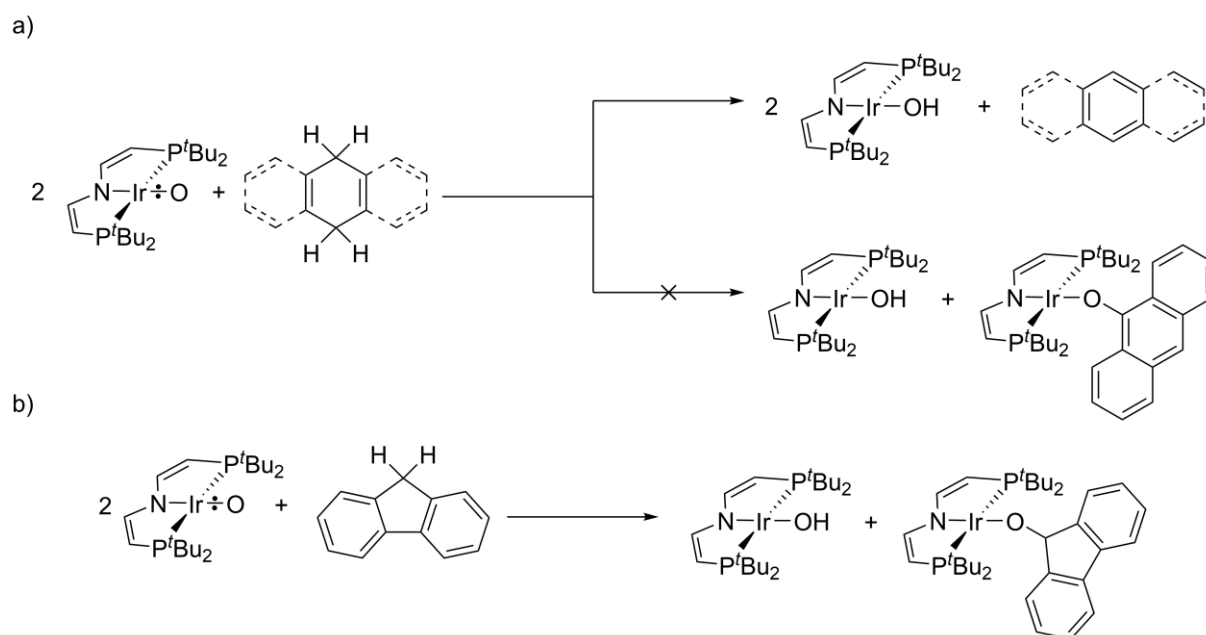


Figure 23: a) Expected reactivity of **4** with HAT donor bearing two active hydrogen atoms forming only **2** and the aromatic by-product. b) Expected reactivity of **4** with single HAT donor reagents with the example of fluorene.

Therefore, single HAT reagents were reacted with **4**. Stirring a solution of xanthene (Figure 22vii) and two equivalents of **4** in THF overnight at 60 °C leads to a colour change to green blue (Figure 24, a). The $^1\text{H-NMR}$ (para) spectrum shows an aromatic, diamagnetic species and two paramagnetic species with main peaks at $\delta = 8.2$ ppm, $\delta = 7.2$ ppm and $\delta = 6.2$ ppm. Here, the signal at $\delta = 7.2$ ppm can be assigned to hydroxo complex **2** (Figure 24b). Column chromatography over silanized silica enables the separation of both complexes but the organic, diamagnetic compound in the aromatic region of the spectrum cannot be separated on this way (Figure 24c). LIFDI-mass spectrometry gives one single complex product signal at $m/z = 746.2$ hinting towards the desired C-O bond formation towards an $[(\text{PNP})\text{Ir}(\text{II})(\text{xanthenolate})]$ complex **11** (Calculated: $m/z = 746.3$) (Figure 24d). Structural proof of the C-O bond formation was obtained by XRD analysis (Figure 24e). The xanthenolate complex **11** is in a square-planar coordination environment (angle sum around Ir = 360°), but the N-Ir-O and O-Ir-P1# angles deviate from an ideal square-planar coordination (167° and 111°, respectively). The elongated Ir-O bond of $d_{\text{Ir-O}} = 1.98$ Å and the Ir-O-C angle of 130° indicates no multibonding character in the Ir-O unit or in the xanthene fragment. A closer look at the $^1\text{H-NMR}$ spectra reveals two main *tert*-butyl peaks for **11** suggests a C_s symmetric structure in solution. The integration of both peaks ($\delta = 8.2$ ppm and $\delta = 6.2$ ppm) of **11** combined does however not reach the integral of the main peak of **2** which speaks for a non-selective reaction. Here, the organic side product helps to identify the second reaction pathway and gives inside into the mechanism of the reaction. The signal at $\delta = 4.0$ ppm in the $^1\text{H-NMR}$ spectrum can be assigned to the $C_{\text{sp}^3}\text{-H}$ proton of dimeric xanthene, integrating 4:2 with the aromatic protons, instead of 2:2 for monomeric xanthene.^[190] Therefore, the first step in the xanthene activation is the hydrogen atom abstraction forming one molecule of **2** and an intermediate xanthenyl radical. At this point the reaction pathways divide to 1) C-O bond formation between a second equivalent of **4** and the xanthenyl radical and 2) Dimerization of two xanthenyl radicals towards bixanthenone. Independent synthetic routes towards **11**, like ligand substitution to the chlorine complex **5** or the amide complex $[(\text{PNP})\text{IrNH}_2]$ **13** with free xanthenol under basic conditions unfortunately failed by now, which hinders the full characterisation of **11**.

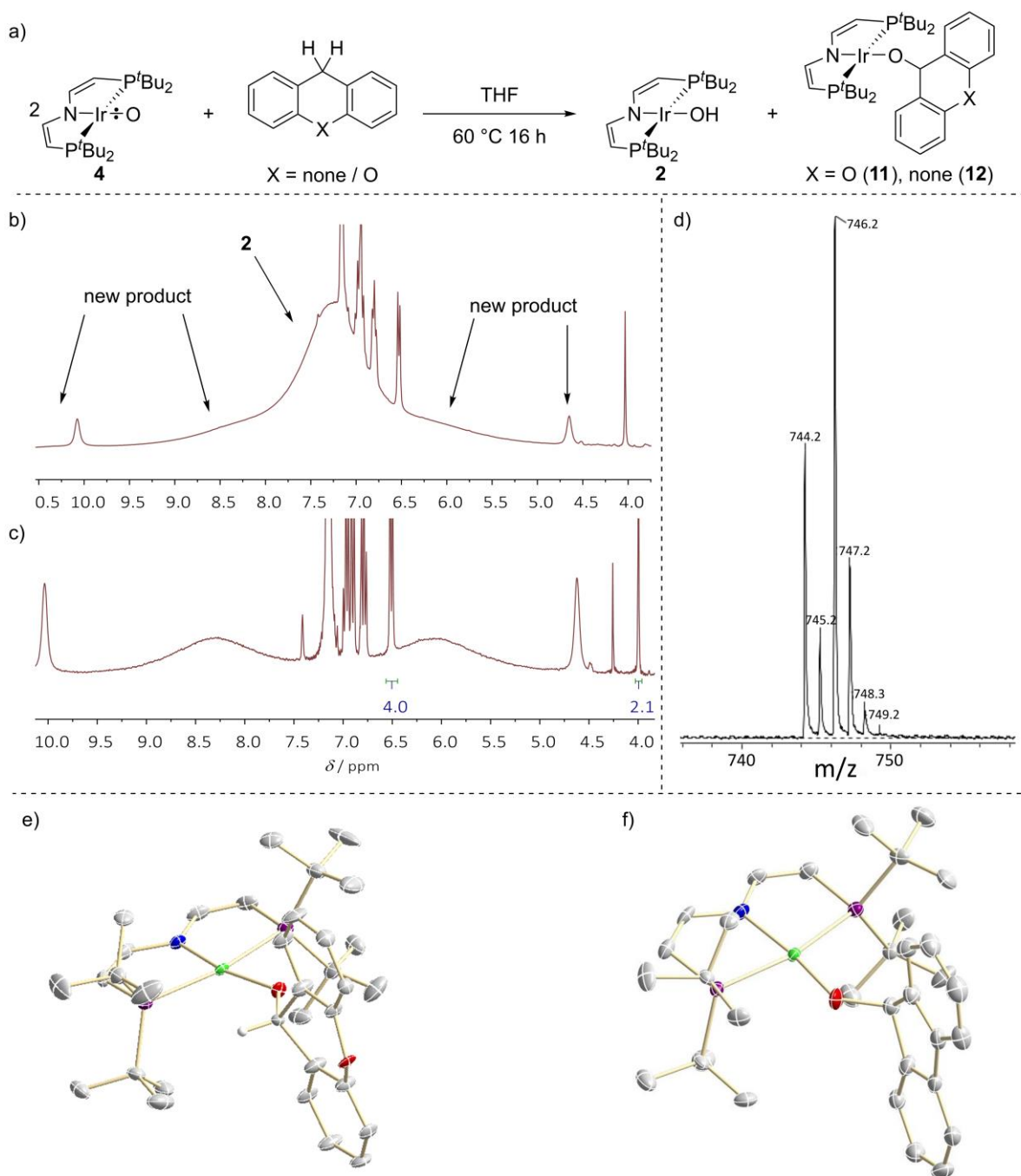


Figure 24: a) Reaction of **4** in THF at 60 °C for 16 h with xanthene (X = O) or fluorene (X = none) forming **2** and **11** or **12**, respectively. b) ¹H(para)-NMR spectrum of the reaction mixture for xanthene in C₆D₆ at 25 °C. c) Pentane phase of the reaction mixture after column chromatography over silanized silica for xanthene. d) LIFDI-mass spectrometry results of **12**, creation parameters: Average(MS[1] Time 0.66..0.72). e+f) Molecular structure in the solid state obtained by XRD analysis of **11** (e) and **12** (f), respectively. The ORTEP plots are shown with anisotropic displacement parameters at 50 %. All C-H hydrogen atoms and disorder of the molecule omitted for clarity. Selected parameters **11**: Ir-O₂: 1.983(5) Å, Ir-N: 1.988(4) Å, Ir-P1: 2.3327(9) Å, C1=C2: 1.327(6) Å, O₂-C₂₃: 1.385(8) Å, N-Ir-O₂: 166.75(14)°, N-Ir-P₁: 82.44(3)°, P-Ir-P: 164.87(5)°, O₂-Ir-P_{1#}: 110.74(14)°, Ir-O₂-C₂₃: 129.5(4)°. f) Selected parameters **12**: Ir-O₂: 1.960(4) Å, Ir-N: 1.988(4) Å, Ir-P1: 2.3091(17) Å, C1=C2: 1.340(9) Å, O₂-C₂₇: 1.387(7) Å, N-Ir-O₂: 170.5(2)°, N-Ir-P₁: 82.69(17)°, P-Ir-P: 164.99(5)°, O₂-Ir-P₂: 106.68(14)°, Ir-O₂-C₂₃: 131.5(4)°.

The same picture arises, when **4** is reacted with fluorene (Figure 22iv) with the corresponding [(PNP)Ir(II)(fluorenolate)] complex **12** as the main product, besides other diamagnetic species.⁴⁹ The solid state structure of **12** resembles the structure of **11** (Figure 24f) but with a smaller angle distortion of the N-Ir-O and P₂-

⁴⁹ One signal can be assigned to the dihydride complex **6**, while the other one is commonly observed with wet reagents which speaks for an impurity of fluorene.

Ir-O, which can be ascribed to the lower steric demand of the fluorenoate ligand. It should be noted that the reaction of **4** with xanthene also proceeds slowly at room temperature, while heating to 60 °C is mandatory for the reaction with fluorene, which reflects the decreasing driving force (BD(F)E difference) of the two compounds compared to **2**.

Benzaldehydes are an ideal platform to test for the concurrence reaction between HAT abstraction of the aldehyde C-H proton vs. a nucleophilic attack at the carbonyl atom, since they feature a relatively weak and sterically unprotected C-H bond ($BDE(\text{PhC}(\text{O})\text{-H}) \sim 365 \text{ kJ mol}^{-1}$)^[191] and an electrophilic carbonyl group in close proximity. Thermal reactivity could not be observed, but the filter less irradiation with a mercury arc lamp of **4** in benzene with 10-fold excess of the benzaldehyde is yielding two paramagnetic products (Figure 25b).

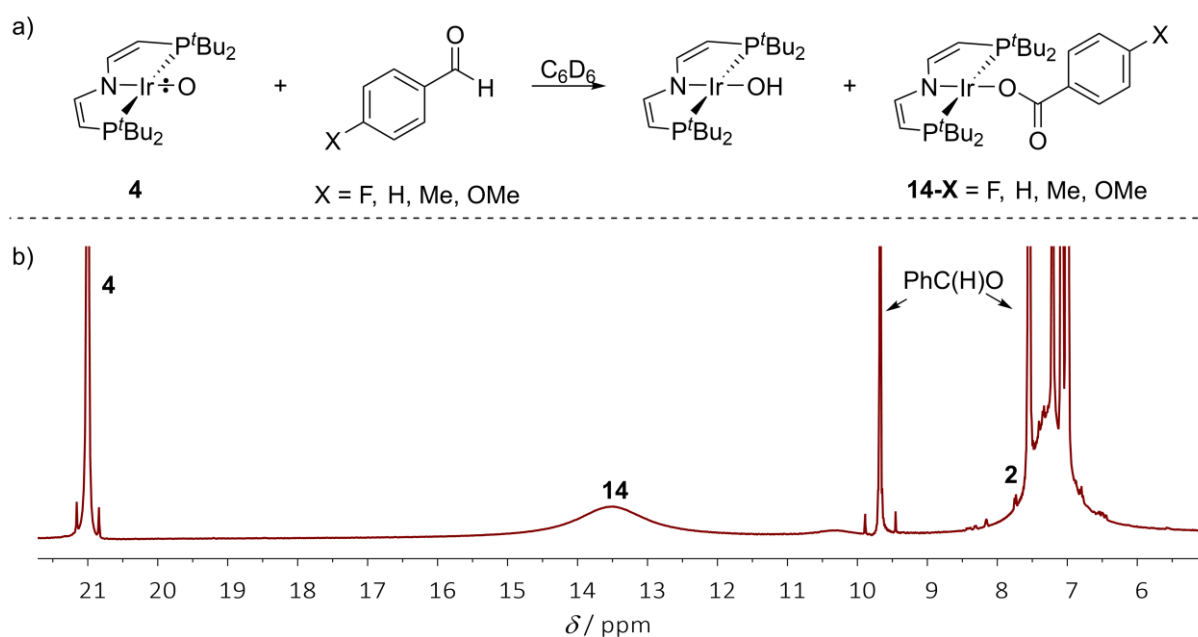
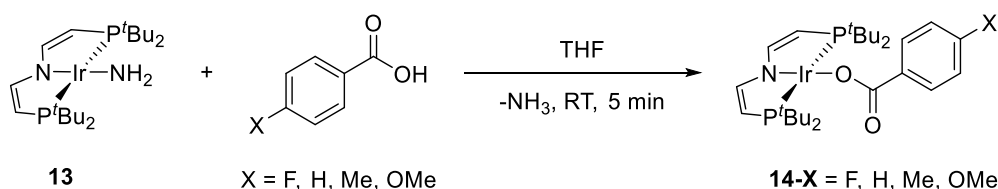


Figure 25: a) Irradiation of **4** with a mercury arc lamp (no filter) in benzene with different benzaldehydes (10 eq.) present (X = F, H, Me, OMe) forming **2** and the corresponding benzoate complex. **9-x**. b) ¹H-NMR spectrum after 30 min irradiation of **4** with benzaldehyde X = H after 30 min.

From the characteristic peak at $\delta=7.2$ ppm in the ¹H-NMR the formation of hydroxo complex **2** can be concluded, while besides **2** a second paramagnetic product with signals at ($\delta \sim 13$ ppm, $\delta = 4.9$ ppm, $\delta = 2.8$ ppm, $\delta = -4.9$ ppm and $\delta = -5.7$ ppm) can be observed, suggesting the coordination of benzaldehyde to **4**. A rational guess for benzaldehyde activation is the HAT transfer of the substrate to one molecule **4**, forming **2**, followed by the oxygenation of the benzaldehyde residue with a second equivalent of **4**, which yields the corresponding [(PNP)Ir(O₂CPh-X)] complex **14-x**, analogous to the reaction with xanthene and fluorene. To test this hypothesis an independent synthetic route towards **14-x** was probed. Reaction of the corresponding benzoic acid with the iridium amido complex **13**, yields one paramagnetic product with the exact same NMR signature as observed in the irradiation experiment, confirming the oxygenation of benzaldehydes by **4** under irradiative conditions (Scheme 3).



Scheme 3: Independent synthetic route towards **9-x** by reaction of **13** with the corresponding benzoic acid in THF at ambient temperature.

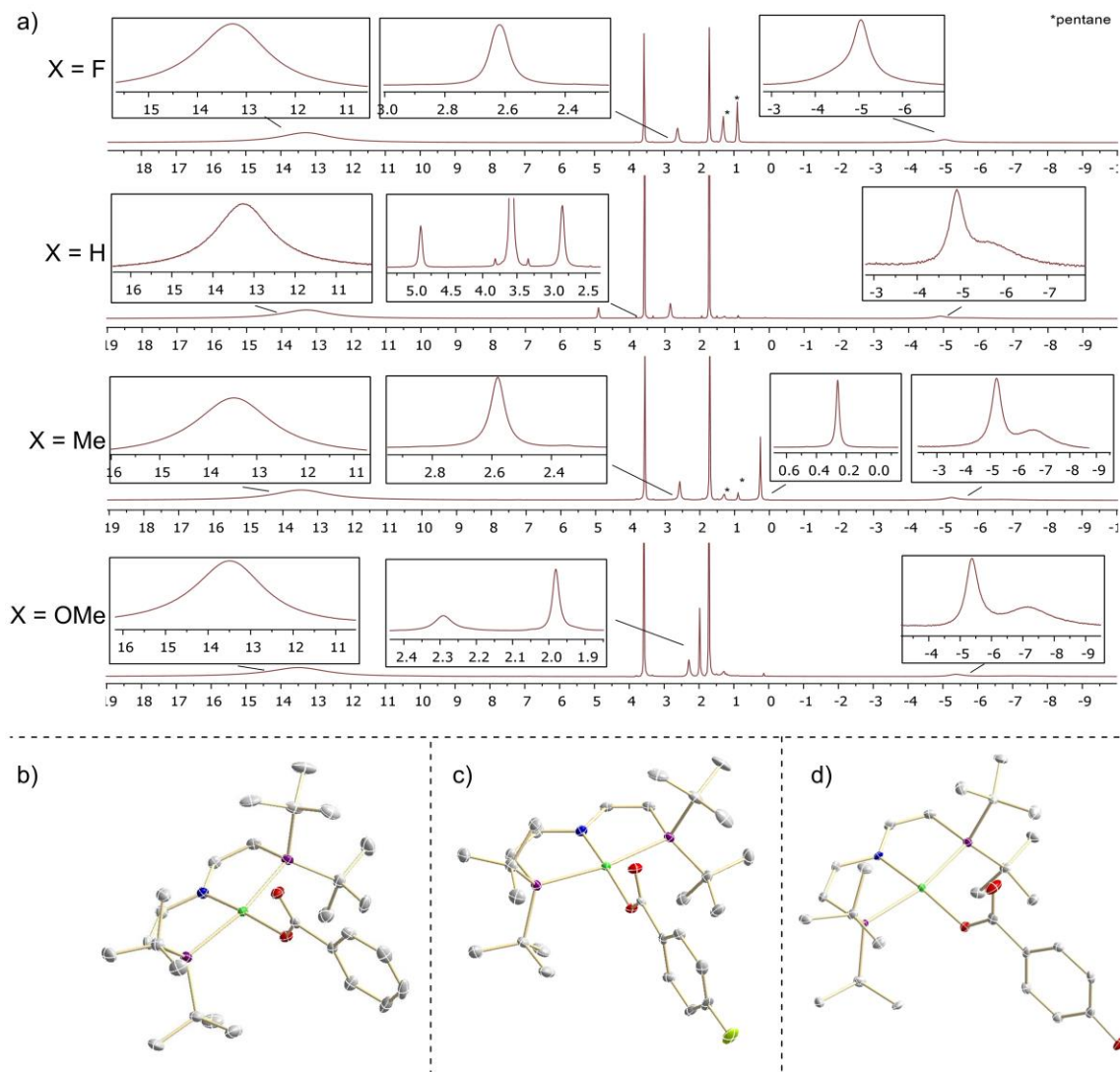


Figure 26: a) ^1H (para)-NMR spectra of the benzoate complexes **14-x** with (X = F, H, Me, OMe). Molecular structure in the solid state of b) **14-H**, c) **14-F** and d) **14-OMe** obtained by X-ray single crystal diffraction. The ORTEP plot shown with anisotropic displacement parameters at 50%. All C-H hydrogen atoms are omitted for clarity. For b) Two molecules crystallized in the asymmetric unit only one is shown for clarity. Selected parameters: Ir-O₁: 2.061(2) Å, Ir-N: 1.960(3) Å, Ir-P1: 2.3159(9) Å, C1=C2: 1.344(4) Å, O₁-C₂₁: 1.293(4) Å, O₂-C₂₁: 1.231(4) Å, N-Ir-O₁: 177.14(9)°, N-Ir-P₁: 82.82(8)°, P-Ir-P: 165.53(3)°, O₁-Ir-P₂: 97.08(6)°. For c) Two molecules crystallized in the asymmetric unit only one is shown for clarity. Selected parameters: Ir-O₁: 2.048(2) Å, Ir-N: 1.963(3) Å, Ir-P1: 2.3149(10) Å, C1=C2: 1.340(5) Å, O₁-C₂₁: 1.288(4) Å, O₂-C₂₁: 1.226(4) Å, N-Ir-O₁: 174.24(12)°, N-Ir-P₁: 82.84(9)°, P-Ir-P: 166.43(3)°, O₁-Ir-P₂: 95.75(7)°. For d) Selected parameters: Ir-O₁: 2.0316(19) Å, Ir-N: 1.972(2) Å, Ir-P1: 2.3257(7) Å, C1=C2: 1.332(4) Å, O₁-C₂₁: 1.297(3) Å, O₂-C₂₁: 1.225(4) Å, N-Ir-O₁: 172.86(9)°, N-Ir-P₁: 83.30(8)°, P-Ir-P: 166.56(3)°, O₁-Ir-P₂: 94.82(6)°.

The ^1H -NMR signals of the benzoate complexes **14-H**, **9-F**, **14-Me** and **14-OMe** are paramagnetically shifted with the main peak, corresponding to the *tert*-butyl groups at $\delta \sim 13$ ppm. Further, the signal at $\delta = 4.9$ ppm (X = H) is not present for X = F, therefore this signal can be assigned to the para-H in the phenyl ring, while the new signals at $\delta = 0.3$ ppm (X = Me) and $\delta = 2.0$ ppm (X = OMe) can be assigned to the methyl groups in this compounds. The

assignment of the other signals is more uncertain. It can be seen, that the signal at $\delta \sim 2.5$ ppm is shifting less within the complex series and thus suggests that it is not close to the rest X and therefore most likely a pincer backbone signal, while the two signals at $\delta \sim -5.0$ ppm exhibit a higher shift with different rests X and thus can be assigned to the ortho and meta phenyl protons (Figure 26a). Final structural proof is obtained by single XRD analysis ($X = \text{H}^{50}$, F, OMe⁵¹) (Figure 26b). All benzoate complexes are in square-planar coordination environment (angle sum around iridium = 360°). The Ir-O bond is elongated compared to **4** to $d_{\text{Ir-O}} \geq 2.0 \text{ \AA}$, which indicates no multi-bond character in the Ir-O unit, while the uncoordinated oxygen atom of the aldehyde bears a shorter bond to the carbonyl centre $d_{\text{C21-O2}} \leq 1.23 \text{ \AA}$ than the coordinated one $d_{\text{C21-O1}} \leq 1.29 \text{ \AA}$, which suggests double bond character in the carbonyl group. A Hammett analysis of the irradiation reaction is performed to get insight into the reaction mechanism.⁵² The analysis reveals a clear positive slope of the linear regression, and supports either a C-H bond weakening of the excited state benzaldehyde and thus fast HAT from the aldehyde to **4**, forming **2**, in the first step or a nucleophilic attack of the excited state **4** at the carbonyl centre. Since the reactivity of **4** has been previously shown to exhibit nucleo- to ambiphilic character, the latter explanation is more convenient.

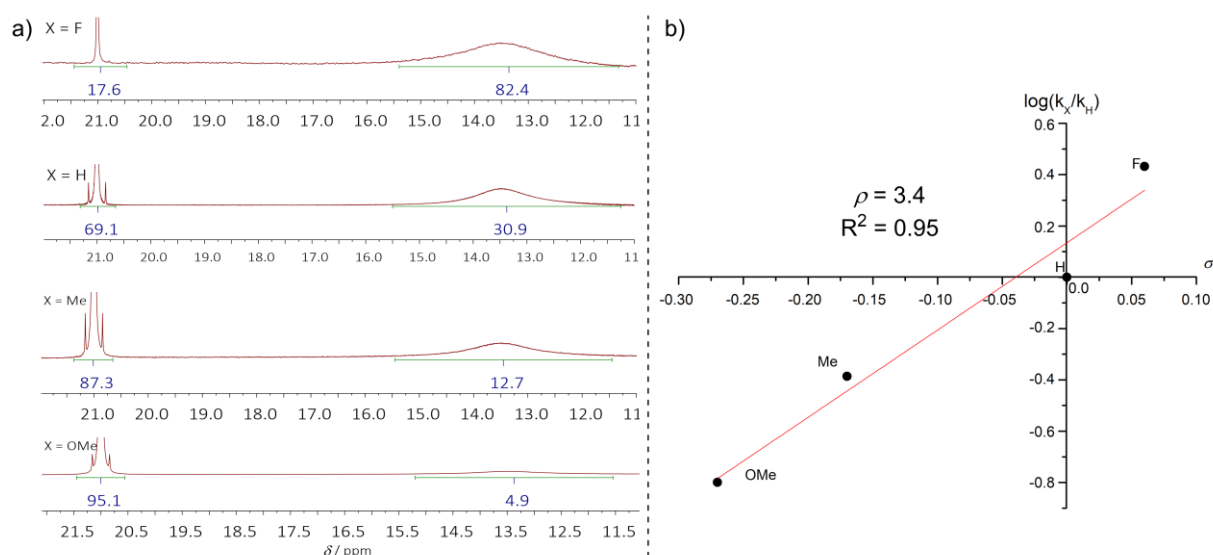


Figure 27: Irradiation of **4** in benzene solution at ambient temperature.⁵³ b) ¹H(para)-NMR spectra of the irradiation of **4** in benzene. c) Hammett analysis of the irradiation experiment, with the Hammett/Taft parameters for the para position of the substituents.^[192]

⁵⁰ Crystals grown by Niklas Welker and measured by Dr. Christian Würtele.

⁵¹ Crystals grown by Matthieu Haake and measured by Dr. Matthias Otte.

⁵² See Section 2.11 in chapter VI for experimental details.

⁵³ Experiment performed by Niklas Welker.

4. Summary of Chapter II

In summary the isolation and full characterisation of an open-shell terminal iridium oxo complex was presented. Spectroscopic and crystallographic characterisation led to the assignment of an iridium oxygen double bond in contrast to the triple bond character of the only other terminal iridium oxo complex by **XXI** Wilkinson et al. SQUID magnetometry revealed a thermally well separated (650 cm^{-1}) triplet ground state with large TIP from SOC. The zero-field splitting is 200 cm^{-1} higher than for the isoelectronic terminal imido complex **XXII**, which can be rationalised by a smaller relativistic nephelauxetic effect of **4** due to less covalent Ir-E ($E = \text{N/O}$) bonding, which results in a higher effective SOC parameter ζ_{eff} for **4**. Multi-reference computations reproduce this picture and predict a triplet ground state with a high zero-field splitting (750 cm^{-1}). Additionally, a small but non-negligible SOC effect on the PCET thermochemistry of hydroxo/oxo couple **2/4** is predicted. The oxo complex **4** is therefore best described as a rare biradical species with substantial oxyl radical character as confirmed by Mulliken spin density and NBO/NPA analysis. **4** exhibits a versatile nucleo- to ambiphilic oxygenation chemistry as shown by reaction with PMe_3 , CO, CO_2 , H_2 and benzaldehydes. The calorimetrically determined O-H BD(F)E of the hydroxo/oxo complex couple **2/4** (350 kJ mol^{-1} , (325 kJ mol^{-1})) is in line with the predicted value from *ab initio* computations ($\text{BDE}^{\text{ab initio}+\text{SOC}} = 343\text{ kJ mol}^{-1}$) and is in the thermodynamic region of activated C-H bonds. Indeed, by reaction with xanthene ($\text{BDE} = 326\text{ kJ mol}^{-1}$) and fluorene ($\text{BDE} = 343\text{ kJ mol}^{-1}$) the C-H oxygenation products are obtained.

The transient cationic iridium(IV) oxo species **4+** is accessible at very mild oxidation potentials ($E_{1/2} = -0.13\text{ V}$ vs. Fc/Fc^+), which reflects the high covalent iridium-oxygen bonding and therewith the low validity of oxidation numbers in such systems. The almost axial X-band EPR spectrum of **4+** is further supporting a ligand centred oxyl radical which is backed up by DFT analysis. The Mulliken spin density of **4+** (O: 75%) is mainly oxygen centred, speaking for a rare oxyl radical complex, but with a lower oxygen spin density as for **4** (O: 88%). A comparison of the O-H BD(F)E of neutral oxo **4** ($\text{BDE} = 350\text{ kJ mol}^{-1}$) with its cationic counterpart **4+** ($\text{BDE} = 372\text{ kJ mol}^{-1}$) supports the key message of James Mayer, that not radical character is rendering PCET chemistry, but the driving force of the reaction.

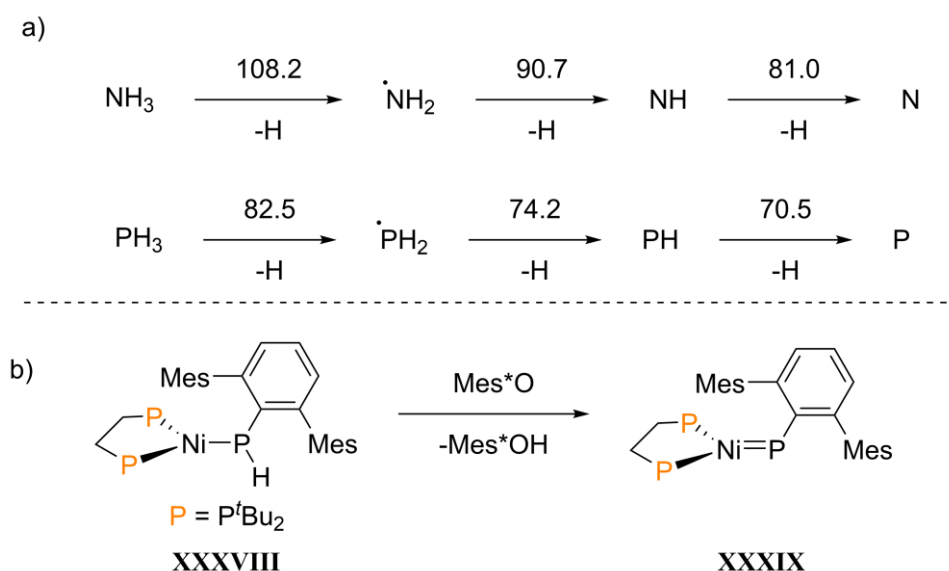
Chapter III

III. Excursuses

1. Excursus 1: Interconversion of Phosphinyl Radical and Phosphinidene Complexes by Proton Coupled Electron Transfer

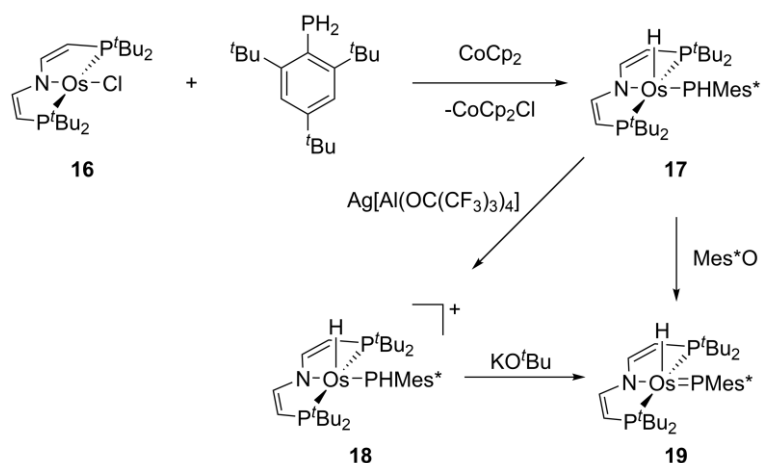
Parts of this Chapter are published in: J. Abbenseth, D. Delony, M. C. Neben, Christian Würtele, B. de Bruin, S. Schneider, *Angew. Chemie. Int. Ed.* **2019** 58 6338. "Interconversion of Phosphinyl Radical and Phosphinidene Complexes by Proton Coupled Electron Transfer". The synthetic work presented here was performed under the supervision of Dr. Josh Abbenseth by Marc. C. Neben.

Phosphorous compounds like phosphinyl radicals (PR_2) are key intermediates in P-C bond formations, due to their electronically unsaturated nature.^[193–197] Catalytic P-R bond formation processes remain nevertheless scarce, while the analogue nitrene transfer reactions are commonly catalytically utilized in organic synthesis.^[24,40,198–200] A possible explanation is the lack of suitable oxidizing transfer reagents for PR moieties. Here, primary phosphines present attractive precursors from a thermochemical point of view, since their P-H bonds are inherently weaker compared to their N-H analogues (Scheme 4a)^[184]. Additionally, the coordination of the free phosphine to a metal catalyst site might further weaken the P-H bonds, as observed for water and ammonia.^[201,202]



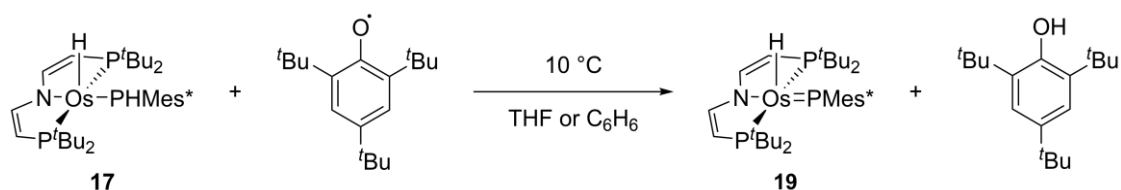
Scheme 4: a) N-H and P-H bond dissociation energies (BDEs) in the gas phase in kcal mol⁻¹.^[184] b) Synthesis of a nickel phosphinidene complex by PCET reported by Hillhouse et al. (Mes = 2,4,6-trimethyl-phenyl, Mes* = 2,4,6-tris-*tert*-butyl-phenyl).^[203]

While N-H bond homolysis from amide ligands is an active field of chemistry, P-H bond homolysis was only reported by Hillhouse et al. from the nickel platform **XXXVIII** (Scheme 4b).^[203] In this light the [Os(H)(PHMes*)(PNP)] phosphinyl radical complex **17** was synthesized by oxidative addition of PH_2Mes^* to the previously reported square-planar [Os(Cl)(PNP)] complex **16**, followed by subsequent reduction with cobaltocene in benzene.^[204] Insight into the PCET chemistry of the thermally unstable phosphinyl radical complex **17** was obtained by a square scheme approach and by direct HAT (Scheme 5). Oxidation of **17** using the silver "crossing" salt ($\text{Ag}[\text{Al}(\text{OC}(\text{CF}_3)_4)_4]$) at -35°C gave access to the thermally instable, cationic osmium(IV) phosphide complex **18**. Cyclic Voltammetry gave a reversible oxidative wave ($E_{1/2} = -0.88\text{ V vs. FeCp}_2^{+/0}$) which indicates that the chemical decomposition is not happening within the time frame of CV.



Scheme 5: Synthesis of the phosphinyl radical complex **17** by oxidative addition of PH₂Mes* to **16** and subsequent reduction with CoCp₂ in benzene and PCET chemistry of **10** by oxidation with silver “crossing” salt and subsequent deprotonation with KO^tBu or HAT with Mes*O.

Deprotonation of **18** with KO^tBu at $-80\text{ }^{\circ}\text{C}$ yields quantitatively a purple product, which could be assigned to the phosphinidene complex **19** with ³¹P-NMR by its characteristic signal at $\delta_{\text{P}} = 825\text{ ppm}$ for the PMes* group. The thermal instability of **18** nevertheless hampered the determination of a reliable pK_A value. Thus, the direct determination of the P-H bond strength of **17** by HAT was focused. Reaction with Mes*O gave the clean formation of **17**, which supports this reaction as suitable for further analysis by isothermal titration calorimetry. The BDE determination was carried out at $10\text{ }^{\circ}\text{C}$ to suppress the thermal decomposition of both **17** and **19**, respectively (Figure 28a).



Scheme 6: PCET reaction of **17** with Mes*O forming **19** and Mes*OH analysed by Isothermal Titration Calorimetry in THF and benzene at $10\text{ }^{\circ}\text{C}$.

The ITC was recorded in THF and benzene and reveals a very exothermic reaction with $\Delta H(\text{THF}) = -69\text{ kJ mol}^{-1}$ and $\Delta H(\text{C}_6\text{H}_6) = -71\text{ kJ mol}^{-1}$ leading to a P-H BDE of 67 kcal mol^{-1} in THF and of $65.5\text{ kcal mol}^{-1}$ in benzene (Figure 28c and d). A reliable determination of the free bond dissociation energy (BDFE) in both solvents was hampered by the thermal instability of **19**. Here, the thermal decomposition led to increased tailing of the peaks around the equivalence point, thus a meaningful fit of the titration curve is hampered (Figure 28b). The effect of P-H bond weakening upon coordination mentioned above is supported by computational analysis by means of DFT.⁵⁴ Here, the free HPMes*/PMes* couple exhibits a 6 kcal mol^{-1} higher BDE compared to the coordinated fragment, supporting the general assumption that primary phosphines are suitable precursors for PR transfer reactivity. With the P-H BDE value and oxidation potential of **17** in THF at hand, the calculation of the pK_A value of **18** by a thermochemical square-scheme is possible (Figure 28e). With the Bordwell equation^[205] $\text{BDE} = 1.37\text{pK}_A + 23.06E^{\circ} + C_{\text{H}}$, with $C_{\text{H}}(\text{THF}) = 66\text{ kcal mol}^{-1}$ ^[187], the value can be calculated to $\text{pK}_A(\mathbf{18}, \text{THF}) = 16$.

⁵⁴ The computations discussed here are not presented in the publication. They are nevertheless on a comparable level of theory (PBE-D3/defsvp but without the RI-J approximation). A detailed discussion of the computations can be found in chapter VI Section 4.4.

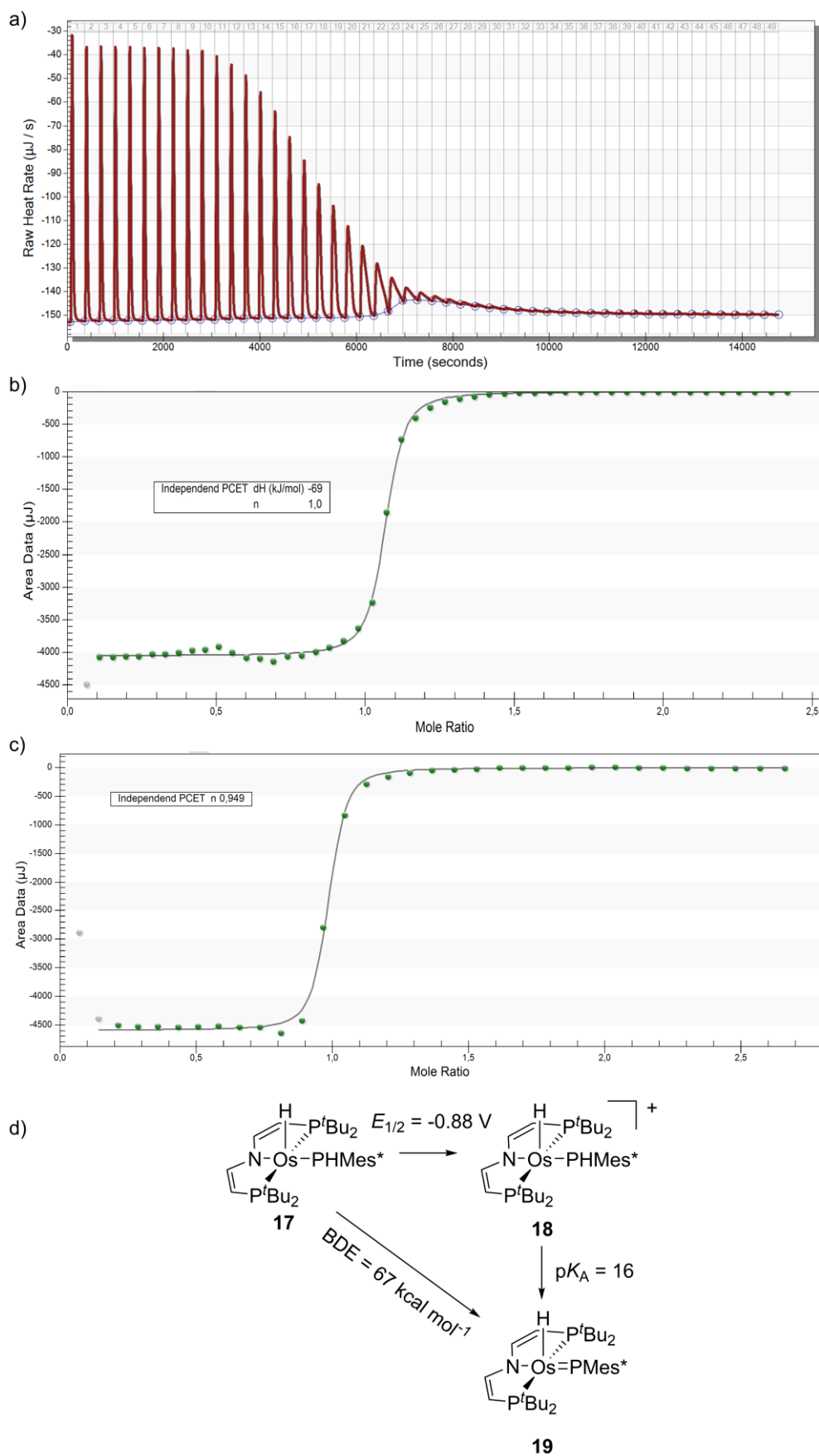
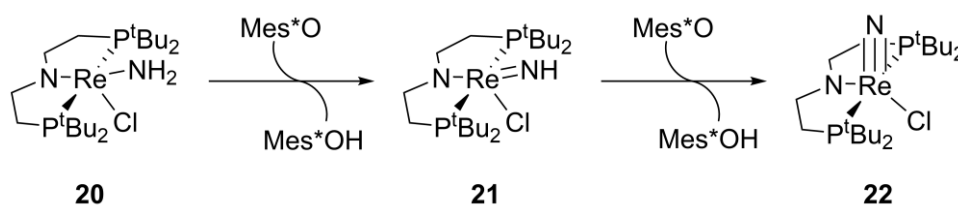


Figure 28: a) Representative thermogram of the titration curve in THF with peak tailing around the equivalence point. b) Representative integrated thermogram in benzene fitted with an independent PCET model (see Chapter 7, Section C). c) Representative integrated thermogram in THF fitted with an independent PCET model. d) Thermochemical square scheme for the pK_A determination of **18**.

2. Excursus 2: Facile Conversion of Ammonia to a Nitride in a Rhenium System that Cleaves Dinitrogen

The manuscript of this Chapter is currently in progress in collaboration with Prof. Holland and Prof. Mayer (Yale University). G. Connor, D. Delony, B. Q. Mercado, J. B. Curley S. Schneider., J. M. Mayer, P. L. Holland "Working title: Facile Conversion of Ammonia to a Nitride in a Rhenium System that Cleaves Dinitrogen". The synthetic work presented here was performed by Gannon Connor.

The interconversion of atmospheric dinitrogen to NH_3 is one of the most important syntheses developed in the 20th century, since the so obtained fertilizers are responsible for around 40 % of our food production and thus supply the growing world population.^[206] The microscopic reverse reaction from NH_3 to N_2 is equally of high research interest, since the enormous energy density of ammonia ($\omega_{\text{NH}_3} = 22.5 \text{ MJ/kg}$) renders it as a candidate for carbon-free fuels.^[207] For the realisation of the potential of such an ammonia-based fuel cell, the underlying principles and chemical reaction steps must be investigated in detail. Here, the analysis of the single PCET steps from ammonia to a nitride ligand, which finally couples to N_2 , is of special interest on the search for potential bottle necks in the interconversion. A promising system for this reaction is a complex which already has shown to be active in N_2 fixation and cleavage. Here, rhenium pincer complexes have recently gained attention.^[158,208,209] The rhenium(V) nitride complex $[(\text{PNP})\text{Re}(\text{V})(\text{Cl})(\text{N})]$ **22** is capable of nitrogen incorporation into nitriles, but was shown to be unreactive towards organic hydrogen atom transfer reagents or H_2 . Thus, the PCET thermochemistry of the microscopic reverse reaction from the rhenium(III) amide complex $[(\text{PNP})\text{Re}(\text{III})(\text{Cl})(\text{NH}_2)]$ **20** towards the nitride complex **22** will be analysed, to gain insight into this bottle neck (Scheme 7).



Scheme 7: Analyzed PCET reaction in this excursus of **20** to **22** with intermediate imido complex **21**.

The mean N-H BDE of the **20/22** couple is determined by isothermal titration calorimetry by titration of **20** with Mes*O ($\text{BDE}_{\text{O-H}}(\text{Mes}^*\text{OH}) = 354 \text{ kJ mol}^{-1}$) in THF.⁵⁵ The heat of reaction does not change after the addition of one equivalent Mes*O (Figure 29a), which is reproduced by NMR spectroscopy, in which the intermediately formed terminal imido complex $[(\text{PNP})\text{Re}(\text{IV})(\text{Cl})(\text{NH})]$ **21** cannot be observed. Since the single PCET steps are not separable calorimetrically, only the determination of a mean N-H BDE is possible. Exactly after the addition of the second equivalent of Mes*O, the reaction stops with a step slope. This indicates that the (double) PCET step is irreversible (Figure 29a). The data is fitted with the independent PCET model (see Section C), to obtain the stoichiometry of the reaction, while the reaction enthalpy is determined by the mean heat of reaction until the equivalence point (Figure 29b). To benchmark the so obtained data, the experiment is independently performed three times, resulting in a weighted average reaction enthalpy of $\Delta H^{\text{Double PCET}} = -213 \pm 2 \text{ kJ mol}^{-1}$. Therefore, for each single PCET

⁵⁵ A detailed discussion of the performed experiments can be found in Section 3.6 of chapter VI.

step an average of $\Delta H^{\text{Single PCET}} = -107 \pm 1 \text{ kJ mol}^{-1}$ is released, which results in a mean binding energy of $\text{BDE}^{\mathbf{20}} = 59.2 \pm 0.25 \text{ kcal mol}^{-1}$. This remarkable weak BDE also explains why the microscopic reverse reaction from **22** towards **20** does not take place, since most of the standard hydrogen atom donors possess stronger bonds than **20**.

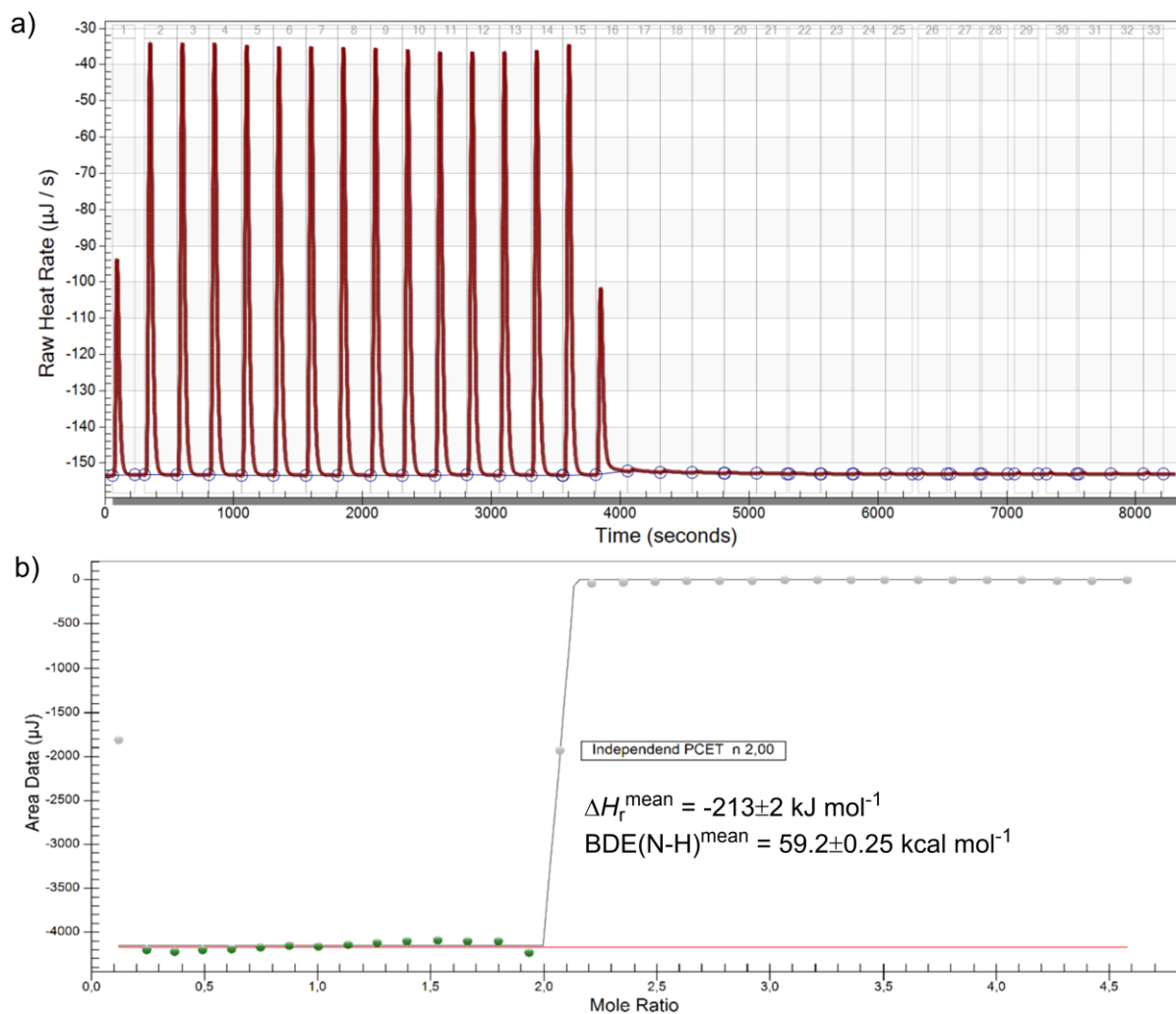
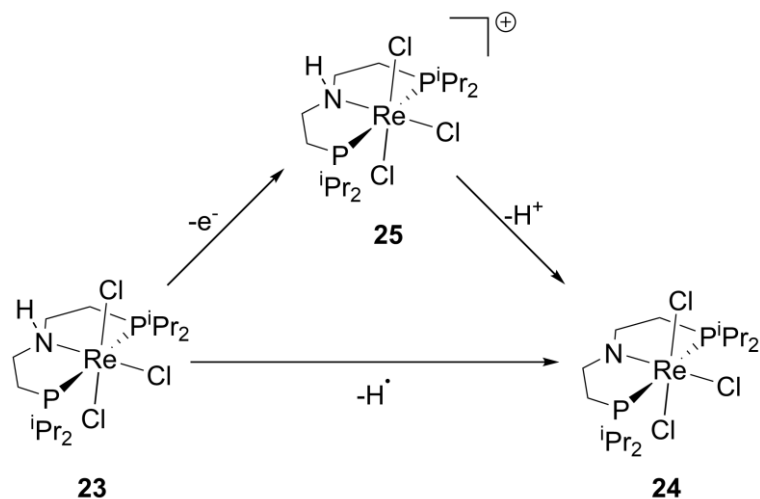


Figure 29: a) Representative thermogram of the titration of **20** with **22** with Mes*O in THF at 298 K. b) Integrated heat curve of the titration of **20** with **22** with Mes*O in THF at 298 K and results of the titrations.

Chapter IV

IV. On the Effect of Spin-Orbit Coupling in Solution Thermochemistry

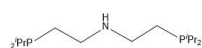
For parts of the results of this Chapter a manuscript is in progress: D. Delony, F. Wätjen, M. Diefenbach, S. Demeshko, M. Orlita, M. C. Holthausen, S. Schneider "Evaluating the Effect of Spin-Orbit Coupling on the Thermochemistry of Proton Coupled Electron Transfer" The synthesis and characterisation of the rhenium(III) amine complex **23** and the rhenium(IV) amide complex **24** was described by Dr. F. Wätjen born Schendzielorz in F. Schendzielorz, M. Finger, J. Abbeneth, C Würtele, V. Krewald, S. Schneider, *Angew. Chem. Int. Ed.* **2019** 58, 830. This Section will resume these results and extend the characterisation by further magnetic and spectroscopic data. The vital problem of the small SOC effect (see Chapter II Section 3.2) of the terminal iridium hydroxo/oxo couple **2** and **4** was the nearly unchanged metal centred spin at the "spin-orbit coupling centre" iridium (see page 43), thus both complexes **2** and **4** were highly stabilised by SOC which led to the near cancellation of the differential SOC effect ($\Delta\Delta\text{SOC}$). Thus, for a high $\Delta\Delta\text{SOC}$, a significant spin change at the metal centre upon reaction must take place. In a recent work from our group on benzonitrile formation from N_2 the rhenium(III) amine complex **23**⁵⁶ exhibited an extraordinary shift of the ^{31}P -NMR signal to $\delta = -1536$ ppm, which was assigned to high temperature independent paramagnetism (TIP) as a result of strong SOC.^[158] Additionally, the corresponding rhenium(IV) amide complex **23** was well accessible by HAT from **23**, rendering this reaction a promising candidate to investigate the influence of SOC on the PCET reaction (Scheme 8).



Scheme 9: Square scheme for the PCET reaction of **23** to **24** by direct HAT (bottom) or via oxidation to **25** and subsequent deprotonation (top).

In the following Chapter the rhenium(III) amine **23**, the rhenium(IV) amide **24** and the cationic rhenium(IV) amine **25** will be characterized by spectroscopic and magnetic means and their properties will be rationalized by *ab initio* computations. The SOC effect on the PCET thermochemistry will then be analysed as the difference of the *ab initio* computed reaction (free) enthalpy (with and without SOC) to the experimentally determined value.

⁵⁶ Please note: The pincer ligands referred to in this chapter differ from the ligand in chapter II. Here $[\text{P}^{\text{H}}\text{NP}]$ stands for Bis(di-isopropylphosphinoethyl)amine:



1. Characterisation of the Rhenium(III/IV) Amine Complexes **23**, **25** and of Rhenium(IV) Amide **24**

This Section will be about the characterisation of the three rhenium complexes **23**, **24** and **25**. To present a full picture, also the experimental data obtained by Dr. Florian Wätjen born Schendzielorz published in the publication mentioned above are presented.^[158]

1.1 Characterisation of Rhenium(III) Amine Complex **23**

The rhenium(III) amine complex **23** is coordinated meridionally by the pincer ligand with near C_s symmetry as confirmed by XRD analysis (Figure 31a).^[158] **23** possesses, due to the rapid electronic relaxation of Re^{III} ,^[210] sharp but extraordinary paramagnetically shifted NMR signals ($\delta(^1H) = 156$ ppm to -11 ppm; $\delta(^{31}P) = -1526$ ppm), which were assigned to strong temperature independent paramagnetism (TIP) as a result of strong spin-orbit coupling on the ground state of **23**. This is a typical phenomenon for heavy d^4 metal ions like rhenium(III) or osmium(IV).^[158,211] For a closer insight into the nature of the paramagnetic behaviour of **23**, variable temperature NMR measurements between 190 K and 310 K were performed (Figure 30). The N-H proton experiences the strongest, temperature dependent shift of 10 ppm over the whole temperature range (Figure 30, top left), while the other signals only experience very minor (<2 ppm) or no shifts (Figure 30, top right, bottom). This can be rationalised by solvation effects on the N-H bond. All NMR signals exhibit a linear $\delta \propto T$ (non-Curie type) behaviour, which supports TIP arising from admixture of thermally not populated excited state as the origin of the NMR shifts.^[212–216] Further insight into the magnetic nature of **23** was obtained by SQUID magnetometry (Figure 31, b). The magnetic moment in the solid state at room temperature of **23** $\mu_{eff} = 1.60 \mu_B$ is in the typical range for an open-shell, octahedrally coordinated rhenium(III) complex but significantly lower than the expected spin-only value for a triplet ground state ($\mu_{eff} = 2.83 \mu_B$).^[211,215,217] The linear non-Curie magnetism of **23** from the VT-NMR is as well reflected by the SQUID data, where in a temperature range from 2 to 300 K a complete linear curve of $\chi_M T$ vs. T could be observed. This is in contrast to the magnetic data of oxo complex **4** (c.f. Figure 30, b black dots, Figure 9), which showed a bend SQUID curve at higher temperatures.⁵⁷ The magnetic data can be fitted with two different models, which are both based on a spin-Hamiltonian picture (Figure 31, b red line). 1) A singlet ground state with strong mixing to open-shell excited states, which results in an extremely high TIP value of $1063.4 \cdot 10^{-6} \text{ cm}^3 \text{ mol}^{-1}$ or 2) A triplet ground state with a very high zero-field splitting parameter of $D \geq 1302 \text{ cm}^{-1}$, which is twice the zero-field splitting of terminal oxo **4** (650 cm^{-1}) (Figure 31, b). Both models are only approximations for the electronic structure of **23**, since the spin-Hamiltonian is losing its physical meaning, when large SOC contributions lead to the splitting into spin-orbit states. The spectroscopic and magnetic data of **23** therefore support the picture of a non-magnetic ($J = 0$) ground state, thermally well separated ($\gg k_B T$) by SOC from the excited states.^[218]

⁵⁷ SQUID measurement and fitting by Dr. Serhiy Demeshko sample preparation by Dr. Florian Wätjen.

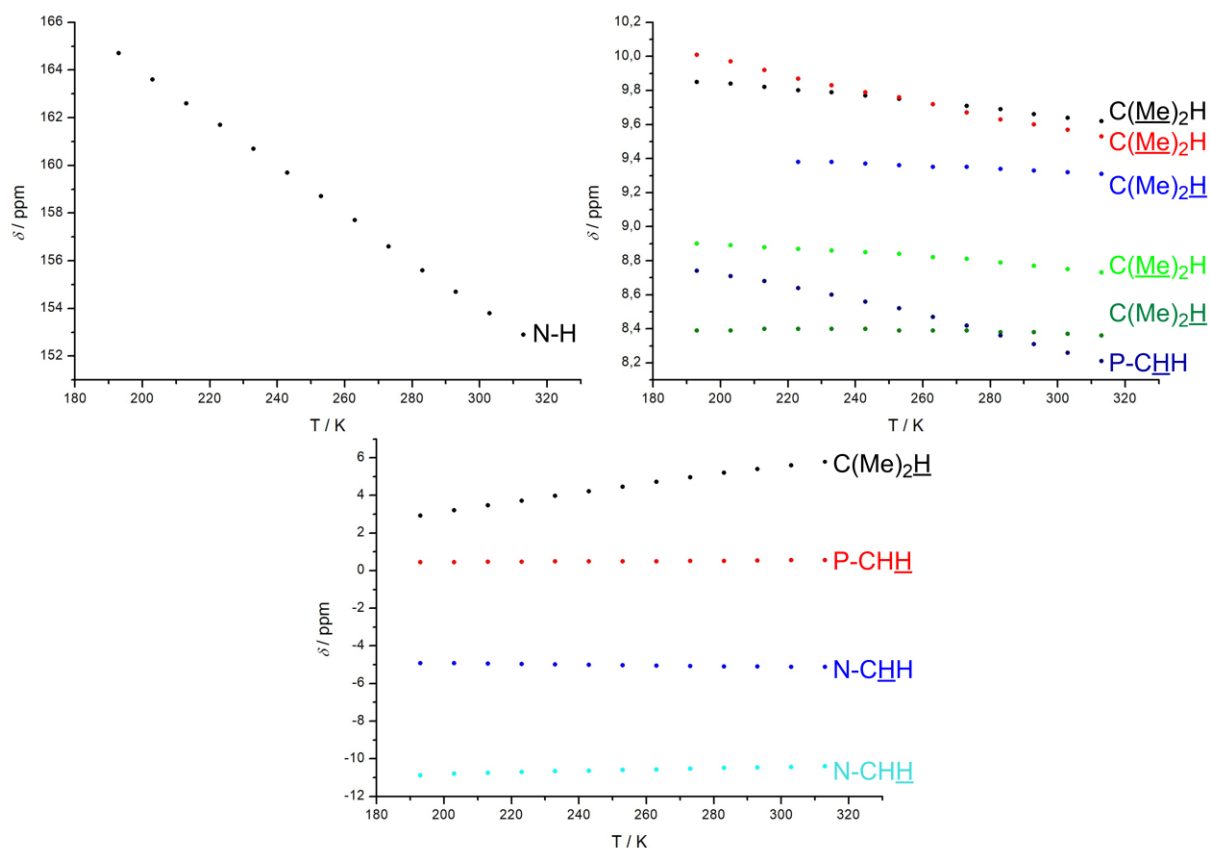


Figure 30: ^1H -VT-NMR plots recorded from 193 K to 313 K in THF of **23**. For each data point an independent lock and shim were performed after at least 10 min equilibration time at the given temperature.

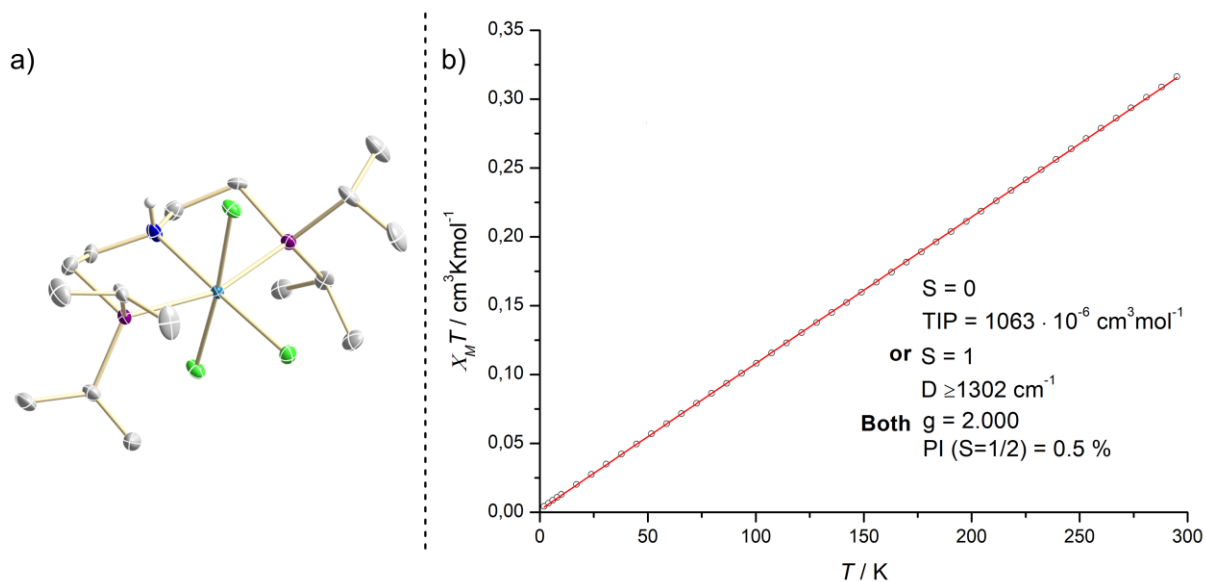


Figure 31: a) Solid state structure of **23** obtained by single crystal X-ray diffraction. All C-H protons neglected for clarity. Selected parameters: Re-N: 2.158(6) Å, Re-Cl_{ax,1}: 2.3728(17) Å, Re-Cl_{ax,2}: 2.3791(18) Å, Re-Cl_{eq}: 2.4117(18) Å, Re-P₁: 2.4463(18) Å, Re-P₂: 2.4408(17) Å, N-H: 0.85(7) Å, N-Re-Cl_{ax,1}: 89.58(18)°, N-Re-Cl_{ax,2}: 85.19(18)°, Cl_{ax}-Re-Cl_{ax}: 174.73(7)°, N-Re-Cl_{eq}: 177.47(18)°, N-Re-P₁: 81.22(16)°, N-Re-P₂: 80.50(16)°. b) $X_M T$ vs. T plot from SQUID-magnetometry measurement of solid **15** from 2 K to 300 K (dots measured data, red line Spin-Hamiltonian fit) for a detailed description of the fitting procedure see Section 1.2.10 in Chapter VI.

The mid-IR spectrum of **23** exhibits three signals beyond the fingerprint region. Besides the C-H vibrations at around 2900 cm^{-1} , one weak but sharp band at 3183 cm^{-1} and one intense, broad transition at 3510 cm^{-1} are found. Here, the weak band at 3183 cm^{-1} can be assigned to the N-H stretch by a deuteration experiment ($\nu_{\text{N-D}} = 2363\text{ cm}^{-1}$) (Figure 32a).⁵⁸ In previous publications, broad transitions in the mid-IR spectral range of rhenium phosphine complexes were tentatively assigned to arise from ligand field transitions, but their electronic nature was never proven spectroscopically.^[219,220] In contrast to a vibrational transition, electronic transitions to $|M_J| > 0$ states should change in an applied magnetic fields. A magnetic field dependent IR measurement of the band at 3510 cm^{-1} would therefore enable the definite assignment to an electronic transition. In collaboration with *Dr. Milan Orlita*⁵⁹ mid-IR spectra at differing magnetic fields from 0-11 T were recorded. The normalized transmission T_B/T_0 shows a rising signal intensity at increasing magnetic field only for the transition at 3510 cm^{-1} , which confirms unequivocally an electronic transition in the mid-IR range (Figure 51c). The further analysis of the rhenium(III) amine complex **23** therefore supports the description of a complex with high SOC stabilisation of the ground state and encourages the further investigation on the SOC effect on the PCET reaction (Scheme 9).

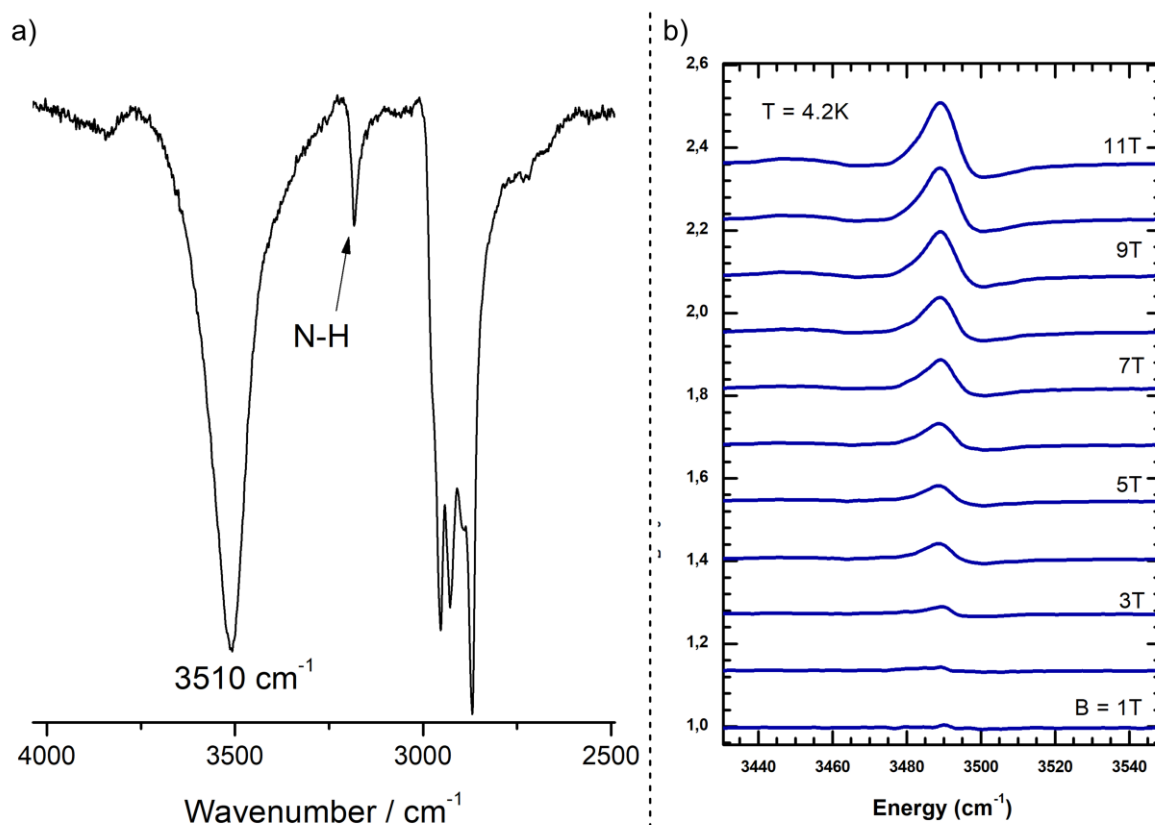


Figure 32: a) Section of the mid-IR(ATR) region above the fingerprint region of **23**. b) Magnetic field dependent IR(KBr) data of **23** showing the transmission spectrum with applied field (T_B) divided by the zero-field spectrum (T_0).

⁵⁸ Spectroscopy and deuteration experiment (see Section 2.16 of Chapter VI) performed by Dr. Florian Wätjen.

⁵⁹ Laboratoire National des Champs Magnetiques Intenses.

1.2 Characterisation of the Rhenium(IV) Amide Complex **24**

Next, the product of the PCET reaction, the rhenium(IV) amide **24**, is further analysed. By addition of 1 eq. Mes*O to **23** in THF **24** can be selectively synthesized. **24** also adopts a meridional coordination with the pincer ligand as confirmed by XRD analysis (Figure 33b).^[158] While the solid state structure is slightly deviating from any symmetry, **24** adopts C_{2v} symmetry in solution, as shown by the two signals for the methyl groups in the NMR spectrum (Figure 33a).⁶⁰

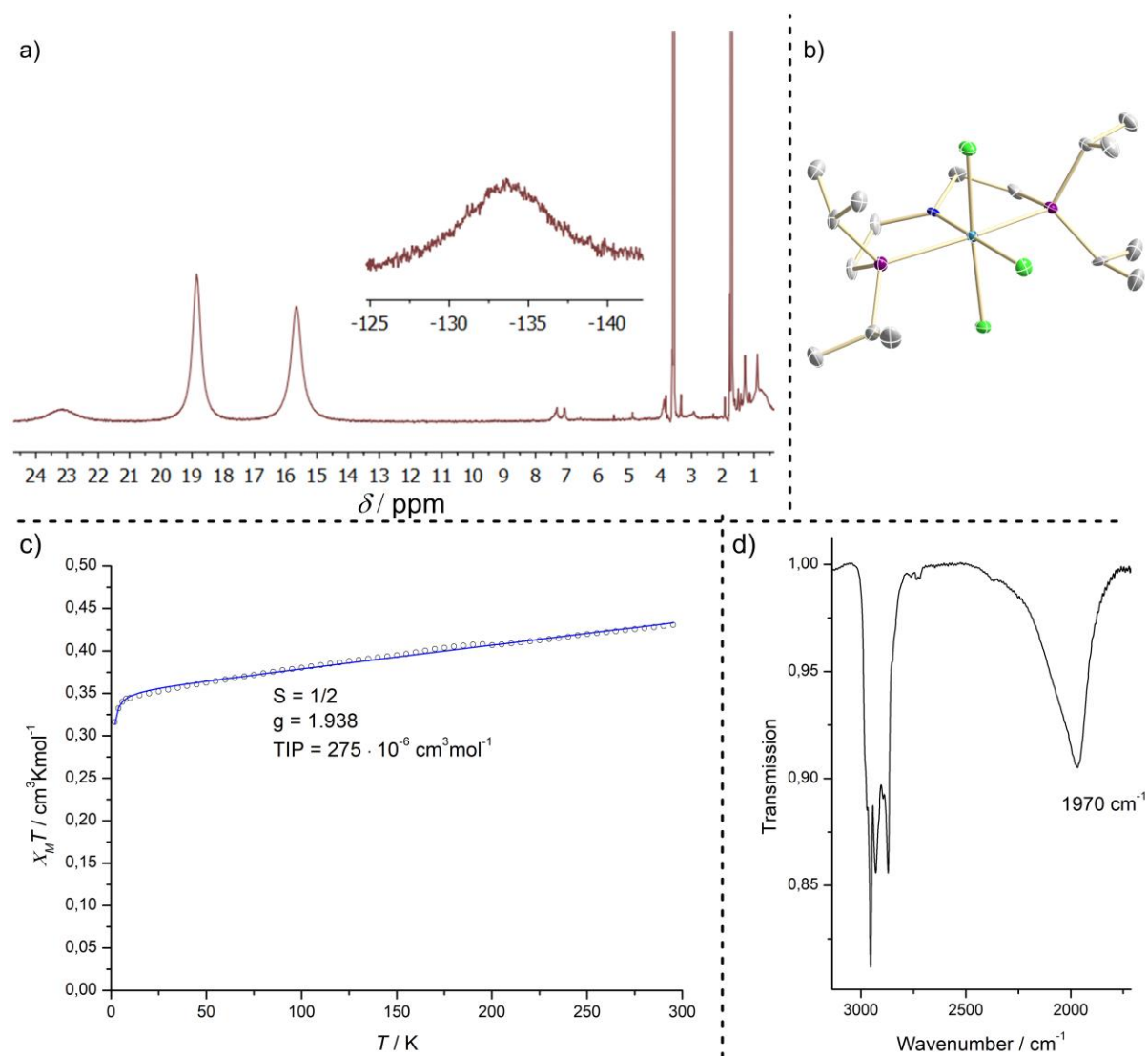


Figure 33: a) $^1\text{H-NMR}$ (para) of **24** in THF-d_8 at r.t. b) Structure of **24** in the solid state obtained by single crystal X-ray diffraction. Selected bond parameters: Re-N: 1.902(7) Å, Re-Clax,1: 2.379(2) Å, Re-Clax,2: 2.369(2) Å, Re-Cleq: 2.429(2) Å, Re-P1: 2.438(2) Å, Re-P2: 2.442(2) Å, N-Re-Clax,1: 93.3(2)°, N-Re-Clax,2: 92.6(2)°, Clax-Re-Clax: 174.01(8)°, N-Re-Cleq: 178.7(2)°, N-Re-P1: 81.9(2)°, N-Re-P2: 82.4(2)°. c) $\chi_M T$ vs. T plot from SQUID-magnetometry measurement of solid **24** from 2 K to 300 K (dots measured data, red line Spin-Hamiltonian fit) for a detailed description of the fitting procedure see Section 1.2.10 in Chapter VI. d) Section of the mid-IR(ATR) region above the fingerprint region of **24**.

⁶⁰ Improved synthesis using one equivalent of Mes*O in THF. The Re(III) imide impurities at around 10 ppm reported in the publication are gone. Additionally, the “lost” signal is found at -134 ppm.

In comparison to **23** the signals are still paramagnetically shifted but broader, reflecting the formally $1e^-$ oxidized metal centre resulting in an odd electron count. The magnetic properties of **23** were analysed by SQUID magnetometry (Figure 33c).⁶¹ The obtained data (black dots) can be fitted within a spin-Hamiltonian picture (blue line) to a doublet ground state. The magnetic moment in the solid state at room temperature of **24** ($\mu_{\text{eff}} = 1.86 \mu_{\text{B}}$), is higher than the expected spin-only value for a doublet ground state ($\mu_{\text{eff}} = 1.73 \mu_{\text{B}}$), which speaks for a SOC induced admixture of excited quartet states to the ground state. This is described by the pronounced TIP value of $275 \cdot 10^{-6} \text{ cm}^3 \text{ mol}^{-1}$. The low-spin ground state of **24** can be rationalized to strong p-donation of the amide ligand, which rises one of the two MOs with *b* character in energy. The mid-IR spectrum of **24** features a broad band at 1968 cm^{-1} comparable to the electronic band of **23** (Figure 33d). The presented data support **24** to exhibit a doublet ground state with significant, but lower, SOC stabilisation than **23** (cf. $\text{TIP}(\mathbf{23}) = 1063.4 \cdot 10^{-6}$, $\text{TIP}(\mathbf{24}) = 275 \cdot 10^{-6} \text{ cm}^3 \text{ mol}^{-1}$), which anticipates a high differential SOC effect on the PCET reaction.

1.3 Characterisation of Cationic rhenium(IV) Amine Complex **25**

For the measurement of the PCET free reaction enthalpy by a square-scheme formalism (see Scheme 9), the cationic rhenium(IV) amine species **25** must be synthesised and characterised. Oxidation of **23** with ferrocenium tetrakis[3,5-bis(trifluoromethyl)phenyl]borate (BARF_{24}) in dichloromethane leads to a direct colour change to deep red (Figure 34, a). Crystallisation from benzene yields material suitable for single crystal XRD analysis and confirms the successful synthesis of the cationic rhenium(IV) amine complex $[(\text{P}^{\text{H}}\text{NP})\text{Re}(\text{Cl})_3][\text{BARF}_{24}]$ **25** (Figure 34b). The nitrogen atom is in distorted tetrahedral coordination (angle sum around nitrogen 339°) which supports an amine species and the ligand backbone as well as directly coordinated ligands are close to C_s symmetry in the solid-state structure, while the isopropyl groups do not show any symmetry in the solid state. The Re-Cl bonds are drastically shortened by up to 0.13 \AA compared to **23**, which can be rationalized by less π -backbonding to the chlorine ligands, while all angles to the ligands do not significantly differ.

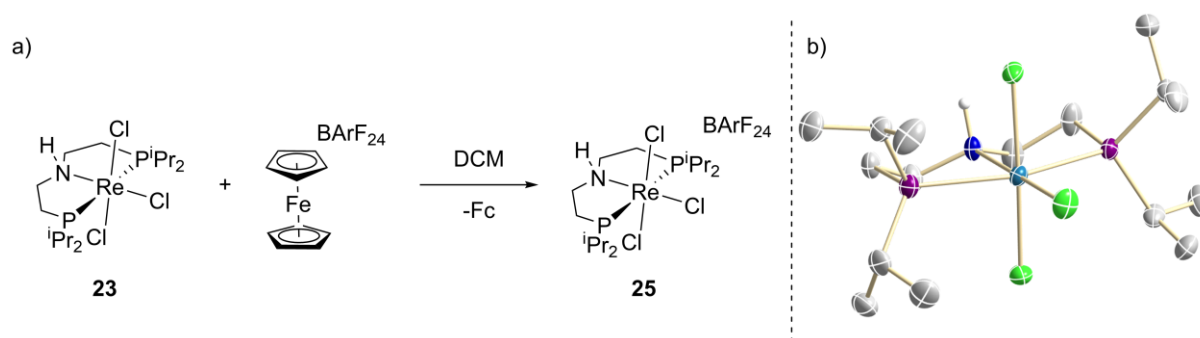


Figure 34: a) Reaction scheme for the synthesis of **25** by oxidation of **23** with ferrocenium BARF_{24} in DCM at ambient temperature. b) Structure of **25** in the solid state obtained by single crystal X-ray diffraction. Cocrystallized benzene and the counter ion BARF_{24} are omitted for clarity. Selected bond parameters: Re-N: $2.204(4) \text{ \AA}$, Re-Cl_{ax,1}: $2.3193(12) \text{ \AA}$, Re-Cl_{ax,2}: $2.3277(12) \text{ \AA}$, Re-Cl_{eq}: $2.2850(12) \text{ \AA}$, Re-P₁: $2.4912(13) \text{ \AA}$, Re-P₂: $2.4927(13) \text{ \AA}$, N-Re-Cl_{ax,1}: $87.07(11)^\circ$, N-Re-Cl_{ax,2}: $86.45(11)^\circ$, Cl_{ax}-Re-Cl_{ax}: $173.42(5)^\circ$, N-Re-Cl_{eq}: $179.50(11)^\circ$, N-Re-P₁: $80.07(10)^\circ$, N-Re-P₂: $79.09(10)^\circ$.

⁶¹ SQUID measurement and fitting by Dr. Serhiy Demeshko sample preparation by Dr. Florian Wätjen.

The signals in the $^1\text{H-NMR}$ spectrum are broadened compared to **23**, but significantly sharper than for **24** and give a C_s symmetric signal set (Figure 35c). The signals for the methyl groups can be found around 30 ppm, while the backbone- and tertiary C-H protons are shifted over a wide range from 15 ppm to -105 ppm. The N-H proton signal overlaps with the two isopropyl group signals at 30.5 ppm as indicated by the integral of 13. The effective magnetic moment of **25** was determined by the Evans method in THF-d_8 to $\mu_{\text{eff}} = 2.9 \mu_{\text{B}}$ and is therefore significantly over the expected spin-only value for a doublet ground state ($\mu_{\text{eff}} = 1.73 \mu_{\text{B}}$). Since, its electron count must be odd, the best rationalisation is a quartet ground state for **25**. In the infrared spectrum of **25** a weak signal at 3095 cm^{-1} is found, which can be tentatively assigned to the N-H vibration but in contrast to the complexes **23** and **24** no broad electronic transition over the whole range from $500\text{-}6500 \text{ cm}^{-1}$ was found for **25**. The N-H vibration is 88 cm^{-1} lower in energy compared to neutral **23**, which supports a higher degree of activation of the N-H bond for **25** (Figure 35d). With the electronic, spectroscopic and magnetic data of the complexes **23-25** at hand, the next step is their rationalisation by *ab initio* computations.

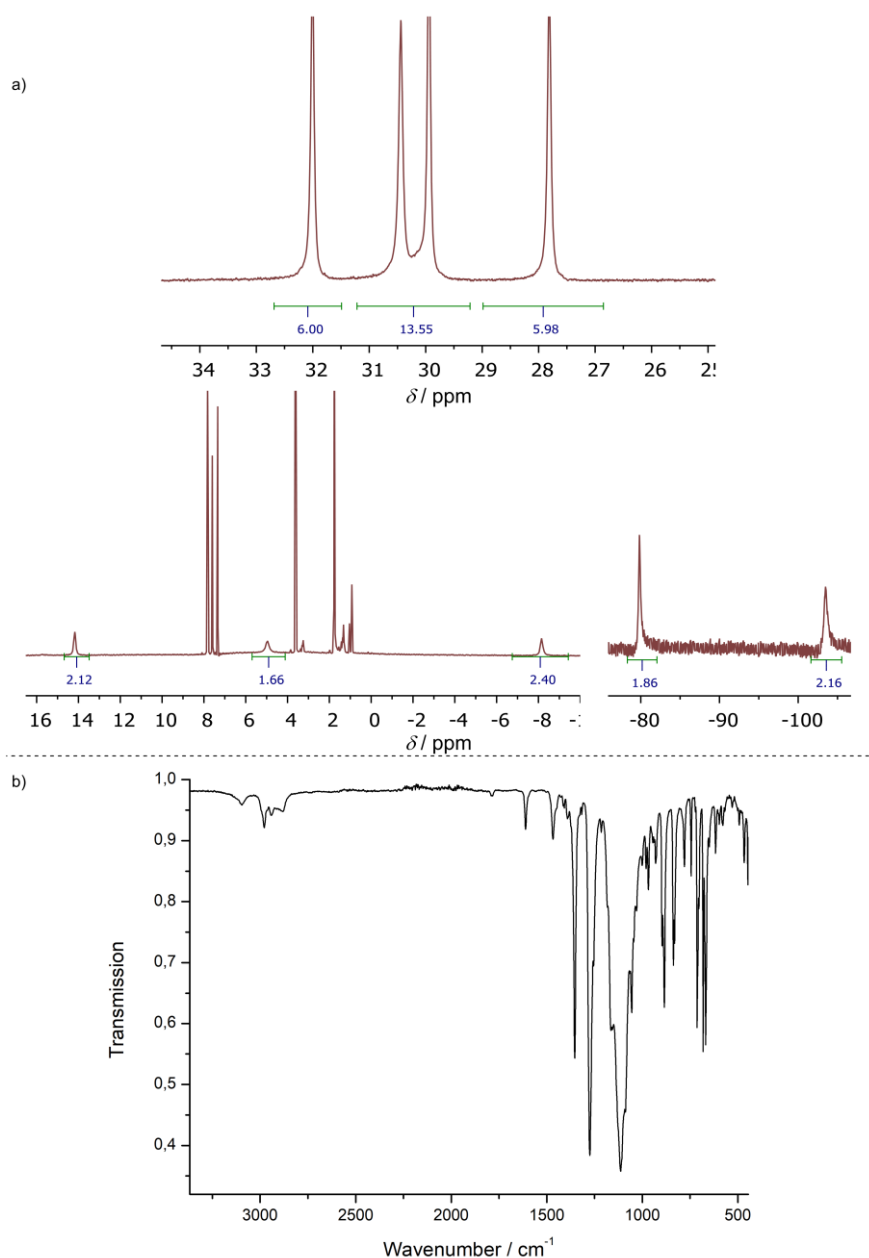


Figure 35: a) $^1\text{H-NMR}$ (para) spectrum of **25** in THF-d_8 at ambient temperature. c) IR (ATR) spectrum of **25**.

2. Computational Rationalisation of the Spectroscopic and Magnetic Features

Features

For the rationalisation of the spectroscopic and magnetic features of the complexes **23-25**, reported in Section 1, state averaged CASSCF calculations were performed. The computations are corrected by the NEVPT2 ansatz to include dynamic correlation effects and are further refined by spin-orbit coupling contributions by quasi-degenerate perturbation theory (QDPT).⁶²

2.1. Computational Rationalisation of Rhenium(III) Amine Complex **23**

DFT analysis of **23** on the PBE0-D3/def2TZVP level of theory places the triplet state below the singlet by $\Delta E_{T/S} = 38.7 \text{ kJ}\cdot\text{mol}^{-1}$ and therefore confirms the electronic ground state picture which evolved from the spectroscopic and magnetic characterisation (Figure 36a). The calculated structure for the triplet ground state converged in C_s symmetry and is in good agreement with the found structure by XRD analysis, while the singlet structure gives higher deviations, especially for the equatorial chlorine bond length. The Mulliken and NBO/NPA spin densities support mainly metal centred radical character (Mulliken: 1.85; NBO/NPA:⁶³ 1.61) and give reason to expect a high SOC contribution if excited states are accessible. (Figure 36b)

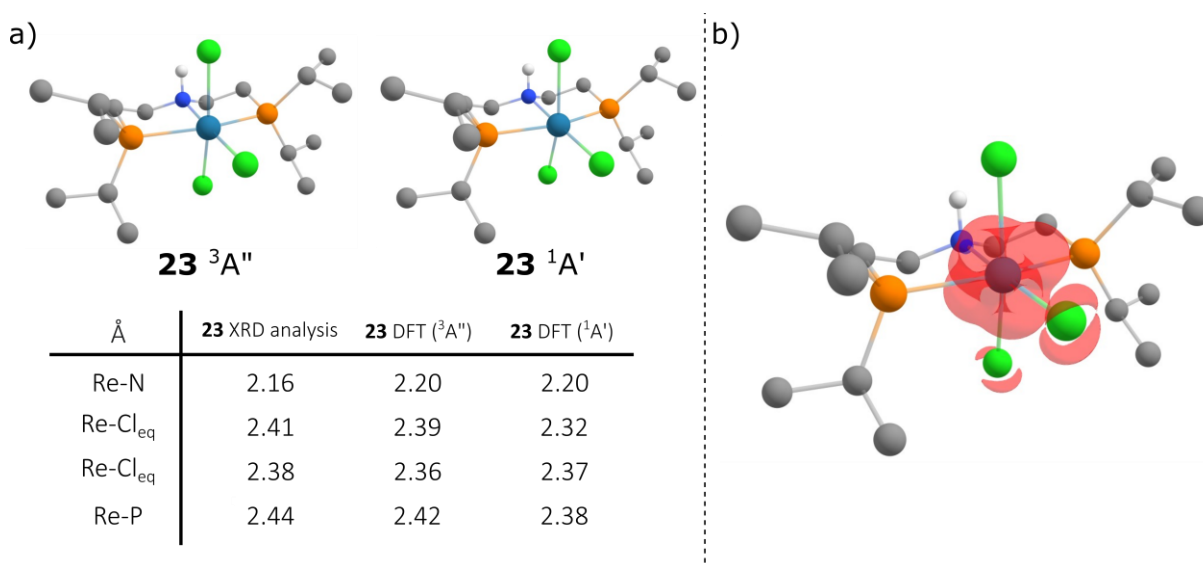


Figure 36: a) C_s symmetric computed structures for **23** (Triplet ³A'' and Singlet ¹A') on the PBE0-D3/def2TZVP level of theory and comparison of selected bond length to the experimental found structure by XRD analysis. b) DFT spin-density plot at isovalue 0.0075 a_0^{-3} for the ³A'' ground state of **23** showing a mainly metal centred spin-density.

For the CASSCF computations two different active spaces were probed. A small CAS space, only including the 5d orbitals of the rhenium metal centre (4x5) (Figure 37, left) and a bigger CAS space, additionally including the rhenium bonding interactions with the ligand environment resulting in a (14,10) CAS extension (Figure 37, right).

⁶² For a detailed discussion of the performed computations in this Section see Section 4.3.1 in chapter VI.

⁶³ NBO/NPA: Natural Bond Orbital/Natural Population Analysis

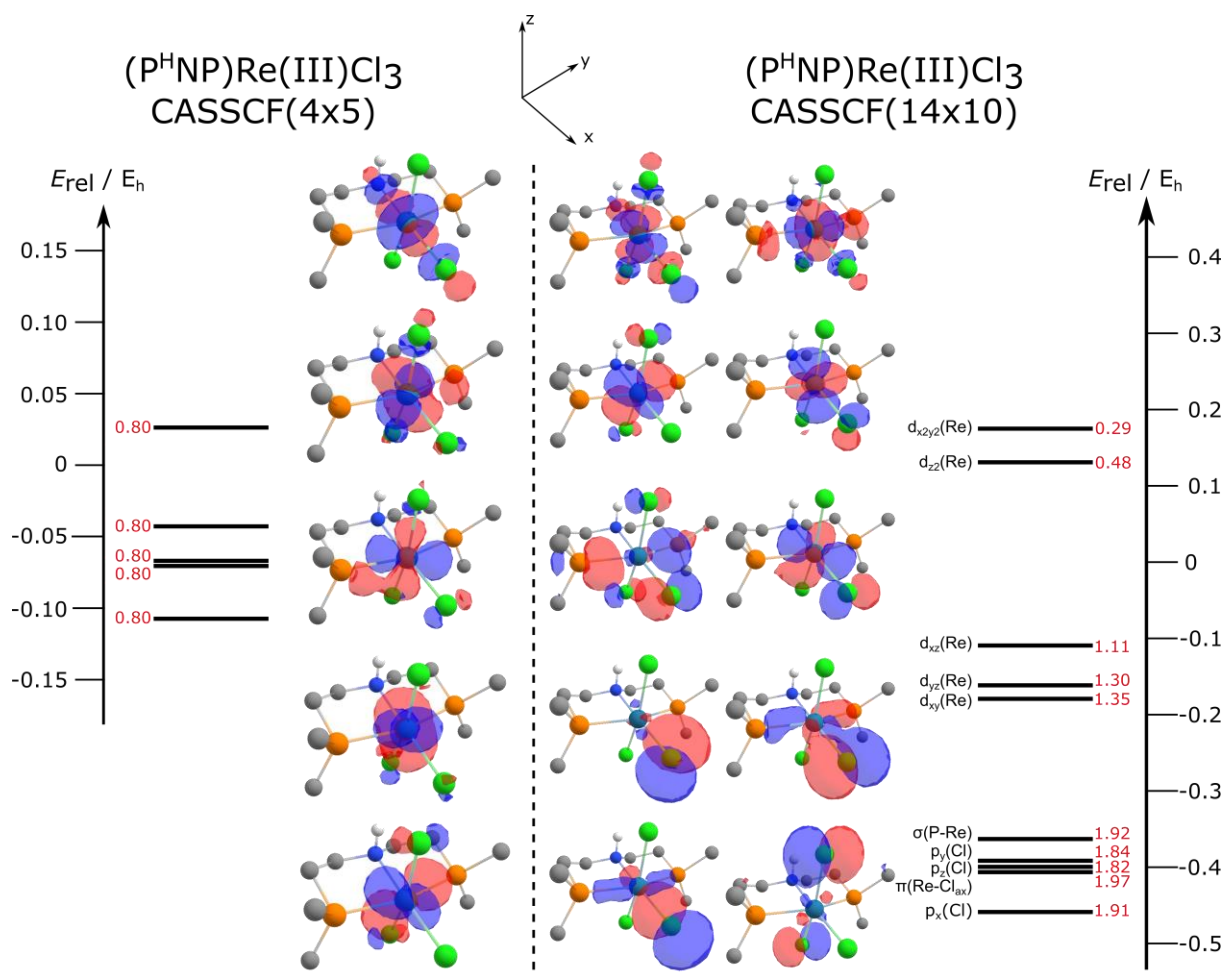


Figure 37: CASSCF orbitals of **23** for the small (4,5) CAS space with only d orbitals encountered (left) and CASSCF orbitals for the large (14,10) CAS space with the d-orbitals and the ligand bonding interactions encountered (right) orbital order shown from bottom left to top right.

The CASSCF/NEVPT2 wavefunctions place the triplet electromer over the singlet by 58.6 kJ mol^{-1} and 39.6 kJ mol^{-1} for the small and big CAS space, respectively and thus reproduce the electronic ground state picture obtained by DFT (Figure 38). The ground state of **23** in the big CAS space on the NEVPT2 level is dominated by the $[(d_{xy}^2)(d_{yz}^1)(d_{xz}^1), (68\%)]$ configuration and the first excited state $[(d_{xy}^1)(d_{yz}^2)(d_{xz}^1), (68\%)]$ is only 5 cm^{-1} higher in energy, which results in an effective twofold degenerate (3E) ground state. These two states are separate by over 1000 cm^{-1} in the small CAS space. Treatment of spin-orbit coupling by means of QDPT leads to extensive mixing of the triplet states of **23**, which results in a high SOC stabilisation of -44.9 and $-46.4 \text{ kJ mol}^{-1}$ for the small and big CAS space, respectively. Delightfully, for both CAS spaces bright transitions from the ground state to the 4th/5th excited state are predicted. While the small CAS space places these transitions at 4400 cm^{-1} , the big CAS space predicts them at 3900 cm^{-1} .

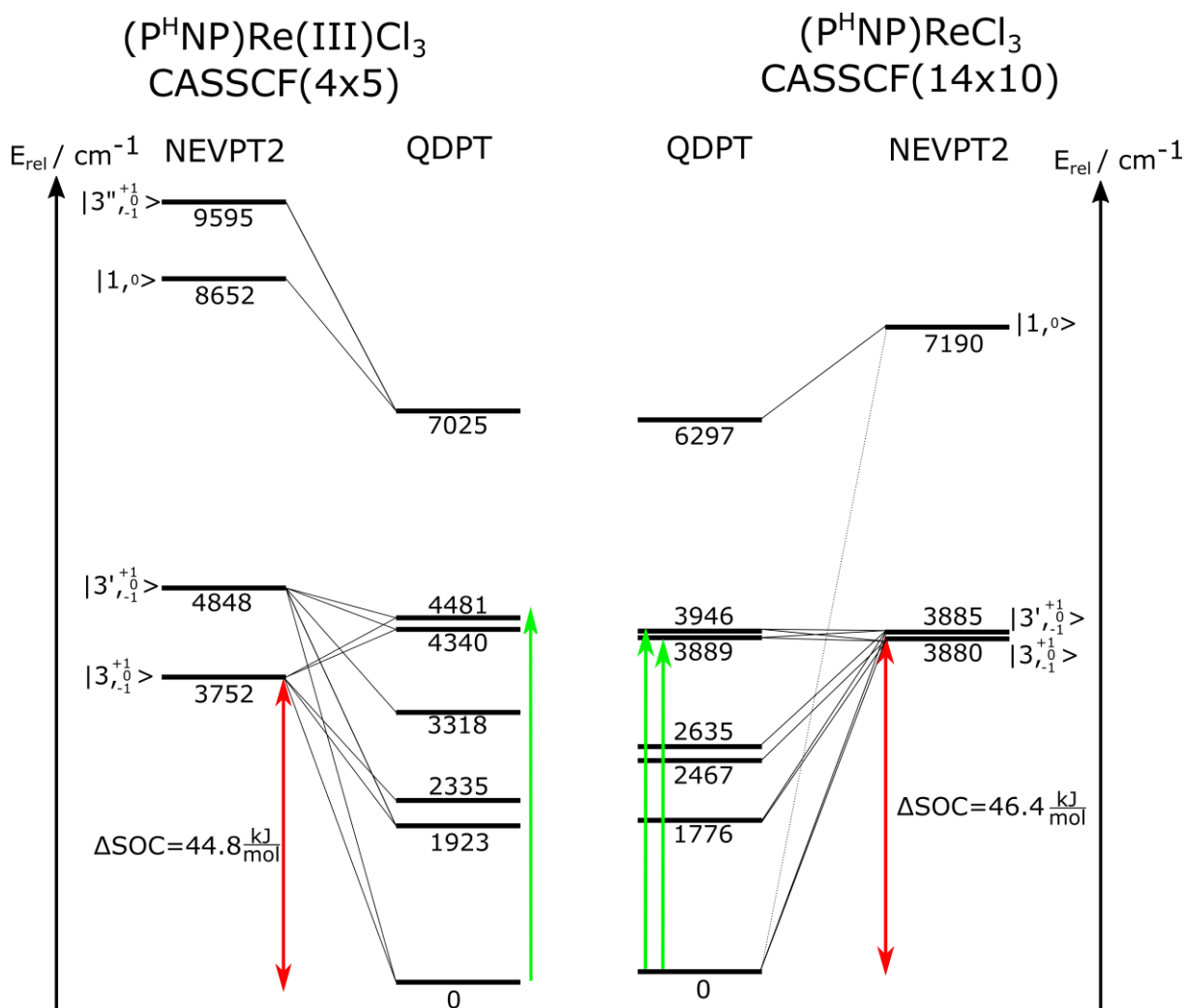


Figure 38: State correlation diagrams for the small (4,5) and big (14,10) complete active spaces from NEVPT2 calculations with (QDPT) and without (NEVPT2) spin-orbit coupling for **23**.

A comparison between the predicted values to the observed transition in the midIR spectrum of **23** at 3500 cm^{-1} (Figure 32) gives a significantly higher agreement of the experiment with the big CAS space than with the small CAS space. For this reason, the big (14,10) CAS space is analysed in more detail. The lowest eigenstate of **23** on the QDPT level is equally composed of the two “degenerate” triplet states and also the first singlet is mixed in with a minor amount ($|3\rangle$ ($m_s = \pm 1$) (40 %); $|3'\rangle$ ($m_s = \pm 1$) (40%); $|1\rangle$ (6%)). The computed temperature dependent magnetisation of **23** (Figure 39, a yellow) is in line with the experimentally found data by SQUID magnetometry and only underestimates to a minor degree the experimentally found values (Figure 39, b). To benchmark the CASSCF wavefunction further, also the UV-Vis and NIR spectra were recorded. **23** shows one intense charge transfer transition at 409 nm (24400 cm^{-1}) and two weak d-d transitions at 523 nm (19100 cm^{-1}) and 800 nm (12500 cm^{-1}) respectively, while in the NIR region three small transitions at 1000 nm (10000 cm^{-1}), 1500 nm (6700 cm^{-1}) and 1750 nm (5700 cm^{-1}) are observed (Figure 39c black and red).⁶⁴

The computed spectrum on the CASSCF-NEVPT2/QDPT level of theory (Figure 39c magenta) reproduces the experimental spectrum, even though some differences can be observed. The intense charge transfer transition at

⁶⁴ The spectra are shown with a linear energy scale (in cm^{-1}) for a better comparability to the computed spectra.

409 nm in the experimental spectrum is computed to 358 nm on the *ab initio* level of theory. This quite high deviation from the experiment can be explained by solvent interactions with the N-H proton, since charge transfer bands are commonly observed to be highly solvent dependent.^[221] TD-DFT computations were performed to test this hypothesis (Figure 39, b). Without solvent correction by SMD, a transition at 404 nm is predicted (Figure 39b black), while the band shifts upon treatment with SMD(DCM) to 424 nm (Figure 39b red), which confirms the charge transfer character. The transitions in the NIR spectrum of **23** are all well represented, even though blue shifted. Here again, solvation effects as well as vibrational coupling in the NIR region are possible explanations for the deviations from the experimental spectra. Both effects are neglected within the CASSCF computations. All together, the *ab initio* model satisfactorily reproduces the experimental found spectroscopic and magnetic features of **23**.

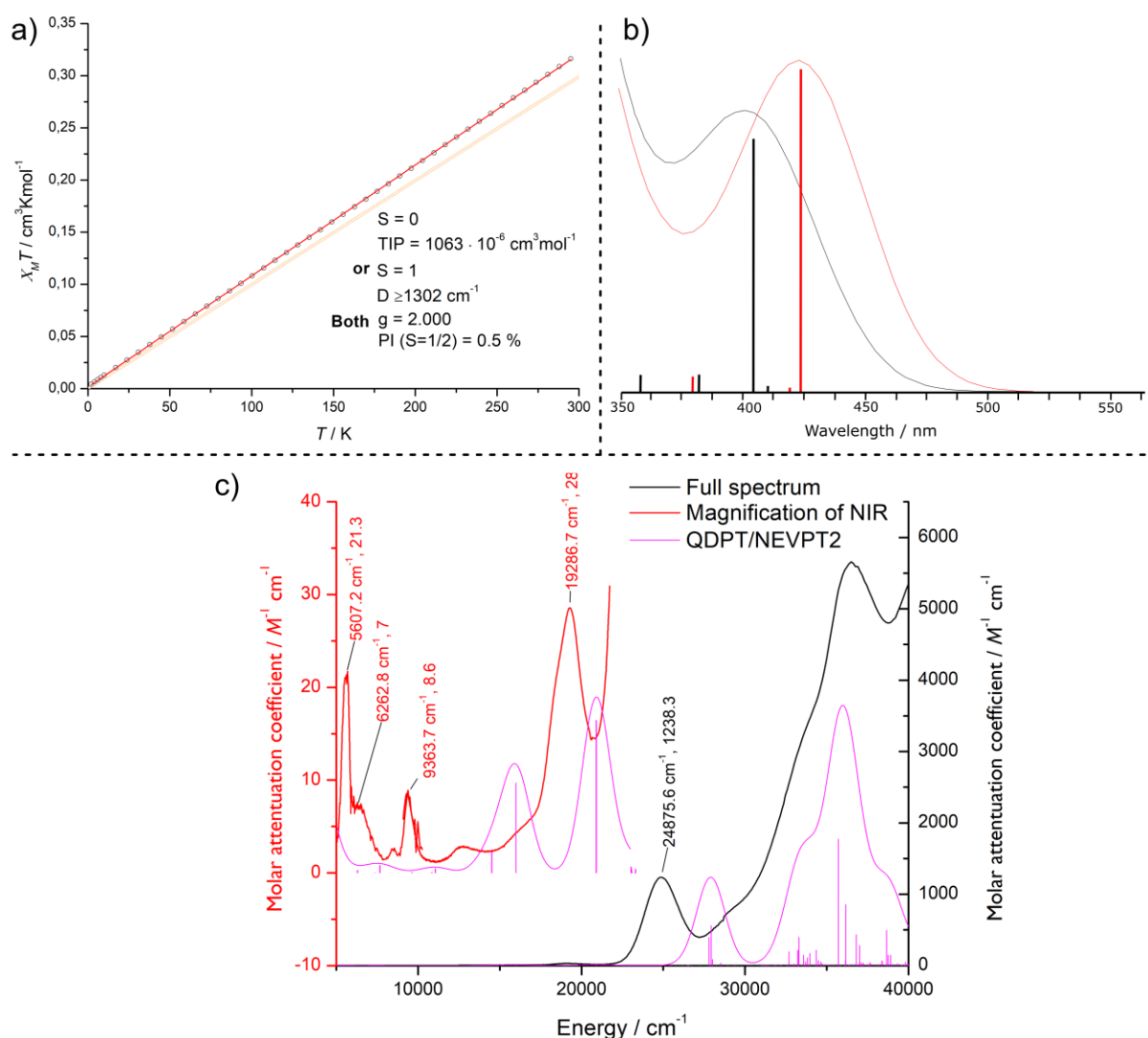


Figure 39: a) Comparison of the computed magnetisation for **23** on the (14,10) CASSCF/NEVPT2-QDPT level of theory (orange) vs. the found magnetisation by SQUID magnetometry (black+red fit). b) Comparison of the TD-DFT(50 states) data of **23** with and without solvent correction by SMD for dichloromethane. c) Computed UV/Vis and NIR spectra of **23** on the (14,10) CASSCF/NEVPT2-QDPT level of theory (pink) compared to the experimental spectra (black and red).

2.2. Computational Rationalisation of Rhenium(IV) Amide Complex **24**

Next, the electronic structure of the rhenium(IV) amide was analysed. DFT analysis on the PBE0-D3/def2TZVP level of theory confirms the doublet ground state ($\Delta E_{D/Q} = 15.3 \text{ kJ}\cdot\text{mol}^{-1}$) of **24**, which reproduces the electronic ground state picture from the spectroscopic and magnetic characterisation (Figure 40a). The calculated structure for the doublet ground state converged in C_s symmetry and is in very good agreement to the found structure by XRD analysis, while the quartet structure exhibits higher deviations especially for the Re-N bond length. The Mulliken and NBO/NPA analysis yield again mainly metal centred spin densities (Mulliken: 0.96; NBO/NPA: 0.84) and give reason to expect a high, but smaller SOC contribution than for **23** (Figure 40, b).

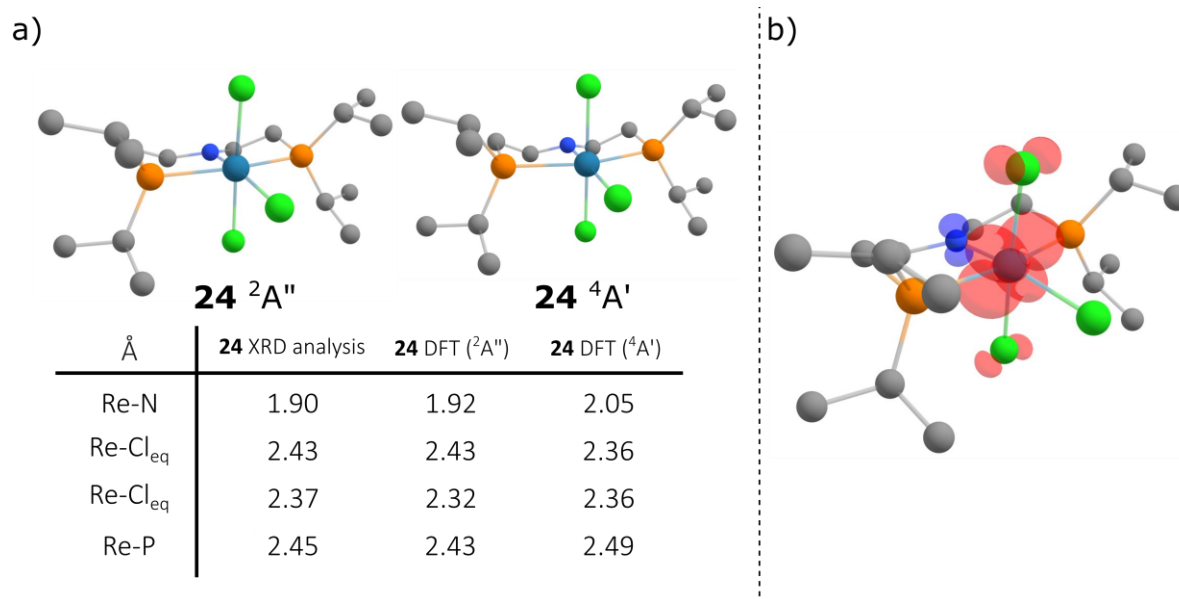


Figure 40: a) C_s symmetric computed structures for **24** (Doublet $^2A''$ and Quartet $^4A'$) on the PBE0-D3/def2TZVP level of theory and comparison of selected bond length to the experimental found structure by XRD analysis. b) DFT spin-density plot at isovalue 0.0075 a_0^{-3} for the $^2A''$ ground state of **24**.

A more detailed analysis of the electronic structure was again reached by CASSCF-NEVPT2 analysis. The same CAS spaces as for **23** were chosen with the difference, that for the big CAS space the additional N-Re π -bond was considered, leading to a (3,5) and (15,11) CAS extension, respectively (Figure 41, left and right). The CASSCF-NEVPT2 wavefunctions place the doublet electromer over the singlet by 60.4 kJ mol^{-1} for the small CAS space and by 43.3 kJ mol^{-1} for the big CAS space and thus reproduce the electronic ground state picture obtained by DFT (Figure 41, bottom). The ground state is dominated by the $(d_{xy}^2)(d_{yz}^1)$ configuration (82 %) and experiences strong mixing with the first excited doublet state ($|2\rangle (m_s \pm 1/2)$ (54%); $|2'\rangle (m_s \pm 1/2)$ (35%)) upon treatment of spin-orbit coupling by means of QDPT, which leads to a stabilisation of $-22.3 \text{ kJ mol}^{-1}$ and $-18.5 \text{ kJ mol}^{-1}$ for the small and big CAS space, respectively (Figure 41, bottom). Delightfully, the SOC stabilisation of **24** is therefore 28 kJ mol^{-1} lower in energy compared to the SOC stabilisation of **23**, thus a high SOC effect on the PCET thermochemistry is expected. Additionally, also a transition from the ground state to the 1st/2nd excited state of **23** with non-negligible oscillator strength is found in both CAS spaces. Again, the bigger (15,11) CAS space performs significantly better with a predicted transition at 2200 cm^{-1} , compared to the found transition at 2000 cm^{-1} , while the small (3,5) CAS places the same transition at 2600 cm^{-1} .

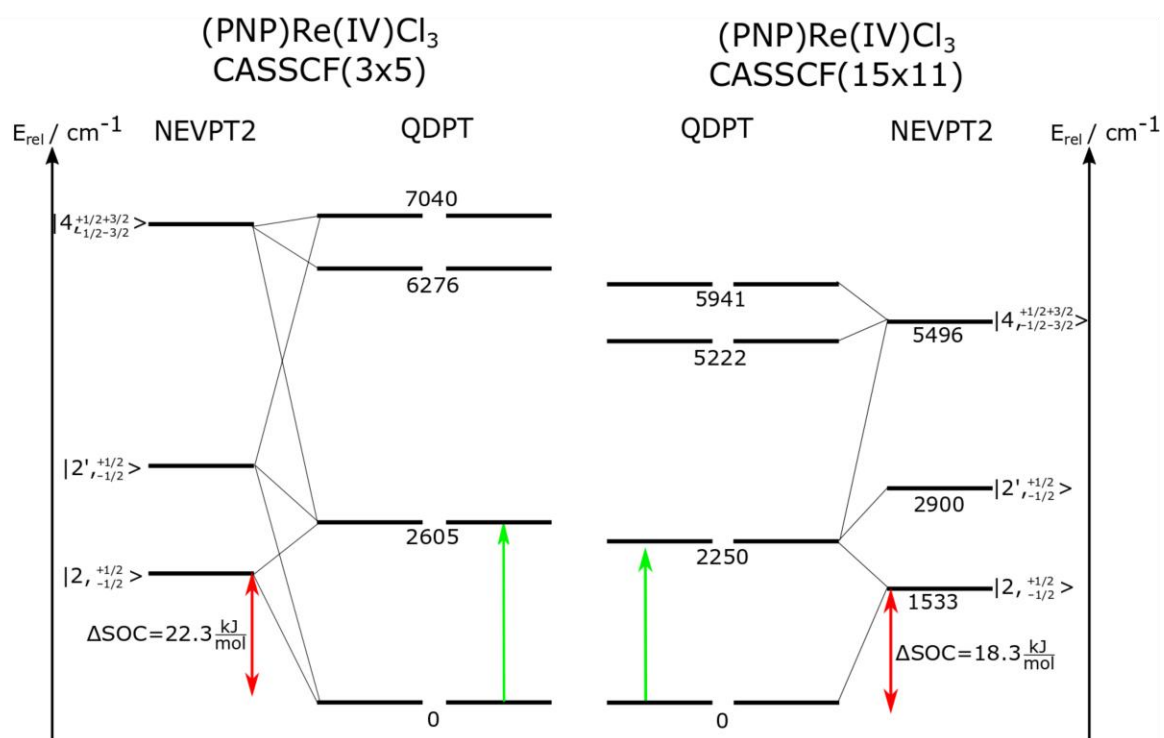
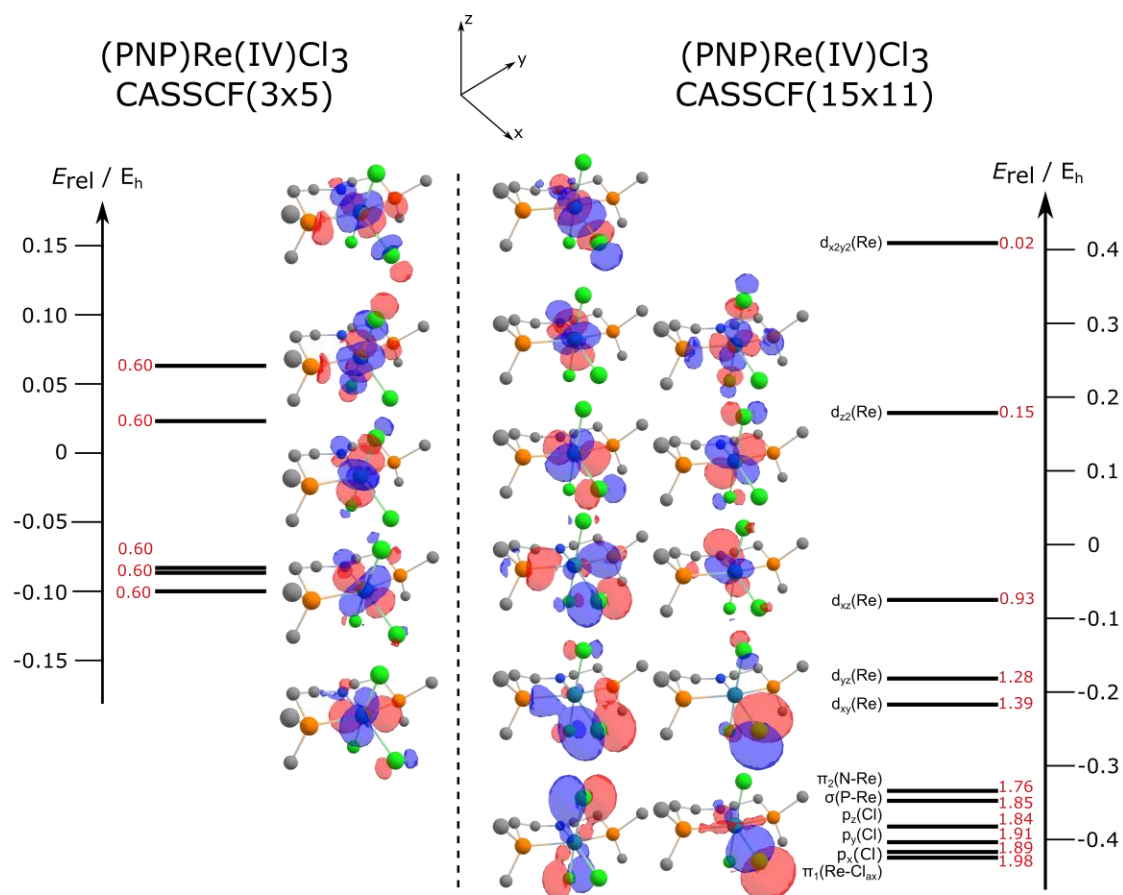


Figure 41: Top) CASSCF orbitals of the small (3,5) CAS space (left) CASSCF orbitals of the big (15,11) CAS space (right) for **24**, orbitals shown from lowest in energy left bottom to top. bottom) State correlation diagrams for the big (15,11) (left) and small (3,5) (right) complete active spaces from NEVPT2 calculations with (QDPT) and without spin-orbit coupling for **24**.

The computed temperature dependent magnetisation of **24** (Figure 42a cyan) reproduces the experimentally found data by SQUID magnetometry and the computed TIP is only underestimated to a minor degree compared to the experimentally found values (cf. Figure 42, cyan/blue). The CASSCF wavefunction is further benchmarked by a comparison of the computed (Figure 42c magenta) to the experimentally recorded UV-Vis and NIR spectra of **24** (Figure 42c red and black). The UV-Vis spectrum of **24** has an intense transition at 290 nm (34440 cm^{-1}), a dominant charge transfer band at 520 nm (19200 cm^{-1}) with a low intensity edge around 600 nm (16700 cm^{-1}), which can be assigned to a d-d transition, while in the NIR region only one very broad signal at 1600 nm (6250 cm^{-1}) can be found (Figure 42). The intense transition at 290 nm is very well reproduced to 286 nm, while the computed oscillator strength does not match at all the observed intensity. The chosen CAS space might be too small to describe the high energy of this transition, since not all MOs of the axial chlorine atoms are treated in the computation and thus their contribution to the transition is neglected. The intense transition at 520 nm is reproduced nicely by the computation to 533 nm.

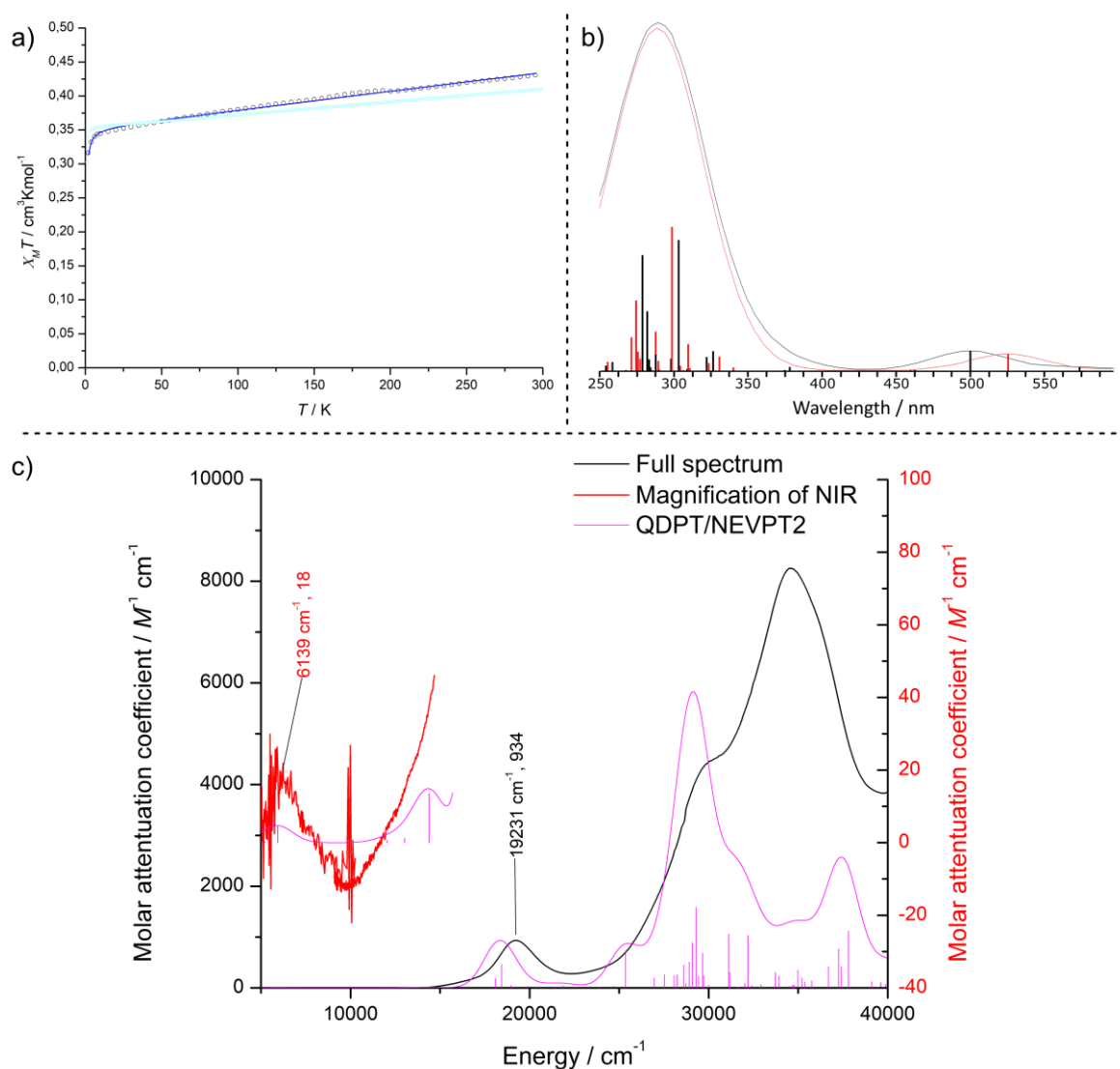


Figure 42: a) Comparison of the computed magnetisation for **24** on the (15,11) CASSCF/NEVPT2-QDPT level of theory (cyan) vs. the found magnetisation by SQUID magnetometry (black+blue fit). b) Comparison of the TD-DFT(50 states) data of **24** with and without solvent correction by SMD for dichloromethane. c) Computed UV/Vis and NIR spectra of **24** on the (15,11) CASSCF/NEVPT2-QDPT level of theory (pink) compared to the experimental spectra (black and red). c) Computed UV/Vis and NIR spectra of **24** on the (15,11) CASSCF/NEVPT2-QDPT level of theory (pink) compared to the experimental spectra (black and red).

The charge transfer character of this band could be confirmed again by TD-DFT computations by the difference between the computed spectra with and without SMD correction. (Figure 42b). The better agreement on this band compared to **23** could be explained by less solvent interactions due to the abstracted N-H proton for **24**. In the end, the NIR region is as well, excellently reproduced by the computations. All together, the *ab initio* computation is satisfactorily reproducing the experimental found spectroscopic and magnetic features of **24** and additionally predicts an enormous differential spin-orbit coupling effect between **23** and **24** of $\Delta\Delta\text{SOC} = 28 \text{ kJ mol}^{-1}$.

2.3. Computational Rationalisation of Rhenium(IV) Amine Complex **25**

At the end the electronic structure of the cationic rhenium(IV) amine **25** is computationally rationalized. DFT analysis on the PBE0-D3/def2TZVP level of theory confirms the predicted quartet ground state ($\Delta E_{\text{D/Q}} = 73 \text{ kJ mol}^{-1}$). The calculated structure for the quartet ground state converged in C_s symmetry and is in very good agreement with the found structure by XRD analysis, while the doublet structure gives higher deviations especially for the Re-P bond length (Figure 44, a). The Mulliken spin density is mainly metal centred, with small contributions of the coordinated chlorine atoms (Re: 2.56; Cl_{eq} : 0.21; 2Cl_{ax} : 0.25) and gives reason to expect a high SOC contribution (Figure 44b). A more detailed analysis of the electronic structure was again obtained by CASSCF-NEVPT2 analysis. For comparability, the same CAS space as for **23** and **24** was chosen resulting in a (13,10) expansion (Figure 44, left). The CASSCF-NEVPT2 wavefunction places the quartet electromer over the doublet by 93 kJ mol^{-1} and thus reproduces the electronic ground state picture derived by DFT (Figure 44, right). The ground state is dominated by the $(d_{xy}^1)(d_{yz}^1)(d_{xz}^1)$ configuration and stabilizes upon treatment of spin-orbit coupling by means of QDPT by only $-11.6 \text{ kJ mol}^{-1}$. The lowest eigenstates experience neglectable mixing with the excited states, explaining the low spin-orbit stabilisation, even though the spin density is metal centred. For this reason, also no IR active electronic transition was found, since the first excited states are insignificantly stabilized by SOC and thus located in the NIR region.

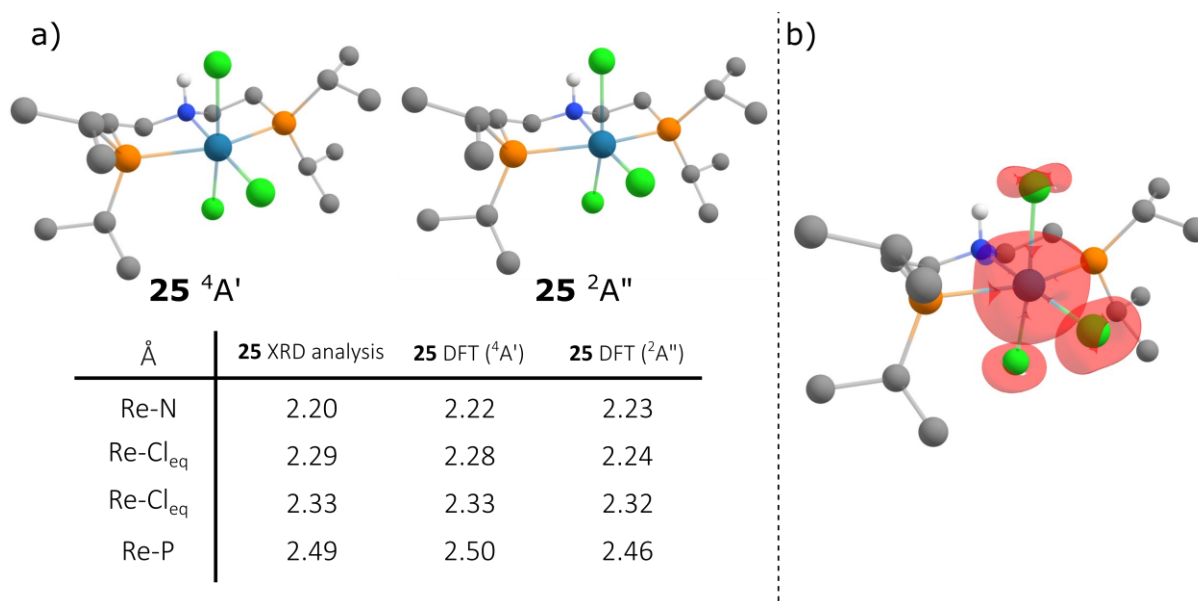


Figure 43: a) C_s symmetric computed structures for **25** (Doublet $^2A''$ and Quartet $^4A'$) on the PBE0-D3/def2TZVP level of theory and comparison of selected bond length to the experimental found structure by XRD analysis. b) DFT spin-density plot at isovalue 0.0075 a_0^{-3} for the $^4A'$ ground state of **25**.

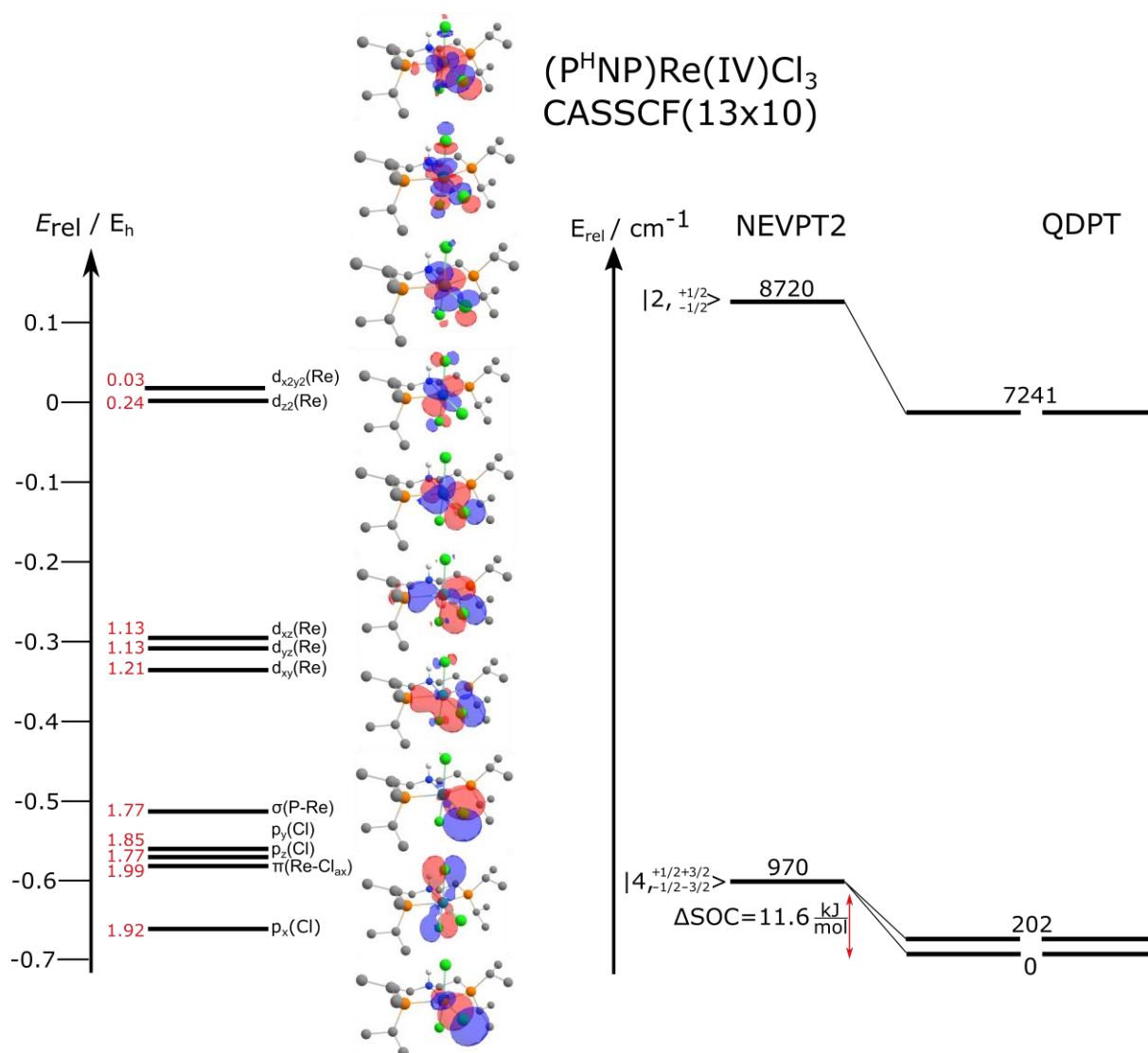
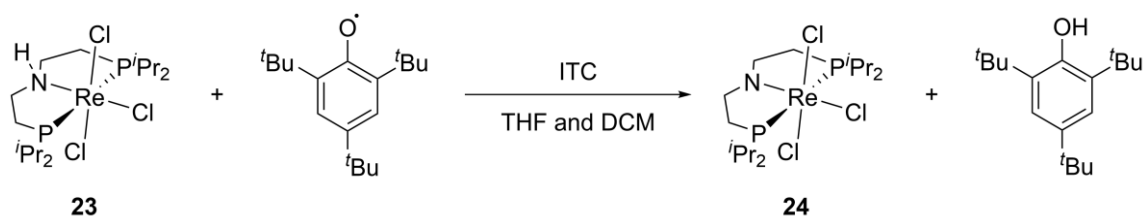


Figure 44: Left: CASSCF orbital scheme of **25** Right: State correlation diagrams of the (13,10) complete active space from NEVPT2 calculations with (QDPT) and without spin-orbit coupling for **25**.

3. Reaction (Free) Enthalpy Determination

3.1. Experimental (Free) Reaction Enthalpy Determination

Next, the reaction (free) enthalpy of the PCET reaction of **23** forming **24** is measured as a benchmark by isothermal titration calorimetry (ITC)⁶⁵ for comparison of the spin-free computational results with the experiment. Therefore, the strong hydrogen atom acceptor Mes*O was titrated in small steps with **23** in THF and DCM (Scheme 10).



Scheme 10: Reaction of **23** with Mes*O in THF or DCM at 25 °C analysed by isothermal titration calorimetry.

The obtained data was integrated over time and fitted with an independent PCET model (Figure 45).⁶⁶ On the one hand, the measured enthalpies all scatter within a narrow window of less than 1 kJ mol⁻¹ and 0.1 kJ mol⁻¹ for THF and DCM, respectively and are thus very precisely determined, while the free enthalpy of the reaction on the other hand could not be derived by ITC. Here, the too steep slope around the equivalence point hampered a meaningful fit of the titration curve. The reaction enthalpy is significantly changing between the two chosen solvents. While in THF -40 kJ mol⁻¹ are released (Figure 45a), the enthalpy sums up to -51 kJ mol⁻¹ in DCM (Figure 45b). The high solvent dependency can be tentatively attributed to the higher tendency of THF to form hydrogen bonds with the N-H and O-H protons of **23** and Mes*OH. Since the N-H proton of **23** is sterically less shielded than the O-H proton of Mes*OH, **23** could be higher stabilized by solvation in THF than in DCM, resulting in a lower reaction enthalpy. Since the free reaction enthalpy could not be determined by ITC, a square scheme approach was probed to access the Gibbs energy of reaction on a different way (Figure 46a). In the literature, the Bordwell equation (Figure 46b left)⁶⁰ is used to determine the binding free dissociation energy (BDFE), where the C_G value of this equation is a correction to capture the free enthalpy of reaction of the formally formed hydrogen atom (including e.g. solvation and the potential of the H⁺/H couple in the respective solvent). Since the solvation of the hydrogen atom can only be estimated, the obtained BDFE may have a systematical error. This is of no importance, if relative values in the respective solvents are compared, but hinders the absolute free reaction enthalpy determination as obtained from the computational site.⁶⁷ This problem can be surpassed by the determination of the square scheme parameters for both reagents **23** and Mes*OH and rearranging the equation to a form, in which C_G cancels out (Figure 46b).

⁶⁵ A comprehensive description and analysis of the performed ITC experiments, including detailed measurement conditions and all titration plots can be found in Section 3 of chapter VI.

⁶⁶ The details of the independent PCET model can be found in Section C of chapter 7.

⁶⁷ For more details about PCET thermochemistry see Section 2.2 of chapter I.

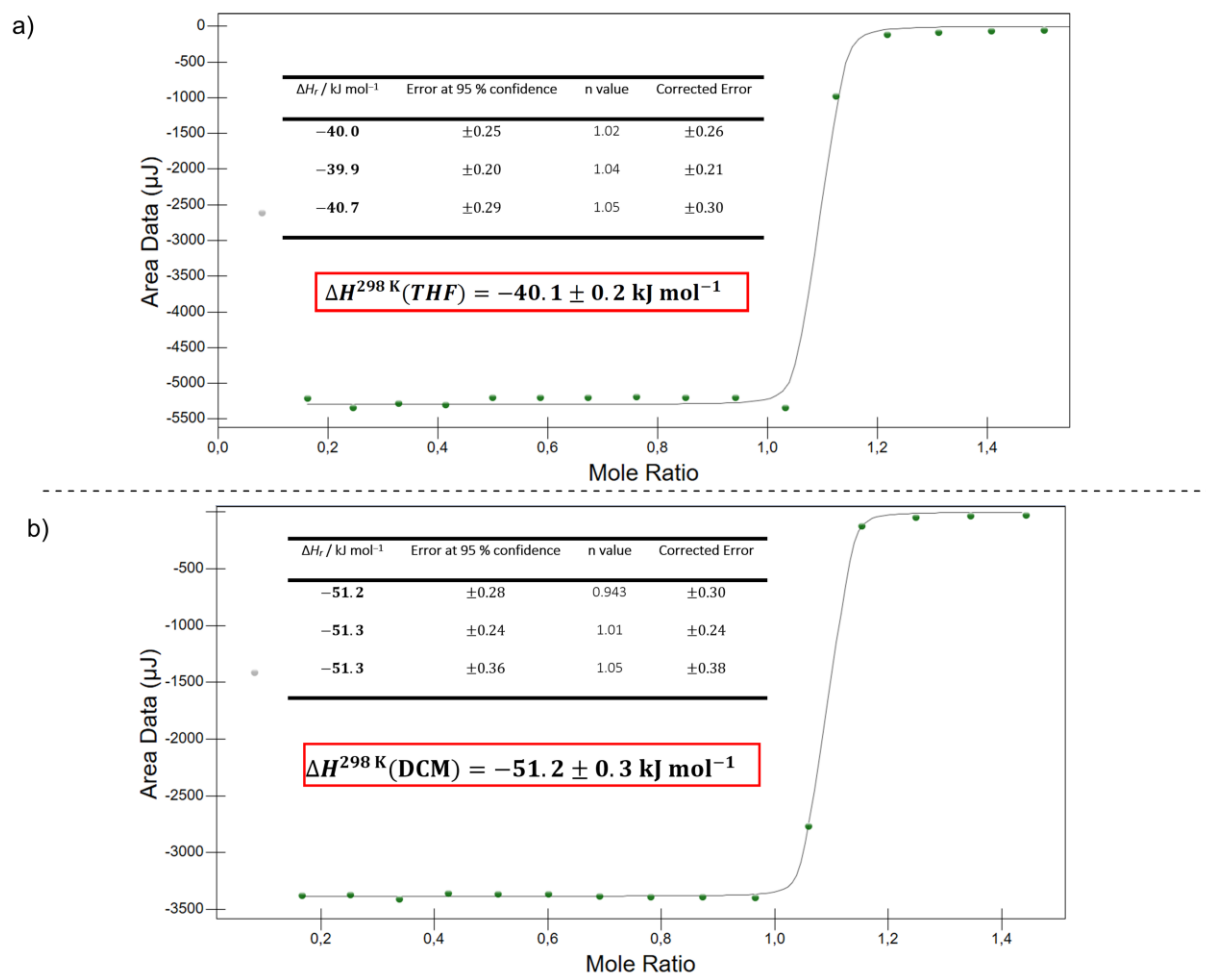


Figure 45: a) Representative titration plot and results table of three independent runs of the PCET reaction (Scheme 10) in THF. c) Representative titration plot and results table of three independent runs of the PCET reaction (Scheme 10) DCM.

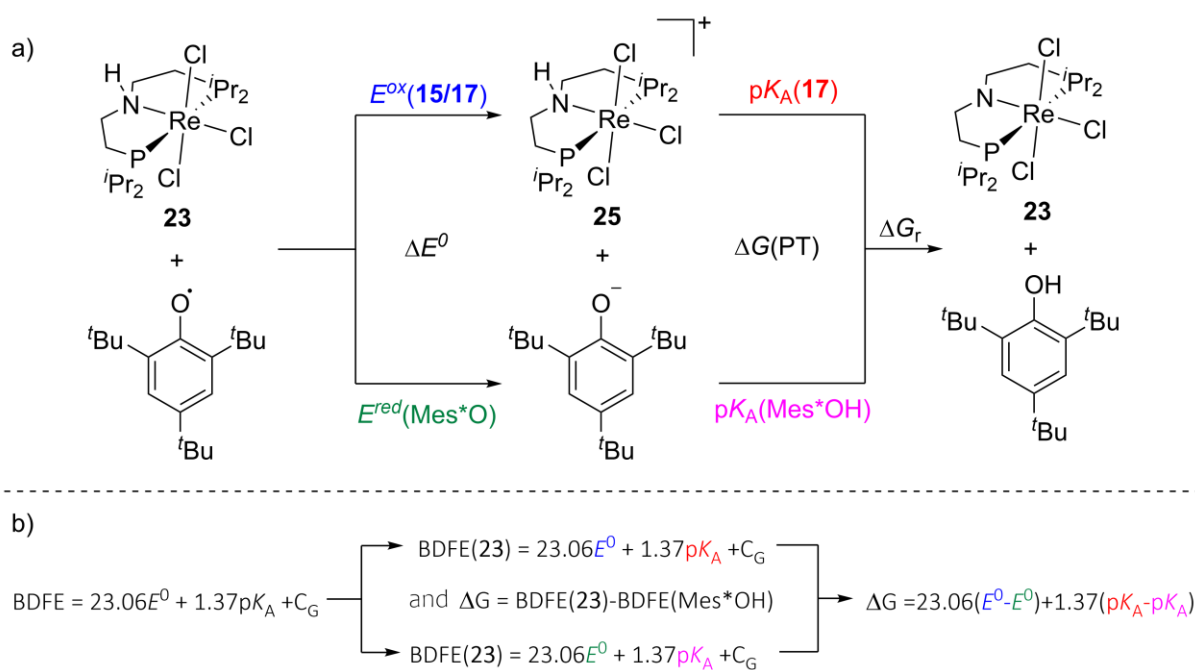


Figure 46: a) Approach for the determination of the free reaction enthalpy of the PCET reaction between **23** and Mes*O b) Rearrangement of the Bordwell equation for the cancelation of C_G .

Therefore, the electrochemical potentials of the **23/25** oxidation and Mes*O/Mes*O⁻ reduction as well as the pK_A values of **25** and Mes*OH in THF must be determined. The Mes*O/Mes*O⁻ electrochemical couple was reported previously^[184] to $E^0(\text{Mes}^*\text{O}/\text{Mes}^*\text{O}^-) = -0.96 \text{ V vs. Fc/Fc}^+$. The oxidation potential of **23** had to be reevaluated to $E^0(\mathbf{23}/\mathbf{25}) = -0.29 \text{ V vs. Fc/Fc}^+$ in contrast to the published value of $E^0(\mathbf{23}/\mathbf{25}) = -0.24 \text{ V vs. Fc/Fc}^+$, which suffered from internal reference issues.^{[158],68}

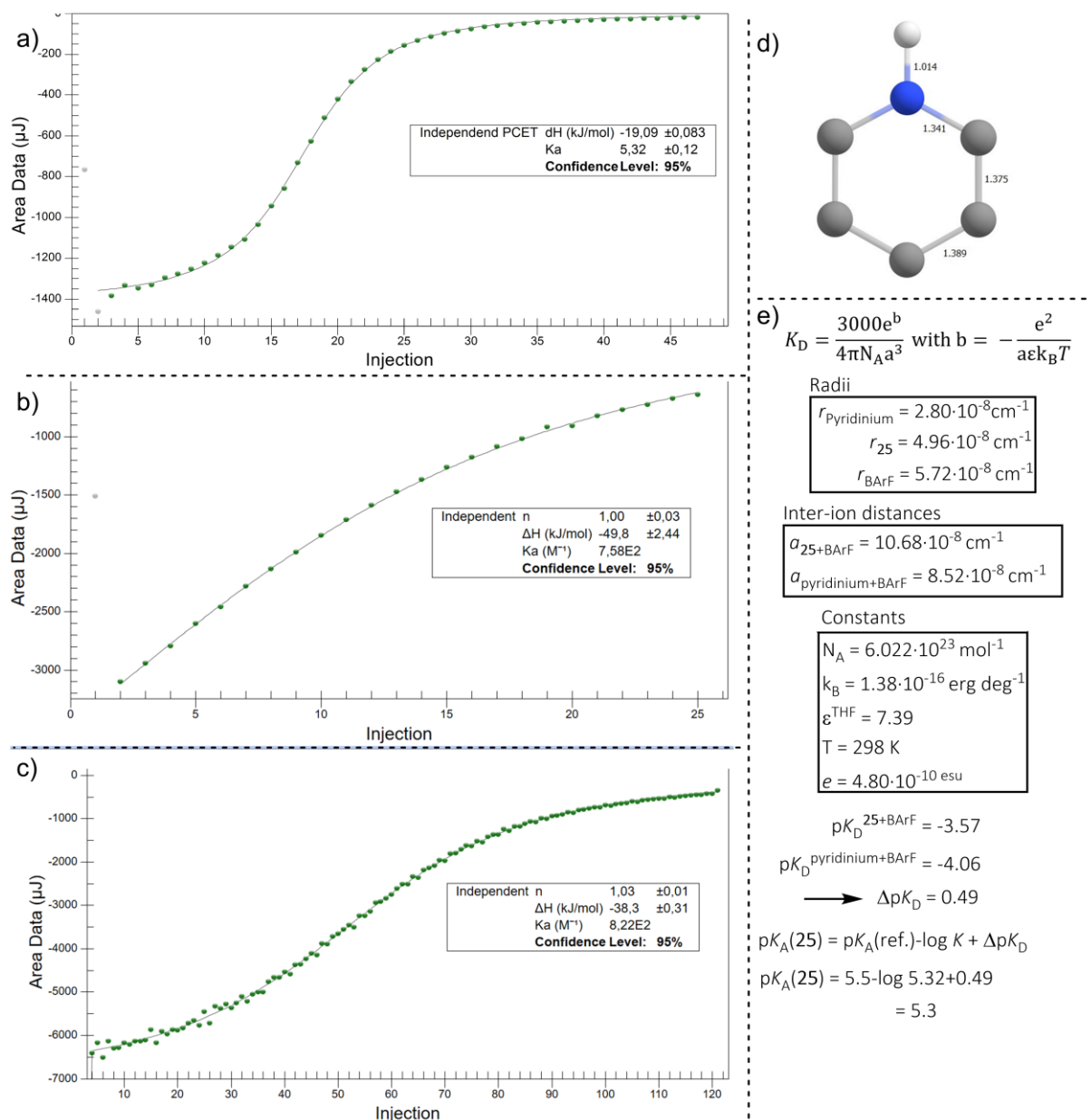


Figure 47: a) Representative titration plot and results table of the titration of **25** with pyridine in THF at 25 °C. b) Titration plot of the titration of Mes*OH with P₂-Et base in THF at 25 °C at low concentration. c) Titration plot and results table of the titration of Mes*OH with P₂-Et base in THF at 25 °C at high concentration. d) Converged C_s symmetric structure of a pyridinium ion on the PBE0-D3/def2TZVP level of theory. All C-H protons are omitted for clarity. e) Fuoss equation (top) and the values for the calculation of the ΔpK_D value as well as the overlapping indicator equation (bottom) for the calculation of the pK_A value.

The pK_A values of **25** and Mes*OH were derived by isothermal titration calorimetry. Pyridine as a base (pK_A^{THF} = 5.5)^[222] is sufficient to deprotonate **25** and the titration of **25** vs. pyridine gives an ideal, s-shaped titration curve, sufficient for the determination of an equilibrium constant $K = 5.32$ (Figure 47a). To obtain the pK_A value of a

⁶⁸ See Chapter VI Section 2.17

substance in THF, ion-pairing must be considered, which can be done by an electrostatic model based on work by Fuoss (Figure 47e).^[223] Since no crystal structure of an uncoordinated pyridinium-ion is known in the literature, its radius is estimated based on a structure computed on the PBE0-D3/def2TZVP level of theory (Figure 47d),⁶⁹ while the radii of **25** and the BARF₂₄ counterion are derived on basis of the found crystal structure (see Section 1.3). With this data the acidity of **25** is calculated to $pK_A^{\text{THF}}(\mathbf{25}) = 5.3$ (Figure 47e).

The situation is more complicated for the pK_A value derivation of Mes*OH. A diluted titration of Mes*OH with the strong phosphazene base P₂-Et⁷⁰ ($pK_A^{\text{THF}} = 25.3$) gives a titration curve with a shallow slope (Figure 47, b). This speaks either for a reaction with low driving force with dissociating ions or for an association reaction, in which the formed Mes*O⁻/HP₂-Et⁺ couple is not dissociating. To distinguish between these two situations, the titration was repeated with a ten-fold higher concentration, since only the association reaction is concentration dependent, while the titration curve would not change for a reaction with low driving force. At higher concentrations, the shape of the titration curve changes drastically to a s-shaped character, proofing the association mechanism (Figure 47c). Therefore, the titration curve has to be fitted by an independent model based on an association reaction.^[224] The so obtained fit of the titration curve already includes the ion-pairing correction and makes an additional Fuoss correction obsolete. With the equilibrium constant of $K = 806$ the acidity of Mes*OH is calculated to $pK_A^{\text{THF}}(\text{Mes*OH}) = 22.4$, which finally enables the calculation of the free reaction enthalpy of the PCET reaction to $\Delta G_r^{\text{THF}} = -33 \pm 8 \text{ kJ mol}^{-1}$.⁷¹

3.2. Computational (Free) Enthalpy Determination

At last, the reaction (free) enthalpy of the PCET reaction (Scheme 10) is computed based on two different *ab initio* models. A hybrid ONIOM(CCSD(T)-F12b/PBE0) approach including CCSD(T)-F12b single point computations on truncated model systems and a localized DLPNO-CCSD(T)⁷² approach with single points on the full systems, extrapolated to the CBS from the triple and quadruple zeta basis (see Chapter I Section 3.1). The *ab initio* computations are performed based on structures obtained DFT level of theory (PBE0-D3/def2TZVP). Additionally, also the (free) enthalpic contributions for standard conditions (298 K/1 atm) are obtained on the DFT level of theory.⁷³

Two different truncation levels were probed to test the size consistency of the ONIOM approach. 1) Hydrogen truncation, where hydrogen atoms substitute the isopropyl and tert-butyl groups of **23/24** and of Mes*O/Mes*OH, respectively and 2) Methyl truncation, where methyl groups are used for the substitution. Additionally, a single point CCSD(T) calculation without truncation was computed for the Mes*O/Mes*OH couple. Table 2 summarizes the obtained *ab initio* benchmarks for the PCET reaction (free) enthalpy with (SOC) and

⁶⁹ xyz data of the converged structure can be found in Section D of chapter 7. The collision diameter was derived with Chemcraft V.1.8, www.chemcraftprog.com.

⁷⁰ P₂-Et = Tetramethyl(tris(dimethylamino)phosphoranylidene)phosphorictriamid-Et-imin, CAS = 165535-45-5.

⁷¹ The error of ΔG is estimated (Fuoss correction, pK_A reference values have no reported errors, cumulative error of four independent experiments) to 8 kJ mol⁻¹.

⁷² DLPNO computations performed by Dr. Martin Diefenbach.

⁷³ A comprehensive discussion of the performed computations can be found in Section 4.3.4 of chapter VI.

without (spin-free) spin-orbit coupling ($\Delta\Delta\text{SOC} = 28 \text{ kJ mol}^{-1}$).⁷⁴ Truncation of the tert-butyl groups has a very minor effect ($\Delta\Delta E = 3 \text{ kJ mol}^{-1}$) on the total energy of the Mes*O/Mes*OH couple (Table 2, 1-3) as well as on the **23/24** couple ($\Delta\Delta E = 0.5 \text{ kJ mol}^{-1}$) (Table 2, 1 and 4), which proves the validity of the ONIOM approach for this reaction. A comparison between the VDZ-F12b and VTZ-F12b basis sets results in a higher deviation of $\Delta\Delta E = 5\text{-}7 \text{ kJ mol}^{-1}$ than for the different truncation levels, but still supports that a sufficient amount of electronic correlation is captured already with the double-zeta basis (Table 2, 1/7,2/8). The DLPNO-CCSD(T₀) computations do not differ between the correlation consistent Dunning basis sets and the Ahlrich basis sets (Table 2, 9 and 10), thus the more expensive T₁ triples, were probed with the Ahlrich basis set (Table 2, 11). All together, the *ab initio* models place the reaction (free) enthalpy at $\Delta H/G_r = -74$ to -82 kJ mol^{-1} without including spin-orbit coupling, but with SOC the picture drastically changes. Here, the (free) reaction enthalpy is computed to $\Delta H/G_r = -46$ to -54 kJ mol^{-1} , which is in very good agreement to the experimentally found values of $\Delta H/G_r^{\text{THF}} = -40.1 \pm 0.2 / -33 \pm 8 \text{ kJ mol}^{-1}$ and $\Delta H^{\text{DCM}} = -51.2 \pm 0.3 \text{ kJ mol}^{-1}$. The small difference between experiment and theory can tentatively be accounted to solvation effects (THF/DCM) and to the methodical error of the performed computations (basis set limit, truncations, symmetry, active orbitals). These results finally proof the spin-orbit coupling effect on the thermochemistry of a PCET reaction.

⁷⁴ SOC value from the CASSCF/NEVPT2-QDPT computations, see Section 2.

Table 2: *Ab initio* computations summary table for the PCET reaction (see Figure 45, a), the (relative) highest levels of theory are marked bold. **[a]** All *ab initio* data are based on structures optimized on PBE0-D3/def2TZVP level of theory. ONIOM energies computed with: $E^{ONIOM} = E_{Model}^{CCSD(T)} - E_{Model}^{DFT} + E_{Fullsystem}^{DFT}$. Results shown for the triplet ground state of **23** and the doublet ground state of **24** **[b]** (Free) Enthalpic contribution based on the DFT results on PBE0-(D3)/def2TZVP level of theory. **[c]** Spin-orbit contribution based on CASSCF/NEVPT2-QDPT results for **15** (14x10) and **16** (15x11). **[d]** CCSD(T)-f12/VDZ computations based on hydrogen truncated model systems. **[e]** CCSD(T)-f12/VDZ computations based on hydrogen truncated model systems for **23** and **24** and methyl truncation on the Mes*OH/Mes*O couple. **[f]** CCSD(T)-f12/VDZ computations based on hydrogen truncated model systems for **23** and **24** and no truncation on the Mes*OH/Mes*O couple. **[g]** CCSD(T)-f12/VDZ computations based on methyl truncated model systems for **23** and **24** and hydrogen truncated model systems for the Mes*OH/Mes*O couple. **[h]** CCSD(T)-f12/VDZ computations based on methyl truncated model systems. **[i]** CCSD(T)-f12/VDZ computations based on methyl truncated model systems for **23** and **24** no truncation on the Mes*OH/Mes*O couple. **[j]** CCSD(T)-f12/VTZ computations on hydrogen truncated model systems. **[k]** CCSD(T)-f12/VTZ computations on hydrogen truncated model systems of **23** and **24** and methyl truncated model systems of the Mes*OH/Mes*O **[l]** DLPNO with CCSD(T0) using Dunning basis sets extrapolated to the CBS limit from the triples and quadruples results. **[m]** DLPNO with CCSD(T0) using Ahlrichs basis sets extrapolated to the CBS limit from the triples and quadruples results **[n]** DLPNO with CCSD(T1) using Ahlrichs basis sets extrapolated to the CBS limit from the triples and quadruples results.

	Method ^[a]	$\Delta H/G_r^{spin-free}$ ^[b] / kJ mol ⁻¹	$\Delta H/G_r^{SOC}$ ^[c] / kJ mol ⁻¹
1	ONIOM (H: ⁱ Pr/ ^t Bu, VDZ) ^[d]	-79.5/-80.0	-51.4/-51.9
2	ONIOM (H: ⁱ Pr, Me: ^t Bu, VDZ) ^[e]	-82.5/-83.0	-54.4/-54.9
3	ONIOM (H:ⁱPr ^tBu:^tBu, VDZ)^[f]	-81.4/-81.8	-53.3/-53.7
4	ONIOM (Me: ⁱ Pr, H: ^t Bu, VDZ) ^[g]	-80.0/-80.4	-51.8/-52.4
5	ONIOM (Me: ⁱ Pr/ ^t Bu, VDZ) ^[h]	-83.0/-83.4	-54.9/-55.3
6	ONIOM (Me:ⁱPr, ^tBu:^tBu, VDZ)^[i]	-81.8/-82.3	-53.7/-54.2
7	ONIOM (H: ⁱ Pr/ ^t Bu, VTZ) ^[j]	-72.4/-72.8	-44.3/-44.7
8	ONIOM (H:ⁱPr, Me:^tBu, VTZ)^[k]	-77.1/-77.6	-49.0/-49.5
9	DLPNO(CCSD(T ₀)/cc-pV(T,Q)Z(PP)) ^[l]	-69.4/-69.8	-41.3/-41.7
10	DLPNO(CCSD(T ₀)/def2-p(T,Q)ZVPP) ^[m]	-69.1/-69.5	-41.0/-41.4
11	DLPNO(CCSD(T₁)/def2-p(T,Q)ZVPP)^[n]	-74.2/-74.7	-46.1/-46.6

4. Summary of Chapter IV

In summary, in this Chapter the effect of spin-orbit coupling on the thermochemistry of a PCET reaction was analysed in detail. For this purpose, the rhenium(III) amine complex **23** was chosen which has shown to be greatly influenced by SOC in a previous publication. The thorough investigation of the spectroscopic and magnetic data of **23** led to the assignment of a triplet ground state, which is thermally well separated ($> 1300 \text{ cm}^{-1}$) from excited states as a reason of extensive SOC. The SOC splits the triplet root into its microstates, resulting in an effective non-magnetic $J = 0$ ground state. The temperature independent mixing with magnetic excited states explains the sharp but paramagnetically shifted $^1\text{H-NMR}$ spectra of **23** as well as the linear $\chi_M T$ vs. T slope over the whole temperature range. Additionally, a broad and intense transition in the midIR region at 3500 cm^{-1} was observed with differing intensity upon applying a magnetic field. Therefore, a midIR transition of a transition metal complex could be unequivocally assigned to be of electronic nature. The PCET counterpart, the rhenium(IV) amide complex **24**, exhibits a doublet ground state which is also significantly influenced by TIP even though only with a third of the magnitude of **23**. The effective magnetic moment at room temperature $\mu_{\text{eff}} = 1.83 \mu_{\text{B}}$ of **24** is in line with the expected spin-only value of $\mu_{\text{eff}}^{\text{SO}} = 1.73 \mu_{\text{B}}$ of a doublet ground state, but already hints for the mixing of excited states with the ground state. The midIR spectrum of **24** is featuring like **23** a broad, intense band at 1970 cm^{-1} which is tentatively assigned as well to be of electronic nature. For the determination of the thermodynamic PCET characterisation, the cationic rhenium(IV) amine complex **25** was successfully synthesised and characterised. The effective magnetic moment at room temperature in solution of **25** $\mu_{\text{eff}} = 2.9 \mu_{\text{B}}$ is well beyond the expected spin-only value for a doublet ground state, suggesting a quartet ground state for **25**, but no broad transition in the midIR as for **23** and **24** was observed.

DFT analysis on the PBE0-D3/def2TZVP level of theory confirmed the experimental ground state picture and excellently reproduced the found structures by XRD analysis. Additionally, for all three complexes mainly metal centred radical character is predicted by Mulliken and NBO/NPA analysis, thus giving reason to expect high SOC contributions, especially for the amine complexes **23** and **25**. The electronic structure was analysed in more detail by *ab initio* CASSCF-NEVPT2-QDPT computations. For **23** an effective 3E like ground state on the spin-free NEVPT2 level is computed, which strongly splits upon SOC into its microstates. This results in a huge SOC stabilisation of $\Delta\text{SOC} = -46.4 \text{ kJ mol}^{-1}$. The *ab initio* wavefunction was further benchmarked with SQUID, UV/Vis and (N)IR spectra of **23** and is in excellent agreement with the experiment. Here, especially the midIR transition is very well predicted to 3900 cm^{-1} (cf. 3500 cm^{-1} experimentally). The *ab initio* wavefunction nicely reproduces the experimental benchmarks of the rhenium(IV) amide complex **24** as well and predicts the midIR transition to 2200 cm^{-1} (cf. 2000 cm^{-1} experimentally). The computed SOC stabilisation of **24** ($-18.5 \text{ kJ mol}^{-1}$) is almost three times lower than for **23** and therewith follows an enormous SOC effect on the PCET thermochemistry of $\Delta\Delta\text{SOC} = 28 \text{ kJ mol}^{-1}$. For the cationic amine **25** a very high doublet/quartet gap of 93 kJ mol^{-1} was computed, resulting in a decreased mixing by SOC ($\Delta\text{SOC} = -11.6 \text{ kJ mol}^{-1}$) even though the spin density at the metal centre was the highest of the series.

The enthalpy of the PCET reaction was measured by isothermal titration calorimetry (ITC) and gives a $\Delta H_r = -40.1 \pm 0.2 \text{ kJ mol}^{-1}$ in THF and $\Delta H_r = -51.2 \pm 0.3 \text{ kJ mol}^{-1}$ in DCM, while the free reaction enthalpy in THF was calculated by a square scheme approach via the determination of the oxidation potentials of **23** ($E^0 = -0.29 \text{ V}$, vs.

Fc/Fc⁺), Mes*O⁻ ($E^0 = -0.96$ V vs. Fc/Fc⁺) and the pK_A values of **25** (pK_A = 5.3) and Mes*OH (pK_A = 22.4) to $\Delta G_r = -33 \pm 8$ kJ mol⁻¹. Here, the high solvent dependency was attributed to the higher tendency of THF to form hydrogen bonds.

The spin-free *ab initio* techniques ONIOM and DLPNO place the reaction (free) enthalpy of the PCET reaction at $\Delta H/G_r^{ab\text{ initio}} = -74$ to -82 kJ mol⁻¹ while the consideration of the SOC effect corrects the predicted value to $\Delta H/G_r^{ab\text{ initio}+SOC} = -46$ to -54 kJ mol⁻¹, which is in perfect agreement to the experimentally found values. The SOC effect ($\Delta\Delta SOC = 28$ kJ mol⁻¹) is in the same order of magnitude as the computed SOC effect on reduction potentials of osmium(II/III) (300 mV, 28 kJ mol⁻¹) reported by KÝvala and Ruliřek.^[140] These results corroborate the fundamental importance a differential SOC effect can have in heavy metal chemistry. A $\Delta\Delta SOC$ effect especially needs to be considered when a spin change at the metal centre upon reaction takes place and excited states close to the ground state are available for mixing (**23/24** vs. **25**).

Chapter V

V. Conclusion and Outlook

This dissertation helped in the deeper understanding of two research topics:

1) Electronic structure and reactivity of late, electron rich terminal oxo complexes

2) Proton coupled-electron transfer thermochemistry at heavy metal sites with a special emphasis on the effect of spin-orbit coupling.

The synthesis and characterisation of a series of terminal iridium hydroxo complexes [(PNP)Ir(OH)] (**1**, **2**, **3**), including the first open-shell iridium hydroxo complex **2**, enabled the targeted synthesis of a terminal iridium(III) oxo complex **4** by either deprotonation of the cationic hydroxo complex **3** or direct HAT from neutral hydroxo complex **2**. The iridium-oxygen bonding of **4** was investigated by XRD analysis and IR spectroscopy, including ^{18}O -isotopic labelling, and revealed an elongated (0.1 \AA) and weakened (60 cm^{-1} red shifted) Ir-O bond, compared to the Ir-O triple bond of Wilkinson's iridium oxo complex **XXI**, thus **4** was assigned to exhibit an Ir-O double bond. Variable temperature NMR spectroscopy and SQUID magnetometry revealed an open-shell ground state of **4** with a linear $\chi_M T$ vs. T slope. A triplet ground state with a very high zero-field splitting (ZFS) of $D = 647 \text{ cm}^{-1}$ was assigned to **4** by a spin-Hamiltonian fit of the SQUID data. The ZFS is almost 200 cm^{-1} higher than for the isoelectronic terminal imido complex **XXII**. This is in line with a less covalent Ir-E (E=N/O) bonding interaction, which leads to a smaller relativistic nephelauxetic effect for **4** and therefore to a higher effective spin-orbit coupling parameter ζ_{eff} . The magnetic and spectroscopic data of **4** led to the assignment of an unprecedented oxo biradical species.

Electrochemical analysis of **4** revealed a reductive event at $E = -1.95 \text{ V}$ and a remarkably low potential for the oxidation at $E = -0.13 \text{ V}$ vs. Fc/Fc^+ for a formally iridium(III/IV) couple, again confirming the covalent bonding within the Ir-O unit and thus making oxidation states a bad descriptor for such complexes. The oxidation of **4** yields the thermally unstable **4+** complex, which was analysed in situ by NMR and EPR spectroscopy to exhibit C_{2v} symmetry. The very low g -anisotropy speaks for a ligand centred radical, which is supported by DFT computations with a Mulliken spin density at the oxygen atom of 75%.

The electronic structure of **2** and **4** was further analysed by high level *ab initio* techniques. The CASSCF-NEVPT2-QDPT computations support the triplet ground state of **4** which is heavily split by spin-orbit coupling into its microstates. Here, the computed zero-field of 750 cm^{-1} was in very good agreement to the experiment. A second noteworthy outcome of the CASSCF computations was the small, but non negligible differential SOC effect, which formally strengthens the O-H bond of **2** by 2.9 kJ mol^{-1} . The bond dissociation (free) energy (BD(F)E) of **2** was examined by isothermal titration calorimetry revealing a bond strength, in the regime of activated C-H bonds. Here, *ab initio* computations on the CCSD(T)-F12b and DLPNO-CBS level of theory excellently support the experimentally found BDE values. With all these thermodynamic parameters at hand, a full square scheme for all discussed oxo species was formulated. With a BDE value of 350 kJ mol^{-1} **4** can activate weak C-H bonds but not the strong C-H bonds of most solvents. The same picture arises for the $\text{p}K_{\text{A}}$ value of **4**, which is in the medium range of $\text{p}K_{\text{A}}$ values in THF. The cationic hydroxo complex **3** is bearing the strongest O-H bond with 372 kJ mol^{-1} . A comparison of the computed spin densities at the oxygen atom of **4** (O: 95%) and **4+** (O: 75%) reveals that the transient **4+** has less radical character but is more reactive which supports the statement of James Mayer that:

“Not radical character but bond strength is defining radical reactivity”^[25]

At last, the versatile reactivity of **4** was investigated within this thesis. Carbon monoxide could be oxidized to CO₂, which was confirmed by head space analysis. CO₂ could also serve as a reagent forming the iridium(III) carbonate complex **8** and thus revealing nucleophilic reactivity of **4**. **8** was also found to be a site product in the CO oxidation and therefore represents a thermodynamically more favoured product compared to the CO oxidation. With hydrogenolysis the iridium(III) dihydride complex **6** and water are formed, while the amphiphilic test reagent PMe₃ can be oxygenated to OPMe₃. The C-H bond activation capability of **4** was tested with the reagent's xanthene and fluorene in which in both cases a thermal reaction towards the C-O bond formation product (**11/12**) was found. While the reaction with xanthene also proceeds slowly at room temperature, the reaction must be heated to 60 °C for fluorene, which nicely reflects the decreasing BDE difference of the substrate to **4**. At last the irradiative oxygenation of benzaldehydes was reported and the formed benzoate complexes (**14-x**, X = F, H, Me, OMe) were independently characterized. A Hammett analysis revealed a positive slope of 3.7 for different benzaldehyde para-substituents, thus supporting the nucleophilic reactivity of **4**.

Future work in this field should focus on the deeper understanding of the C-H bond activation reactivity of **4**. Here, isotopic labelling experiments would give valuable insight into the rate determining step of the C-O bond formation and a detailed kinetic investigation could further help to distinguish between a pure concerted CPET or more asynchronous pathways (Figure 48A). The oxidation potential of the hydroxo complex **2** has shown to be very mild ($E^0 = -0.37$ V vs. Fc/Fc⁺) and the pK_a value of the corresponding cationic hydroxo complex **3** is as well accessible with comparably weak bases (pK_a^{THF} = 19) thus a potential catalytic hydroxylation process can be proposed. Here, **2** is electrochemically oxidized and subsequently deprotonated by a base, yielding the terminal oxo complex **4**. This step is followed by the C-H oxygenation, yielding one equivalent of **2** and of the alkoxide product (analogous to **12/11**). Since **2** is synthesised in a THF/water mixture, water is the ideal reagent for the substitution of the alkoxide recovering **2** and the free alcohol (Figure 48B). In the end a further investigation by XRD analysis of the cationic oxo species **4+** would help in the understanding of late transition metal multi-bonding interactions. Here, trapping experiments at very low temperatures in inert solvents as fluorobenzene could lead to the successful isolation of **4+**. A comparison of the reactivity of the cationic oxo **4+** with neutral **4** could additionally give insight into general philicity trends of terminal oxo complexes. **4** exhibited nucleophilic to ambiphilic reactivity but for cationic oxo **4+** electrophilic reactivity is expected due to the cationic charge. Here, olefin epoxidation or water oxidation would be promising starting points for the reactivity investigation of **4+** (Figure 48C). A second research field is the synthesis and characterisation of the terminal oxo complex of the lighter homologue rhodium [(PNP)Rh(O)] **4^{Rh}**. Preliminary computations on the PBE0-D3/def2TZVP level of theory (see Section D of Chapter 7 for xyz data) predict a 21 kJ mol⁻¹ higher O-H bond strength of the rhodium hydroxo **2^{Rh}**/vs. **2** which is close to aliphatic C-H bonds (cf. BDE(THF) = 92 kcal mol⁻¹, BDE(**2^{Rh}**) = 89 kcal mol⁻¹) (Figure 48D). Even if the isolation of the rhodium oxo **4^{Rh}** would be hampered by its high reactivity, a similar approach like in Figure 48B could enable the catalytic oxygenation of a broader substrate scope with **4^{Rh}** compared to **4**.

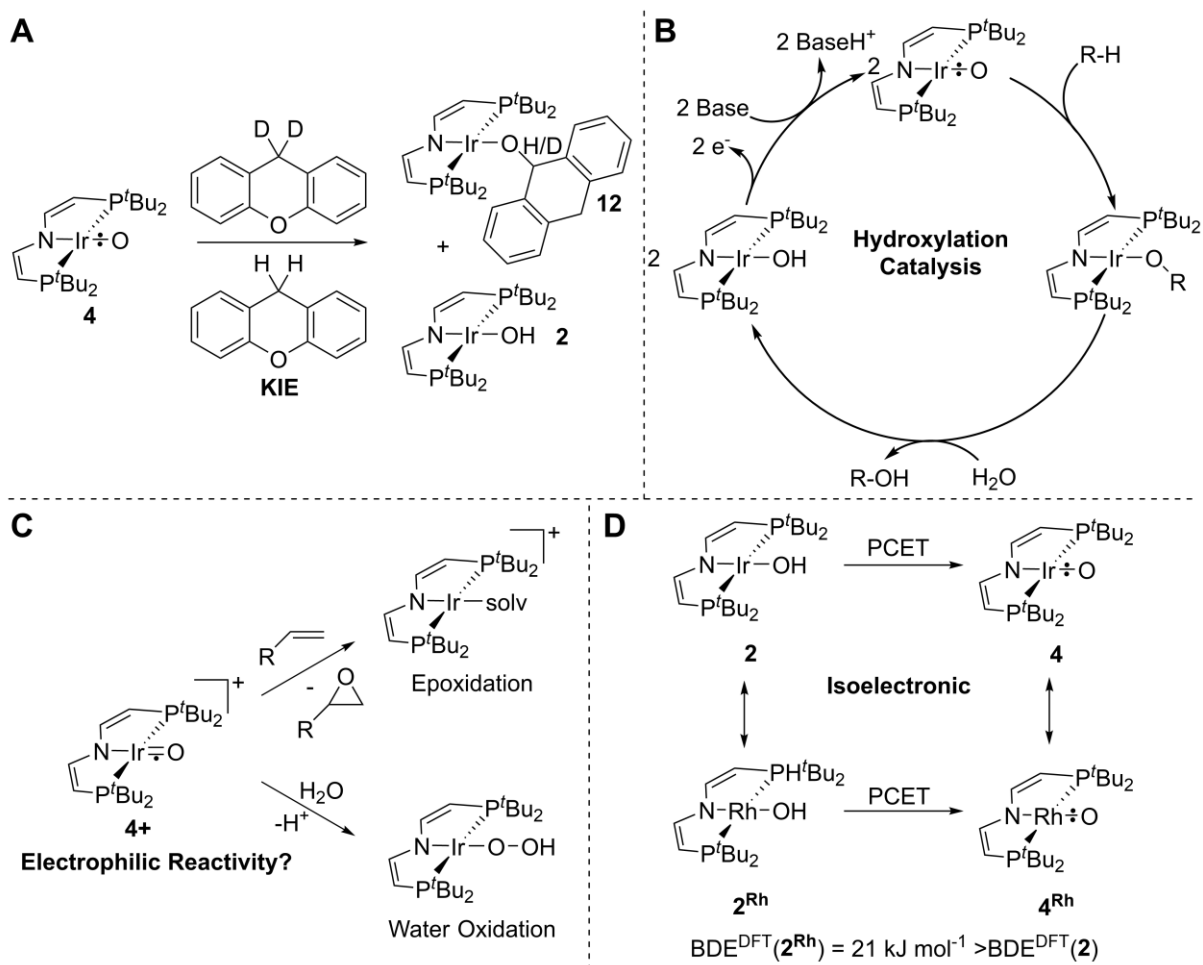


Figure 48: A) Kinetic isotope experiment for the mechanistic investigation of the C-H oxygenation reactivity. B) Possible catalytic hydroxylation reactivity of **2**. C) Proposed electrophilic reactivity of **4+**. D) Isoelectronic relationship of **2^{Rh}**/**2** and **4^{Rh}**/**4** and predicted BDE difference on the PBE0-D3/def2TZVP level of theory.

The small but non-negligible SOC effect on the thermochemistry of the **2/4** couple inspired for the detailed and general investigation of SOC effects in PCET solution thermochemistry. For this purpose, the rhenium(III) amine complex **23** was chosen which has shown to be greatly influence by SOC in a previous publication.^[158] Detailed analysis of the spectroscopic and magnetic features led to the assignment of a triplet $J = 0$ ground state with pronounced TIP. **23** exhibits an intense, broad peak at 3510 cm^{-1} in the mid-infrared spectrum, which arises from an electronic transition as assigned by magnetic field dependent IR spectroscopy. A similar picture arises for the rhenium(IV) amide complex **24**. The magnetic data obtained by SQUID magnetometry gives a doublet ground state with a significant, but three times lower, contribution of temperature independent paramagnetism. The midIR spectrum of **24** is as well featuring a broad, intense band at 1970 cm^{-1} which can be tentatively assigned as well to an electronic transition. A new cationic rhenium(IV) amine complex **25** was synthesised by oxidation of **23** with FcBARF_{24} and fully characterized. The effective magnetic moment at room temperature of **25** led to the assignment of a quartet ground state, but no comparable IR band as for **23** and **24** was found for **25**.

DFT analysis on the PBE0-D3/def2TZVP level of theory confirmed the experimental ground state pictures and excellently reproduced the found structures by XRD analysis. Additionally, for all three complexes mainly metal centred radical character is predicted by Mulliken and NBO/NPA analysis, thus giving reason to expect high SOC

contributions, especially for the amine complexes **23** and **25**. The electronic structure was analysed in more detail by *ab initio* CASSCF-NEVPT2-QDPT computations. For **23** a 3E like ground state on the spin-free NEVPT2 level is computed, which strongly splits upon SOC into its microstates, resulting in a huge SOC stabilisation of $\Delta\text{SOC} = -46.4 \text{ kJ mol}^{-1}$. The *ab initio* wavefunction was further benchmarked with SQUID, UV/Vis and NIR spectra of **23** and gave a good agreement with the experiment. Here, especially the midIR transition is very well predicted to 3900 cm^{-1} (cf. 3500 cm^{-1} experimentally). For amide complex **24** the *ab initio* wavefunction very well reproduces the experimental benchmarks as well and predicts the midIR transition to 2200 cm^{-1} (cf. 1970 cm^{-1} experimentally). The computed SOC stabilisation of **24** of $-18.5 \text{ kJ mol}^{-1}$ is three times lower than for **23** and therewith predicts an enormous SOC effect on the PCET thermochemistry of $\Delta\Delta\text{SOC} = 28 \text{ kJ mol}^{-1}$. For the cationic amine **25** a very high doublet/quartet gap of 93 kJ mol^{-1} was computed, which results in a decreased mixing by SOC ($\Delta\text{SOC} = -11.6 \text{ kJ mol}^{-1}$) even though the spin density at the metal centre was the highest of the series.

The enthalpy of the PCET reaction was measured by isothermal titration calorimetry (ITC) and gives an enthalpy of $\Delta H_r = -40.1 \pm 0.2 \text{ kJ mol}^{-1}$ in THF and $\Delta H_r = -51.2 \pm 0.3 \text{ kJ mol}^{-1}$ in DCM, while the free reaction enthalpy in THF was calculated by a square scheme approach via the determination of the oxidation potentials of **23** ($E^0 = -0.29 \text{ V}$, vs. Fc/Fc^+), Mes^*O^- ($E^0 = -0.96 \text{ V}$ vs. Fc/Fc^+) and the $\text{p}K_a$ values of **25** ($\text{p}K_a = 5.3$) and Mes^*OH ($\text{p}K_a = 22.4$) to $\Delta G_r = -33 \pm 8 \text{ kJ mol}^{-1}$.

The spin-free *ab initio* techniques ONIOM and DLPNO place the reaction (free) enthalpy of the PCET reaction at $\Delta H/G_r^{ab \text{ initio}} = -74$ to -82 kJ mol^{-1} , while the consideration of the SOC effect corrects the predicted value to $\Delta H/G_r^{ab \text{ initio}+\text{SOC}} = -46$ to -54 kJ mol^{-1} , which is in perfect agreement to the experimentally found values. These results corroborate the fundamental importance differential SOC effects can have in heavy metal chemistry. By consideration of the different SOC stabilisation of **23/24** vs. **25** and their spin-densities the following conclusion can be drawn:

SOC has an important effect on heavy metal PCET thermochemistry when a metal centred spin change upon reaction takes place and excited open-shell states close to the ground state are available for mixing.

Future work on this topic should focus on general trends of thermochemical SOC contributions. Here, especially the evaluation of the rhenium tri-halogen series $[(\text{PNP})\text{Re}(\text{III})(\text{Cl})_3]$ **23**, $[(\text{PNP})\text{Re}(\text{III})(\text{Br})_3]$ **23^{Br}** and $[(\text{PNP})\text{Re}(\text{III})(\text{I})_3]$ **23^I** could bring valuable insight (Figure 49A). A second field of interest is the theoretical maximum of SOC effects which can be observed in solution thermochemistry. The analysed SOC effect in this thesis was reduced by the still high SOC stabilisation of the rhenium(IV) amide complex **24**. **24** had a highly metal centred spin density (Re: Mulliken: 0.96; NBO/NPA: 0.84) and a relatively close excited doublet state ($\Delta E = 16 \text{ kJ mol}^{-1}$, NEVPT2) which resulted in the high SOC stabilisation of $-18.5 \text{ kJ mol}^{-1}$ which overall reduced the differential SOC effect. The analysis of open-shell/closed-shell reactions could therefore lead to a significantly higher differential SOC effect. Here, HAT from closed-shell metal hydrides like the iridium(III) hydrid-chloride complex **15**⁷⁵, are interesting starting platforms. **15** exhibits a diamagnetic ground state and HAT yields the paramagnetic iridium(II) chloride complex **5**, which may have significant contributions from SOC (Figure 49B).

⁷⁵ Complex **15** is fully characterised but not discussed within the main chapters of this thesis. For characterisation and XRD analysis see chapter VI Section 2.13 and chapter 7 Section A.11.

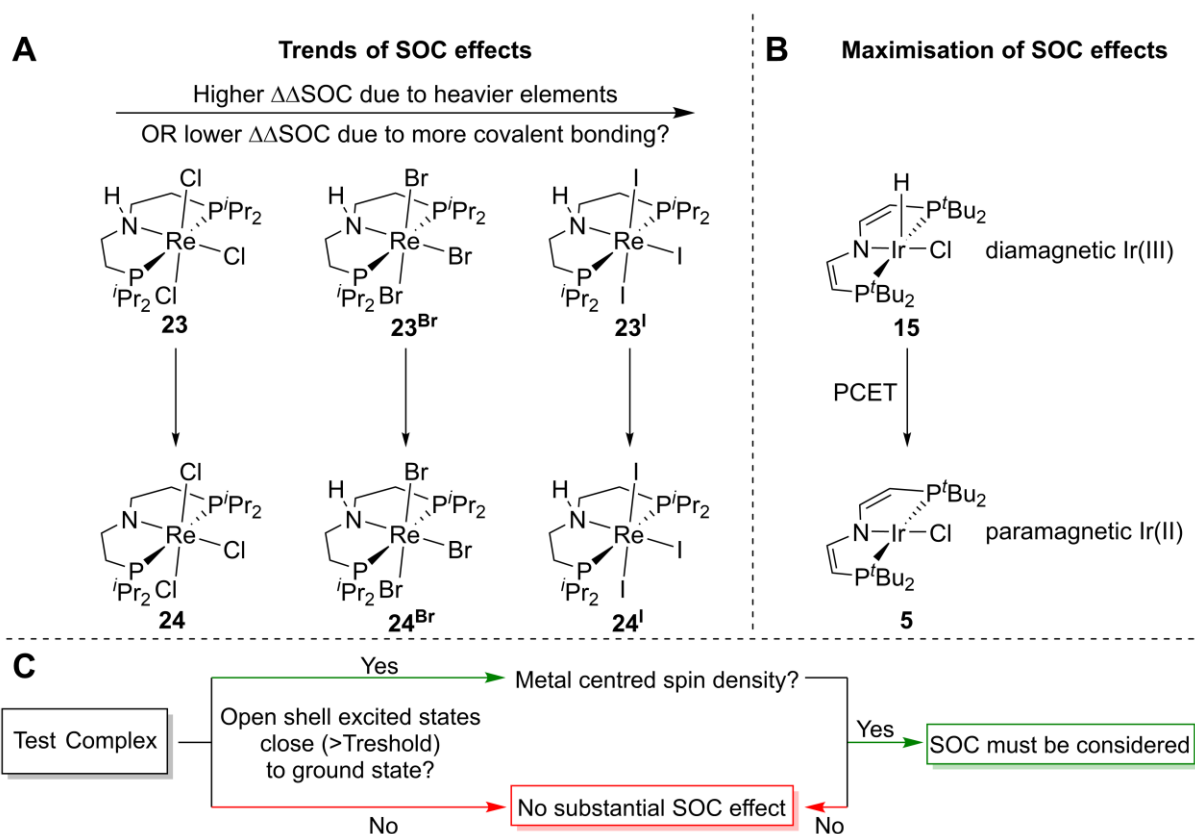


Figure 49: **A)** Trend analysis of the differential thermodynamic SOC effect on a PCET reaction within a halogen complex series (Cl, Br, I). **B)** Maximisation of the SOC effect by interconversion of a closed-shell metal hydride to an open-shell complex. **C)** Basic flow scheme for the theoretical prediction if a SOC effect must be explicitly encountered in a complex system.

This thesis has emphasised the importance of metal centred spin-density and accessible open-shell states for a high SOC effect. Therefore, the development of a theoretical procedure for the prediction, if a SOC effect must be considered computationally in the accurate thermochemical description of a reaction, is feasible. Such a procedure should include the computation of 1) At least the ground state/first excited state gap to test for accessible states for SOC mixing 2) The metal centred spin density. With a decent benchmark set at hand, thresholds could be defined which indicate for an unknown complex system, if SOC must be explicitly treated for its thermochemical description (Figure 49C).

Chapter VI

VI. Experimental Details

1. Materials and Methods

1.1 General remarks

All synthetic procedures were performed under an inert atmosphere of Ar (5.0 Linde gas) unless otherwise noted, using standard *Schlenk* and glovebox techniques. CO₂ is purified by passing through P₄O₁₀, DRIERITE and cooling to -40 °C. H₂ was purified from water impurities by cooling with liquid nitrogen prior to use. All glassware was cleaned by a KOH/*iso*-propanol bath followed by an HCl bath and finished by rinsing with demineralized water. Unless otherwise stated, all glassware was heated to 120 °C prior to use. Reactions in a small scale (~5 mg) were usually performed in J-Young NMR tubes. All solvents were purchased in HPLC quality from MERCK. Benzene, dichloromethane, ether, Pentane, tetrahydrofuran and Toluene, were pre-dried by an MBRAUN SOLVENT PURIFICATION SYSTEM. All solvents except dichloromethane and acetonitrile were dried additionally by stirring over Na/K alloy for several days and subsequent trap-to-trap condensation. Dichloromethane and acetonitrile were additionally dried by stirring over CaH₂ with subsequent trap-to-trap condensation. Deuterated solvents were obtained from EURISO Top GmbH and were purified by the same procedures as their non-deuterated analogues.

List of literature procedures:

The iridium(II) chloride complex **5** was synthesised after Meiners et al.^[160], the iridium(II) amide complex **13** was synthesised after Scheibel et al.^[225], the phenoxy radical Mes*O was synthesised after Manner et al.^[226] The pincer ligands P^HNP(tBu, iPr) were synthesised by our lab technician Kai Sebastian Kopp after Meiners et al.^[227] FcBARF can be obtained by ion exchange between NaBARF₂₄ and FcPF₆ (Dissolve in DCM, remove solvent in vacuo, extract with ether).

List of bought chemicals:

NaOH	Sigma-Aldrich	PhC(H)O	Sigma-Aldrich
AgPF ₆	Sigma-Aldrich	<i>p</i> -F-PhC(H)O	Sigma-Aldrich
FcPF ₆	Sigma-Aldrich	<i>p</i> -Me-PhC(H)O	Sigma-Aldrich (Merck)
Mes*OH	Sigma-Aldrich	<i>p</i> -OMe-PhC(H)O	Sigma-Aldrich
AgSbF ₆	Sigma-Aldrich	PhCO ₂ H	Sigma-Aldrich
H ₂	Linde	<i>p</i> -F-PhCO ₂ H	Sigma-Aldrich
CO	AirLiquid	<i>p</i> -Me-PhCO ₂ H	Sigma-Aldrich
CO ₂	Linde	<i>p</i> -OMe-PhCO ₂ H	Sigma-Aldrich
PMe ₃	Sigma-Aldrich	KO ^t Bu	Sigma-Aldrich
Xanthene	Sigma-Aldrich	Pyridine	VWR
H ₂ ¹⁸ O	Sigma-Aldrich	P ₂ -Phosphazene base	Santa Cruz Biotechnology
Fluorene	Sigma-Aldrich		

1.2 Analytical Methods

1.2.1 Cyclic Voltammetry

Electrochemical data was recorded with a METROHM PGSTAT101 using the NOVA 2.0/2.1 software. The cyclic voltammograms were recorded in a 0.1 M $N^nBu_4PF_6$ solution within a UV/Vis cell equipped with a glassy carbon ($\varnothing=1.6$ mm) working electrode, a Pt wire as counter electrode and an Ag wire as pseudo-reference electrode. The data was finally internally referenced vs. the Fc/Fc^+ couple. The internal resistance was compensated by standard procedures within the NOVA 2.0 software.

To test for reversibility of redox events of freely diffusing-non adsorbed analytes, the scan rate dependence of the peak currents were analysed according to the *Randles-Sevcik* equation.^[228]

$$i_p = 0.446nFAC^0 \sqrt{\frac{nFvD_0}{RT}} \quad \text{Eq. 1.1}$$

With i_p = Peak current, F = Faraday's constant^[229], A = Electrode surface area / cm^2 , C^0 = Bulk concentration of the analyte / $mol\ cm^{-3}$, n = Number of transferred electrons, v = scan rate / $V\ s^{-1}$, D_0 = Diffusion coefficient of the oxidized species / $cm^2\ s^{-1}$.

1.2.2 Elemental Analysis

Elemental analysis data were obtained from the ANALYTICAL LABORATORIES at the Georg-August University Göttingen using an ELEMENTAR VARIO EL 3 analyser.

1.2.3 EPR spectroscopy

X-band EPR spectra were recorded on a Bruker ELRXXSYS E 500 spectrometer with an ER 4131 VT temperature control device for liquid N_2 (MW = 9.42 GHz) and an ER 4112 HV for liquid He (MW =9.39 GHz) cooled measurements. The spectra were simulated by Prof. Bas de Bruin University of Amsterdam.

1.2.4 Head space Analysis

Head space analysis was performed with a SHIMADZU-GC-2014 equipped with a TCD detector and a SHINCARBON ST80/100 Silico column.

1.2.5 Irradiation Experiments

Photolysis experiments were performed using a 150 W Hg(Xe) arc lamp with a lamp housing and arc lamp power supply from LOT QUANTUM DESIGN GmbH. A water bath was used to ensure a constant temperature.

1.2.6 Mass spectrometry

LIFDI mass spectra were measured on a LINDEN CMS and ESI mass spectra on a BRUKER HCT ultra ESI-MS device by the "Zentrale Massenabteilung" at the Georg-August Universität Göttingen.

1.2.7 NMR spectroscopy

All NMR data was recorded on machines from Bruker (AVANCE III 300, AVANCE III 400 and referenced to residual solvent signals (cyclohexane-d₁₂: $\delta^{1H} = 1.38$ ppm,^[230] THF-d₈: $\delta^{1H} = 3.58$ ppm^[230], $\delta^{13C} = 67.6$ ppm^[230]; C₆D₆: $\delta^{1H} = 7.16$ ppm,^[231] $\delta^{13C} = 128.1$ ppm^[231]; toluene-d₈: $\delta^{1H} = 2.08$ ppm^[230], $\delta^{13C} = 20.4$ ppm^[230]; CD₂Cl₂: $\delta^{1H} = 5.32$ ppm^[230], $\delta^{13C} = 54.0$ ppm)^[230]. ³¹P-NMR chemical shifts are reported relative to the shift of Phosphoric acid ($\delta = 0.00$ ppm). For paramagnetic compounds ¹H-NMR pulse sequences with reduced relaxation times were used (¹H-para). Signal multiplicity is denoted as broad (br), singlet (s), doublet (d), triplet(t), virtual triplet (vt) etc. For complex spin systems with higher order coupling effects multiplet (m) is used.

1.2.8 IR spectroscopy

IR spectra of pure compounds were recorded at a BRUKER Alpha FT-IR spectrometer with a Platinum ATR module inside a glovebox. For IR measurements in the magnetic field, the spectra were recorded in a KBR pellet using a commercial Fourier transform spectrometer (VERTEX 80v) coupled to a superconducting coil with magnetic fields up to 11 T. To measure transmittance, the radiation of the globar was delivered from the spectrometer using light-pipe optics to the sample inside the magnet and detected by a silicon composite bolometer (IRLABS) placed below the sample. Sample and bolometer were surrounded by a helium exchange gas and cooled down to 4.2 K. Measurements in NUJOL were carried out with a Thermo Scientific Nicolet iZ10 FT/IR spectrometer at room temperature.

1.2.9 Isothermal Titration Calorimetry

Isothermal Titration Calorimetry was performed in a NANOITC device by TA INSTRUMENTS equipped with a 24 K gold cell and a sample volume of 1 mL operated in overfill mode. Measurement by ITCRun Version 3.4.6.0, TA INSTRUMENTS 2017 and evaluation by the NANOANALYZE software package Version 3.7.5, TA INSTRUMENTS 2015.

1.2.10 SQUID magnetometry

Temperature-dependent magnetic susceptibility measurements were performed with a QUANTUM-DESIGN MPMS-XL-5 SQUID magnetometer equipped with a 5 T magnet. The temperature range was from 2 K to 295 K at a magnetic field of 0.5 T. The powdered sample was contained in a Teflon bucket and fixed in a non-magnetic sample holder. The data is corrected for the diamagnetic contribution of the Teflon bucket by $M_{dia}(\text{bucket}) = Xg \cdot m \cdot H$. with an experimentally determined gram susceptibility of the bucket. Experimental data were modelled with the JulX program^[232] for $S = 0$, $S = \frac{1}{2}$ and $S = 1$. Temperature Independent Paramagnetism (TIP) was modeled by $\chi_{exp} = (1 - PI) \cdot \chi_{sample} + PI \cdot \chi_{PI} + TIP$. For Zeeman and Zero-Field splitting the isotropic spin Hamiltonian $\hat{H} = g\mu_B \vec{B}\vec{S} + D \left(\hat{S}_Z^2 - \frac{1}{3}S(S+1) \right)$ was used.

1.2.11 UV/Vis spectroscopy

UV/Vis spectra were recorded in a cuvette equipped with a J-YOUNG cap at an AGILENT CARY 300 spectrometer using the SCAN software. Background measurements of the blank solvent were performed in an identical constructed cuvette and subtracted.

1.2.12 X-ray-diffractometry

Suitable single crystals for X-ray structure determination were selected from the mother liquor under an inert gas atmosphere and transferred into protective perfluoro polyether oil on a microscope slide. The selected and mounted crystals were transferred to the cold gas stream on the diffractometer. The diffraction data were obtained at 100 K on a Bruker D8 three-circle diffractometer, equipped with a PHOTON 100 CMOS detector and an INCOATEC microfocus source with Quazar mirror optics (Mo-K α radiation, $\lambda = 0.71073 \text{ \AA}$). The data obtained were integrated with SAINT and a semi-empirical absorption correction from equivalents with SADABS was applied. The structure was solved and refined using the Bruker SHELX 2016 software package.^[233–236] All non-hydrogen atoms were refined with anisotropic displacement parameters. All C-H hydrogen atoms were refined isotropically on calculated positions by using a riding model with their U_{iso} values constrained to 1.5 U_{eq} of their pivot atoms for terminal sp^3 carbon atoms and 1.2 times for all other atoms.

1.2.13 Evans Method

Magnetic moments in solution were determined by NMR spectroscopy using the Evans' method as modified by Sur and co-workers and corrected for diamagnetic contribution.^[237,238]

$$X_P = X_0 + \frac{3000\Delta\nu}{4\pi\nu_0cM}$$

2. Synthesis

2.1. Improved synthesis for [(PNP)IrOH] **2**

Degassed water (4 mL) is added to a suspension of **5** (200 mg, 354 μmol , 1.00 eq.) and NaOH powder (424 mg, 10.6 mmol, 30 eq.) in THF (14 mL). The suspension is vigorously stirred at 25 °C for 16 h. The solvent is removed *in vacuo* and the residue extracted with pentane and evaporated *in vacuo*. Washing the residue with cold pentane yields **5** as a blue greenish micro crystalline solid (176 mg, 322 μmol , 91%).

Elemental Analysis: Anal. Calc. for $\text{C}_{20}\text{H}_{41}\text{IrNOP}_2$ (565.72): C, 42.46; H, 7.31; N, 2.48.

Found: C, 42.40; H, 7.52; N, 2.41

NMR (C_6D_6 , 25 °C): ^1H (300 MHz) δ (ppm) = 7.1 (brs, 36H, $(\text{P}^t\text{Bu}_2)_2$), -32 (brs, 2H, $(\text{CH})_2$), -107 (brs, 2H, $(\text{CH})_2$).

LIFDI-MS: Calculated: 566.23. Found: 566.2.

IR-spectroscopy (Nujol): $\nu_{\text{O-H}}$: 3627 cm^{-1}

CV (THF, 25 °C): $E_{1/2}(\text{red}) = -2.11 \text{ V}$; $E_{1/2}(\text{ox}) = -0.37 \text{ V}$

2.2. Synthesis of [Na(thf)(PNP)IrOH]₂ **1**

2 (25.0 mg, 44.2 μmol, 1.00 eq.) is dissolved in THF (5 mL) and sodium amalgam (1.0 M, 900 mg, 44.2 μmol, 1.5 eq.) is added and shaken for 5 min. The amalgam is removed, and the solution is cooled to -40 °C yielding the product as a temperature sensitive orange, crystalline material.

NMR (THF-d₈, 25 °C):

¹H-NMR (300 MHz) δ (ppm) = 6.89 (m, 4 H, 4xCH), 4.02 (m, 4 H, 4xCH), 1.35 (vt, 72 H, (P^tBu₂)₂), -2.06 (m, 2 H, OH).

³¹P-NMR: 57 ppm (broad).

2.3. Improved synthesis of [(PNP)IrOH][PF₆] **3**

AgPF₆ (22 mg, 87.0 μmol, 0.98 eq.) in dichloromethane (2 mL) is slowly added to a stirred solution of **2** (50 mg, 88.4 μmol, 1.0 eq.) in dichloromethane (5 mL) at room temperature. The solution is stirred for additional 2 min and filtered. The crude product precipitates upon addition of pentane. The residue is washed with pentane (2 × 2 mL), extracted with dichloromethane (5 × 0.5 mL) and the product is obtained as dark violet crystals after concentrating the solution and crystallization via gas diffusion layering with pentane (57.8 mg, 81.3 μmol, 92%).

Elemental Analysis:

Anal. Calc. for C₂₀H₄₁F₆IrNOP₃ (710.68): C, 33.80; H, 5.82; N, 1.97.
Found: C, 33.82; H, 6.11; N, 1.95.

NMR (CD₂Cl₂, 25 °C):

¹H{³¹P} (300 MHz) δ (ppm) = 14.60 (s, 1H, OH), 7.15 (d, *J* = 6.4 Hz, 1H, NCH), 5.22 (d, *J* = 6.4 Hz, 1H, PCH), 1.84 (s, 36H, (P^tBu₂)₂).

³¹P{¹H} (121.4 MHz): δ (ppm) = 41.3 (s, P^tBu₂)₂, -145 (hept. ¹J_{PF} = 710.7 Hz, PF₆).

¹³C{¹H} (75.4 MHz): δ (ppm) = 170 (2C, PCH), 147.9 (2C, NCH), 37.3 (4C, PC(CH₃)₃), 32.1 (12C, PC(CH₃)₃).

IR-spectroscopy (Nujol):

ν_{O-H}: 3577 cm⁻¹

2.4. Synthesis of [(PNP)IrO] **4**

Route A: A solution of Mes*O (234 mg, 895 μ mol, 10.1 eq.) in HMDSO (3 mL) is added to a stirred solution of **2** (50.0 mg, 88.3 μ mol, 1.00 eq.) in HMDSO (3 mL) at 25 °C. The solution is filtered and the remaining solid washed with pentane (2 \times 0.5 mL). Extraction with toluene (3 \times 0.5 mL) and crystallization at -40 °C yields the product as purple crystals (14.2 mg, 70.7 μ mol, 80%).

Route B: KO^tBu (1.5 mg, 13 μ mol, 1.0 eq.) is added to a solution of **3** (9.4 mg, 13 μ mol, 1.0 eq.) in THF (1 mL) at room temperature. The solution is stirred for additional 10 minutes and the solvent evaporated. The residue is washed with pentane (3 \times 0.5 mL). Crystallization from toluene at -40 °C yields the product (4.4 mg, 7.8 μ mol, 59 %).

Preparation of the ¹⁸O isotopologue: Sodium (7.5 mg) is added to H₂¹⁸O (250 μ L) at 4 °C and the produced H₂ gas is removed by three freeze-pump-thaw cycles. A THF solution (4 mL) of **5** (50 mg, 85.6 μ mol) is added and vigorously stirred for 5 d. The solvents are removed in vacuo and the residue extracted with pentane. Without further purification a solution of Mes*O (234 mg, 895 μ mol, 10.5 eq.) in pentane (3 mL) is added and the reaction mixture stirred for 5 min. The solution is filtered off and the precipitate washed with pentane (3 \times 0.5 mL). The residue is extracted with toluene (5 \times 0.5 mL), evaporated to dryness and washed with pentane (3 \times 0.5 mL). Removing the solvents in vacuo yielded material suitable for further analysis.

Elemental Analysis: Anal. Calc. for C₂₀H₄₀IrNOP₂ (564.71): C, 42.54; H, 7.14; N, 2.48.
Found: C, 42.94; H, 7.19; N, 2.47.

NMR (C₆D₆, 25 °C): ¹H (400 MHz) δ (ppm) = 20.88 (s, 36H, (P^tBu₂)₂), 61.8 (s, 2H, (CH)₂), -75.2 (s, 2H, (CH)₂).
³¹P{¹H} (162 MHz): no signal from -2000 and +2000 ppm

LIFDI-MS: Calculated: 565.22. Found: 565.2.

IR-ATR: $\nu_{\text{Ir-160}}$: 743 cm⁻¹; $\nu_{\text{Ir-180}}$: 712 cm⁻¹

CV (THF, 25 °C): $E_{1/2}(\text{red}) = -1.95$ V; $E_{1/2}(\text{ox}) = -0.13$ V

SQUID magnetometry: $g = 2.318$, $D = 647$ cm⁻¹, PI = 5.1 %

2.5. Synthesis of [(PNP)IrCO₃] **8**

A solution of **4** (25 mg, 44 μmol, 1.0 eq.) in THF (3 mL) is freeze-pump-thaw degassed and thawed to room temperature under an atmosphere of CO₂. All volatiles are removed *in vacuo* and the residue is washed with pentane (2 x 0.5 mL) and extracted with toluene (3 x 0.5 mL). Crystallization at -40 °C yields **8** as red brown needles (19 mg, 31 μmol, 71%).

Elemental Analysis: Anal. Calc. for C₂₁H₄₀IrNO₃P₂ (608.72): C, 41.44; H, 6.62; N, 2.30.
Found: C, 41.44; H, 6.02; N, 2.30.

NMR (THF-d₈, 25 °C): ¹H (500 MHz) δ (ppm) = 6.40 (m, 2H, 2xCH), 5.46 (m, 2H, 2xCH), 1.48 (m, 36H, 4xC(CH₃)).
³¹P{¹H} (202 MHz): δ (ppm) = 46.2 (s, P^tBu₂)₂.
¹³C{¹H} (75.4 MHz): δ (ppm) = 173.35 (s, CO₃), 170 (m, 2C, 2xCH), 105 (m, 2C, 2xCH), 36.1 (m, 4C, 4xC(CH₃)), 29.7 (m, 12C, 4xC(CH₃)).

LIFDI-MS: Calculated: 551.23. Found 551.2.

IR- spectroscopy (ATR): 1663 cm⁻¹, 1625 cm⁻¹, 1553 cm⁻¹

2.6. Synthesis of [(PNP)IrPMe₃] **10**

PMe₃ (1.8 μ L, 18 μ mol, 2.0 eq.) is added to a solution of **4** (5.0 mg, 8.9 μ mol, 1.0 eq.) in cyclohexane-*d*₁₂ (0.4 mL). The solution is stirred for 2d. Quantitative precipitation of OPMe₃ is revealed by filtration. **10**, can be isolated by removal of the solvent *in vacuo* and crystallization from HMDSO -40 °C as a yellow crystalline solid, which was characterized by NMR spectroscopy. Any attempts to achieve elemental analysis data from the crystalline material failed, which is attributed to thermal instability.

NMR (Cyclohexane-*d*₁₂, 25 °C):

¹H-NMR (300 MHz) δ (ppm) = 7.00 (m, 2 H, 2xCH), 4.19 (m, 2 H, 2xCH), 1.82 (d, J_{HP} = 7.4 Hz), 9 H, P(CH₃)₃, 1.31 (m, 36 H, 4xC(CH₃)).
³¹P-NMR (121 MHz) δ (ppm) = 61.7 (d, 2 P, $^2J_{PP}$ = 16.9 Hz, 2xP^tBu₂), -52.6 (t, 1 P, $^2J_{PP}$ = 16.9 Hz, PMe₃).
¹³C-NMR (100.6 MHz) δ (ppm) = 162 (m, 2 C, 2xCH), 86.5 (m, 2 C, 2xCH), 36.7 (m, 4 C, 4xC(CH₃)₃), 31.2 (m, 12 C, 4xC(CH₃)₃), 29.4 (m, 3 C, P(CH₃)₃).

LIFDI-MS:

Calculated: 625.27. Found 625.3

2.7. Reactivity of **4** towards H₂

A degassed solution of **4** (5.0 mg, 8.9 μmol) in C₆D₆ (0.4 mL) is set under an atmosphere of H₂ (1 bar) and shaken vigorously. Monitoring of the reaction by ¹H-NMR (400 MHz) gives formation of [(PNP)Ir(H)₂] **6**^[37] and water after 5 min and full conversion to **6** and water after 30 min.

2.8. Reactivity of **4** towards CO

A solution of **4** (5.0 mg, 8.9 μmol) in C₆D₆ (0.4 mL) is degassed and stirred under CO (1 bar) for 5 min resulting in near quantitative formation of [(PNP)IrCO] **7** by NMR spectroscopy.^[179] Gas-chromatographic headspace analysis confirms the release of CO₂.

2.9. Synthesis of [(PNP)IrO(C₁₂H₈O)] “Xanthenolate” **11**

To a solution of **4** (25 mg, 44 μmol, 2.0 eq.) in THF (10 mL) a solution of xanthene (4.0 mg, 22 μmol, 1.0 eq.) in THF (10 mL) was added. The solution was heated to 60 °C for 24 h and the solvent was removed in vacuo. The residue is solved in pentane and purified with column chromatography over silianized silica. Removal of the solvent in vacuo yields the product as blue-green crystals contaminated with xanthene-dimer.

2.10. Synthesis of [(PNP)IrO(C₁₃H₉)] “Fluorenoate” **12**

To a solution of **4** (15 mg, 27 μmol, 2.0 eq.) in THF (10 mL) a solution of fluorene (2.2 mg, 13 μmol, 1.0 eq.) in THF (10 mL) was added. The solution was heated to 60 °C for 24 h and the solvent was removed in vacuo. The residue is solved in pentane and purified with column chromatography over silianized silica. Removal of the solvent in vacuo yields the product as blue-green crystals contaminated with fluorene-dimer.

LIFDI-MS: Caluclated: 746.3; Found: 746.2

2.11. Reactivity of **4** towards benzaldehydes (X^{para} = H, Me, OMe, F)

To a solution of **4**: (5.0 mg, 8.9 μmol, 1.0 eq.) in benzene-d₆ (0.5 mL) the corresponding benzaldehyde was added in 10-fold excess. For the irradiation NMR tubes with borosilicat were used. After irradiating for 30 min without a filter the ¹H-para spectra were recorded.

2.12. General synthesis of [(PNP)IrO₂CPh-X] **14-X** with X^{para} = F, OMe, Me, H)

To a solution of **13** (25.0 mg, 44.3 μmol, 1.00 eq.) in pentane a solution of the corresponding benzaldehyde (1.00 eq.) in THF is added. The solution is stirred for 5 min and the solvents removed in vacuo. The residue is taken up in few pentane and the solution is crystalized at -40 °C yielding turquoise crystals.

14-H:

Elemental Analysis: Anal. Calc. for C₂₁H₄₀IrNO₃P₂ (670.26): C, 48.42; H, 6.77; N, 2.09.
Found: C, 48.38; H, 6.49; N, 2.11.

NMR (THF-d₈, 25 °C): **¹H-para** (300 MHz) δ (ppm) = 13.31 (brs, 36H, 4xC(CH)₃), 4.90 (brs, 1H, p-Ar-CH), 2.83 (brs, 2H), -4.92 (brs, 2H), -5.52 (brs, 2H), -125 (vbrs, 2H).

LIFDI-MS: Calculated: 670.3. Found 670.2.

14-OMe:

Elemental Analysis: Anal. Calc. for C₂₁H₄₀IrNO₃P₂ (700.27): C, 47.56; H, 6.84; N, 2.04.
Found: C, 48.05; H, 6.77; N, 2.00.

NMR (THF-d₈, 25 °C): **¹H-para** (300 MHz) δ (ppm) = 13.43 (brs, 36H, 4xC(CH)₃), 2.29 (brs, 2H), 1.98 (brs, 3H, O-CH₃), -5.37 (brs, 2H), -7.14 (brs, 2H), -135 (vbrs, 2H).

LIFDI-MS: Calculated: 700.27. Found 700.3.

14-Me:*Elemental Analysis:*Anal. Calc. for C₂₁H₄₀IrNO₃P₂ (684.27): C, 49.18; H, 6.93; N, 2.04.

Found: C, 48.69; H, 6.50; N, 1.92.

*NMR (THF-d₈, 25 °C):***¹H-para** (300 MHz) δ (ppm) = 13.43 (brs, 36H, 4xC(CH)₃), 2.58 (brs, 2H), 0.26 (brs, 3H, *p*-CH₃), -5.26 (brs, 2H), -6.62 (brs, 2H), -128 (vbrs, 2H).*LIFDI-MS:*

Calculated: 684.3. Found 684.3.

14-F:*Elemental Analysis:*Anal. Calc. for C₂₁H₄₀IrNO₃P₂ (688.25): C, 47.15; H, 6.45; N, 2.04.

Found: C, 46.74; H, 6.08; N, 2.01.

*NMR (THF-d₈, 25 °C):***¹H-para** (300 MHz) δ (ppm) = 13.30 (brs, 36H, 4xC(CH)₃), 2.62 (brs, 2H), -5.05 overlaid (2xbrs, 2x2H), -134 (vbrs, 2H).*LIFDI-MS:*

Calculated: 688.2. Found 688.2.

2.13. Synthesis of [(PNP)Ir(H)(Cl)] **15**

To a solution of **5** (33.0 mg, 56.5 μmol , 1.00 eq.) in pentane (20 mL) *n*-BuLi (1.6 M (hexane), 50 μL , 80 μmol , 1.4 eq.) is added under stirring. When the green colour of **5** has vanished to a pale yellow benzoic acid (15.0 mg, 123 μmol , 2.17 eq.) in THF (1 mL) is added under stirring. The solvents are removed in vacuo and the solution is extracted with pentane (3x1 mL). Concentration of the solution in vacuo and crystallization at $-40\text{ }^\circ\text{C}$ yields the product as deep pink crystals (25.3 mg, 43.2 μmol , 77%).

Elemental Analysis:

Anal. Calc. for $\text{C}_{20}\text{H}_{41}\text{IrNP}_2$ (585.17): C, 41.05; H, 7.06; N, 2.39.

Found: C, 40.98; H, 7.02; N, 2.31.

NMR (THF- d_6 , 25 $^\circ\text{C}$):

$^1\text{H-NMR}$ (300 MHz) δ (ppm) = 1.31 (m, 36H, $4\times\text{C}(\text{CH}_3)_3$), 4.35 (m, 2H), 2xCH), 7.05 (m, 2H, 2xCH), -47.3 (t, 1 H, $^2J_{\text{P-H}} = 11.5\text{ Hz}$, Ir-H).

$^{31}\text{P}\{^1\text{H}\}\text{-NMR}$ (121 MHz) δ (ppm) = 62.8 ppm.

LIFDI-MS:

Calculated: 585.2. Found: 585.2.

2.14. Synthesis of [(ⁱPrP^HNP)ReCl₃][BarF₂₄] **25**

To a solution of **23** (21.8 mg, 41.8 μmol, 1.00 eq.) in DCM (5 mL) a solution of Fc[BarF₂₄](36.9 mg, 40.3 μmol, 0.96 eq.) (5 mL) is added under stirring and the reaction is stirred for 5 min. The solvent is removed, and the residue washed with pentane (5x2 mL) and extracted with ether until the ether phase remained colourless. Removal of the solvent yields the product as a red solid (43.2 mg, 33.4 μmol, 81 %). Crystals suitable for XRD analysis can be obtained by crystallisation at -40°C from ether.

Elemental Analysis: Anal. Calc. for C₂₀H₄₀IrNOP₂ (564.71): C, 39.46; H, 3.38; N, 0.96.
Found: C, 40.02; H, 3.33; N, 0.93.

NMR (THF-d₈, 25 °C): ¹H-para (400 MHz) δ (ppm) = 32.0 (s, 6H, 2x(PC(H)(CH₃))), 30.4 (s, 6H, 2x(PC(H)(CH₃))), 29.9 (s, 6H, 2x(PC(H)(CH₃))), 27.8 (s, 6H, 2x(PC(H)(CH₃))), 14.2 (s, 2H), 4.9 (s, 2H), -8.2 (s, 2H), -79.8 (s, 2H), -103.4 (s, 2H).

IR-ATR: ν_{N-H} = 3095 cm⁻¹

Evans method: μ_{eff} = 2.9 μ_B

2.15. Deprotonation of [(ⁱPrP^HNP)ReCl₃][BarF₂₄] **25**

¹H(para)- NMR is measured after the addition of pyridine (0.5 μL mg, 6 μmol, 0.6 eq.) to a solution of **25** (13.6 mg, 9.31 μmol, 1.00 eq.) in THF-d₈ (0.5 mL) leads to clean conversion to **24**.

2.16. N-H/D exchange of **23**

Experiment performed by Dr. F. Wätjen. **23** (6.0 mg, 10.0 μmol, 1.0 eq) is suspended in a 4:1 DCM/D₂O mixture (0.5 mL) and stirred overnight. Afterwards the solvent is removed *in vacuo* and the spectroscopically clean product [(P^DNP)ReCl₃] (**23-d**) is measured in CD₂Cl₂. The NMR spectra show largely identical signals to those of **1**. The signal corresponding to the NH proton is almost gone (~ 2 % remaining) and the signals at δ_{1H} = -5.10 and -10.44 ppm exhibit different coupling patterns.

NMR (CD₂Cl₂, 25 °C): ²H-NMR (46.1 MHz) δ (ppm) = 152.6 (s, ND).

ATR-IR: ν_{N-D} = 2362.9 (ν_{ND}) and 3506.4 (br, electronic absorption)

2.17. Reevaluation of the **23/25** redox potential

Cyclic voltammetry performed by Dr. F. Wätjen. The spectrum is now measured vs. acetylferrocene ($E^{\text{ox}}(\text{THF}) = 0.24 \text{ V}$, unpublished data Richt van Alten).

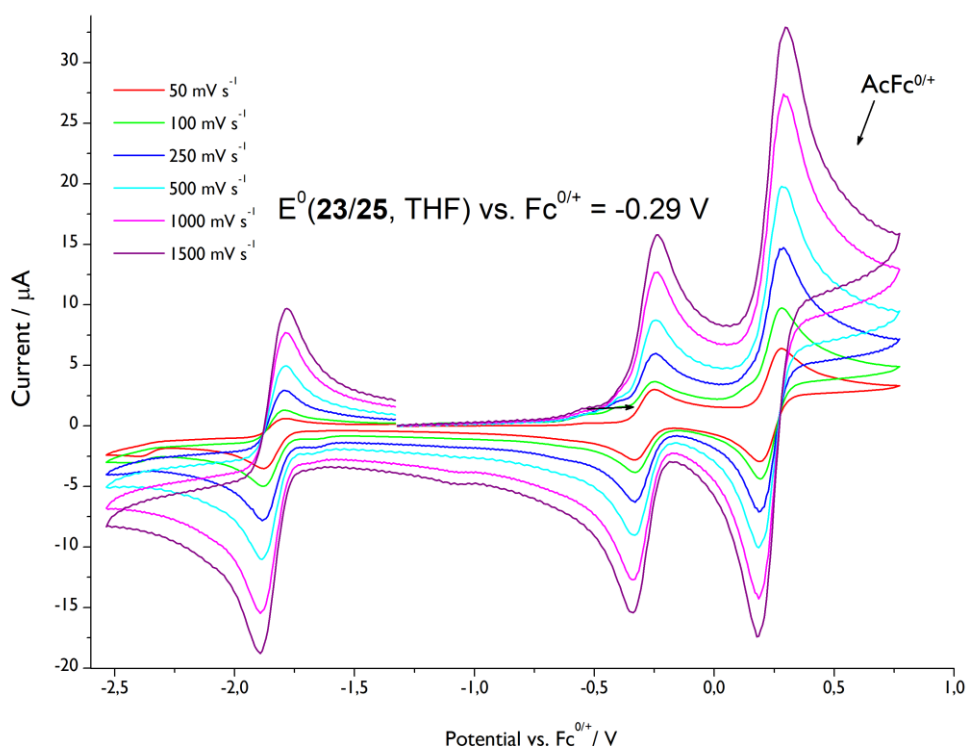


Figure 50: Cyclic voltammogram of **23** in THF with AcFc^{0/+} present.

3. Isothermal Titration Calorimetry

3.1 BD(F)E determination of **4**

Measurement Conditions

The O-H bond dissociation (free) energy BD(F)E of **2** is determined by reaction with the Mes*O ($BDE_{O-H}(\text{Mes}^*\text{OH}) = 354 \text{ kJmol}^{-1}$) as a titrant with the experimental conditions shown in Table 3.

Table 3: ITC measurement conditions for the BD(F)E determination of **2**.

Concentration and volume of 2	2.0 mM/950 μL
Concentration and volume of Mes*O	15.3 mM/250 μL
Injection Steps/Injected Volume	50@ 5 μL
Waiting time between two additions	300 s
Stirring rate	350 rpm
Equilibration Time before experiment start	1229 s

Titration

A representative thermogram, integrated titration curve and measurement of the heat of dissolution of Mes*-O in THF are shown below. For each integrated titration step a constant value of 7.9 μJ is subtracted from the heat of reaction to correct for the heat of dissolution. The first titration data point is generally neglected due to a dilution effect within pre-experiment equilibration. The plot of the integrated heat curve is fitted with an independent model in analogy to Brandt's et al. but adjusted for a PCET process (see C, appendix).^[224]

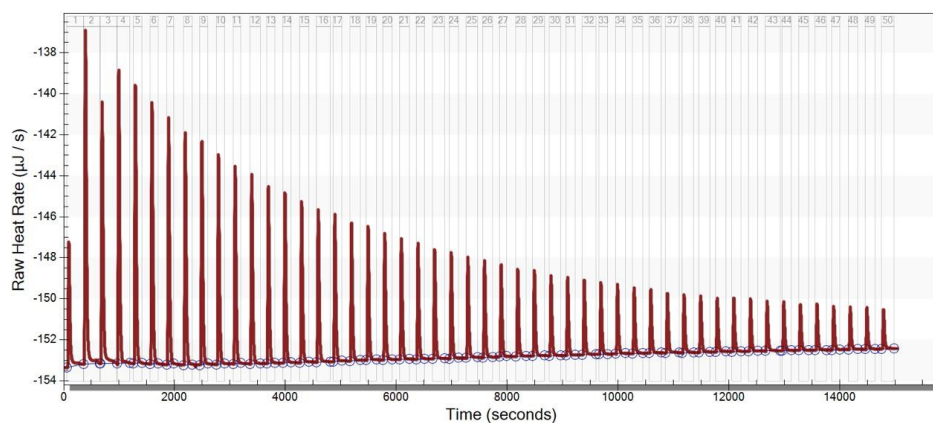


Figure 51: Heat vs. time thermogram of the titration of **2** vs. Mes*O in THF at 25 °C.

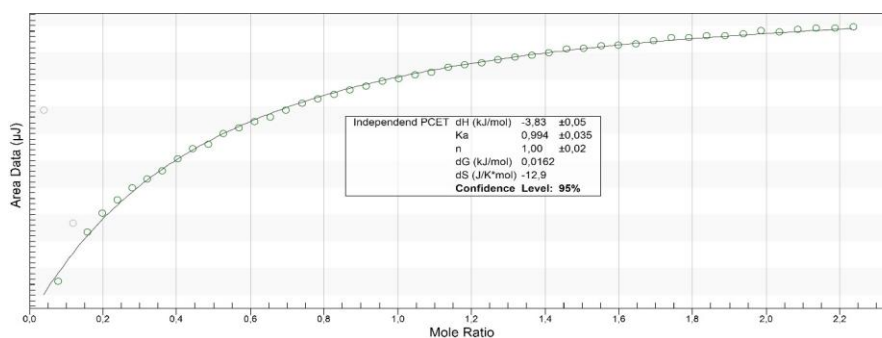


Figure 52: Integrated heat curve of the titration of **2** vs. Mes*O in THF at 25 °C. Shaded points were not included in the fitting process.

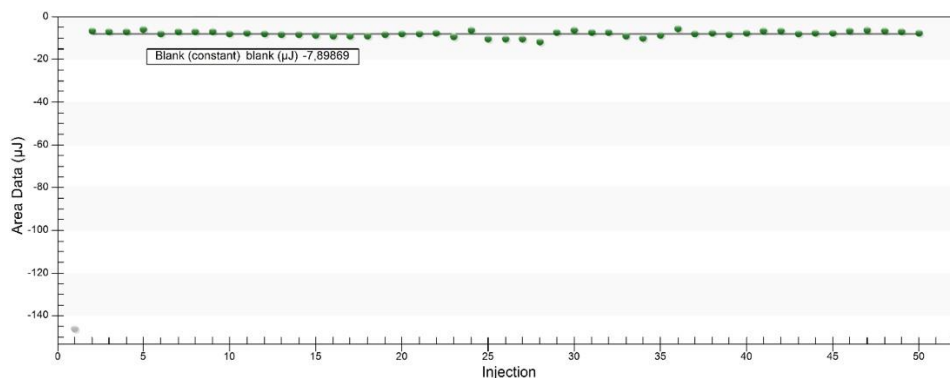


Figure 53: Heat of dissolution of Mes*-O in THF at 25 °C.

Results	
ΔH_r	$-3.8 \pm 0.1 \frac{\text{kJ}}{\text{mol}}$
K	0.994 ± 0.035

3.2 BDE determination of **23**

3.2.1 Enthalpy determination of the PCET reaction in THF

Measurement conditions

The heat of reaction of the **23/24** complex couple in THF was determined by titration with the Mes*-O. The experimental conditions were the following (Table 4).

Table 4: ITC measurement conditions

	First Run/Second Run	Third Run
Concentration and volume of 23 [mM / μL]	1.69/950	1.69/950
Concentration and volume of Mes*-O [mM / μL]	13.3/250	12.9/250
Injection Steps/Injected Volume [μL]	25@10	25@10
Waiting time between two additions [s]	200*	200*
Stirring rate [rpm]	350	350
Equilibration time before start of experiment[s]	1200/1200	1174

* The waiting time for injection 13 was raised to 600 s to encounter slower kinetics around the equivalence point

Titration

The following figures show the thermograms and integrated titration curves of $(\text{P}^{\text{H}}\text{NP})\text{ReCl}_3$ **23** vs. Mes*-O in THF at 298 K. Greyed out points are not taken into account in the fitting process. The first point is generally neglected due to the dilution effect within the pre-experiment equilibration time. An Independent PCET model determined the heat of reaction and the stoichiometry.

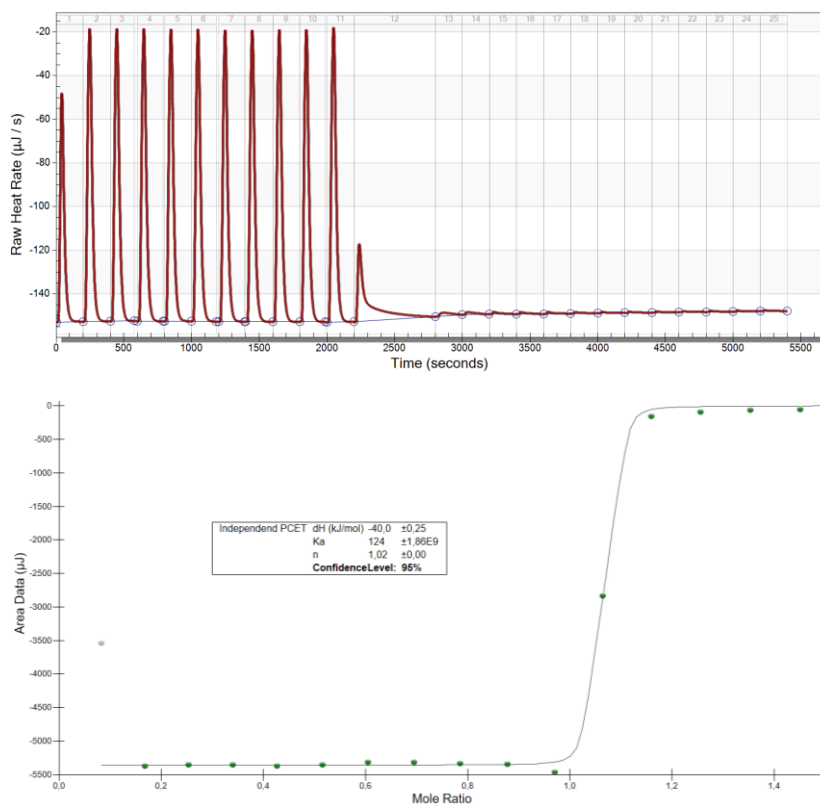


Figure 54: Thermogram (top) and integrated heat curve (bottom) of the first titration of **23** vs. Mes*-O at 298 K, THF.

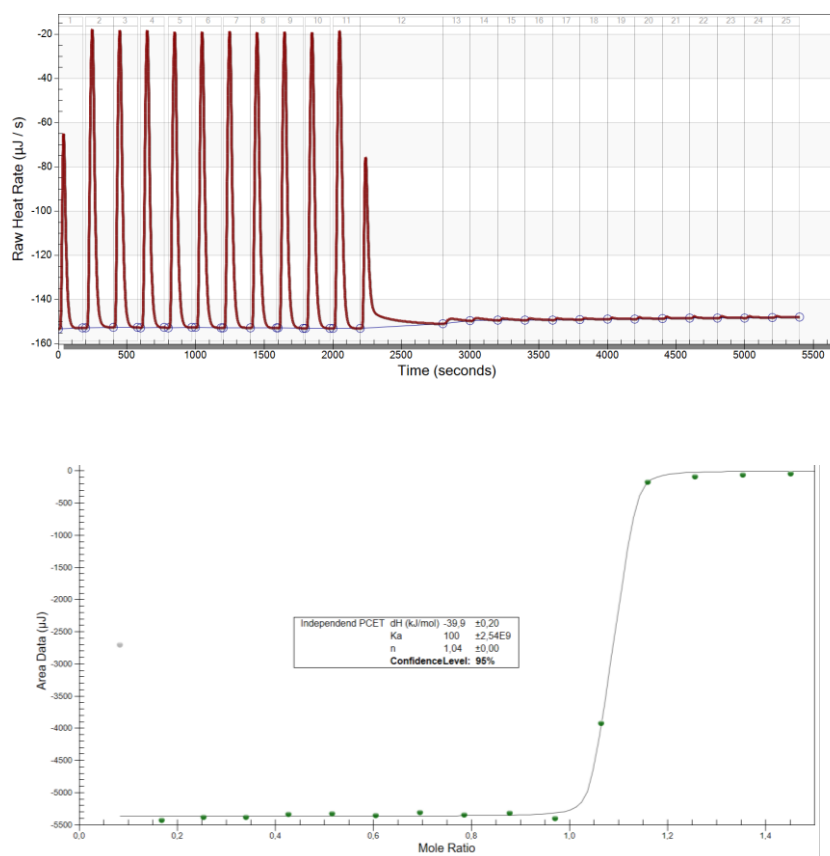


Figure 55: Thermogram (top) and integrated heat curve (bottom) of the second titration of **23** vs. Mes*-O at 298 K, THF.

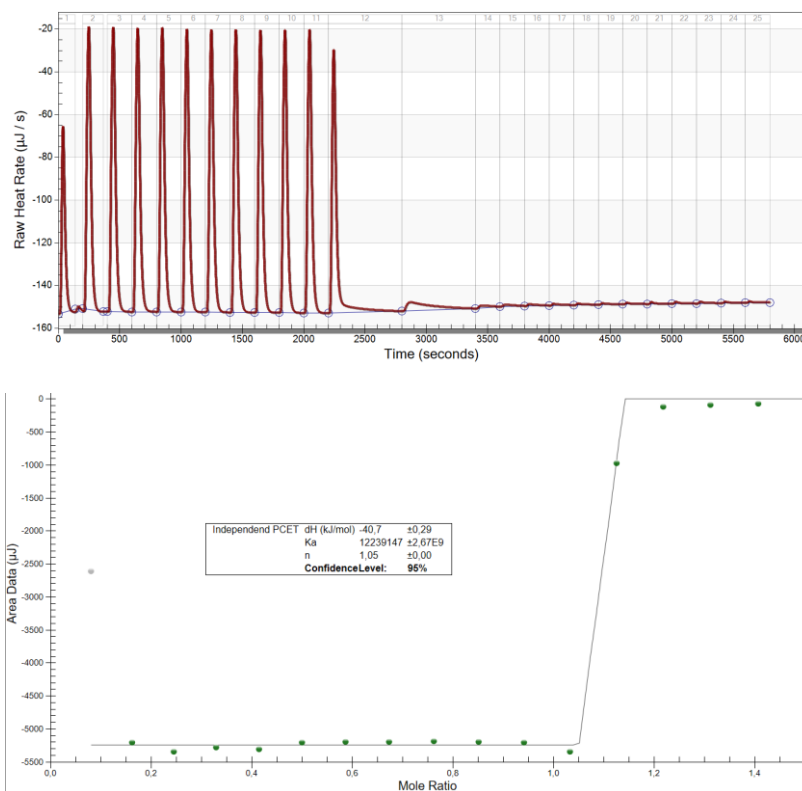


Figure 56: Thermogram (top) and integrated heat curve (bottom) of the third titration of **23** vs. Mes*-O at 298 K, THF.

Evaluation and error discussion

Table 5: Summarized Results of the reaction enthalpy determination in THF.

$\Delta H_r / \text{kJ mol}^{-1}$	Error at 95 % confidence	n value	Corrected Error
-40.0	± 0.25	1.02	± 0.26
-39.9	± 0.20	1.04	± 0.21
-40.7	± 0.29	1.05	± 0.30

The weighted average enthalpy of the reaction sums up to:

$$\Delta H^{298\text{ K}}(\text{THF}) = -40.1 \pm 0.2 \text{ kJ mol}^{-1}$$

3.2.2 Enthalpy determination of the PCET reaction in DCM

Measurement Conditions

The heat of reaction of the **23/24** complex couple in DCM was determined by titration with the (Mes^{*}-O). The experimental conditions were the following (Table 6).

Table 6: ITC measurement details

	First Run/Second Run	Third Run
Concentration and volume of 23 [mM / μ L]	0.836/950	1.69/950
Concentration and volume of Mes [*] -O [mM / μ L]	6.54/250	12.9/250
Injection Steps/Injected Volume [μ L]	14/16@10	16@10
Waiting time between two additions [s]	200 ^[a]	200*
Stirring rate [rpm]	350	350
Equilibration time before start of experiment[s]	1200	1200

[a] Following the decelerating kinetics around the equilibrium point the injection time was raised from injection 8 on by 50 s each up to 400 s at injection 11, injection 12: 250 s. [b] same as [a] but injection 12: 400s, injection 13 250 s.

Titration

The following figures show the thermograms and integrated titration curves of **23** vs. Mes^{*}-O in DCM at 298 K. Greyed out points are not considered in the fitting process. The first point is generally neglected due to the dilution effect within the pre-experiment equilibration time. An Independent PCET model determined the heat of reaction and the stoichiometry.

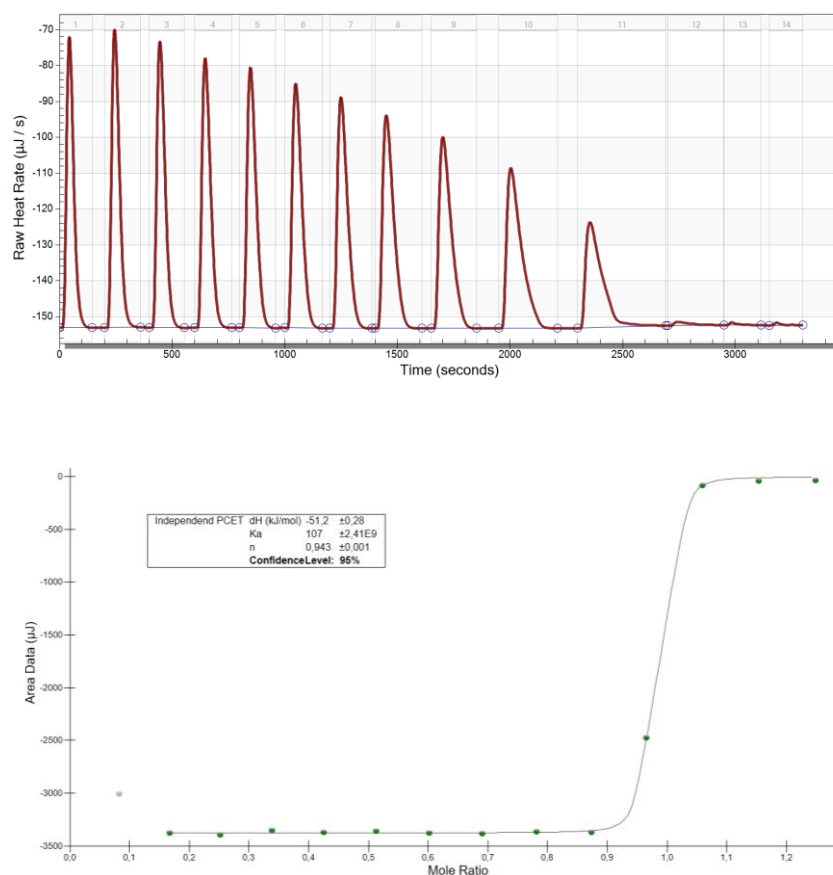


Figure 57: Thermogram (top) and integrated heat curve(bottom) of the first titration of **23** vs. Mes^{*}-O at 298 K, DCM.

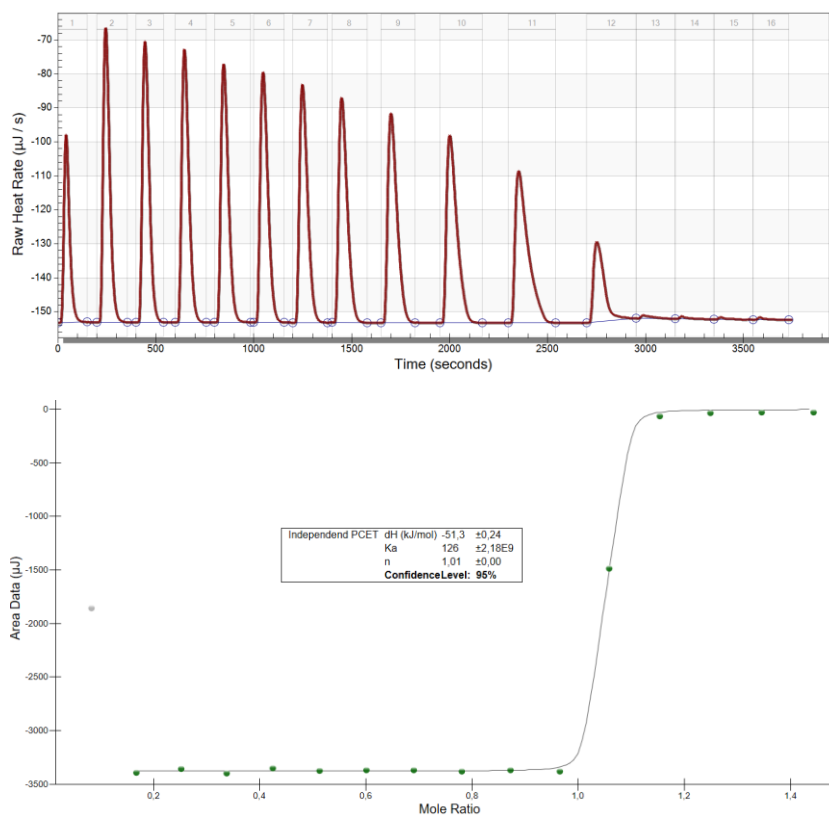


Figure 58: Thermogram (top) and integrated heat curve(bottom) of the second titration of **23** vs. Mes*-O at 298 K, DCM.

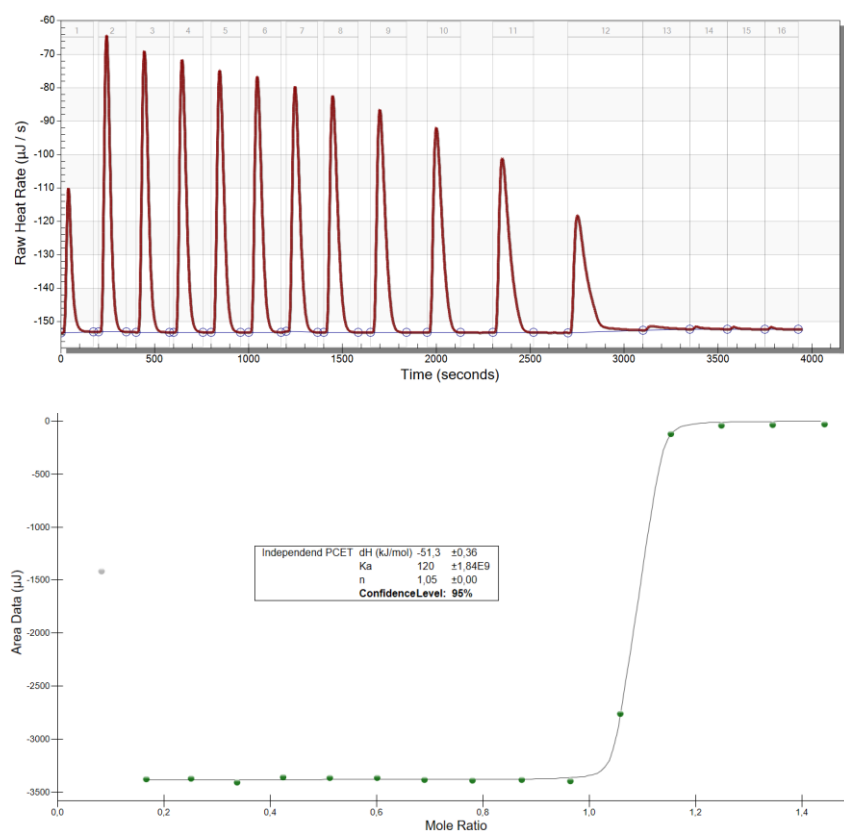


Figure 59: Thermogram (top) and integrated heat curve(bottom) of the third titration of **23** vs. Mes*-O at 298 K, DCM.

Evaluation and error discussion

The extremely large error on the equilibrium constant within the fitting process indicates, that the data is only sufficient for ΔH determination. Table 7 summarizes the results of the three independent runs.

Table 7: Summarized results of the reaction enthalpy determination in DCM

$\Delta H_r / \text{kJ mol}^{-1}$	Error at 95 % confidence	n value	Corrected Error
-51.2	± 0.28	0.943	± 0.30
-51.3	± 0.24	1.01	± 0.24
-51.3	± 0.36	1.05	± 0.38

The weighted average enthalpy of the reaction sums up to:

$$\Delta H^{298 \text{ K}}(\text{DCM}) = -51.2 \pm 0.3 \text{ kJ mol}^{-1}$$

Thermodynamic Summary

Table 8: Summarized results on the reaction enthalpy in THF and DCM.

Solvent	THF	DCM
$\Delta H / \text{kJ mol}^{-1}$	-40.1 ± 0.2	-51.2 ± 0.3

3.3 pK_A value determination of **25**

Measurement Conditions

The pK_A value of **25** was determined by titration with pyridine as a base ($pK_A^{\text{THF}} = 5.5$).^[222] The experimental conditions were the following (Table 6).

Table 9: ITC measurement details

	First Run	Second Run
Concentration and volume of 25 [mM / μL]	1.4/950	1.44/950
Concentration and volume of pyridine [mM / μL]	12.4/250	12.4/250
Injection Steps/Injected Volume [μL]	47@5	33@5
Waiting time between two additions [s]	300	300
Stirring rate [rpm]	350	350
Equilibration time before start of experiment[s]	2040	1305

Titration

The following figures show the thermograms and integrated titration curves of **25** vs. pyridine in THF at 298 K. Greyed out points are not considered in the fitting process. The first point is generally neglected due to the dilution effect within the pre-experiment equilibration time. An Independent PCET model was fitted to the obtained data. 10 μL per injection are subtracted to correct for the heat of dissolution.

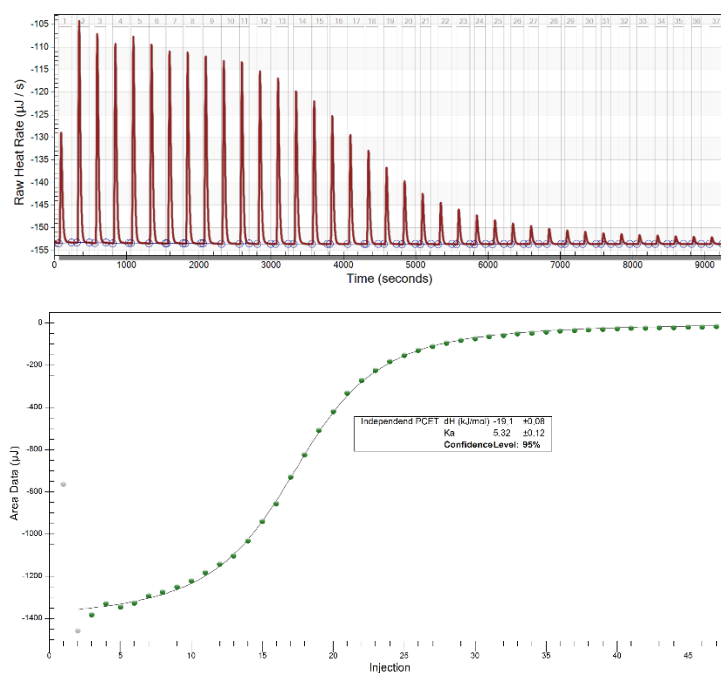


Figure 60: Thermogram (top) and integrated heat curve (bottom) of the first titration of **25** vs. pyridine at 298 K, THF.

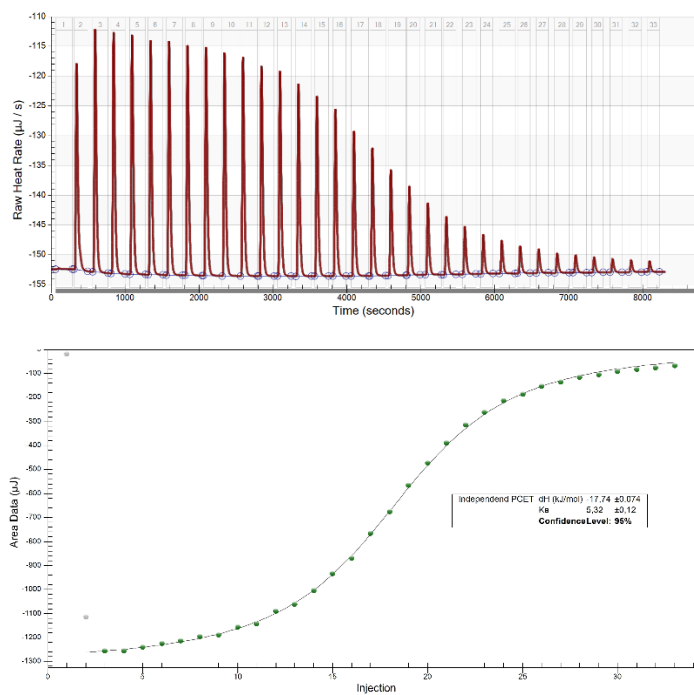


Figure 61: Thermogram (top) and integrated heat curve(bottom) of the second titration of **25** vs. pyridine at 298 K, THF.

Evaluation and error discussion

Table 10: Results of the pK_A titration of **25** with pyridine.

Run	K	95 % Confidence Error
1	5.32	0.12
2	5.32	0.12
Mean equilibrium constant	5.32 ± 0.12	

The titration curves have s-shaped character and are sufficient for the derivation of the equilibrium resulting in a value of $K = 5.3 \pm 0.1$. Therefore, together with the Fuoss correction (see Section 3 of Chapter II) the acidity of **25** is calculated to $pK_A(\mathbf{25}) = 5.3$.

3.4 pK_A value determination of Mes*OH

Measurement Conditions

The pK_A value of Mes*OH was determined by titration with P₂-Et as a base ($pK_A^{\text{THF}} = 25.3$).^[222] The experimental conditions were the following (Table 6).

Table 11: ITC measurement details

	First Run	Second and third Run
Concentration and volume of Mes*OH [mM / μL]	1.57/950	12.6/950
Concentration and volume of P ₂ -Et mM / μL]	12.5/250	93.1/250
Injection Steps/Injected Volume [μL]	25@10	125@2
Waiting time between two additions [s]	250	300
Stirring rate [rpm]	350	350
Equilibration time before start of experiment[s]	1200	827/1800

Titration

The following figures show the thermograms and integrated titration curves of Mes*OH vs. P₂-Et in THF at 298 K. Greyed out points are not considered in the fitting process. The first point(s) is generally neglected due to the dilution effect within the pre-experiment equilibration time. An Independent model was fitted to the obtained data. 10 μL and 20 μL per injection were subtracted to correct for the heat of dissolution for the diluted and concentrated titrations, respectively.

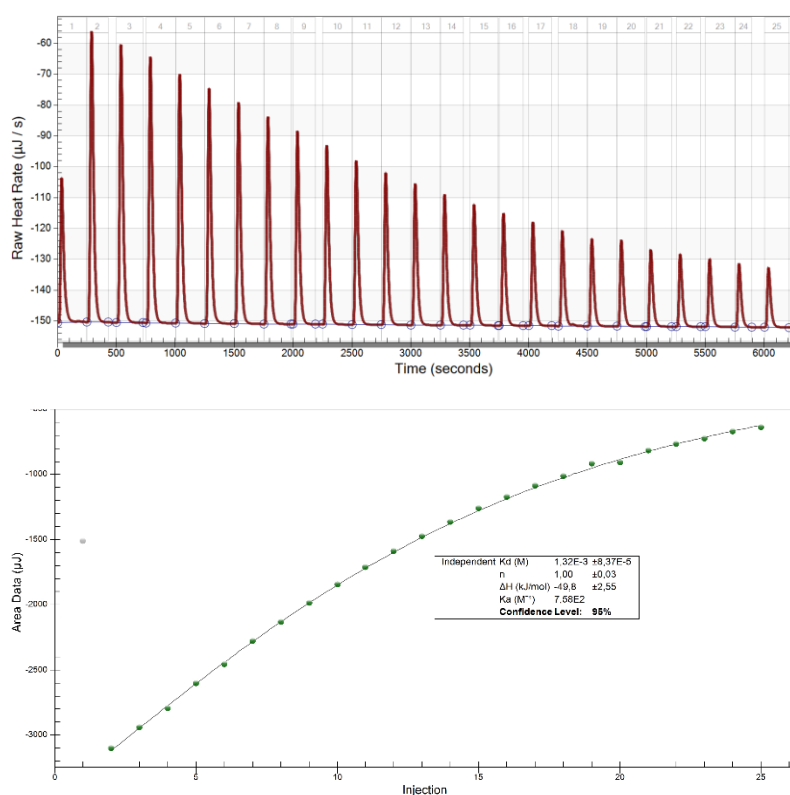


Figure 62: Thermogram (top) and integrated heat curve (bottom) of the first (diluted) titration of Mes*OH vs. P₂-Et at 298 K, THF.

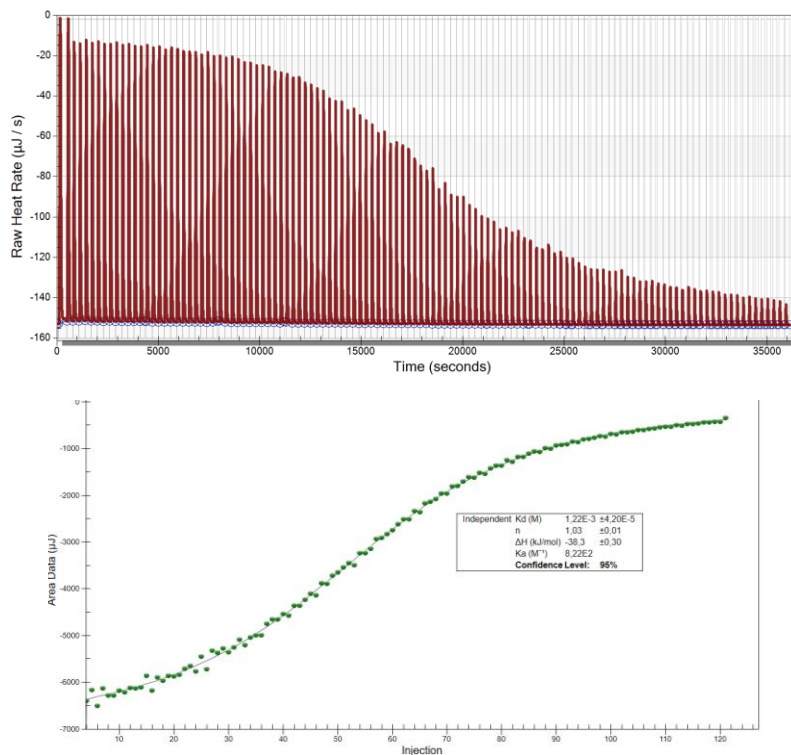


Figure 63: Thermogram (top) and integrated heat curve(bottom) of the second titration of Mes*OH vs. P₂-Et at 298 K, THF.

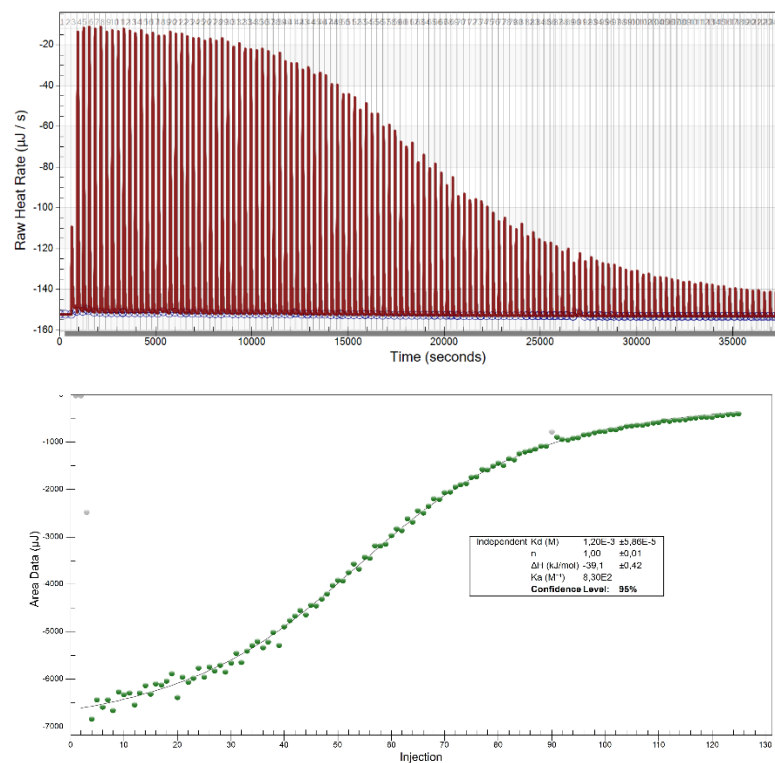


Figure 64: Thermogram (top) and integrated heat curve(bottom) of the third titration of Mes*OH vs. P₂-Et at 298 K, THF.

Evaluation and error discussion

Due to the concentration dependence of the titration curve shape, an independent model for an association reaction had to be used in the fitting process. The results of the first titration are included in the final results but weighted only half, due to the lower amount of data points.

Table 12: Results table for the titration of Mes*OH with P₂-Et base in THF at 298 K.

$K_D / \text{mol L}^{-1}$	Error at 95 % confidence	n value	Corrected Error
$1.32 \cdot 10^{-3}$	$\pm 0.08 \cdot 10^{-3}$	1.00	$\pm 0.08 \cdot 10^{-3}$
$1.22 \cdot 10^{-3}$	$\pm 0.04 \cdot 10^{-3}$	1.03	$\pm 0.04 \cdot 10^{-3}$
$1.20 \cdot 10^{-3}$	$\pm 0.06 \cdot 10^{-3}$	1.00	$\pm 0.06 \cdot 10^{-3}$

The weighted average enthalpy of the reaction sums up to $K_D = 1.24 \pm 0.06 \cdot 10^{-3} \text{ M}^{-1}$, which gives a weighted averaged association constant as $K_A = 806 \pm 39 \text{ M}$. Since this fit already includes the ion-pairing interaction, the pK_A value is directly obtained by $pK_A(\text{Mes}^*\text{OH}) = 25.3 - \log(806 \pm 39) = 22.4 \pm 0$.

3.5 P-H BDE value determination of **17**

Measurement Conditions

The BDE of **17** was determined by isothermal titration calorimetry by titration with Mes*O (BDE(O–H)Mes*OH: a) $\text{C}_6\text{H}_6 = 81.6 \text{ kcal mol}^{-1}$; THF = $84.5 \text{ kcal mol}^{-1}$)^[53,184] was used as titrant. Titrations were carried out at 10 °C to suppress the decay of **17** and corrected vs. the addition of Mes*O to the solvent in the sample cell (18 μL p. addition). Further experimental conditions are summarized in Table 13 and Table 14.

Table 13: Experimental details of the BDE determination of **17** in benzene.

Concentration and volume of 17 / mM and μL	1.02/950
Concentration and volume of Mes*O / mM and μL	9.18 mM/250 μL
Injection Steps/Injected Volume / μL	33@7.5
Waiting time between two additions / s	350-650
Stirring rate /rpm	350
Equilibration time before experiment start / s	1514

*The peaks for the BDE determination had a waiting time of 350 s.

Table 14: Experimental details of the BDE determination of **17** in THF.

Concentration and volume of 17 / mM and μL	1.4/950
Concentration and volume of Mes*O / mM and μL	11.7 mM/250 μL
Injection Steps/Injected Volume / μL	49@5
Waiting time between two additions / s	300
Stirring rate /rpm	350
Equilibration time before experiment start / s	1671

Titration

The first injection(s) of each titration were generally neglected due to diffusion of reactant solution into the cell during the equilibration of the instrument. Around the addition of one equivalent of Mes*O, the peaks show increased tailing, which is tentatively attributed to follow-up reactivity of **17**. The P–H BDE was therefore determined at an early titration stage from the average of the heat of injections 3–6 for benzene and 2–5 for THF, respectively, while reliable data BDFE determination was not available. A representative titration is shown in Figure 65 for benzene and in Figure 66 for THF, respectively. The integrated results are summarized in Table 15 and Table 16.

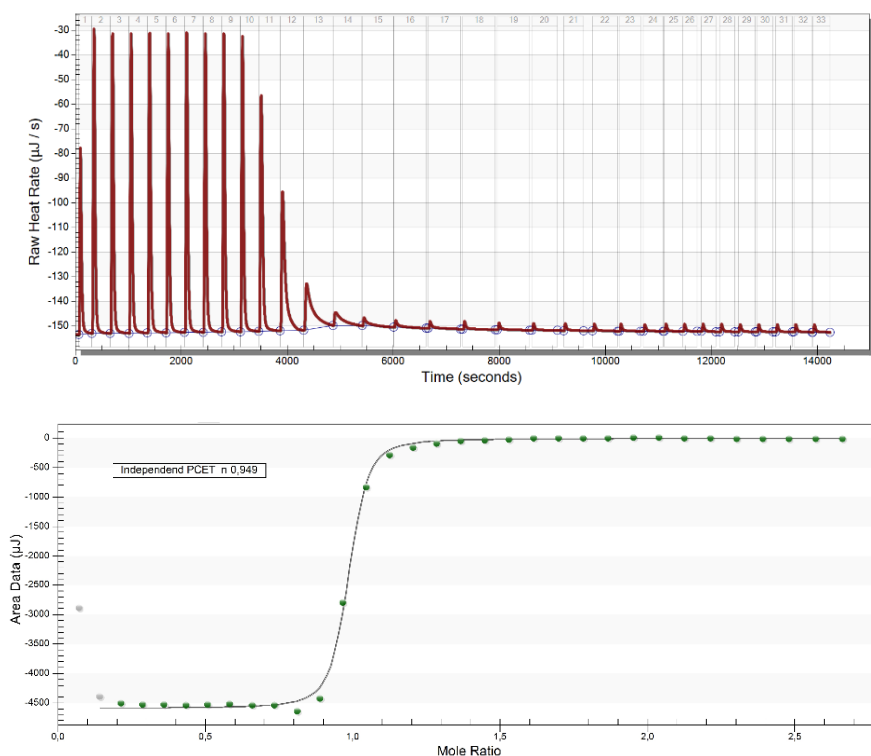
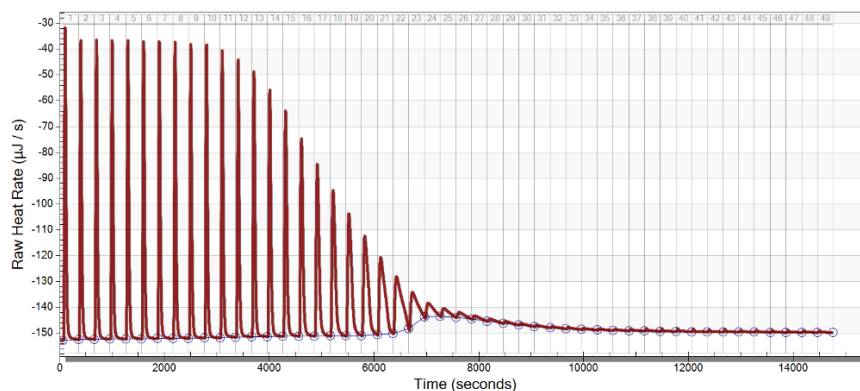


Figure 65: Thermogram of the titration of **17** with Mes*O at 283 K in benzene (top) and integrated titration curve of the titration (bottom).



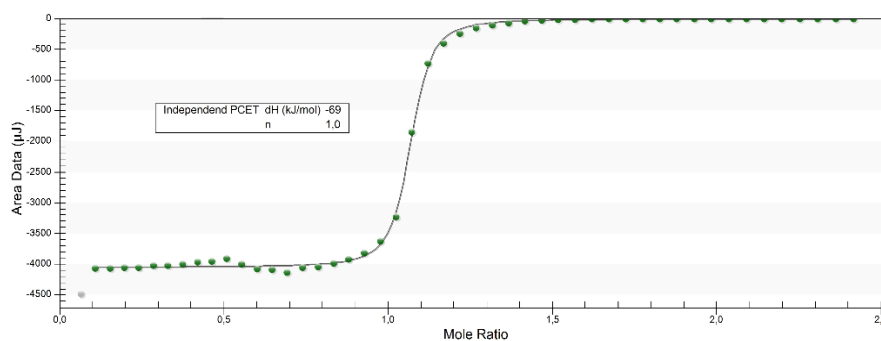


Figure 66: Thermogram of the titration of **17** with Mes*O at 283 K in THF (top) and integrated titration curve of the titration (bottom).

Results and Error Discussion

Table 15: ITC results of the BDE determination of **17** in benzene.

Injection	Heat of injection of the 1 st run / μJ	Heat of injection of the 2 nd run / μJ	Added moles per injection / nmol
3	-4682	-4678	68.2
4	-4708	-4678	68.2
5	-4703	-4709	68.2
6	-4716	-4711	68.2
Mean	-4702 ± 20	-4694 ± 17	
Weighted Mean		-4697 ± 13	
Reaction Enthalpy / kJ mol^{-1}		$-68.9 \pm 3.6^*$	
P-H BDE(C₆H₆) kcal mol^{-1}		$65.1 \pm 0.9^*$	

*A cumulative error of 5% for stock solution preparation and weighting errors was estimated from the fitted n-value (0.95) and multiplied with the weighted mean error.

Table 16: ITC results of the BDE determination of **17** in THF.

Injection	Heat of injection of the 1 st run / μJ	Added moles per injection / nmol
2	-4069	56.9
3	-4066	56.9
4	-4050	56.9
5	-4049	56.9
Mean	-4059 ± 10	
Reaction Enthalpy / kJ mol^{-1}		-71
P-H BDE(THF) kcal mol^{-1}		67.5 ± 1

3.6 Mean BDE determination of $[(\text{PNP})\text{Re}(\text{Cl})(\text{NH}_2)]$ **20**

Measurement Conditions

The mean N-H BDE of the **20/22** couple is determined by titration with Mes*O ($\text{BDE}_{\text{O-H}}(\text{Mes}^*\text{OH}) = 354 \text{ kJ mol}^{-1}$) with the experimental conditions shown below.

Table 17: Measurement details of the mean N-H BDE determination of **20**.

	First Run	Second/Third Run
Concentration and volume of 20 [mM/ μL]	0.341/950	0.341/950
Concentration and volume of Mes*O [mM/ μL]	5.28/250	5.05/180
Injection Steps/Injected Volume [μL]	33@7.5	24@7.5
Waiting time between two additions [s]	250	250
Stirring rate [rpm]	350	350
Equilibration time before start of experiment [s]	1885	1453 and 1525

Titration

The following figures show the thermograms and integrated titration curves of **20** with Mes*-O in THF. Greyed out points are not considered in the fitting process. The first point is generally neglected due to the dilution effect within the pre-experiment equilibration time. The mean heat value was determined for the titration steps before the equivalence point. The stoichiometry was determined by an Independent PCET model. (see C).

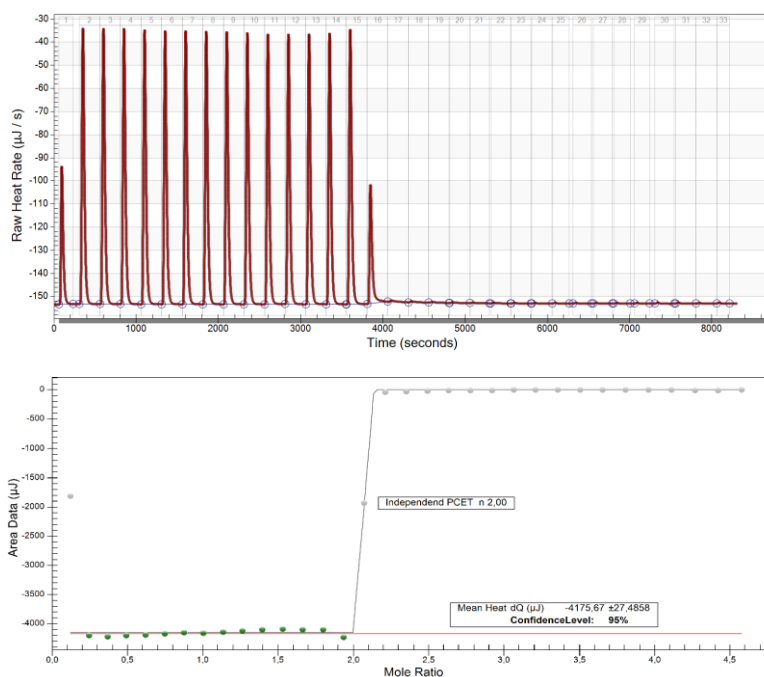


Figure 67: Thermogram of the first titration of **20** vs. Mes*O (4 eq.) 33@7.5 μL , 250 s waiting time in THF@298 K (top) and integrated heat curve of the first titration of **20** vs. Mes*O (4 eq.) 33@7.5 μL , 250 s waiting time in THF@298 K (bottom).

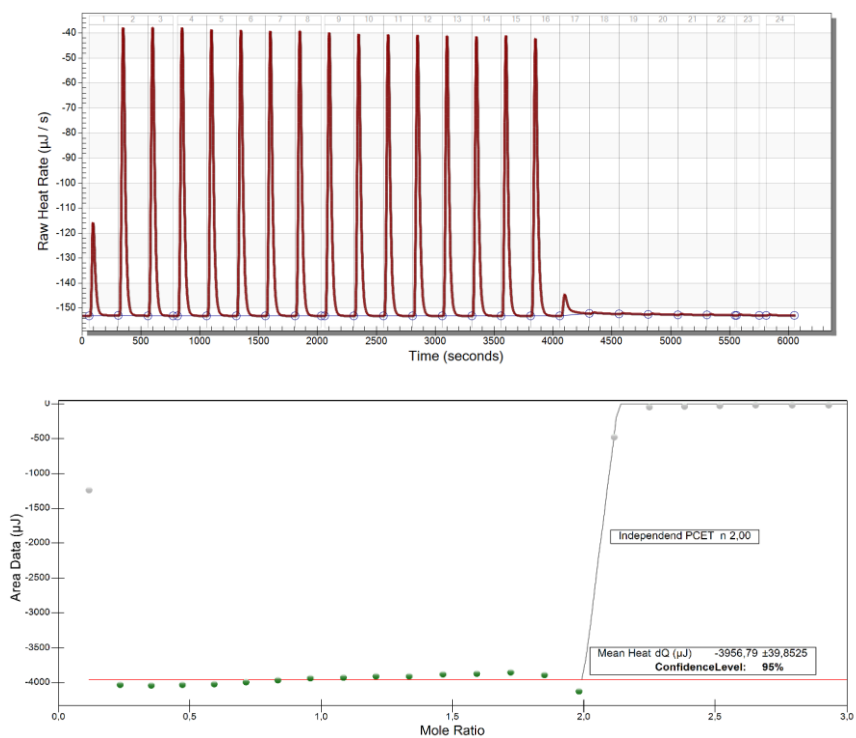


Figure 68: Thermogram of the second titration of **20** vs. Mes*O (4 eq.) 33@7.5 µL, 250 s waiting time in THF@298 K (top) and integrated heat curve of the second titration of **20** vs. Mes*O (4 eq.) 33@7.5 µL, 250 s waiting time in THF@298 K. (bottom).

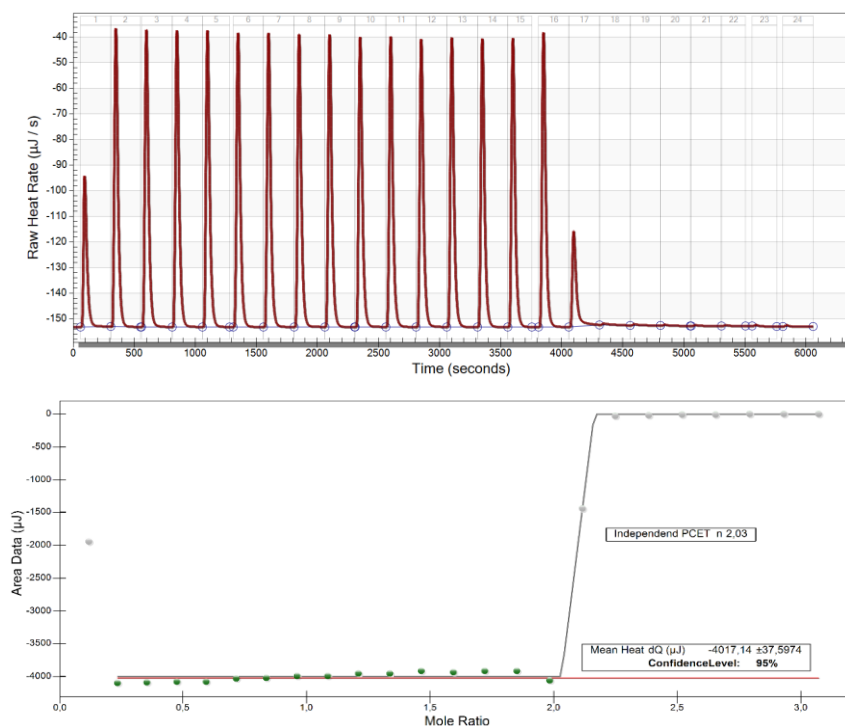


Figure 69: Thermogram of the third titration of **20** vs. Mes*O (4 eq.) 33@7.5 µL, 250 s waiting time in THF@298 K (top) and integrated heat curve of the third titration of **20** vs. Mes*O (4 eq.) 33@7.5 µL, 250 s waiting time in THF@298 K (bottom).

Results and Error Discussion

Results		
Mean Heat [μJ]	Consumed moles per injection [nmol]	Enthalpy [kJ/mol]
-4176 ± 27	19.62	-213 ± 1
-3957 ± 40	18.76	-211 ± 2
$-4017 \pm 39^*$	18.76	-214 ± 2
Weighted mean enthalpy = $-213 \pm 2 \frac{\text{kJ}}{\text{mol}}$		

*The error for the third measurement is raised to scale for the deviation from the ideal n value of n=2.00.

The enthalpy for the double PCET reaction is $-50.9 \text{ kcal mol}^{-1}$. The mean Re-N(H)-H BDE is calculated to:

$$\text{BDE}_{[\text{Re}]\text{N}(\text{H})-\text{H}}^{\text{THF}} = \text{BDE}_{\text{Mes}^*\text{O}-\text{H}}^{\text{THF}} - \frac{\Delta H}{2}$$

$$\text{BDE}_{[\text{Re}]\text{N}(\text{H})-\text{H}}^{\text{THF}} = \left(84.6 - \frac{50.9}{2} \right) \frac{\text{kcal}}{\text{mol}} = 59.2 \pm 0.2 \frac{\text{kcal}}{\text{mol}}$$

4. Computational Details

4.1. General Remarks

All computations were performed on the Goethe CRC computation cluster in Frankfurt am Main. Optimizations of molecular geometries and analyses of the Hessian matrices were carried out with the Gaussian program^[239] under gas-phase conditions utilizing the dispersion-corrected^[240] B3LYP(V)-D3 functional^[241] (iridium complexes and related structures) and the PBE0-D3 functional^[242] (rhenium complexes and related structures) the def2TZVP^[118] orbital basis set including the quasi-relativistic 60-electron pseudopotentials (ECP60MWB) for iridium and rhenium^[243] Thermal contributions to enthalpies were obtained from these results for 298.15 K and 1 atm. The effect of solvents was estimated via an implicit polarized continuum solvent model (SMD,^[244] solvent: tetrahydrofuran, dichloromethane) by computation of the single-point energy difference between gas-phase and solvent-based total energies. Improved relative energies were computed in single-point calculations on the full molecular systems with the Orca program^[245,246] using the domain-based local-pair natural orbital coupled-cluster approximation^[95] employing tight accuracy settings (TightPNO, without full LMP2 guess also in the closed-shell calculations to ensure identical results for the RHF and UHF limits in Orca DLPNO/TightPNO computations) with single and double excitations and perturbative triples. For iridium the correlation-consistent triple- and quadruple-zeta valence basis sets^[119,120,247] which include the relativistic pseudopotential (ECP60MDF) on Ir^[145] were used in conjunction with the corresponding correlation fitting basis sets^[248] and extrapolated to the complete basis set (CBS) limit, DLPNO-CCSD(T)/CBS(T,Q), as implemented in Orca, i.e. $E_{\text{ref}}(\text{CBS}) = E_{\text{ref}}(\text{Q}) + (E_{\text{ref}}(\text{Q}) - E_{\text{ref}}(\text{T}) / \exp(\alpha (\sqrt{4} - \sqrt{3})) - 1)$; $E_{\text{corr}}(\text{CBS}) = 3\beta E_{\text{corr}}(\text{T}) - 4\beta E_{\text{corr}}(\text{Q})$ $3\beta - 4\beta$, where $\alpha = 5.46$ and $\beta = 3.05$. For the rhenium computations the correlation-consistent triple- and quadruple-zeta valence basis sets^[119,120,247] which include the relativistic pseudopotential (ECP60MDF) on Re^[145] were used in conjunction with the corresponding correlation fitting basis sets^[248] and extrapolated to the complete basis set (CBS) limit. Additionally the Ahlrich basis sets def2-(T,Q)ZVPP were used with the normal T0 triples as well as with the improved T1 triples^[94] and extrapolated to the CBS limit DLPNO-CCSD(T0/T1)/CBS(T,Q), as implemented in Orca, i.e. $E_{\text{ref}}(\text{CBS}) = E_{\text{ref}}(\text{Q}) + (E_{\text{ref}}(\text{Q}) - E_{\text{ref}}(\text{T}) / \exp(\alpha (\sqrt{4} - \sqrt{3})) - 1)$; $E_{\text{corr}}(\text{CBS}) = 3\beta E_{\text{corr}}(\text{T}) - 4\beta E_{\text{corr}}(\text{Q})$ $3\beta - 4\beta$, where $\alpha = 5.46$ and $\beta = 3.05$ for cc-pVnZ and $\alpha = 7.88$ and $\beta = 2.97$ for the def2 basis set., respectively. Further, a composite ONIOM-like^[97,98] approach was employed to combine the DFT results of the full molecular systems with the highly accurate explicitly correlated F12B ansatz^[249] for truncated model systems, in which all ^tBu/^{Pr} groups in each molecular system were either replaced by methyl groups (Me-truncated) or by hydrogen atoms (H-truncated). The CCSD(T*)-F12b^[250] variant was chosen as implemented in Molpro,^[251] where the perturbative triples contributions, denoted (T*), are improved towards the complete basis set limit via F12-scaling^[37] according to the scale factor $E_{\text{corr}}(\text{MP2-F12})/E_{\text{corr}}(\text{MP2})$. The one particle space was described with the valence double- and triple-zeta orbital basis sets (OBS) cc-pV{D,T}Z-F12 for the non-metal atoms and aug-cc-pV{D,T}Z-PP^[145] for iridium and rhenium, in conjunction with the corresponding triple-zeta auxiliary fit basis sets^[252-255] (also with the double-zeta OBSs), i.e., the JKfit sets for the Fock and exchange integrals, the MP2fit sets for density fitting and the OptRI/JKfit sets for construction of the complementary auxiliary basis set (OptRI for non-metal atoms, JKfit for iridium). Me- or H-truncated model systems were treated at the high F12 level, and effects of the replaced ^tBu groups were included by lower level

DFT calculations, ONIOM(F12b:DFT). To ensure a closest possible structural match to the fully optimized geometry of the real system, in the ONIOM approach the truncated model systems were constructed in constrained geometries at the DFT level. Thus, only the C–H or P–H bond lengths of the newly added hydrogen atoms (which replace the corresponding methyl or ^tBu/ⁱPr fragments of the ^tBu/ⁱPr groups) were allowed to relax, i.e., all angles and dihedrals are kept fixed and all remaining coordinates are unaltered.

Spin–orbit eigenstates were calculated at the DFT ground state geometries within the ORCA program^[245,246] from state-averaged CASSCF/NEVPT2^[110–112] calculations followed by a quasi-degenerate perturbation theory treatment via a full spin–orbit mean field (SOMF) operator.^[155] CASSCF wavefunctions were optimized employing the ZORA approximation^[256] along with the ZORA-def2TZVP basis sets,^[143] which include the segmented all-electron relativistically contracted SARC-ZORA-TZVPP basis set for iridium and rhenium. The RIJK algorithm for fitting of the Coulomb and exchange integrals was used in conjunction with the def2/JK auxiliary basis sets.^[257] The active space of **4** comprises the five Ir-based 5d orbitals, the p- σ and the two p- π orbitals of oxygen, and two occupied pincer-ligand based orbitals, giving rise to a CAS(16,10) expansion; the active space of **2** includes the bonding p- σ (O)–H and additionally the antibonding p- σ^* (O)–H orbitals, thus leading to a CAS(17,11) expansion. For the oxo-species, the CASSCF orbitals were optimized by the average of 5 quintet, 45 triplet and 50 singlet roots arising from the formal d⁶ configuration of the iridium(III) centre. The formal d⁷ iridium(II) hydroxo species gives rise to an average of 10 quartet and 40 doublet roots accordingly. Magnetic data were obtained by setting the ORCA keywords “MagneticField” and “dosusceptibility” to true. For the rhenium complexes two different active spaces were probed. For the small active space only the 5d orbitals of the complexes were analysed leading to a CAS(3x5) expansion for the amido complex and to a CAS(4x5) expansion for the amine complex. For both CAS expansions, the CASSCF orbitals for the amine species were optimized by the average of 5 quintet, 45 triplet and 50 singlet roots arising from the formal d⁴ configuration of the rhenium(III) centre. The formal d³ rhenium(IV) amido species gives rise to an average of 10 quartet and 40 doublet roots respectively. The big active space in the rhenium amido complex comprises the five Re-based 5d orbitals, three p-orbitals of the axial chlorine, two occupied pincer-ligand/equatorial chlorines orbitals, and a filled Re-N π -based orbital, giving rise to a CAS(15,11) expansion; the amine-species is comprised of the same orbital set, but without filled Re-N π -based orbital, thus leading to a CAS(14,10) expansion. The final energies are obtained from NEVPT2 calculations, and the energies that enter the infinite-order SOC QDPT treatment via the SOMF operator are thus corrected to second order.

4.2. A Terminal Iridium Oxo with a Triplet Ground State

4.2.1. Molecular Geometries

Figure 70 shows selected parameters of the optimized geometries for the full molecular systems. The C_s symmetric iridium-oxo **4** exhibits a square-planar environment in the open-shell $^3A''$ ground state and a slightly distorted structure in the less favourable closed-shell $^1A'$ state. The iridium-hydroxo **2** features a doublet electronic configuration in a square-planar environment. Compared to the triplet oxo species, the Ir–O bond length increases by 0.18 Å in the hydroxo complex and the Ir–N contact shortens by 0.08 Å; the O–H bond lies within the square-plane of the complex. Both, the 2,4,6-tri-tert-butyl-phenol (Mes^*OH) and the corresponding phenoxy-radical (Mes^*O) also exhibit C_s symmetry, concomitant with a difference in C–O bond lengths of 0.12 Å. The xyz. data of all structures can be found in the appendix Section D.

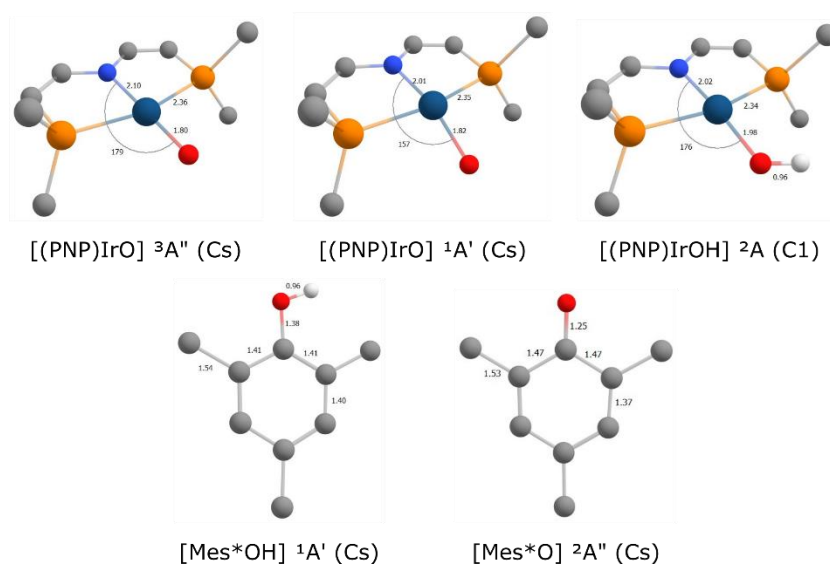


Figure 70: DFT-optimized molecular geometries (B3LYP(V)-D3/def2TZVP) for the triplet ground-state and the first singlet isomer of oxo species (PNP)IrO, and for the doublet ground-state of hydroxo-species (PNP)IrOH (top), as well as for the 2,4,6-tri-tert-butylphenol/phenoxy (Mes^*OH/Mes^*O) couple (bottom). All tBu groups and carbon-bonded hydrogen atoms are omitted for clarity.

4.2.1. Spin State and Reaction Energetics

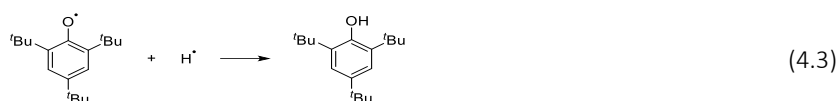
The relative spin-state and reaction energies were computed with DFT and coupled cluster methods. The results are collected in Table 24. The triplet-singlet gap $\Delta E(T/S)$ of **4** complex is computed following reaction 4.1.



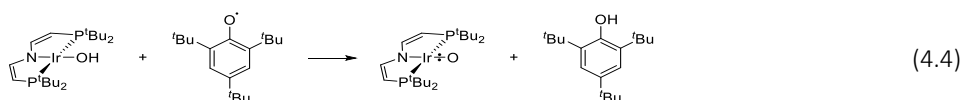
The half reaction energetics of the **4/2** couple was computed for reaction 4.2.



The half reaction energetics of the Mes*OH/Mes*O couple was computed for reaction 4.3.



The half reaction energetics of the PCET reaction was computed for reaction 4.4.



All computational approaches predict a triplet ground state for **4**. The hybrid functional places the singlet electromer at $\Delta E(T/S) = 74 \text{ kJ mol}^{-1}$ above the triplet, while coupled cluster expansions converge at a value of 40–41 kJ mol^{-1} . Reaction (4.2) is strongly endothermic with to $\Delta_r H_{\text{soliv}}^{\text{SOC}}(4.2) = 325 \text{ kJ mol}^{-1}$ at the DFT level and 352 kJ mol^{-1} at the DLPNO-CCSD(T) level, while at the explicitly correlated coupled cluster ONIOM(F12:DFT) level it converges to 342 kJ mol^{-1} . The enthalpy for reaction (3) amounts to -311 kJ mol^{-1} at the DFT level and -338 kJ mol^{-1} at the DLPNO-CCSD(T) level, and it reaches -331 to -334 kJ mol^{-1} at the ONIOM(F12:DFT) approach, thus introducing a slightly larger uncertainty than the (PNP)IrO–H bond formation reaction (2). In summary, the PCET reaction (4) is computed endothermic with a reaction enthalpy of 14 kJ mol^{-1} at the DFT and at the DLPNO-CCSD(T) levels of theory, and between 12 and 9 kJ mol^{-1} ONIOM(F12b:DFT) approach.

4.2.2. Total Energies

Table 18: Total energies E_{tot} in Hartree for the full (^tBu) complexes **4** and **2** as well as the Mes*OH/Mes*O couple, and the corresponding Me- and H- truncated model systems, computed at the B3LYP(V)-D3/def2TZVP level of theory.

Species	State	B3LYP(V)-D3/def2TZVP				
		^t Bu			Me	H
		E_{tot}	ΔE_{tot}	ΔH_{solv}	E_{tot}	E_{tot}
H	² S	-0.498763	0.000416	0.002360		
4	³ A''	-1703.034516	-0.020352	0.602065	-1231.404966	-1074.147082
4	¹ A'	-1703.006333	-0.023075	0.601908	-1231.375861	-1074.118083
2	² A	-1703.665929	-0.019095	0.613674	-1232.037457	-1074.782449
Mes*OH	¹ A'	-779.033070	-0.012793	0.464384	-425.325965	-307.412571
Mes*O	² A''	-778.405765	-0.012633	0.451440	-424.694213	-306.770251

Table 19: Total energies E_{tot} in Hartree for the Me- and H-truncated model systems of the oxo/hydroxo complexes iroxo and **2** as well as of the Mes*OH/Mes*O couple with CCSD(T*)-F12/VnZ (n =D,T).

Species	State	CCSD(T*)-F12 @Me		CCSD(T*)-F12 @H	
		VDZ	VTZ	VDZ	VTZ
H	2S	-0.499811	-0.499946	-0.499811	-0.499946
4	³ A''	-1229.759513	-1229.842592	-1072.701371	-1072.765121
4	¹ A'	-1229.744546	-1229.826262	-1072.686589	-1072.749105
2	2A	-1230.399599	-1230.482968	-1073.344184	-1073.408341
Mes*OH	¹ A'	-424.784878	-424.837218	-307.022741	-307.061313
Mes*O	² A''	-424.144118	-424.195793	-306.372488	-306.410402

Table 20: Total Energies E_{tot} in Hartree on the ONIOM(CCSD(T*)-F12-F12/VnZ:B3LYP(V)-D3/def2TZVP level of theory.

Species	State	ONIOM(CCSD(T*)-F12/VnZ:B3LYP(V)-D3/def2TZVP ^[a])			
		F12/VDZ(Me: ^t Bu)	F12/VTZ(Me: ^t Bu)	F12/VDZ(H: ^t Bu)	F12/VTZ(H: ^t Bu)
4	³ A''	-1701.389063	-1701.472142	-1701.588805	-1701.652555
4	¹ A'	-1701.375018	-1701.456734	-1701.574839	-1701.637355
2	2A	-1702.028071	-1702.111440	-1702.227664	-1702.291821
Mes*OH	¹ A'	-778.491983	-778.544323	-778.643240	-778.681812
Mes*O	² A''	-777.855670	-777.907345	-778.008002	-778.045916

[a] Total energy according to e.g., $E_{\text{tot}}^{\text{H,iroxo}}(\text{F12/VTZ:DFT}) = E_{\text{tot}}^{\text{H,iroxo}}(\text{F12/VTZ}) - E_{\text{tot}}^{\text{H,iroxo}} + E_{\text{tot}}^{\text{iroxo}}$

Table 21: Total Energies Etot in Hartree on the DLPNO-CCSD(T)-CBS(T,Q) level of theory for 4/2 as well as for Mes*OH and Mes*O.

Species	State	DLPNO-CCSD(T)		
		cc-pVTZ	cc-pVQZ	CBS(T,Q)
H	² S	-0.499810	-0.499946	-0.499986
4	³ A ^g	-1700.712855	-1701.099834	-1701.346959
4	¹ A ^g	-1700.695123	-1701.083273	-1701.331292
2	² A	1701.350845	-1701.740892	-1701.990023
Mes*OH	¹ A ^g	-777.817247	-778.044800	-778.187044
Mes*O	² A ^g	-777.180946	-777.406958	-777.548300

4.2.3. State-Averaged CASSCF computations

The CASSCF MO correlation diagram Figure 71 shows the relative energies and average occupation numbers of the active orbitals in the oxo and hydroxo species. The π_y (Ir–O) orbital of the oxo complex splits into the bonding and antibonding σ (O–H) MOs of the hydroxo species and a smaller splitting occurs for the d_{xy} (Ir) orbital. Spin-orbit coupling from QDPT treatment of the CASSCF/NEVPT2 wavefunctions has only a very minor effect of less than 3 kJmol⁻¹ ($\Delta\Delta E_{\text{SOC}} = -254 \text{ cm}^{-1} = -2.9 \text{ kJmol}^{-1}$, Figure 72), which is of comparable magnitude as the estimate for solvation effects in tetrahydrofuran ($\Delta\Delta E_{\text{sol}} = 2.2 \text{ kJmol}^{-1}$). Note that the computed zero-field splitting parameter $D = 775 \text{ cm}^{-1}$ for the triplet iridium-oxo complex is in good agreement with the experimentally determined value of 647 cm⁻¹. Also note that the vertical excitation energy at the triplet geometry of ΔE (T/S) = 4349 cm⁻¹ = 52.0 kJ mol⁻¹ computed at the NEVPT2/CAS(16,10) level is in nice agreement with an upper bound to the (state-specifically relaxed) ONIOM(F12-VnZ/DFT) in Table 20. The state energies of the CAS and NEVPT2 wavefunctions are collected in Table 22 and Table 23.

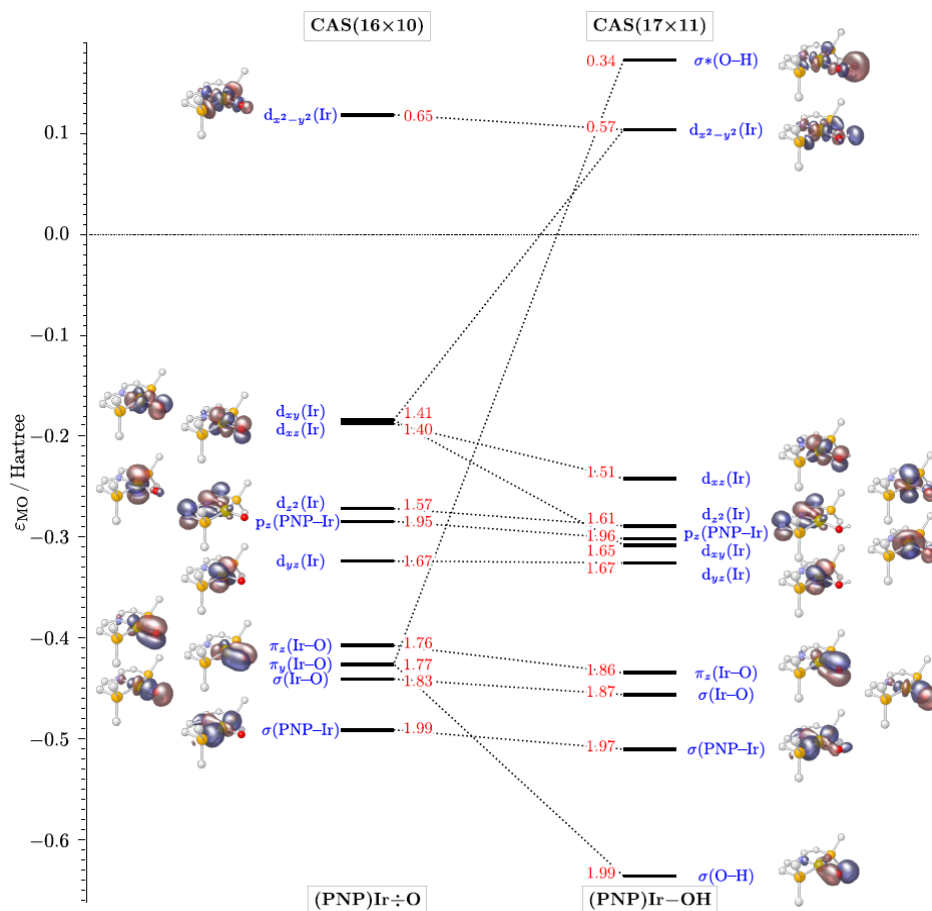


Figure 71: MO correlation diagram from CASSCF wavefunctions state-averaged over all roots which arise from excitations within the 5d shell of the metal centre. MOs are computed for the iridium oxo species in a CAS(16×10) expansion averaged over 50 singlet, 45 triplet, and 5 quintet states, and for the iridium hydroxo species in a CAS(17×11) expansion averaged over 40 doublet and 10 quartet states. MO isosurfaces plotted at an isovalue of $0.05 a_0^{-3/2}$.

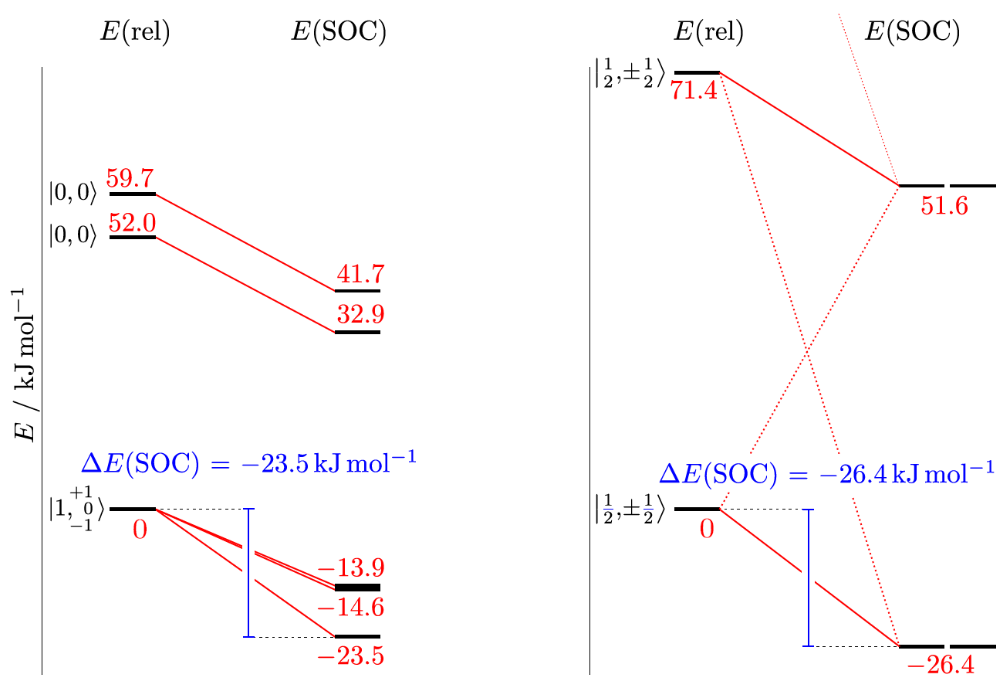


Figure 72: State correlation diagram from NEVPT2 calculations without and with spin-orbit coupling.

Table 22: State energies of the first ten states per multiplicity sorted by CAS energy. ΔE state and spin-orbit eigenvalues ΔE_{SOC} in cm^{-1} from NEVPT2/SA-CASSCF(16,10)/def2TZVP(ZORA) calculations for **4**.

root	mult	$\Delta E_{\text{state}}^{[a]}$		$\Delta E_{\text{state}}^{[b]}$
		CAS(16x10)	NEVPT2	NEVPT2/QDPT
0	3	0.0	0.0	0.0
0	1	3499.4	4348.7	745.8
1	1	3731.1	4992.6	804.0
1	3	8529.4	11629.4	4715.0
2	1	9330.0	9065.6	5452.5
3	1	10044.6	13439.0	10644.8
2	3	11270.1	14515.1	10867.0
4	1	14142.9	17839.3	11938.8
3	3	15412.1	18248.2	12337.3
4	3	16899.5	19730.2	13213.9

[a] Lowest root in $E_h E_{\text{CAS}}(16 \times 10) = -20321.802195$; $E_{\text{NEVPT2}}(16 \times 10) = -20326.823387$ [b] Lowest SOC eigenvalue in $E_h E_{\text{NEVPT2/QDPT}} = -20326.832335$. Energy Stabilisation -1964.1 cm^{-1} .

Table 23: State energies of the first ten states per multiplicity sorted by CAS energy. ΔE state and spin-orbit eigenvalues ΔE_{SOC} in cm^{-1} from NEVPT2/SA-CASSCF(16,10)/def2TZVP(ZORA) calculations for **2**.

root	mult	$\Delta E_{\text{state}}^{[a]}$		$\Delta E_{\text{state}}^{[b]}$
		CAS(16x10)	NEVPT2	NEVPT2/QDPT
0	2	0.0	0.0	0.0
1	2	4161.5	5967.9	0.0
2	2	10451.3	11909.9	6523.3
3	2	12301.7	11685.4	6523.3
0	4	30639.0	32424.9	12853.6
1	4	31271.1	33268.2	12853.6
2	4	33384.9	35550.9	15989.8
4	2	34739.2	32053.9	15989.8
3	4	36655.2	40278.6	26863.0
5	2	38385.0	38144.9	26863.0

[a] Lowest root in $E_h E_{\text{CAS}}(17 \times 11) = -20322.357149$; $E_{\text{NEVPT2}}(17 \times 11) = -20327.419124$ [b] Lowest SOC eigenvalue in $E_h E_{\text{NEVPT2/QDPT}} = -20327.429190$. Energy stabilisation -2209.2 cm^{-1} .

Overall, the computational approaches presented in Table 24 produce a consistent energetic picture, and, moreover, all *ab initio* coupled cluster methods show good agreement. The DLPNO-CCSD(T)/CBS(T,Q) and the ONIOM(F12:DFT) approaches thus operate at a comparable level in the current context. In particular the explicitly correlated ONIOM(F12:DFT) approaches are on a par, independent of basis set size and of truncation model.

Table 24: Relative energies in kJ mol^{-1} for the triplet–singlet gap (4.1), $\Delta E(\text{T/S})$, in **4** complex and for the enthalpies $\Delta_r H_{\text{sol}}^{298}$ of the O–H bond formation reaction (4.2), of the O–H bond homolysis reaction (4.3), and of the corresponding proton-coupled electron transfer (PCET) reaction (4.4) for the conversion of **2** towards the **4**.

Method ^[a]	$\Delta E(\text{T/S})$ ^[b]		$\Delta_r H_{\text{sol}}^{298}$ ^[c]	
	Reaction (4.1) ^[b]	Reaction (4.2) ^[d]	Reaction (4.3) ^[e]	Reaction (4.4) ^[f]
DFT ^[g]	74.0	324.7	-311.2	13.5
DLPNO-CCSD(T) ^[h]	41.1	352.1	-338.0	14.1
ONIOM(F12/VDZ:DFT)(H: ^t Bu) ^[i]	36.7	341.5	-329.3	12.2
ONIOM(F12/VTZ:DFT)(H: ^t Bu) ^[j]	39.9	342.2	-330.7	11.6
ONIOM(F12/VDZ:DFT)(Me: ^t Bu) ^[k]	36.9	341.9	-332.1	9.8
ONIOM(F12/VTZ:DFT)(Me: ^t Bu) ^[l]	40.5	342.3	-333.5	8.8
$\Delta\Delta_r E_{\text{sol}}^{\text{[m]}}$		-2.2	-1.5	-3.7
$\Delta\Delta_r E_{\text{SOC}}^{\text{[n]}}$		2.9		

[a] All molecular geometries and thermal contributions to energies computed at B3LYP(V)-D3/def2TZVP level. **[b]** Excitation energy at 0 K from $^3\text{A}''(\text{Cs})$ triplet ground-state of **4** to the lowest-energy $^1\text{A}'(\text{Cs})$ singlet. **[c]** Reaction enthalpies computed at 298 K, corrected for solvent effects in THF $\Delta\Delta_r E(\text{sol})$ and for spin-orbit coupling contributions $\Delta\Delta_r E(\text{SOC})$. **[d]** Reaction enthalpy for reaction (4.2) computed at 298 K, corrected for solvent effects in THF $\Delta\Delta_r E(\text{sol}) = -2.21 \text{ kJ mol}^{-1}$ and for spin-orbit coupling contributions $\Delta\Delta_r E(\text{SOC}) = 254 \text{ cm}^{-1} = 2.93 \text{ kJ mol}^{-1}$. **[e]** Reaction enthalpy for reaction (4.3) computed at 298K and corrected for solvent effects in thf, $\Delta\Delta_r E(\text{sol}) = 1.51 \text{ kJ mol}^{-1}$. **[f]** Reaction enthalpy for reaction (4.4) computed at 298 K, corrected for solvent effects in thf $\Delta\Delta_r E(\text{sol}) = 3.72 \text{ kJ mol}^{-1}$ and for spin-orbit coupling contributions $\Delta\Delta_r E(\text{SOC}) = -254 \text{ cm}^{-1} = -2.93 \text{ kJ mol}^{-1}$. **[g]** B3LYP(V)-D3/def2TZVP level. **[h]** DLPNO-CCSD(T)/CBS(T,Q) // B3LYP(V)-D3/def2TZVP level. **[i]** ONIOM(CCSD(T*)-F12/VDZ: B3LYP(V)-D3/def2TZVP) level for H-truncated vs. full system. **[j]** ONIOM(CCSD(T*)-F12/VTZ: B3LYP(V)-D3/def2TZVP) level for H-truncated vs. full system. **[k]** ONIOM(CCSD(T*)-F12/VDZ: B3LYP(V)-D3/def2TZVP) level for Me-truncated vs. full system. **[l]** ONIOM(CCSD(T*)-F12/VTZ: B3LYP(V)-D3/def2TZVP) level for Me-truncated vs. full system. **[m]** QDPT/NEVPT2 level.

As an extension, the cationic oxo species **4+** was computed on the PBE0-D3/def2TZVP level of theory. A doublet ground state is predicted for **4+** with a doublet/quartet gap of $\Delta E(\text{D/Q}) = 46 \text{ kJ mol}^{-1}$. With a reduced Ir–O bond length ($d_{\text{Ir-O}} = 1.75 \text{ \AA}$) of 0.05 \AA the doublet structure is nicely resembling the formally higher bond order due to less π^* population (Figure 73). The computed energies are summarised in Table 25 while the xyz data can be found in Section D of Chapter 7.

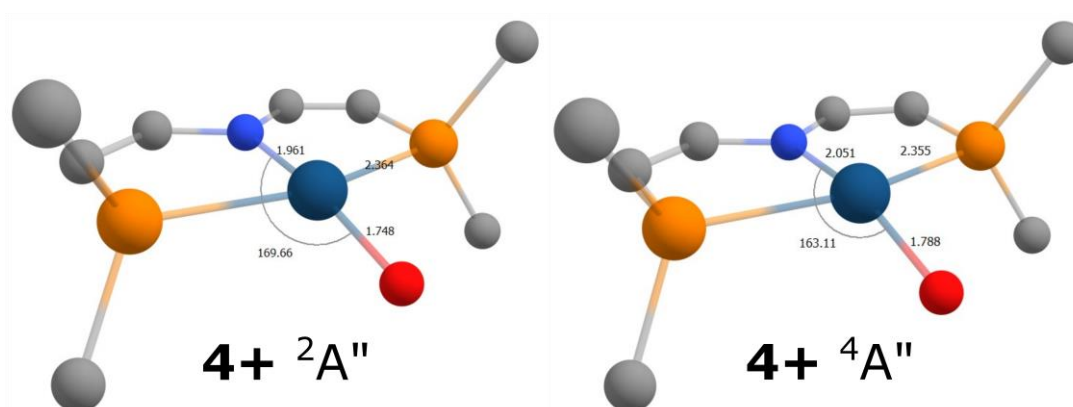


Figure 73: Computed structures of **4+** on the PBE0-D3/def2TZVP level of theory. Methyl groups are omitted for clarity.

Table 25: Relative energies of the DFT results for **4+**.

Species	State	PBE0-D3/def2TZVP			$\Delta E / \text{kJ mol}^{-1}$	$\Delta G / \text{kJ mol}^{-1}$
		E	H(298)	G(298)		
4+	$2\text{A}''(\text{Cs})$	-1702.181177	0.604576	0.507619	0.00	0.00
4+	$4\text{A}''(\text{Cs})$	-1702.163178	0.603585	0.505842	47.25	42.59

4.3. On the Spin-Orbit Coupling influence in solution thermochemistry

4.3.1. Molecular Geometries

Figure 74 shows selected parameters of the optimized geometries of the full molecular systems. All species converged in C_s symmetry. The triplet ground state of **23** exhibits a distorted octahedral coordination sphere with the axial chlorine atoms significantly deviating from the ideal 90° angle. The singlet isomer shows even higher deviation from ideal octahedral geometry. The doublet ground state of **24** is also octahedrally distorted but here the equatorial chlorine is tilted out of the N-Re-P plane, while the quartet isomer shows only minor deviations from an ideal octahedral coordination. Compared to the amine complex **23** the Re-N bond is significantly shortened by 0.28 \AA due to the π -bonding interaction. Also, the Mes*O/Mes*OH couple converged in C_s symmetry. The C-O difference of the Mes*O radical is shortened by 0.12 \AA respectively. The xyz data of all structures can be found in the appendix Section D.

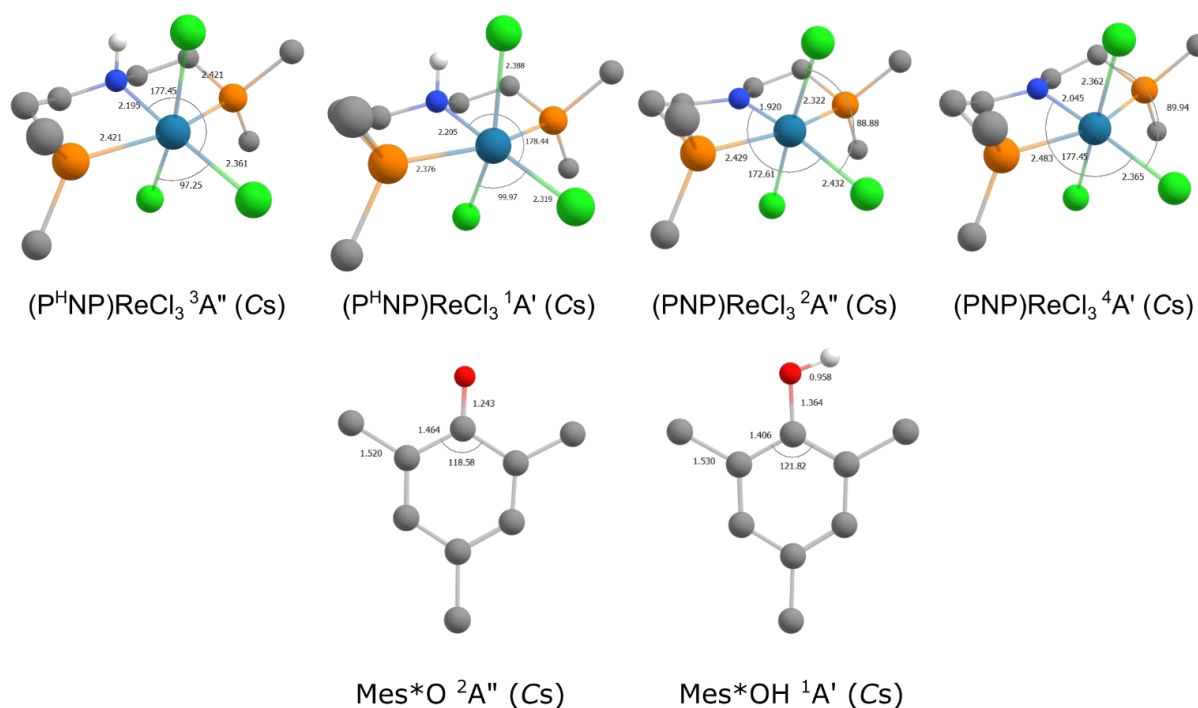


Figure 74: DFT-optimized structures (PBE0/def2TZVP-D3) of the rhenium amine complex **23**, the rhenium amide complex **24** and the Mes*OH/Mes*O couple. (Top: left: Triplet ground state of **23**; middle left: first singlet isomer of **23**; middle right: Doublet ground state of **24**; right: First quartet isomer of **24**; Bottom: left: Mes*O doublet structure; right: Mes*OH singlet structure). All ^tBu and ⁱPr groups and carbon-bonded hydrogen atoms omitted for clarity.

4.3.1. State Averaged CASSCF Computations

The following diagram shows the energies and occupation of the small active spaces of **23** and **24**.

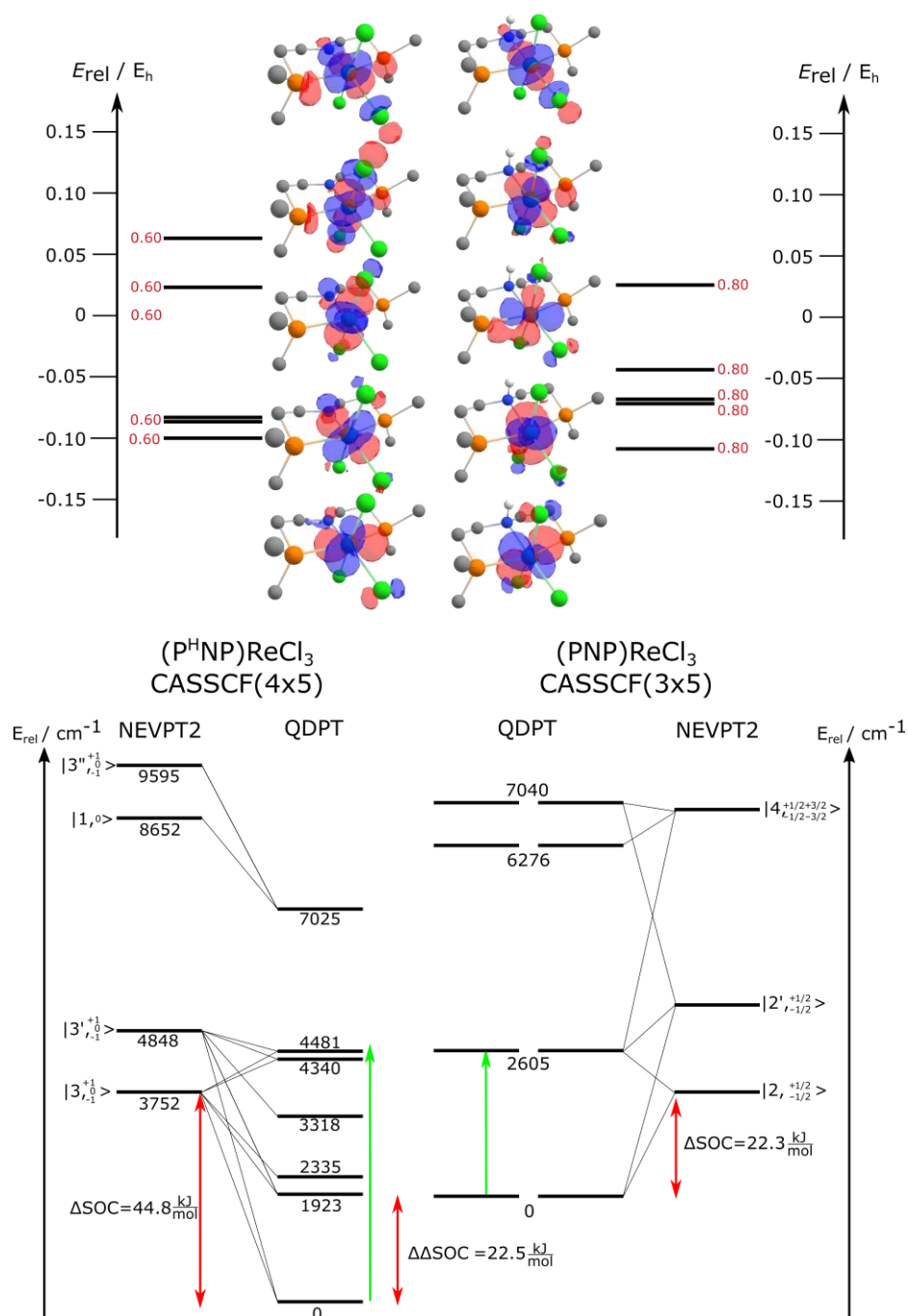


Figure 75: CASSCF wavefunctions state averaged over all excitations arising from the 5d metal centre. MO's (top) are computed for the rhenium amine complex **23** CAS(14x10) averaged over 5 quintet, 45 triplet, and 50 singlet states (top left) and rhenium amide complex **24** CAS(15x11) averaged over 10 quartet and 40 doublet states (top right). Plotted at an isovalue of 0.05 $a_0^{-3/2}$. Bottom: CASSCF state diagram of **1** (bottom left) and **2** (bottom right) with NEVPT2 and QDPT treatment. Red: Spin-orbit coupling stabilization. Green: Computed state transitions with non-negligible oscillator strength.

The following diagram shows the energies and occupation of the big active spaces of **23** and **24**.

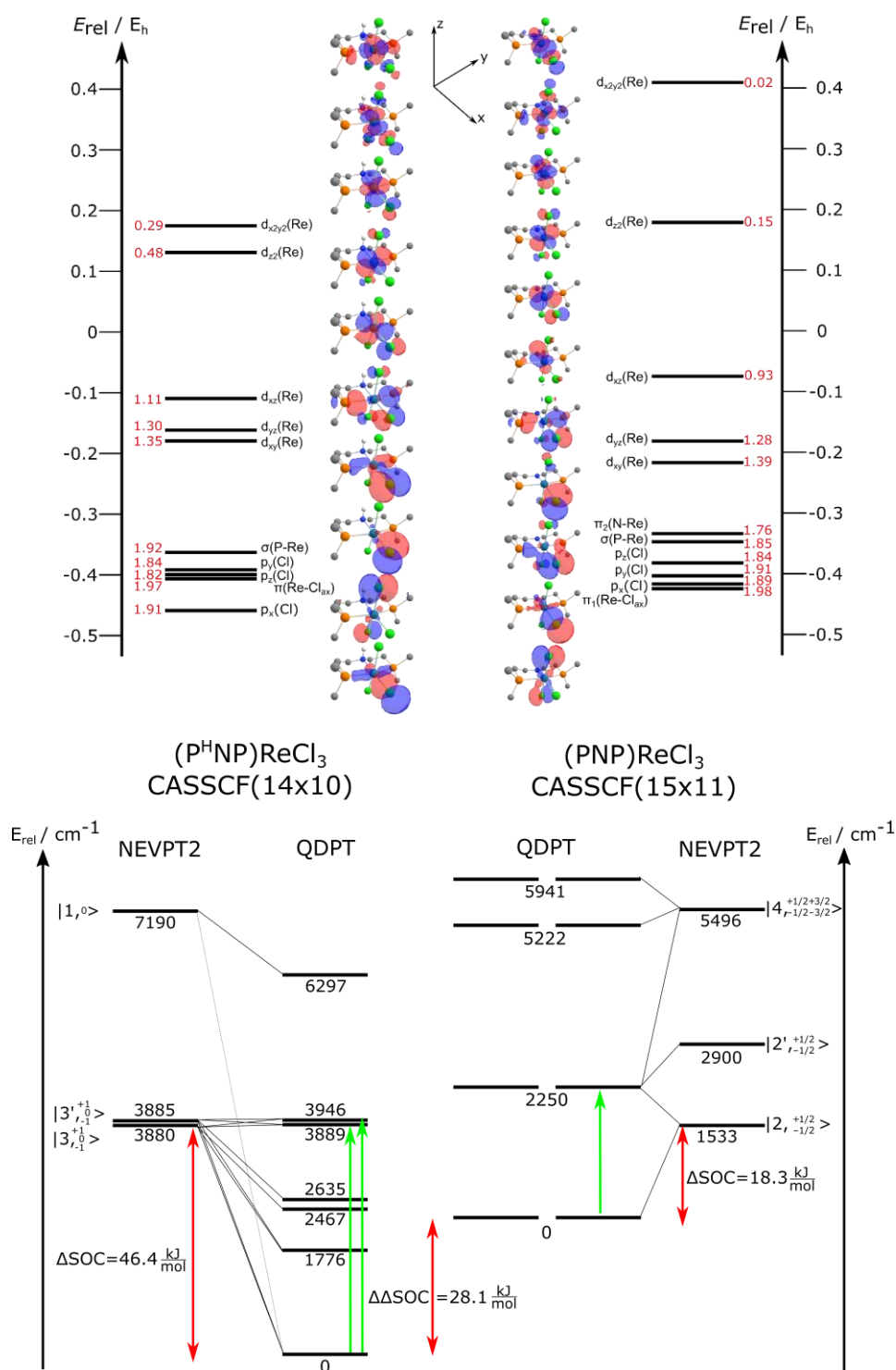


Figure 76: CASCF wavefunctions state averaged over all excitations arising from the 5d metal centre. MOs (top) are computed for **23** CAS(14x10) averaged over 5 quintet, 45 triplet, and 50 singlet states (top left) and **24** CAS(15x11) averaged over 10 quartet and 40 doublet states (top right). Plotted at an isovalue of $0.05 a_0^{-3/2}$. Bottom: CASCF state diagram of **23** (bottom left) and **24** (bottom right) with NEVPT2 and QDPT treatment. Red: Spin-orbit coupling stabilization. Green: Computed state transitions with non-negligible oscillator strength.

4.3.2. CASSCF/NEVPT2 State Composition and QDPT Eigenvectors

Table 26 and Table 27 collect the CASSCF/NEVPT2 state compositions and QDPT eigenvectors of **23** and **24**.

Table 26: CASSCF/NEVPT2 state composition. Weight values rounded to 2 digits. Threshold for printing is Weight: 0.05. States < 10000 cm⁻¹

23 (14x10)					24 (15x11)				
State	Mult	Energy / cm ⁻¹	Weight	Composition	State	Mult	Energy / cm ⁻¹	Weight	Composition
0	3	0	0.68	2222221100	0	2	0	0.82	22222221000
			0.28	2222212100				0.05	22222021200
1	3	5.3	0.68	2222212100	1	2	1368	0.83	22222212000
			0.28	2222221100				0.05	22222012200
2	1	3311	0.81	2222222000	3	4	3964	0.93	22222211100
			0.07	2222220200					
3	1	6005	0.68	2222212100					
			0.25	2222221100					
4	3	6029	0.95	2222211200					
5	1	6335	0.68	2222221100					
			0.25	2222212100					

Table 27: QDPT Eigenvectors, weight values rounded to 2 digits. Threshold for printing is 0.05.

23 (14x10)							24 (15x11)						
State	Energy/ cm ⁻¹	Weight	Block	Root	Spin	ms	State	Energy/ cm ⁻¹	Weight	Block	Root	Spin	ms
0	0	0.38	1	0	1	0	0	0	0.60	1	0	1/2	-1/2
		0.18	1	1	1	1			0.21	1	1	1/2	-1/2
		0.18	1	1	1	-1			0.07	1	0	1/2	-1/2
		0.07	2	0	0	0			0.60	1	0	1/2	1/2
1	1776	0.42	1	1	1	0	1	0	0.21	1	1	1/2	1/2
		0.24	1	0	1	1			0.07	1	0	1/2	1/2
		0.24	1	0	1	-1			0.32	1	1	1/2	-1/2
2	2467	0.43	1	0	1	1	2	2250	0.24	1	1	1/2	1/2
		0.43	1	0	1	-1			0.15	1	0	1/2	1/2
3	2635	0.44	1	1	1	1	3	2250	0.08	0	0	3/2	1/2
		0.44	1	1	1	-1			0.05	0	0	3/2	-3/2
4	3889	0.34	1	1	1	0	4	2250	0.32	1	1	1/2	1/2
		0.16	1	0	1	0			0.24	1	1	1/2	-1/2
		0.14	1	0	1	1			0.15	1	0	1/2	-1/2
		0.14	1	0	1	-1			0.08	0	0	3/2	-1/2
5	3946	0.30	1	0	1	0	5	5222	0.05	0	0	3/2	3/2
		0.16	1	1	1	0			0.52	0	0	3/2	-3/2
		0.16	1	1	1	1			0.38	0	0	3/2	1/2
		0.16	1	1	1	-1			0.52	0	0	3/2	3/2
6	6297	0.07	1	0	1	-1	6	5222	0.38	0	0	3/2	-1/2
		0.72	2	0	0	0			0.34	0	0	3/2	-1/2
		0.10	1	2	1	1			0.32	0	0	3/2	3/2
		0.10	1	2	1	-1			0.11	1	1	1/2	1/2
7	5941	0.10	1	2	1	-1	7	5941	0.10	0	0	3/2	1/2
		0.34	0	0	3/2	1/2			0.34	0	0	3/2	1/2
		0.32	0	0	3/2	-3/2			0.32	0	0	3/2	-3/2
		0.11	1	1	1/2	-1/2			0.11	1	1	1/2	-1/2

4.3.3. Comparison of Magnetic Properties Theory vs. Experiment

Figure 77 and Figure 76 show the comparison of the obtained magnetic properties by CASSCF/NEVPT2-QDPT treatment with the experimentally derived magnetic data by SQUID magnetometry for **23** and **24**.

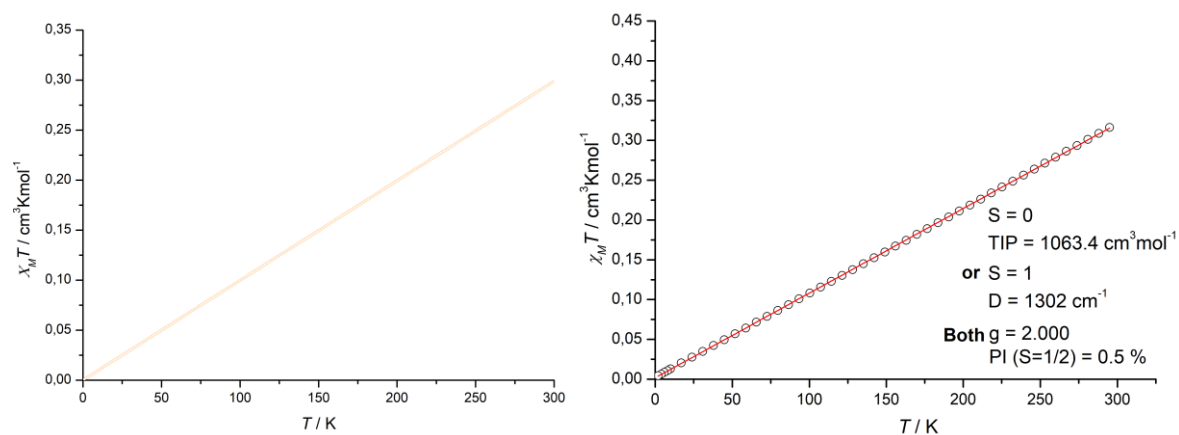


Figure 77: Computed magnetic susceptibility data on the CASSCF/NEVPT2/QDPT def2-TZVP(ZORA) level of theory at 0.5 T for reamin (left) and the experimental data obtained by SQUID magnetometry (right).

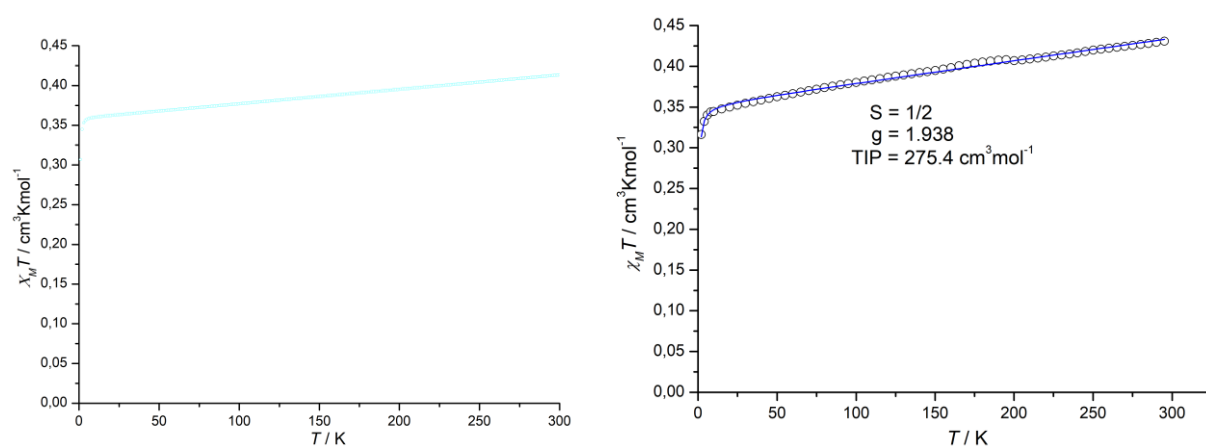
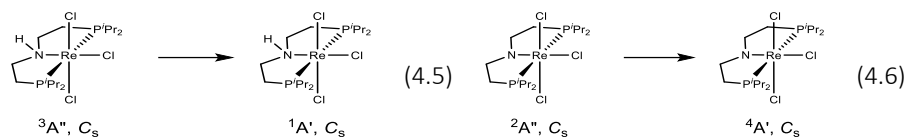


Figure 78: Computed magnetic susceptibility data on the CASSCF/NEVPT2/QDPT def2TZVP(ZORA) level of theory at 0.5 T for **24** (left) and the experimental obtained data by SQUID magnetometry (right).

4.3.4. Spin State and Reactions Energetics

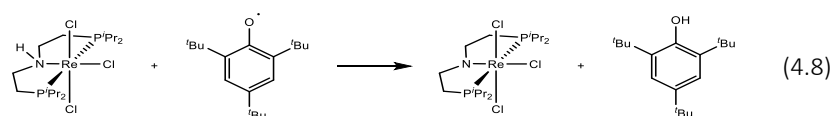
The relative spin-state and reaction energies were computed with DFT, coupled cluster methods and DLPNO. The results are summarized in following tables. Reaction 4.5 and 4.6 are used to compute the triplet/singlet gap $\Delta E(T/S)$ and the doublet/quartet, respectively.



The half reaction energetics were computed for reaction 4.7:



The full reaction energetics were computed for the reaction 4.8:



The ONIOM energies were computed with eq. 4.9:

$$E^{\text{ONIOM}} = E_{\text{X:iPr/tBu}}^{\text{CCSD(T)-f12}} - E_{\text{X:iPr/tBu}}^{\text{PBE0-D3/def2TZVP}} + E_{\text{Fullsystem}}^{\text{PBE0-D3/def2TZVP}} \quad (4.9)$$

Table 28: Total energies in E_h of **23** and **24** and the Mes*OH/Mes*O couple and the corresponding methyl and hydrogen truncated model systems at the level PBE0-D3/def2TZVP.

Method ^[a]	$\Delta E(T/S)^{[b]}$ eq.(4.5)	$\Delta E(D/Q)^{[b]}$ eq.(4.6)	$\Delta E^{[c]}$ eq.(4.7)	Method ^[a]	$\Delta E(T/S)^{[b]}$ eq.(4.5)	$\Delta E(D/Q)^{[b]}$ eq.(4.6)	$\Delta E^{[c]}$ eq.(4.7)
DFT ^[d] (23/24)	38.6	15.0	294				
DFT(Mes*OH/Mes*O) ^[d]			343	ONIOM(f ₁₂ -VDZ:PBE0)(H: ^t Pr) (23/24) ^[l]	16.8	37.8	288
DFT ^h truncation (23/24) ^[e]	14.5	26.4	299	ONIOM(f ₁₂ -VDZ:PBE0)(H: ^t Bu) (Mes*OH/Mes*O) ^[l]			357
DFT ^h truncation (Mes*OH/Mes*O) ^[e]			380	ONIOM(f ₁₂ -VDZ:PBE0)(Me: ⁱ Pr) (23/24) ^[m]	15.2	38.6	278
DFT ^{me} truncation (15/16) ^[f]	30.8	15.2	297	ONIOM(f ₁₂ -VDZ:PBE0)(Me: ^t Bu) (Mes*OH/Mes*O) ^[m]			360
DFT ^{me} truncation (Mes*OH/Mes*O) ^[f]			353	ONIOM(f ₁₂ -VTZ:PBE0)(H: ^t Pr) (23/24) ^[n]	18.5	36.3	286
CCSD(T)-f ₁₂ /VDZ(H: ^t Pr) (23/24) ^[g]	-7.3	49.2	284	ONIOM(f ₁₂ -VTZ:PBE0)(Me: ^t Bu) (Mes*OH/Mes*O) ^[o]			361
CCSD(T)-f ₁₂ /VDZ(H: ^t Bu) (Mes*OH/Mes*O) ^[g]			394	DLPNO-CCSD(TO)/cc- pV(T,Q)Z(PP) (23/24) ^[p]	32.6	18.8	297
CCSD(T)-f ₁₂ /VDZ(Me: ⁱ Pr) (23/24) ^[h]	7.4	38.8	281	DLPNO-CCSD(TO)/cc- pV(T,Q)Z(PP) (Mes*OH/Mes*O) ^[p]			365
CCSD(T)-f ₁₂ /VDZ(Me: ^t Bu) (Mes*OH/Mes*O) ^[h]			371	DLPNO-CCSD(TO)/def2- (T,Q)ZVPP (23/24) ^[q]	34.4	15.4	298
CCSD(T)-f ₁₂ /VDZ(^t Bu: ^t Bu) (Mes*OH/Mes*O) ^[i]			359	DLPNO-CCSD(TO)/def2- (T,Q)ZVPP (Mes*OH/Mes*O) ^[q]			366
CCSD(T)-f ₁₂ /VTZ(H: ^t Pr) (23/24) ^[j]	-5.6	47.7	290	DLPNO-CCSD(T1)/def2- (T,Q)ZVPP (23/24) ^[r]	15.9	18.8	296
CCSD(T)-f ₁₂ /VTZ(H: ^t Bu) (Mes*OH/Mes*O) ^[j]			394	DLPNO-CCSD(T1)/def2- (T,Q)ZVPP (Mes*OH/Mes*O) ^[r]			369
CCSD(T)-f ₁₂ /VTZ(Me: ^t Bu) (Mes*OH/Mes*O) ^[k]			372				

[a] All molecular geometries and thermal contributions to energies are at PBE0-D3/def2TZVP level. [b] Excitation energy at 0 K from the triplet(3A'')/doublet(2A'') ground state of **23** and **24** to the lowest energy singlet(1A')/quartet(4A') electromer. [c] Reaction energies for reaction (3) computed at 0 K, without correction for thermal contributions or SOC effects. [d] PBE0-D3/def2TZVP level. [e] PBE0-D3/def2TZVP level for the hydrogen truncated model systems (H: ⁱPr/^tBu). [f] PBE0-D3/def2TZVP level for the methyl truncated model systems (Me: ⁱPr/^tBu). [g] CCSD(T)-f₁₂/VDZ level for hydrogen truncated model systems (H: ⁱPr/^tBu) [h] CCSD(T)-f₁₂/VDZ level for methyl truncated model systems (Me: ⁱPr/^tBu). [i] CCSD(T)-f₁₂/VDZ level for the untruncated Mes*OH/Mes*O couple. [j] CCSD(T)-f₁₂/VTZ level for hydrogen truncated model systems (H: ⁱPr/^tBu). [k] CCSD(T)-f₁₂/VTZ level for the methyl truncated Mes*OH/Mes*O couple. [l] ONIOM results from eq. (5) on the CCSD(T)-f₁₂/VDZ level with hydrogen truncated model systems. [m] ONIOM results from eq. (5) on the CCSD(T)-f₁₂/VDZ level with methyl truncated model systems. [n] ONIOM results from eq. (5) on the CCSD(T)-f₁₂/VTZ level with hydrogen truncated model systems. [o] ONIOM results from eq. (4.7) on the CCSD(T)-f₁₂/VTZ level with methyl truncated model systems. [p] DLPNO-CCSD(TO)/-cc-pV(T,Q)Z(PP) level. [q] DLPNO-CCSD(TO)/def2-pV(T,Q)ZVPP level. [r] DLPNO-CCSD(T1)/def2-pV(T,Q)ZVPP level.

Table 29: Relative energies in kJmol⁻¹ for the full reaction (4.6) energetics including enthalpic contribution and SOC effects.

Method	ΔE_r , eq.(4)
PBE0-D3/def2TZVP ^[a]	-48.5
ONIOM(f ₁₂ -VDZ:PBE0)(H: ⁱ Pr/ ⁱ Bu) ^[b]	-78.2
ONIOM(f ₁₂ -VDZ:PBE0)(H: ⁱ Pr/Me: ⁱ Bu) ^[c]	-81.2
ONIOM(f ₁₂ -VDZ:PBE0)(H: ⁱ Pr/ ⁱ Bu: ⁱ Bu) ^[d]	-80.1
ONIOM(f ₁₂ -VDZ:PBE0)(Me: ⁱ Pr/H: ⁱ Bu) ^[e]	-78.7
ONIOM(f ₁₂ -VDZ:PBE0)(Me: ⁱ Pr/Me: ⁱ Bu) ^[f]	-81.7
ONIOM(f ₁₂ -VDZ:PBE0)(Me: ⁱ Pr/ ⁱ Bu: ⁱ Bu) ^[g]	-80.5
ONIOM(f ₁₂ -VTZ:PBE0)(H: ⁱ Pr/ ⁱ Bu) ^[h]	-71.1
ONIOM(f ₁₂ -VTZ:PBE0)(H: ⁱ Pr/Me: ⁱ Bu) ^[i]	-75.8
DLPNO-cc-pV(T,Q)Z(PP) ^[j]	-68.1
DLPNO-CCSD(T0)/def2-(T,Q)ZVPP ^[k]	-67.8
DLPNO-CCSD(T1)/def2-(T,Q)ZVPP ^[l]	-72.9
$\Delta H^{298\text{ K}}$ [m]	-1.29
$\Delta\Delta E(\text{SOC})$ ^[n]	27.4
Results $[\Delta E + \Delta H + \Delta\Delta E(\text{SOC})] = \Delta H_r^{\text{SOC}}$ (eq.4)	
PBE0-D3/def2TZVP	-22.4
ONIOM(f ₁₂ -VDZ:PBE0)(H: ⁱ Pr/ ⁱ Bu)	-52.1
ONIOM(f ₁₂ -VDZ:PBE0)(H: ⁱ Pr/Me: ⁱ Bu)	-55.2
ONIOM(f ₁₂ -VDZ:PBE0)(H: ⁱ Pr/ ⁱ Bu: ⁱ Bu)	-54.0
ONIOM(f ₁₂ -VDZ:PBE0)(Me: ⁱ Pr/H: ⁱ Bu)	-52.6
ONIOM(f ₁₂ -VDZ:PBE0)(Me: ⁱ Pr/Me: ⁱ Bu)	-55.6
ONIOM(f ₁₂ -VDZ:PBE0)(Me: ⁱ Pr/ ⁱ Bu: ⁱ Bu)	-54.4
ONIOM(f ₁₂ -VTZ:PBE0)(H: ⁱ Pr/ ⁱ Bu)	-45.0
ONIOM(f ₁₂ -VTZ:PBE0)(H: ⁱ Pr/Me: ⁱ Bu)	-49.7
DLPNO-cc-pV(T,Q)Z(PP)	-42.0
DLPNO-CCSD(T0)/def2-(T,Q)ZVPP	-41.7
DLPNO-CCSD(T1)/def2-(T,Q)ZVPP	-46.8
EXPERIMENT (THF/DCM)^[o]	-40.1±0.2
	-51.2±0.3

[a]PBE0-D3/def2TZVP level. [b] ONIOM energy for reaction (4.8) on the CCSD(T)-f12/VDZ level with H truncated model systems. [c] ONIOM energy for reaction (4.8) on the CCSD(T)-f12/VDZ level with H truncated model systems for **23** and **24** and Me truncated model systems for the Mes*OH/Mes*O couple. [d] ONIOM energy for reaction (4.8) on the CCSD(T)-f12/VDZ level with H truncated model systems for **23** and **24** and the untruncated Mes*OH/Mes*O couple. [e] ONIOM energy for reaction (4.8) on the CCSD(T)-f12/VDZ level with Me truncated model systems for **23** and **24** and the hydrogen truncated models systems for the Mes*OH/Mes*O couple. [f] ONIOM energy for reaction (4.8) on the CCSD(T)-f12/VDZ level with Me truncated model systems for **23** and **24** and the Me truncated models systems for the Mes*OH/Mes*O couple. [g] ONIOM energy for reaction (4.8) on the CCSD(T)-f12/VDZ level with Me truncated model systems for **23** and **24** and the untruncated the Mes*OH/Mes*O couple. [h] ONIOM energy for reaction (4.8) on the CCSD(T)-f12/VTZ level with H truncated model systems. [i] ONIOM energy for reaction (4.8) on the CCSD(T)-f12/VTZ level with H truncated model systems **23** and **24** and the Me truncated models systems for the Mes*OH/Mes*O couple. [j] DLPNO-CCSD(T0)/-cc-pV(T,Q)Z(PP) energy for reaction (4.8). [k] DLPNO-CCSD(T0)/def2-pV(T,Q)ZVPP energy for reaction (4.8). [l] DLPNO-CCSD(T1)/def2-pV(T,Q)ZVPP energy for reaction (4.8) [m] Thermal contributions on the PBE0-D3/def2TZVP level. [n] Spin-Orbit-Coupling(SOC) contribution by CASSCF NEVPT2/QDPT treatment see Section 4.3.1.

4.3.5. Total Energies

Table 30: Total energies in E_h of **23** and **24** as well as the Mes*OH/Mes*O couple and the corresponding methyl and hydrogen truncated model systems at the PBE0-D3/def2TZVP level.

PBE0-D3/def2TZVP					
Species	State	Fullsystem		Me	H
		E_{tot}	ΔH_{corr}^{298K}	E_{tot}	E_{tot}
Rhenium Amine 23	$^2A''$	-2827.427856	0.554282	-2513.175041	-2355.988952
Rhenium Amine 23	$^1A'$	-2827.413110	0.554224	-2513.163329	-2355.983429
Rhenium Amide 24	$^2A''$	-2826.841094	0.540469	-2512.560877	-2355.373971
Rhenium Amide 24	$^4A'$	-2826.834887	0.54034	-2512.555096	-2355.363929
Mes*OH	$^1A'$	-778.6104991	0.465602	-425.0888723	-307.2358522
Mes*O	$^2A''$	-777.9789138	0.452282	-424.4532747	-306.5900897

Table 31: Total energies at the CCSD(T*)-f12/VnZ (n = D,T) level in E_h of the (H/Me) truncated model systems as well as the un-truncated version of the Mes*OH/Mes*O couple.

Species	State	CCSD(T*)-f12 @ H		CCSD(T*)-f12 @ Me		CCSD(T*)-f12 untruncated
		VDZ	VTZ	VDZ	VTZ	VDZ
Rhenium Amine 23	$^3A''$	-2354.081467	-2354.183069	-2511.14589	-	-
Rhenium Amine 23	$^1A'$	-2354.084254	-2354.185199	-2511.143081	-	-
Rhenium Amide 24	$^2A''$	-2353.473631	-2353.572496	-2510.539028	-	-
Rhenium Amide 24	$^4A'$	-2353.454891	-2353.554311	-2510.524251	-	-
Mes*OH	$^1A'$	-307.0240698	-307.0240698	-424.7861547	-424.8385756	-778.044967
Mes*O	$^2A''$	-306.3741126	-306.3741126	-424.1452075	-424.1969558	-777.408469

Table 32: Total energies at the ONIOM(CCSD(T*)-f12/VnZ (n = D,T)/PBE0) level in E_h of the (H/Me) truncated model systems as well as the untruncated version of the Mes*OH/Mes*O couple.

Species	State	ONIOM (H:Pr;H:Bu)		ONIOM (Me:Pr;Me:Bu)	
		VDZ	VTZ	VDZ	VTZ
Rhenium Amine 23	$^2A''$	-2825.52037	-2825.62197	-2825.398705	-
Rhenium Amine 23	$^4A'$	-2825.51393	-2825.61488	-2825.392862	-
Rhenium Amide 24	$^3A''$	-2824.91439	-2825.01326	-2824.792882	-
Rhenium Amide 24	$^1A'$	-2824.89987	-2824.99929	-2824.778062	-
Mes*OH	$^1A'$	-777.762937	-777.762937	-777.6708466	-777.7357124
Mes*O	$^2A''$	-778.398717	-778.398717	-778.3077814	-778.3602023

Table 33: Total energies in E_h computed at the DLPNO-cc-pV(T,Q)Z(PP) level of theory.

Species	State	DLPNO-cc-pV(T,Q)Z(PP)		
		cc-pVTZ	cc-pVQZ	CBS(T,Q)
Rhenium Amine 23	$^3A''$	-2825.107629	-2825.490213	-2825.736087
Rhenium Amine 23	$^1A'$	-2825.093800	-2825.477307	-2825.723677
Rhenium Amide 24	$^2A''$	-2824.496800	-2824.878193	-2825.123150
Rhenium Amide 24	$^4A'$	-2824.491424	-2824.871825	-2825.115995
Mes*OH	$^1A'$	-777.816691	-778.044694	-778.187228
Mes*O	$^2A''$	-777.180270	-777.406721	-777.548343

Table 34: Total energies in E_h computed at the DLPNO-CCSD(T0)def2-(T,Q)ZVPP level of theory.

Species	State	DLPNO-CCSD(T0)-def2-(T,Q)ZVPP		
		cc-pVTZ	cc-pVQZ	CBS(T,Q)
Rhenium Amine 23	$^3A''$	-2824.765030	-2825.164712	-2825.406985
Rhenium Amine 23	$^1A'$	-2824.751862	-2825.151617	-2825.393868
Rhenium Amide 24	$^2A''$	-2824.153006	-2824.551895	-2824.793466
Rhenium Amide 24	$^4A'$	-2824.147898	-2824.546390	-2824.787589
Mes*OH	$^1A'$	-777.832086	-778.047275	-778.186284
Mes*O	$^2A''$	-777.195596	-777.409059	-777.546938

Table 35: Total energies in E_h computed at the DLPNO-CCSD(T1)/def2-(T,Q)ZVPP level of theory.

Species	State	DLPNO-CCSD(T1)-def2-(T,Q)ZVPP		
		cc-pVTZ	cc-pVQZ	CBS(T,Q)
Rhenium Amine 23	$^3A''$	-2824.775277	-2825.173306	-2825.414356
Rhenium Amine 23	$^1A'$	-2824.764930	-2825.165463	-2825.408288
Rhenium Amide 24	$^2A''$	-2824.164967	-2824.561681	-2824.801641
Rhenium Amide 24	$^4A'$	-2824.156341	-2824.553934	-2824.794467
Mes*OH	$^1A'$	-777.838427	-778.053747	-778.192853
Mes*O	$^2A''$	-777.200845	-777.414406	-777.552359

4.4 Interconversion of Phosphinyl Radical and Phosphinidene Complexes by Proton Coupled Electron Transfer

All molecules were optimized on the PBE-D3/def2SVP level of theory. The quartet isomer of the free phosphinyl radical was as well computed to ensure the discussion of the lowest energy structure. The singlet root for the PMes* molecule failed to converge. The BDE values were computed for the equation 4.10:



Where X-H is either **17** or HPMes* and X is **19** or PMes*

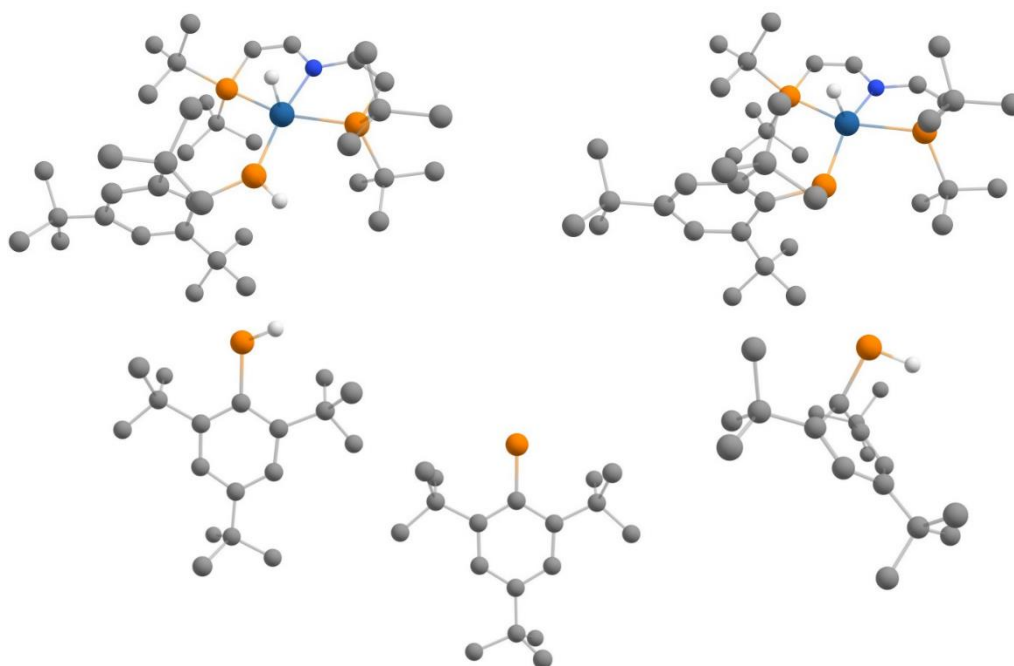


Figure 79: Computed minimum structures of H_nPMes^* ($n = 1, 0$) and the osmium complexes **17** and **19** on the PBE-D3/def2SVP level of theory. Top left: **17** doublet electramer. Top right: **19** singlet electramer. Bottom left: Doublet electramer of HPMes*. Bottom centre: Triplet electramer of PMes*. Bottom right: Quartet electramer of HPMes*.

The quartet isomer of HPMes* is significantly higher in energy with $\Delta(\text{D}/\text{Q}) = 269 \text{ kJ mol}^{-1}$. Coordination has a significant effect of $\Delta\text{BDE} = -23.4 \text{ kJ mol}^{-1}$ on the P-H bond strength compared to the free phosphinyl radical. The total energies of the computed structures can be found in Table 36.

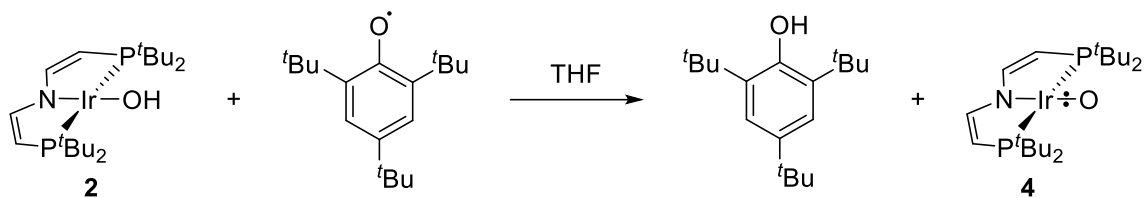
Table 36: Total energies of **17** and **19** as well as the energies of the free phosphinyl radical, its quartet electramer and of PMes* at the PBE-D3/def2SVP level of theory.

Species	State	PBE-D3/def2SVP	
		Fullsystem	
		E_{tot}	ΔH_{corr}^{298K}
Osmium Phosphinyl Radical 17	^2A	-2656.56726	1.038222
Osmium Phosphinidene 19	^1A	-2655.96535	1.029094
HPMes*	^2A	-1043.61561	0.444862
HPMes*	^4A	-1043.51316	0.442785
PMes*	^3A	-1043.00517	0.436193

5. Benchmarked Experimental Results

Within this thesis several thermodynamic parameters have been benchmarked by isothermal titration calorimetry. Since BDE values might be object to changes of reference values only the pure reaction parameters are listed. If not otherwise noted, the experiments were performed at 298 K.

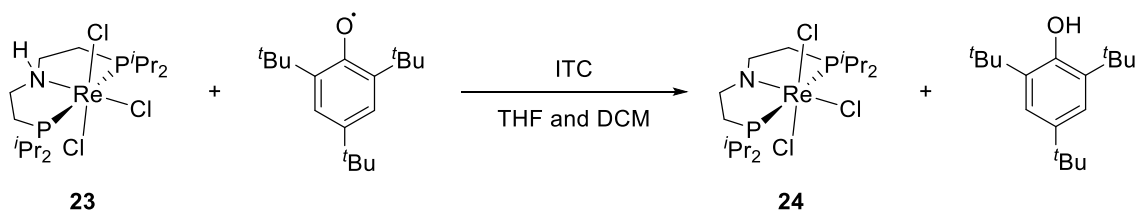
Benchmarked values ΔH_r and K (see Section 3.1):



Results kJ mol^{-1}

$$\Delta H_r \quad -3.8 \pm 2$$

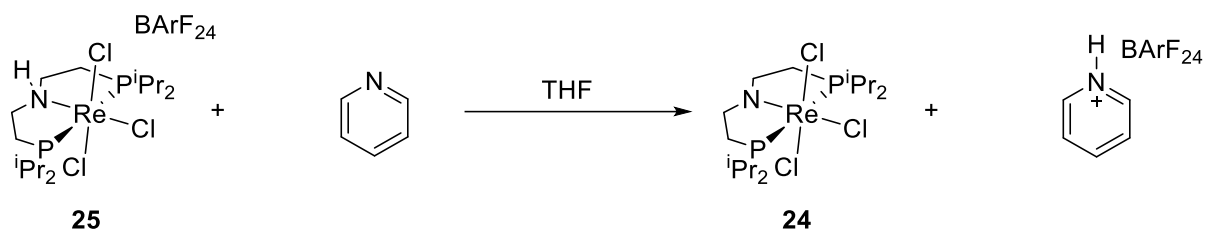
$$\Delta G_r \quad 15 \pm 6$$



Benchmarked value ΔH_r (see Section 3.2):

$\Delta H_r / \text{kJ mol}^{-1}$	Error at 95 % confidence	n value	Corrected Error
-51.2	± 0.28	0.943	± 0.30
-51.3	± 0.24	1.01	± 0.24
-51.3	± 0.36	1.05	± 0.38
Weighted Average	$\Delta H^{298 \text{ K}}(\text{DCM}) = -51.2 \pm 0.3 \text{ kJ mol}^{-1}$		

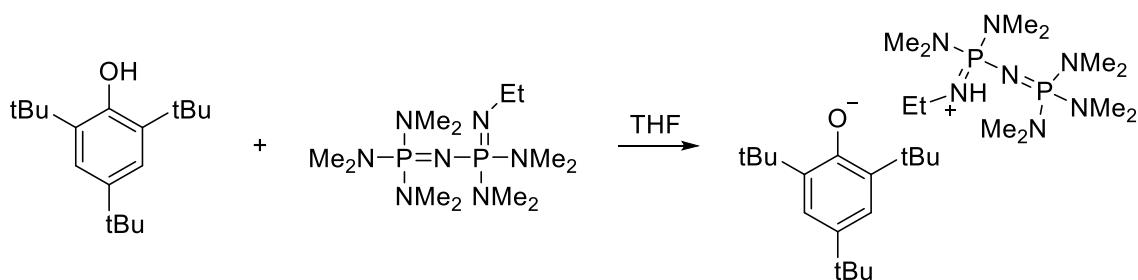
$\Delta H_r / \text{kJ mol}^{-1}$	Error at 95 % confidence	n value	Corrected Error
-40.0	± 0.25	1.02	± 0.26
-39.9	± 0.20	1.04	± 0.21
-40.7	± 0.29	1.05	± 0.30
Weighted Average	$\Delta H^{298 \text{ K}}(\text{THF}) = -40.1 \pm 0.2 \text{ kJ mol}^{-1}$		



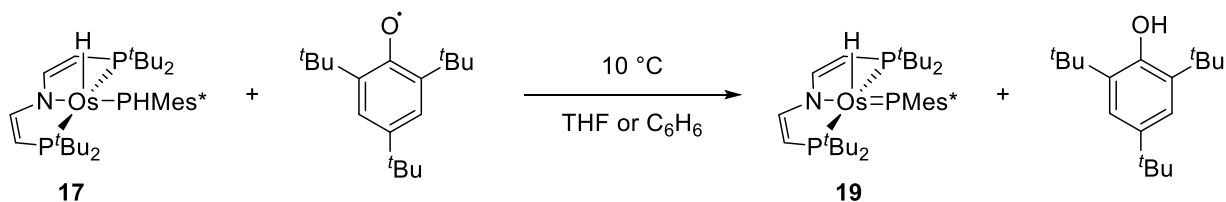
Benchmarked value K (see Section 3.3)

Run	K	95 % Confidence Error
1	5.32	0.12
2	5.32	0.12
Mean equilibrium constant		5.32 ± 0.12

Benchmarked value K_D (see Section 3.4)



$K_D / \text{mol L}^{-1}$	Error at 95 % confidence	n value	Corrected Error
$1.32 \cdot 10^{-3}$	$\pm 0.08 \cdot 10^{-3}$	1.00	$\pm 0.08 \cdot 10^{-3}$
$1.22 \cdot 10^{-3}$	$\pm 0.04 \cdot 10^{-3}$	1.03	$\pm 0.04 \cdot 10^{-3}$
$1.20 \cdot 10^{-3}$	$\pm 0.06 \cdot 10^{-3}$	1.00	$\pm 0.06 \cdot 10^{-3}$
Weighted Average $K_D = 1.24 \pm 0.06 \cdot 10^{-3} \text{ M}^{-1}$			



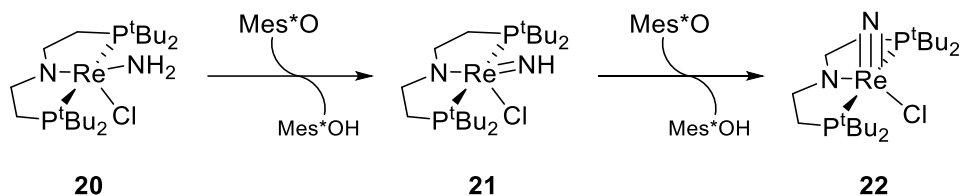
Benchmarked value $\Delta H_r(283\text{ K})$: (see Section 3.5)

Benzene:

Injection	Heat of injection of the 1 st run / μJ	Heat of injection of the 2 nd run / μJ	Added moles per injection / nmol
3	-4682	-4678	68.2
4	-4708	-4678	68.2
5	-4703	-4709	68.2
6	-4716	-4711	68.2
Mean	-4702 ± 20	-4694 ± 17	
Weighted Mean		-4697 ± 13	
Reaction Enthalpy / kJ mol^{-1}		-68.9 ± 3.6	

THF:

Injection	Heat of injection of the 1 st run / μJ	Added moles per injection / nmol
2	-4069	56.9
3	-4066	56.9
4	-4050	56.9
5	-4049	56.9
Mean	-4059 ± 10	
Reaction Enthalpy / kJ mol^{-1}		$-71 \pm 5 \text{ kJ mol}^{-1}$



Benchmarked value ΔH_r (see Section 3.6):

Results		
Mean Heat [μJ]	Consumed moles per injection [nmol]	Enthalpy [kJ/mol]
-4176 ± 27	19.62	-213 ± 1
-3957 ± 40	18.76	-211 ± 2
$-4017 \pm 39^*$	18.76	-214 ± 2
		Weighted mean enthalpy = $-213 \pm 2 \text{ kJ mol}^{-1}$

*The error for the third measurement is raised to scale for the deviation from the ideal n value of n=2.00.

Chapter VII

6. Literature

- [1] I. G. Denisov, T. M. Makris, S. G. Sligar, I. Schlichting, *Chem. Rev.* **2005**, *105*, 2253–2277.
- [2] H. Sitzmann, J. Hartmann-Schreier, “Sauerstoff,” can be found under <https://roempp.thieme.de/lexicon/RD-19-00520>, **2011**.
- [3] T. W. Lyons, C. T. Reinhard, N. J. Planavsky, *Nature* **2014**, *506*, 307–315.
- [4] D. Voet, J. G. Voet, C. W. Pratt, *Fundamentals of Biochemistry: Life at the Molecular Level*, John Wiley & Sons, **2016**.
- [5] N. B. Terwilliger, *J. Exp. Biol.* **1998**, *201*, 1085–1098.
- [6] L. Pauling, C. D. Coryell, *Proc. N. A. S.* **1936**, *22*, 210–216.
- [7] G. Gilardi, G. Di Nardo, *Rend. Fis. Acc. Lincei* **2017**, *28*, 159–167.
- [8] K. L. Bren, R. Eisenberg, H. B. Gray, *Proc. Natl. Acad. Sci.* **2015**, *112*, 13123–13127.
- [9] T. Yamanaka, K. Okunuki, in *Microb. Iron Metab.* (Ed.: J. Neilands), Academic Press, **1974**, pp. 349–400.
- [10] J. Rittle, M. T. Green, *Science* **2010**, *330*, 933–937.
- [11] D. L. Simmons, R. M. Botting, T. Hla, *Pharmacol. Rev.* **2004**, *56*, 387–437.
- [12] J. N. Rodríguez-López, D. J. Lowe, J. Hernández-Ruiz, A. N. P. Hiner, F. García-Cánovas, R. N. F. Thorneley, *J. Am. Chem. Soc.* **2001**, *123*, 11838–11847.
- [13] C. Krebs, D. G. Fujimori, C. T. Walsh, J. M. Bollinger, *Acc. Chem. Res.* **2007**, *40*, 484–492.
- [14] N. Cox, M. Retegan, F. Neese, D. A. Pantazis, A. Boussac, W. Lubitz, *Science* **2014**, *345*, 804–808.
- [15] R. Pal, C. F. A. Negre, L. Vogt, R. Pokhrel, M. Z. Ertem, G. W. Brudvig, V. S. Batista, *Biochemistry* **2013**, *52*, 7703–7706.
- [16] K. Ray, F. Heims, M. Schwalbe, W. Nam, *Curr. Opin. Chem. Biol.* **2015**, *25*, 159–171.
- [17] K. Gunay, A.; Theopold, *Chem. Rev.* **2010**, 1060–1081.
- [18] H. B. Gray, *Chem. Int.* **2019**, *41*, 16–19.
- [19] C. J. Ballhausen, H. B. Gray, *Inorg. Chem.* **1962**, *1*, 111–122.
- [20] J. R. et al. Winkler, in *Mol. Electron. Struct. Transition Met. Complexes I*, **2012**, pp. 17–28.
- [21] U. Hintermair, S. W. Sheehan, A. R. Parent, D. H. Ess, D. T. Richens, P. H. Vaccaro, G. W. Brudvig, R. H. Crabtree, *J. Am. Chem. Soc.* **2013**, *135*, 10837–10851.
- [22] M. Zhou, D. Balcells, A. R. Parent, R. H. Crabtree, O. Eisenstein, *ACS Catal.* **2012**, *2*, 208–218.
- [23] B. A. Vaughan, M. S. Webster-Gardiner, T. R. Cundari, T. B. Gunnoe, *Science* **2015**, *348*, 421–424.
- [24] J. L. Roizen, M. E. Harvey, J. Du Bois, *Acc. Chem. Res.* **2012**, *45*, 911–922.
- [25] J. M. Mayer, *Acc. Chem. Res.* **2011**, *44*, 36–46.
- [26] Y. Park, Y. Kim, S. Chang, *Chem. Rev.* **2017**, *117*, 9247–9301.
- [27] D. M. Jenkins, T. A. Betley, J. C. Peters, *J. Am. Chem. Soc.* **2002**, *124*, 11238–11239.
- [28] X. Hu, K. Meyer, *J. Am. Chem. Soc.* **2004**, *126*, 16322–16323.
- [29] D. T. Shay, G. P. A. Yap, L. N. Zakharov, A. L. Rheingold, K. H. Theopold, *Angew. Chemie - Int. Ed.* **2005**, *44*, 1508–1510.
- [30] R. E. Cowley, R. P. Bontchev, J. Sorrell, O. Sarracino, Y. Feng, H. Wang, J. M. Smith, *J. Am. Chem. Soc.* **2007**, *129*, 2424–2425.
- [31] J. Du, L. Wang, M. Xie, L. Deng, *Angew. Chemie - Int. Ed.* **2015**, *54*, 12640–12644.
- [32] E. R. King, G. T. Sazama, T. A. Betley, *J. Am. Chem. Soc.* **2012**, *134*, 17858–17861.

- [33] M. K. Goetz, E. A. Hill, A. S. Filatov, J. S. Anderson, *J. Am. Chem. Soc.* **2018**, *140*, 13176–13180.
- [34] A. M. Geer, C. Tejel, J. A. López, M. A. Ciriano, **2014**, 5720–5724.
- [35] D. S. Glueck, J. Wu, F. J. Hollander, R. G. Bergman, *J. Am. Chem. Soc.* **1991**, *113*, 2041–2054.
- [36] R. S. Hay-Motherwell, G. Wilkinson, B. Hussain-Bates, M. B. Hursthouse, *Polyhedron* **1993**, *12*, 2009–2012.
- [37] M. Kinauer, M. Diefenbach, H. Bamberger, S. Demeshko, E. J. Reijerse, C. Volkmann, C. Würtele, J. Van Slageren, B. De Bruin, M. C. Holthausen, et al., *Chem. Sci.* **2018**, *9*, 4325–4332.
- [38] B. G. Jacobi, D. S. Laitar, L. Pu, M. F. Wargocki, A. G. DiPasquale, K. C. Fortner, S. M. Schuck, S. N. Brown, *Inorg. Chem.* **2002**, *41*, 4815–4823.
- [39] Y. Shimoyama, T. Kojima, *Inorg. Chem.* **2019**, *58*, 9517–9542.
- [40] P. F. Kuijpers, J. I. van der Vlugt, S. Schneider, B. de Bruin, I. Van Der Vlugt, S. Schneider, B. De Bruin, *Chem. Eur. J.* **2017**, *23*, 13819–13829.
- [41] M. G. Scheibel, B. Askevold, F. W. Heinemann, E. J. Reijerse, B. De Bruin, S. Schneider, *Nat. Chem.* **2012**, *4*, 552–558.
- [42] D. J. Mindiola, G. L. Hillhouse, *J. Am. Chem. Soc.* **2001**, *123*, 4623–4624.
- [43] V. M. Iluc, G. L. Hillhouse, *J. Am. Chem. Soc.* **2010**, *132*, 15148–15150.
- [44] C. A. Laskowski, A. J. M. Miller, G. L. Hillhouse, T. R. Cundari, *J. Am. Chem. Soc.* **2011**, *133*, 771–773.
- [45] A. Grünwald, N. Orth, A. Scheurer, F. W. Heinemann, A. Pöthig, D. Munz, *Angew. Chemie - Int. Ed.* **2018**, *57*, 16228–16232.
- [46] K. M. Carsch, I. M. DiMucci, D. A. Iovan, A. Li, S. L. Zheng, C. J. Titus, S. J. Lee, K. D. Irwin, D. Nordlund, K. M. Lancaster, et al., *Science* **2019**, *365*, 1138–1143.
- [47] E. Poverenov, I. Efremenko, A. I. Frenkel, Y. Ben-David, L. J. W. Shimon, G. Leitun, L. Konstantinovski, J. M. L. Martin, D. Milstein, *Nature* **2008**, *455*, 1093–1096.
- [48] R. L. S. James T. Hynes, Judith P. Klinman, Hans-Heinrich Limbach, Ed., *Hydrogen Transfer Reactions*, Wiley-VCH, Weinheim, Germany, **2007**.
- [49] D. J. Vinyard, G. M. Ananyev, G. Charles Dismukes, *Annu. Rev. Biochem.* **2013**, *82*, 577–606.
- [50] C. J. M. Van Der Ham, M. T. M. Koper, D. G. H. Hetterscheid, *Chem. Soc. Rev.* **2014**, *43*, 5183–5191.
- [51] D. C. Miller, K. T. Tarantino, R. R. Knowles, *Top. Curr. Chem.* **2016**, *374*, 1–59.
- [52] C. J. Gagliardi, B. C. Westlake, C. A. Kent, J. J. Paul, J. M. Papanikolas, T. J. Meyer, *Coord. Chem. Rev.* **2010**, *254*, 2459–2471.
- [53] J. J. Warren, T. A. Tronic, J. M. Mayer, *Chem Rev.* **2010**, *110*, 6961–7001.
- [54] M. H. V. Huynh, T. J. Meyer, *Chem. Rev.* **2007**, *107*, 5004–5064.
- [55] R. A. Binstead, B. A. Moyer, G. J. Samuels, T. J. Meyer, *J. Am. Chem. Soc.* **1981**, *103*, 2897–2899.
- [56] C. Costentin, D. H. Evans, M. Robert, J. M. Savéant, P. S. Singh, *J. Am. Chem. Soc.* **2005**, *127*, 12490–12491.
- [57] M. K. Goetz, J. S. Anderson, *J. Am. Chem. Soc.* **2019**, *141*, 4051.
- [58] D. Bím, M. Maldonado-Domínguez, L. Rulíšek, M. Srnc, *Proc. Natl. Acad. Sci.* **2018**, *115*, E10287–E10294.
- [59] J. M. Mayer, *Acc. Chem. Res.* **1998**, *31*, 441–450.
- [60] F. G. Bordwell, J.-P. Chen, J. A. Harrelson Jr., *J. Am. Chem. Soc.* **1988**, *110*, 1229–1231.
- [61] W. S. Matthews, J. E. Bares, J. E. Bartmess, F. J. Cornforth, G. E. Drucker, R. J. McCallum, G. J. McCollum, N. R. Vanier, F. G. Bordwell, Z. Margolin, *J. Am. Chem. Soc.* **1975**, *97*, 7006–7014.

- [62] F. G. Bordwell, *Acc. Chem. Res.* **1988**, *21*, 456–463.
- [63] M. Tilset, in *Electron Transf. Chem.* (Ed.: V. Balzani), WILEY-VCH Verlag GmbH, Weinheim, Germany, **2001**, pp. 1–800.
- [64] E. Roduner, *Radiat. Phys. Chem.* **2005**, *72*, 201–206.
- [65] V. D. Parker, M. Tilset, *J. Am. Chem. Soc.* **1989**, *111*, 6711–6717.
- [66] E. A. Mader, E. R. Davidson, J. M. Mayer, *J. Am. Chem. Soc.* **2007**, *129*, 5153–5166.
- [67] K. B. WIBERG, *Oxidation-Reduction Mechanisms in Organic Chemistry*, ACADEMIC PRESS INC., **1963**.
- [68] K. B. Wiberg, R. Eisenthal, *Tetrahedron* **1964**, *20*, 1151–1161.
- [69] T. R. Cundari, R. R. Conry, E. Spaltenstein, S. C. Critchlow, K. A. Hall, S. K. Tahmassebi, J. M. Mayer, *Organometallics* **1994**, *13*, 322–331.
- [70] G. K. Cook, J. M. Mayer, *J. Am. Chem. Soc.* **1994**, *116*, 1855–1868.
- [71] G. K. Cook, J. M. Mayer, *J. Am. Chem. Soc.* **1995**, *117*, 7139–7156.
- [72] M. Szostak, N. J. Fazakerley, D. Parmar, D. J. Procter, *Chem. Rev.* **2014**, *114*, 5959–6039.
- [73] T. V. Chciuk, W. R. Anderson, R. A. Flowers, *J. Am. Chem. Soc.* **2016**, *138*, 8738–8741.
- [74] T. V. Chciuk, W. R. Anderson, R. A. Flowers, *Angew. Chemie - Int. Ed.* **2016**, *55*, 6033–6036.
- [75] M. Pourbaix, *Atlas of Electrochemical Equilibria in Aqueous Solutions*, National Association Of Corrosion Engineers, Houston, **1974**.
- [76] W. A. Nugent, J. A. Mayer, *Metal-Ligand Multiple Bonds*, Wiley-Interscience, **1988**.
- [77] W. J. Mijs, C. R. H. I. de Jonge, Eds., *Organic Synthesis by Oxidation with Metal Compounds*, Plenum, New York, **1986**.
- [78] B. A. Moyer, T. J. Meyer, *Inorg. Chem.* **1981**, *20*, 436–444.
- [79] E. L. Lebeau, R. A. Binstead, T. J. Meyer, *J. Am. Chem. Soc.* **2001**, *123*, 10535–10544.
- [80] D. T. Sawyer, *Oxygen Chemistry*, Oxford University Press, New York, **1991**.
- [81] L. Duan, F. Bozoglian, S. Mandal, B. Stewart, T. Privalov, A. Llobet, L. Sun, *Nat. Chem.* **2012**, *4*, 418–423.
- [82] H. S. Yu, S. L. Li, D. G. Truhlar, *J. Chem. Phys.* **2016**, *145*, DOI 10.1063/1.4963168.
- [83] J. P. Perdew, K. Schmidt, *AIP Conf. Proc.* **2001**, *577*, 1–20.
- [84] W. Koch, M. C. Holthausen, *A Chemist's Guide to Density Functional Theory*, Wiley-VCH Verlag GmbH, Weinheim, Germany, **2001**.
- [85] R. J. Bartlett, *J. Chem. Phys.* **2019**, *151*, DOI 10.1063/1.5116338.
- [86] R. A. Friesner, *Proc. Natl. Acad. Sci. U. S. A.* **2005**, *102*, 6648–6653.
- [87] R. J. Bartlett, J. F. Stanton, in *Rev. Comput. Chem.* (Eds.: K.B. Lipkowitz, D.B. Boyd), VCH Publishers, Inc., **1995**, pp. 65–169.
- [88] P.-O. Löwdin, in *Adv. Chem. Phys.* (Ed.: I. Prigogine), John Wiley & Sons, Inc., **1958**.
- [89] M. Kodrycka, K. Patkowski, *J. Chem. Phys.* **2019**, *151*, 070901:1–17.
- [90] H. J. Werner, F. R. Manby, *J. Chem. Phys.* **2006**, *124*, 054114:1–12.
- [91] F. Neese, F. Wennmohs, A. Hansen, *J. Chem. Phys.* **2009**, *130*, 114108:1–18.
- [92] F. Neese, A. Hansen, D. G. Liakos, *J. Chem. Phys.* **2009**, *131*, 064103:1–15.
- [93] C. Riplinger, F. Neese, *J. Chem. Phys.* **2013**, *138*, 034106:1–18.
- [94] Y. Guo, C. Riplinger, U. Becker, D. G. Liakos, Y. Minenkov, L. Cavallo, F. Neese, *J. Chem. Phys.* **2018**, *148*,

011101.

- [95] C. Riplinger, P. Pinski, U. Becker, E. F. Valeev, F. Neese, *J. Chem. Phys.* **2016**, *144*, 024109.
- [96] L. W. Chung, W. M. C. Sameera, R. Ramozzi, A. J. Page, M. Hatanaka, G. P. Petrova, T. V. Harris, X. Li, Z. Ke, F. Liu, et al., *Chem. Rev.* **2015**, *115*, 5678–5796.
- [97] M. Svensson, S. Humbel, K. Morokuma, *J. Chem. Phys.* **1996**, *105*, 3654–3661.
- [98] M. Svensson, R. D. J. Froese, T. Matsubara, S. Sieber, K. Morokuma, *J. Chem. Phys.* **1996**, *100*, 19357–19363.
- [99] C. Edmiston, M. Krauss, *J. Chem. Phys.* **1965**, *42*, 1119–1120.
- [100] C. Edmiston, M. Krauss, *J. Chem. Phys.* **1966**, *45*, 1833–1839.
- [101] G. Czakó, E. Mátyus, A. G. Császár, *J. Phys. Chem. A* **2009**, *113*, 11665–11678.
- [102] P. R. Bunker, P. Jensen, W. P. Krämer, R. Beardsworth, *J. Chem. Phys.* **1986**, *85*.
- [103] G. Wedler, H.-J. Freund, *Lehrbuch Der Physikalischen Chemie*, WILEY-VCH Verlag GmbH, Weinheim, Germany, **2012**.
- [104] B. O. Roos, P. M. Siegbahn, *J. Am. Chem. Soc.* **1977**, *99*, 7716–7718.
- [105] B. O. Roos, P. R. Taylor, P. E. M. Siegbahn, *Chem. Phys.* **1980**, *48*, 157–173.
- [106] P. Siegbahn, A. Heiberg, B. Roos, B. Levy, *Phys. Scr.* **1980**, *21*, 323–327.
- [107] P. E. M. Siegbahn, J. Almlöf, A. Heiberg, B. O. Roos, *J. Chem. Phys.* **1981**, *74*, 2384–2396.
- [108] J. Olsen, *Int. J. Quantum Chem.* **2011**, *111*, 3267–3272.
- [109] P. G. Szalay, T. Müller, G. Gidofalvi, H. Lischka, R. Shepard, *Chem. Rev.* **2012**, *112*, 108–181.
- [110] C. Angeli, R. Cimiraglia, S. Evangelisti, T. Leininger, J. P. Malrieu, *J. Chem. Phys.* **2001**, *114*, 10252.
- [111] C. Angeli, R. Cimiraglia, J. P. Malrieu, *Chem. Phys. Lett.* **2001**, *350*, 297–305.
- [112] C. Angeli, R. Cimiraglia, J. P. Malrieu, *J. Chem. Phys.* **2002**, *117*, 9138–9153.
- [113] K. Andersson, P. Å. Malmqvist, B. O. Roos, A. J. Sadlej, K. Wolinski, *J. Phys. Chem.* **1990**, *94*, 5483–5488.
- [114] K. Andersson, P. Å. Malmqvist, B. O. Roos, *J. Chem. Phys.* **1991**, *96*, 1218–1226.
- [115] J. M. Rintelman, I. Adamovic, S. Varganov, M. S. Gordon, *J. Chem. Phys.* **2005**, *122*, 044105:1–7.
- [116] C. Camacho, H. A. Witek, S. Yamamoto, *J. Comput. Chem.* **2008**, *30*, 468–478.
- [117] B. Nagy, F. Jensen, in *Rev. Comput. Chem.* (Eds.: A.L. Parrill, K.B. Lipkowitz.), John Wiley & Sons, Inc., **2017**, pp. 93–149.
- [118] F. Weigend, R. Ahlrichs, *Phys. Chem. Chem. Phys.* **2005**, *7*, 3297–3305.
- [119] T. H. Dunning, *J. Chem. Phys.* **1989**, *90*, 1007–1023.
- [120] D. E. Woon, T. H. Dunning, *J. Chem. Phys.* **1993**, *98*, 1358–1371.
- [121] K. A. Peterson, T. B. Adler, H. J. Werner, *J. Chem. Phys.* **2008**, *128*, 084102.
- [122] L. Kong, F. A. Bischoff, E. F. Valeev, *Chem. Rev.* **2012**, *112*, 75–107.
- [123] J. G. Hill, K. A. Peterson, G. Knizia, H. J. Werner, *J. Chem. Phys.* **2009**, *131*, 194105:1–13.
- [124] G. Knizia, T. B. Adler, H. J. Werner, *J. Chem. Phys.* **2009**, *130*, 054104.
- [125] W. Klopper, F. R. Manby, S. Ten-No, E. F. Valeev, *Int. Rev. Phys. Chem.* **2006**, *25*, 427–468.
- [126] S. Ten-no, J. Noga, *Wiley Interdiscip. Rev. Comput. Mol. Sci.* **2012**, *2*, 114–125.
- [127] S. Ten-No, *Theor. Chem. Acc.* **2012**, *131*, 1070:1–11.
- [128] A. Einstein, *Ann. Phys.* **1905**, *322*, 891–921.

- [129] P. Pyykkö, in *Adv. QUANTUM Chem.*, Academic Press, **1978**, pp. 354–409.
- [130] P. Pyykkö, *Chem Rev.* **1988**, *12*, 563–594.
- [131] W. H. E. Schwarz, E. M. van Wezenbeek, E. J. Baerends, J. G. Snijders, *J. Phys. B* **1989**, *22*, 1515–1530.
- [132] J. L. Dehmer, *Phys. Rev. A* **1973**, *7*, 4–9.
- [133] B. Lepetit, J. M. Launay, M. LE Dourneuf, *Chem. Phys.* **1986**, *106*, 103–110.
- [134] C. Heinemann, H. Schwarz, W. Koch, K. G. Dyall, *J. Chem. Phys.* **1996**, *104*, 4642.
- [135] T. Fleig, *Relativistic String-Based Electron Correlation Methods*, Springer, Dordrecht, Heidelberg, London, New York, **2010**.
- [136] P. E. M. Siegbahn, M. Svensson, R. H. Crabtree, *J. Am. Chem. Soc.* **1995**, *117*, 6758–6765.
- [137] J. J. Carroll, J. C. Weissarr, P. E. M. Siegbahn, C. A. M. Wittborn, M. R. A. Blomberg, *J. Phys. Chem.* **1995**, *99*, 14388–14396.
- [138] K. Chen, G. Zhang, H. Chen, J. Yao, D. Danovich, S. Shaik, *J. Chem. Theory Comput.* **2012**, *8*, 1641–1645.
- [139] P. Jerabek, L. Vondung, P. Schwerdtfeger, *Chem. - A Eur. J.* **2018**, *24*, 6047–6051.
- [140] M. Srnec, J. Chalupsky, M. Fojta, L. Zendlova, L. Havran, M. Hocek, M. Kyvala, L. Rulisek, *J. Am. Chem. Soc.* **2008**, *130*, 10947–10954.
- [141] P. Pyykkö, *Annu. Rev. Phys. Chem.* **2012**, *63*, 45–64.
- [142] D. Peng, M. Reiher, *Theor. Chem. Acc.* **2012**, *131*, 1081:1–20.
- [143] D. A. Pantazis, X. Y. Chen, C. R. Landis, F. Neese, *J. Chem. Theory Comput.* **2008**, *4*, 908–919.
- [144] D. A. Pantazis, X. Y. Chen, C. R. Landis, F. Neese, *J. Chem. Theory Comput.* **2008**, *4*, 908–919.
- [145] D. Figgen, K. A. Peterson, M. Dolg, H. Stoll, *J. Chem. Phys.* **2009**, *130*, 164108.
- [146] M. Dolg, in *Handb. Relativ. Quantum Chem.*, Springer-Verlag, Berlin Heidelberg, **2017**, pp. 449–478.
- [147] C. Chang, M. Pelissier, P. Durand, *Phys. Scr.* **1986**, *34*, 394–404.
- [148] E. Van Lenthe, R. Van Leeuwen, E. J. Baerends, J. G. Snijders, *Int. J. Quantum Chem.* **1993**, *99*, 4597–4610.
- [149] E. Van Lenthe, E. J. Baerends, J. G. Snijders, *J. Chem. Phys.* **1994**, *101*, 9783–9792.
- [150] R. Van Leeuwen, E. Van Lenthe, E. J. Baerends, J. G. Snijders, *J. Chem. Phys.* **1994**, *101*, 1272–1281.
- [151] E. Van Lenthe, R. Van Leeuwen, E. J. Baerends, J. G. Snijders, *Int. J. Quant. Chem.* **1996**, *57*, 281–293.
- [152] M. Barysz, in *Theor. Chem. Phys. Heavy Super Heavy Elem.* (Ed.: U.K. and S. Wilson), Kluwer Academic Publishers, **2003**, pp. 349–397.
- [153] “ADF Relativistic effects,” can be found under https://www.scm.com/doc/ADF/Input/Relativistic_effects.html, **2020**.
- [154] “ORCA Input Library Relativistic Approximations,” can be found under <https://sites.google.com/site/orcainputlibrary/relativistic-approximations>, **2020**.
- [155] B. A. Heß, C. M. Marian, U. Wahlgren, O. Gropen, *Chem. Phys. Lett.* **1996**, *251*, 365–371.
- [156] D. Ganyushin, F. Neese, *J. Chem. Phys.* **2013**, *138*, 1–18.
- [157] D. Delony, M. Kinauer, M. Diefenbach, S. Demeshko, C. Würtele, M. C. Holthausen, S. Schneider, *Angew. Chemie - Int. Ed.* **2019**, *58*, 10971–10974.
- [158] F. Schendzielorz, M. Finger, J. Abbenseth, C. Würtele, V. Krewald, S. Schneider, *Angew. Chemie - Int. Ed.* **2019**, *131*, 840–844.
- [159] M. Kinauer, Transient and Stable Terminal Imido Complexes of Iridium, Georg-August Universität

Göttingen, 2019.

- [160] J. Meiners, M. G. Scheibel, M. H. Lemée-Cailleau, S. A. Mason, M. B. Boeddinghaus, T. F. Fässler, E. Herdtweck, M. M. Khusniyarov, S. Schneider, *Angew. Chemie - Int. Ed.* **2011**, *50*, 8184–8187.
- [161] D. A. Ortmann, H. Werner, *Zeitschrift für Anorg. und Allg. Chemie* **2002**, *628*, 1373–1376.
- [162] K. Ilg, H. Werner, *Organometallics* **1999**, *18*, 5426–5428.
- [163] R. J. Burford, W. E. Piers, D. H. Ess, M. Parvez, *J. Am. Chem. Soc.* **2014**, *136*, 3256–3263.
- [164] D. Sieh, M. Schlimm, L. Andernach, F. Angersbach, S. Nüchel, J. Schöffel, N. Šušnjar, P. Burger, *Eur. J. Inorg. Chem.* **2012**, 444–462.
- [165] L. M. Green, D. W. Meek, *Organometallics* **1989**, *8*, 659–666.
- [166] D. Morales-Morales, D. W. Lee, Z. Wang, C. M. Jensen, *Organometallics* **2001**, *20*, 1144–1147.
- [167] M. D. Millard, C. E. Moore, A. L. Rheingold, J. S. Figueroa, *J. Am. Chem. Soc.* **2010**, *132*, 8921–8923.
- [168] P. Kläring, S. Pahl, T. Braun, A. Penner, *Dalt. Trans.* **2011**, *40*, 6785–6791.
- [169] J. C. M. Ritter, R. G. Bergman, *J. Am. Chem. Soc.* **1997**, *119*, 2580–2581.
- [170] C. A. Miller, T. S. Janik, C. H. Lake, L. M. Toomey, M. R. Churchill, J. D. Atwood, *Organometallics* **1994**, *13*, 5080–5087.
- [171] F. T. Ladipo, M. Kooti, J. S. Merola, *Inorg. Chem.* **1993**, *32*, 1681–1688.
- [172] B. J. Truscott, D. J. Nelson, C. Lujan, A. M. Z. Slawin, S. P. Nolan, *Chem. - A Eur. J.* **2013**, *19*, 7904–7916.
- [173] V. Chandrasekhar, B. Mahanti, P. Bandipalli, K. Bhanuprakash, *Inorg. Chem.* **2012**, *51*, 10536–10547.
- [174] W. J. Tenn, K. J. H. Young, J. Oxgaard, R. J. Nielsen, W. A. Goddard, R. A. Periana, *Organometallics* **2006**, *25*, 5173–5175.
- [175] H. Jacobs, U. Metzner, *Zeitschrift für Anorg. und Allg. Chemie* **1991**, *597*, 97–106.
- [176] J. U. Rohde, W. T. Lee, *J. Am. Chem. Soc.* **2009**, *131*, 9162–9163.
- [177] I. Efremenko, E. Poverenov, J. M. L. Martin, D. Milstein, *J. Am. Chem. Soc.* **2010**, *132*, 14886–14900.
- [178] G. R. Fulmer, A. J. M. Miller, N. H. Sherden, H. E. Gottlieb, A. Nudelman, B. M. Stoltz, J. E. Bercaw, K. I. Goldberg, *Organometallics* **2010**, *29*, 2176–2179.
- [179] M. Kinauer, M. G. Scheibel, J. Abbenseth, F. W. Heinemann, P. Stollberg, C. Würtele, S. Schneider, *Dalt. Trans.* **2014**, *43*, 4506–4513.
- [180] H. Effenberger, K. Mereiter, J. Zemann, *Zeitschrift für Krist. - New Cryst. Struct.* **1981**, *156*, 233–243.
- [181] J. J. Scepaniak, C. G. Margarit, J. N. Harvey, J. M. Smith, *Inorg. Chem.* **2011**, *50*, 9508–9517.
- [182] F. S. Schendzielorz, M. Finger, C. Volkmann, C. Würtele, S. Schneider, *Angew. Chemie - Int. Ed.* **2016**, *55*, 11417–11420.
- [183] Y. Y. Rusakov, I. L. Rusakova, L. B. Krivdin, *Magn. Reson. Chem* **2018**, *56*, 1061–1073.
- [184] J. Abbenseth, D. Delony, M. C. Neben, W. Christian, B. De Bruin, S. Schneider, *Angew. Chemie - Int. Ed.* **2019**, 6404–6407.
- [185] M. H. Abraham, P. L. Grellier, D. V Prior, P. P. Duce, J. J. Morris, P. J. Taylor, *J Chem. Soc. Perkin Trans* **1989**, *II*, 699–711.
- [186] M. H. Abraham, P. L. Grellier, D. V Prior, J. J. Morris, P. J. Taylor, *J Chem. Soc. Perkin Trans* **1990**, *2*, 521–529.
- [187] E. P. Cappellani, S. D. Drouin, G. Jia, P. A. Maltby, R. H. Morris, C. T. Schweitzer, *J. Am. Chem. Soc.* **1994**,

116, 3375–3388.

- [188] G. B. Shul'Pin, *Catalysts* **2016**, *6*, 1–40.
- [189] F. Jia, Z. Li, *Org. Chem. Front.* **2014**, *1*, 194–214.
- [190] P. C. Li, T. S. Wang, G. H. Lee, Y. H. Liu, Y. Wang, C. T. Chen, I. Chao, *J. Org. Chem.* **2002**, *67*, 8002–8009.
- [191] Z. B. Alfassi, D. M. Golden, *J. Am. Chem. Soc.* **1973**, *95*, 319–323.
- [192] C. Hansch, A. Leo, R. W. Taft, *Chem. Rev.* **1991**, *91*, 165–195.
- [193] S. Marque, P. Tordo, in *New Asp. Phosphorous Chem. V, Top. Curr. Chem.* (Ed.: J. Majoral), Springer, Berlin, Heidelberg, **2005**, p. 43.
- [194] P. P. Power, *Chem. Rev.* **2003**, *103*, 789–809.
- [195] A. Armstrong, T. Chivers, R. T. Boéré, *The Diversity of Stable and Persistent Phosphorus-Containing Radicals*, ACS Symposium Series, **2005**.
- [196] C. D. Martin, M. Soleilhavoup, G. Bertrand, *Chem. Sci.* **2013**, *4*, 3020–3030.
- [197] V. Nesterov, D. Reiter, P. Bag, P. Frisch, R. Holzner, A. Porzelt, S. Inoue, *Chem. Rev.* **2018**, *118*, 9678–9842.
- [198] J. K. Pagano, B. J. Ackley, R. Waterman, *Chem. - A Eur. J.* **2018**, *24*, 2554–2557.
- [199] K. Pal, O. B. Hemming, B. M. Day, T. Pugh, D. J. Evans, R. A. Layfield, *Angew. Chemie - Int. Ed.* **2016**, *55*, 1690–1693.
- [200] G. Dequierez, V. Pons, P. Dauban, *Angew. Chemie - Int. Ed.* **2012**, *51*, 7384–7395.
- [201] M. J. Bezdek, S. Guo, P. J. Chirik, *Science* **2016**, *354*, 730.
- [202] S. S. Kolmar, J. M. Mayer, *J. Am. Chem. Soc.* **2017**, *139*, 10687–10692.
- [203] R. Melenkivitz, D. J. Mindiola, G. L. Hillhouse, *J. Am. Chem. Soc.* **2002**, *124*, 3846–3847.
- [204] J. Abbenseth, M. Diefenbach, S. C. Bete, C. Würtele, C. Volkmann, S. Demeshko, M. C. Holthausen, S. Schneider, *Chem. Commun.* **2017**, *53*, 5511–5514.
- [205] F. G. Bordwell, J. Cheng, *J. Am. Chem. Soc.* **1991**, *113*, 1736–1743.
- [206] P. H. Pfromm, *J. Renew. Sustain. Energy* **2017**, *9*, 034702:1–11.
- [207] R. Lan, S. Tao, *Front. Energy Res.* **2014**, *2*, 3–6.
- [208] I. Klopsch, M. Kinauer, M. Finger, C. Würtele, S. Schneider, *Angew. Chemie - Int. Ed.* **2016**, *55*, 4786–4789.
- [209] B. M. Lindley, R. S. van Alten, M. Finger, F. Schendzielorz, C. Würtele, A. J. M. Miller, I. Siewert, S. Schneider, *J. Am. Chem. Soc.* **2018**, *140*, 7922–7935.
- [210] *Coord. Chem. Rev.* **1996**, *150*, 77–110.
- [211] B. H. P. Gunz, G. J. Leigh, *J. Chem. Soc. A.* **1971**, 2229–2233.
- [212] B. Bleaney, *J. Magn. Reson.* **1972**, *8*, 91–100.
- [213] B. Martin, J. Autschbach, *J. Chem. Phys.* **2015**, *142*, DOI 10.1063/1.4906318.
- [214] J. Chatt, G. J. Leigh, D. M. P. Mingos, *J. Chem. Soc.* **1969**, 1974–1980.
- [215] I. P. Theor, A. Ligands, B. E. W. Randall, D. Shaw, M. College, M. E. Road, E. London, *J. Chem. Soc. A* **1969**, 2867–2872.
- [216] A. Soncini, W. Van Den Heuvel, *J. Chem. Phys.* **2013**, *138*, 021103.
- [217] V. I. Belova, Y. L. Sykrin, E. G. Ippolitov, A. S. Kotelnikova, G. K. Babeshkina, R. A. Dovlyatshina, *Zhurnal Strukt. Khimii* **1964**, *5*, 252–257.
- [218] A. Earnshaw, B. N. Figgis, J. Lewis, R. D. Peacock, *J. Chem. Soc.* **1961**.

- [219] F. Cariati, A. Sgamellotti, F. Morazzoni, V. Valenti, *Inorganica Chim. Acta* **1971**, *5*, 531–535.
- [220] G. Rouschias, G. Wilkinson, G. Wilkinson, *J. Chem. Soc. A* **1967**, 993–1000.
- [221] N. S. Hush, J. R. Reimers, *Chem. Rev.* **2000**, *100*, 775–786.
- [222] S. Tshepelevitsh, A. Kütt, M. Lökov, I. Kaljurand, J. Saame, A. Heering, P. G. Plieger, R. Vianello, I. Leito, *European J. Org. Chem.* **2019**, *2019*, 6735–6748.
- [223] R. M. Fuoss, *J. Am. Chem. Soc.* **1958**, *80*, 5059–5061.
- [224] T. Wiseman, S. Williston, J. F. Brandts, L. N. Lin, *Anal. Biochem.* **1989**, *179*, 131–137.
- [225] M. G. Scheibel, J. Abbenseth, M. Kinauer, F. W. Heinemann, C. Wu, B. De Bruin, S. Schneider, *Inorg. Chem.* **2015**, *54*, 9290–9302.
- [226] V. W. Manner, T. F. Markle, J. H. Freudenthal, J. P. Roth, J. M. Mayer, *Chem. Commun.* **2008**, *246*, 256–258.
- [227] J. Meiners, A. Friedrich, E. Herdtweck, S. Schneider, *Organometallics* **2009**, *28*, 6331–6338.
- [228] N. Elgrishi, K. J. Rountree, B. D. McCarthy, E. S. Rountree, T. T. Eisenhart, J. L. Dempsey, *J. Chem. Educ.* **2018**, *95*, 197–206.
- [229] D. R. Lide, Ed., *CRC Handbook of Chemistry and Physics: A Ready-Reference Book of Chemical and Physical Data*, CRC Press, Boca Raton, **2005**.
- [230] M. J. O. S. Budavari, A. Smith, P. E. Heckelman, *The Merck Index, an Encyclopedia of Chemicals, Drugs, and Biologicals*, Merck Co. Inc., Rahway, NJ, **1989**.
- [231] H. E. Gottlieb, V. Kotlyar, A. Nudelman, *J. Org. Chem.* **1997**, *62*, 7512–7515.
- [232] E. Bill, *JulX, Program for Simulation of Molecular Magnetic Data Matrix Diagonalization Is Done with the Routine ZHEEV from the LAPACK Numerical Package. Parameter Optimization Is Performed with the Simplex Routine AMOEBA from NUMERICAL RECIPES*, Max-Planck Institute For Chemical Energy Conversion,, Mülheim/Ruhr, **2008**.
- [233] Bruker AXS Inc., *APEX2 V2016.9-0 (SAINT/SADABS/SHELXT/SHELXL)*, Madison, WI, USA, **2016**.
- [234] G. M. Sheldrick, *Acta Cryst.* **2015**, *A71*, 3–8.
- [235] G. M. Sheldrick, *Acta Cryst.* **2015**, *C71*, 3–8.
- [236] G. M. Sheldrick, *Acta Cryst.* **2008**, *A64*, 112–122.
- [237] D. F. Evans, *J. Chem. Soc.* **1959**, 2003–2005.
- [238] S. K. Sur, *J. Magn. Reson.* **1989**, *82*, 169–173.
- [239] M. J. Frisch, G. W. Trucks, H. B. Schlegel, G. E. Scuseria, M. A. Robb, J. R. Cheeseman, G. Scalmani, V. Barone, G. A. Petersson, H. Nakatsuji, et al., *Gaussian, Inc., Wallingford, CT* **2016**.
- [240] S. Grimme, J. Antony, S. Ehrlich, H. Krieg, *J Chem Phys* **2010**, *154104*, 1–9.
- [241] A. D. Becke, *J. Chem. Phys.* **1993**, *98*, 5648–5652.
- [242] C. Adamo, *J Chem Phys* **2008**, *110*, 6158–6170.
- [243] D. Andrae, U. Häußermann, M. Dolg, H. Stoll, H. Preuß, *Theor. Chim. Acta* **1990**, 123–141.
- [244] A. V Marenich, C. J. Cramer, D. G. Truhlar, *J. Phys. Chem. B* **2009**, *113*, 6378–6396.
- [245] D. Aravena, M. Atanasov, A. A. Auer, U. Becker, G. Bistoni, M. Brehm, D. Bykov, V. G. Chilkuri, D. Datta, A. K. Dutta, et al., *Max-Planck-Institut für Chem. Energiekonversion, Mülheim a. d. Ruhr, Ger.* **2017**.
- [246] F. Neese, *WIREs Comput Mol Sci* **2012**, *2*, 73–78.

- [247] R. A. Kendall, T. H. Dunning, R. J. Harrison, *J. Chem. Phys.* **1992**, *96*, 6796–6806.
- [248] F. Weigend, A. Köhn, C. Hättig, *J. Chem. Phys.* **2002**, *116*, 3175–3183.
- [249] S. Ten-no, *Chem. Phys. Lett.* **2004**, *398*, 56–61.
- [250] T. B. Adler, G. Knizia, H. J. Werner, *J. Chem. Phys.* **2007**, *127*, 221106.
- [251] H.-J. Werner, P. J. Knowles, G. Knizia, M. F.R, M. Schütz, P. Celani, W. Györffy, D. Kats, T. Korona, R. Lindh, et al., “MOLPRO, version 2015.1 a package of ab initio programs,” **2015**.
- [252] K. E. Yousaf, K. A. Peterson, *J. Chem. Phys.* **2008**, *129*, 184108.
- [253] S. Kritikou, J. G. Hill, *J. Chem. Theory Comput.* **2015**, *11*, 5269–5276.
- [254] F. Weigend, *J. Comput. Chem.* **2007**, *29*, 167–175.
- [255] J. G. Hill, *J. Chem. Phys.* **2011**, *135*, 044105.
- [256] C. Van Wüllen, *J. Chem. Phys.* **1998**, *109*, 392–399.
- [257] F. Weigend, *Phys. Chem. Chem. Phys.* **2002**, *4*, 4285–4291.
- [258] M. Atanasov, D. Aravena, E. Suturina, E. Bill, D. Maganas, F. Neese, *Coord. Chem. Rev.* **2015**, *289–290*, 177–214.
- [259] C. F. Wise, R. G. Agarwal, J. M. Mayer, *J. Am. Chem. Soc.* **2020**, *142*, 10681–10691.
- [260] E. Brunner, *J. Chem. Eng. Data* **1985**, *30*, 269–273.

Chapter VIII

7. Appendix

A. Crystal Structures

A.1. X-Ray Single-Crystal Analysis of **1**

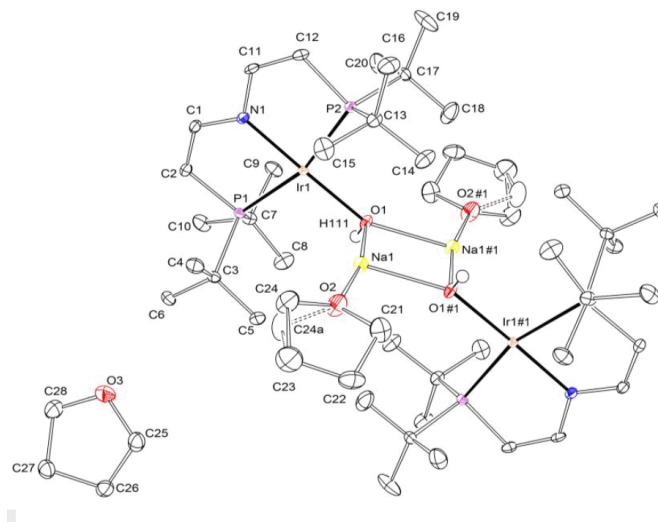


Figure A1: Thermal ellipsoid plot of **1** with the anisotropic displacement parameters drawn at the 50% probability level. The asymmetric unit contains a half disordered complex molecule and one THF solvent molecule. The disordered complex molecule was refined with population of 0.64(3) on the main domain. The O-H hydrogen atom was found from the residual density map and isotropically refined.

Table A1: Crystallographic data and structure refinement for **1**.

Crystal data and structure refinement for 1		
Identification code	CW_DD_131117_a (DD-160)	
CCDC code	1912510	
Empirical formula	C ₅₆ H ₁₁₄ Ir ₂ N ₂ Na ₂ O ₆ P ₄	
Formula weight	1465.75	
Temperature	100(2) K	
Wavelength	0.71073 Å	
Crystal system	Triclinic	
Space group	<i>P</i> ₁	
Unit cell dimensions	<i>a</i> = 11.8784(6) Å	α = 63.788(2)°
	<i>b</i> = 12.2817(6) Å	β = 72.811(2)°
	<i>c</i> = 12.9250(7) Å	χ = 80.412(2)°
Volume	1614.70(15) Å ³	
<i>Z</i>	1	
Density (calculated)	1.507 Mg/m ³	
Absorption coefficient	4.275 mm ⁻¹	
Crystal size	0.494 x 0.382 x 0.306 mm ³	
Crystal shape and color	Block, clear intense orange	
Theta range for data collection	2.210 to 28.395°	
Index ranges	-15 ≤ <i>h</i> ≤ 15, -16 ≤ <i>k</i> ≤ 16, -17 ≤ <i>l</i> ≤ 17	
Reflections collected	88582	
Independent reflections	8083 [R(int) = 0.0727]	
Completeness to theta	25.242° 99.9 %	
Refinement method	Full-matrix least-squares on F ²	
Data / restraints / parameters	8083 / 0 / 351	
Goodness-of-fit on F ²	1.040	
Final R indices [I > 2σ(I)]	R1 = 0.0212,	wR2 = 0.0417
R indices (all data)	R1 = 0.0278,	wR2 = 0.0441
Largest diff. peak and hole	2.276 and -1.314 eÅ ⁻³	

Table A2: Cartesian coordinates from X-Ray single-crystal analysis of **1**

Ir	10.707566	9.649295	2.897519	H	8.44529	5.43972	0.057427	C	5.243511	8.538268	10.510628
P	11.142759	11.887684	3.095774	H	9.402813	4.834156	1.187689	H	4.584323	8.436769	11.187133
P	10.72123	7.463874	2.208846	H	10.027531	5.663	-0.03042	C	5.83307	9.735739	10.34735
Na	10.428574	8.762182	5.885073	C	8.745406	8.004715	0.425493	H	5.634105	10.487533	10.892983
O	9.083787	9.540758	4.278042	H	9.431934	8.089645	-0.268669	C	6.304429	11.139162	7.892532
O	12.117705	8.206201	7.294478	H	8.678465	8.846138	0.923409	C	7.26713	11.511263	6.761045
N	12.176799	9.795448	1.496813	H	7.882076	7.802545	0.008104	H	7.959928	12.112435	7.106056
C	12.750954	10.991658	1.204931	C	11.877878	7.232253	8.317239	H	7.685985	10.698649	6.408032
H	13.416504	11.032161	0.528246	H	12.065004	6.319815	7.98177	H	6.771517	11.960809	6.04504
C	12.401155	12.123741	1.850512	H	10.937609	7.272345	8.624477	H	8.91917	6.97393	6.902323
H	12.789095	12.969725	1.659934	C	12.824064	7.592322	9.443315	C	5.037262	10.511556	7.292648
C	11.971068	12.483777	4.688504	H	13.100813	6.787645	9.949279	H	4.402176	10.307969	8.010719
C	13.235175	11.625091	4.829041	H	12.408875	8.240161	10.066232	H	4.627645	11.140928	6.662973
H	13.846411	11.81988	4.088205	C	13.997936	8.210333	8.713042	H	5.273522	9.685337	6.821537
H	12.989632	10.676559	4.809184	H	14.80076	7.636205	8.790202	C	5.886712	12.424641	8.616687
H	13.676716	11.830493	5.679477	H	14.208276	9.105062	9.080872	H	6.685395	12.892614	8.938394
C	11.082882	12.215667	5.914404	H	14.486331	8.843831	9.296346	H	5.396062	13.003976	7.99698
H	10.329526	12.842437	5.915324	H	14.625929	7.514039	8.395387	H	5.311708	12.198878	9.37748
H	11.609444	12.33661	6.732018	C	13.535893	8.318283	7.225758	C	8.618053	10.379863	9.842081
H	10.74352	11.297059	5.877294	H	13.803575	9.187302	6.834288	C	9.731264	10.513804	8.805345
C	12.376226	13.958389	4.672935	H	13.922594	7.58751	6.681202	H	10.59189	10.619719	9.261964
H	12.877911	14.150672	3.853334	C	13.371415	8.907042	7.587651	H	9.755112	9.709559	8.245859
H	12.937881	14.151092	5.452542	H	13.967783	8.889891	6.797616	H	9.561194	11.298099	8.242885
H	11.572491	14.518315	4.702928	H	13.190252	9.850835	7.825384	C	8.481175	11.666602	10.647437
C	9.774562	13.085254	2.582154	Ir	7.036157	7.605388	8.327431	H	9.298434	11.814962	11.167523
C	8.739797	13.26281	3.697263	P	6.600965	5.366998	8.129176	H	8.34091	12.420526	10.03726
H	7.971186	13.763879	3.352915	P	7.022494	9.790809	9.016104	H	7.716192	11.591683	11.25537
H	9.143554	13.755175	4.442195	Na	7.315149	8.4925	5.339877	C	8.998317	9.249967	10.799457
H	8.44253	12.382961	4.010169	O	8.659936	7.713925	6.946908	H	8.31179	9.165037	11.493619
C	9.100728	12.418336	1.367872	O	5.626018	9.048482	3.930472	H	9.065258	8.408544	10.301541
H	8.376541	12.99166	1.040396	N	5.566924	7.459234	9.728137	H	9.861647	9.452137	11.216845
H	8.734365	11.54924	1.634061	C	4.99277	6.263024	10.020019	C	5.865846	10.022429	2.907711
H	9.762648	12.28983	0.656704	H	4.32722	6.222521	10.696704	H	5.678719	10.934867	3.24318
C	10.264887	14.466258	2.126724	C	5.342569	5.130941	9.374438	H	6.806114	9.982337	2.600473
H	10.955076	14.357586	1.439544	H	4.954628	4.284957	9.565016	C	4.919659	9.66236	1.781635
H	10.639835	14.948789	2.892872	C	5.772656	4.770905	6.536445	H	4.64291	10.467037	1.275671
H	9.512861	14.974314	1.756929	C	4.508548	5.629591	6.395909	H	5.334848	9.014521	1.158718
C	12.500212	8.716414	0.714322	H	3.897313	5.434802	7.136745	C	3.745787	9.04435	2.511908
H	13.1594	8.817913	0.037817	H	4.754092	6.578123	6.415766	H	2.942963	9.618477	2.434748
C	11.910653	7.518943	0.8776	H	4.067007	5.424189	5.545473	H	3.535447	8.14962	2.144078
H	12.109618	6.767149	0.331967	C	6.660842	5.039015	5.310546	H	3.257393	8.410851	1.928604
C	11.439294	6.11552	3.332418	H	7.414198	4.412245	5.309626	H	3.117794	9.740644	2.829563
C	10.476593	5.743419	4.463904	H	6.13428	4.918072	4.492932	C	4.20783	8.936399	3.999191
H	9.783796	5.142247	4.118894	H	7.000204	5.957623	5.347656	H	3.940148	8.06738	4.390662
H	10.057739	6.556033	4.816918	C	5.367497	3.296293	6.552014	H	3.82113	9.667172	4.543747
H	10.972207	5.293873	5.17991	H	4.865813	3.10401	7.371615	C	4.372308	8.34764	3.637299
H	8.824554	10.280752	4.322627	H	4.805842	3.10359	5.772408	H	3.775941	8.364791	4.427334
C	12.706462	6.743126	3.932302	H	6.171233	2.736368	6.522021	H	4.553471	7.403848	3.399566
H	13.341548	6.946713	3.214231	C	7.969162	4.169429	8.642796	O	14.74089	14.277018	7.237073
H	13.116078	6.113754	4.561977	C	9.003927	3.991872	7.527687	C	14.24304	14.085715	8.567196
H	12.470201	7.569345	4.403413	H	9.772537	3.490803	7.872035	H	14.70246	13.323049	9.000075
C	11.857011	4.830042	2.608263	H	8.600169	3.499507	6.782755	H	13.27117	13.898133	8.54707
H	11.058328	4.362068	2.286556	H	9.301193	4.871721	7.21478	C	14.51683	15.368612	9.330717
H	12.347662	4.250706	3.22797	C	8.642996	4.836346	9.857078	H	14.68706	15.191533	10.289766
H	12.432015	5.055804	1.84747	H	9.367183	4.263022	10.184554	H	13.76809	16.010378	9.243443
C	9.125671	6.874819	1.382869	H	9.009358	5.705442	9.590889	C	15.76994	15.871199	8.623456
C	8.01246	6.740878	2.419605	H	7.981076	4.964852	10.568245	H	15.88218	16.848335	8.736109
H	7.151834	6.634963	1.962986	C	7.478837	2.788424	9.098226	H	16.58133	15.408623	8.951752
H	7.988611	7.545124	2.97909	H	6.788647	2.897096	9.785406	C	15.47026	15.509652	7.181195
H	8.182529	5.956583	2.982065	H	7.103889	2.305893	8.332078	H	14.92776	16.216631	6.749944
C	9.262548	5.58808	0.577512	H	8.230863	2.280368	9.468021	H	16.30953	15.395329	6.668709

A.2. X-Ray Single-Crystal Analysis of **3**

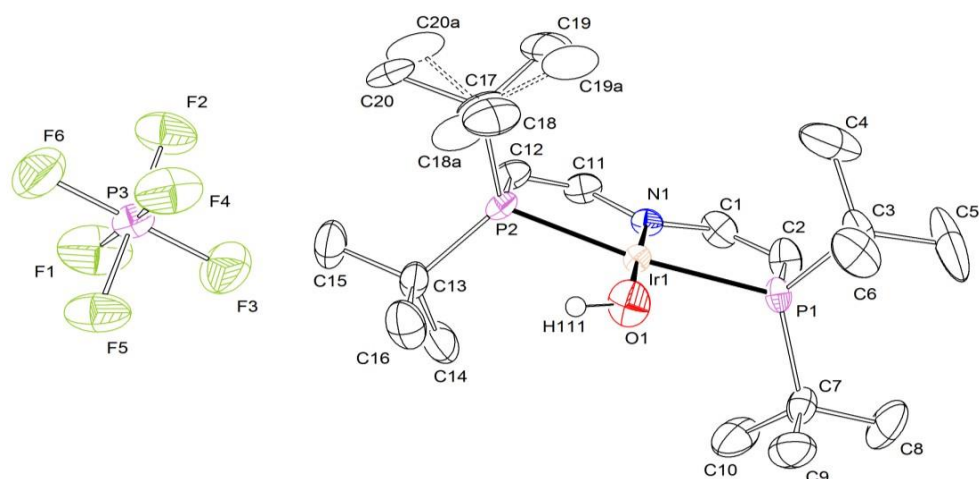


Figure A2: Thermal ellipsoid plot of **3** with the anisotropic displacement parameters drawn at the 50% probability level. The asymmetric unit contains one disordered complex molecule and one PF₆ anion. The disordered complex molecule was refined with population of 0.59(3) on the main domain using some restraints (SADI, RIGU). The O-H hydrogen atom was calculated using AFIX 147 command.

Table A3: Crystal data and structure refinement for **3**.

Crystal data and structure refinement for 3		
Identification code	mo_CW_DD_280717_0m_a (DD-91)	
CCDC Identifier	1912511	
Empirical formula	C ₂₀ H ₄₁ F ₆ IrNOP ₃	
Formula weight	710.65	
Temperature	101(2) K	
Wavelength	0.71073 Å	
Crystal system	Monoclinic	
Space group	P2 ₁ /c	
Unit cell dimensions	a = 8.1470(4) Å	α = 90°
	b = 12.7405(6) Å	β = 97.255(2)°
	c = 26.4460(12) Å	γ = 90°
Volume	163.74(13) Å ³	
Z	2	
Density (calculated)	1.733 Mg/m ³	
Absorption coefficient	5.133 mm ⁻¹	
F(000)	1408	
Crystal size	0.283 x 0.144 x 0.058 mm ³	
Crystal shape and color	Plate, intense brown	
Theta range for data collection	2.228 to 26.461°	
Index ranges	-10<=h<=10, -15<=k<=14, -33<=l<=33	
Reflections collected	67143	
Independent reflections	5588 [R(int) = 0.0500]	
Completeness to theta	100 %	
Refinement method	Full-matrix least-squares on F ²	
Data / restraints / parameters	5588 / 72 / 333	
Goodness-of-fit on F ²	1.137	
Final R indices [I>2sigma(I)]	R1 = 0.0321,	wR2 = 0.0656
R indices (all data)	R1 = 0.0390,	wR2 = 0.0678
Largest diff. peak and hole	d -1.814 eÅ ⁻³	

Table A4: Cartesian coordinates from X-Ray single-crystal analysis of **3**

Ir	3.932826	5.231249	10.178373	H	7.699788	4.854131	12.76035
P	3.174869	6.933253	8.771429	H	6.625512	5.40452	11.708355
P	4.872824	3.324506	11.151139	C	6.81133	2.336608	13.006952
O	2.896504	5.836423	11.69655	H	7.211626	1.89069	12.230417
H	3.166635	5.449112	12.390446	H	6.182822	1.726338	13.445064
N	4.978029	4.720355	8.676198	H	7.517028	2.587596	13.639198
C	4.946648	5.438919	7.450795	C	5.302284	4.227298	13.712654
H	5.49509	5.162451	6.726467	H	4.873868	5.05543	13.41096
C	4.153935	6.492559	7.316476	H	5.92556	4.429872	14.441966
H	4.103122	6.985616	6.506099	H	4.617111	3.604287	14.032712
C	1.397423	6.767754	8.221821	C	3.667761	1.911075	11.35944
C	1.225294	5.326803	7.820436	C	2.505357	2.304756	12.254028
H	0.297385	5.173917	7.544976	H	2.062332	3.094667	11.881502
H	1.439322	4.748384	8.583854	H	2.840852	2.508604	13.15124
H	1.826071	5.121681	7.075383	H	1.867619	1.563259	12.303873
C	1.01881	7.711825	7.093747	C	3.198792	1.590014	9.942789
H	1.63118	7.583146	6.340823	H	2.964279	2.421969	9.481066
H	1.080236	8.638059	7.411182	H	2.408892	1.009048	9.984764
H	0.101533	7.524539	6.80517	H	3.913152	1.133905	9.457455
C	0.487647	7.046771	9.410233	C	4.368692	0.649766	11.952334
H	0.486893	8.008678	9.601743	H	5.180082	0.454836	11.440766
H	0.814691	6.557535	10.194638	H	3.759605	-0.115939	11.905112
H	-0.423836	6.755013	9.197736	H	4.607931	0.819214	12.888898
C	3.726955	8.655896	9.179372	P	5.124841	0.855525	16.992462
C	3.512055	9.668765	8.064415	F	6.689259	0.724934	16.87126
H	3.896887	9.323498	7.230165	F	4.949722	-0.119761	15.758927
H	3.95045	10.512187	8.300524	F	5.126823	2.13276	16.070065
H	2.552556	9.821651	7.941114	F	3.555359	0.967004	17.202074
C	3.043382	9.129842	10.459604	F	5.325509	1.832084	18.246723
H	2.088599	9.272536	10.286458	F	5.071452	-0.412792	17.951325
H	3.449988	9.970715	10.753428	C	2.869756	2.229588	12.655413
H	3.150887	8.452048	11.157436	H	2.471276	3.125245	12.579333
C	5.229601	8.537409	9.439091	H	3.479876	2.214299	13.424077
H	5.685458	8.282599	8.610088	H	2.165304	1.567082	12.781337
H	5.389287	7.854518	10.123805	C	2.646324	2.076702	10.186768
H	5.576026	9.399941	9.751279	H	3.125074	2.019369	9.33153
C	5.848302	3.609384	8.694038	H	2.204701	2.94433	10.2576
H	6.382982	3.420824	7.93062	H	1.979591	1.359411	10.233989
C	5.931675	2.820747	9.767019	C	4.187606	0.486687	11.390921
H	6.499253	2.060139	9.801124	H	3.435875	-0.135049	11.472247
C	6.068145	3.591547	12.54759	H	4.789098	0.375845	12.156961
C	7.091991	4.605691	12.031037	H	4.678495	0.299402	10.561918
H	7.605556	4.206913	11.299101				

A.3. X-Ray Single-Crystal Analysis of **4**

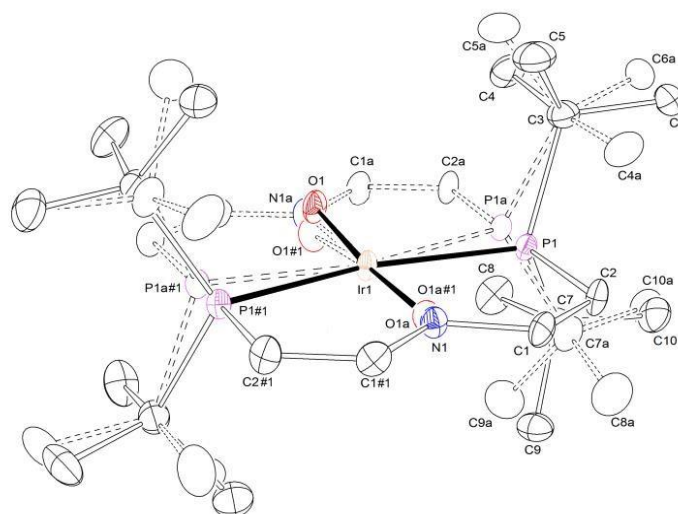


Figure A3: Thermal ellipsoid plot of **4** with the anisotropic displacement parameters drawn at the 50% probability level. The asymmetric unit contains a half disordered complex molecule. The disordered complex molecule was refined with population of 0.910(1) on the main domain using some restraints and constraints (RIGU, SADI, EADP).

Table A5: Crystal data and structure refinement for **4**.

Crystal data and structure refinement for 4	
Identification code	mo_CW_DD_050917_0m_a (DD-109)
CCDC Identifier	1912512
Empirical formula	C ₂₀ H ₄₀ IrNOP ₂
Formula weight	564.67
Temperature	100(2) K
Wavelength	0.71073 Å
Crystal system	Monoclinic
Space group	C2/c
Unit cell dimensions	a = 22.0008(11) Å α = 90° b = 7.6833(4) Å β = 103.429(2)° c = 13.9150(7) Å γ = 90°
Volume	2287.9(2) Å ³
Z	4
Density (calculated)	1.639 Mg/m ³
Absorption coefficient	5.984 mm ⁻¹
F(000)	1128
Crystal size	0.328 x 0.238 x 0.146 mm ³
Crystal shape and color	Plate, clear dark orange
Theta range for data collection	2.817 to 28.368°
Index ranges	-26 < h <= 29, -10 <= k <= 10, -18 <= l <= 18
Reflections collected	32321
Independent reflections	2867 [R(int) = 0.0612]
Completeness to theta	100 %
Refinement method	Full-matrix least-squares on F ²
Data / restraints / parameters	2867 / 159 / 176
Goodness-of-fit on F ²	1.066
Final R indices [I > 2σ(I)]	R1 = 0.0207, wR2 = 0.0360
R indices (all data)	R1 = 0.0346, wR2 = 0.0388
Largest diff. peak and hole	0.680 and -0.613 eÅ ⁻³

Table A6: Cartesian coordinates from X-Ray single-crystal analysis of **4**

Ir	10.192494	5.722637	3.383636	H	6.695531	6.176528	0.419043	C	14.459516	5.665112	0.885416
C	6.815715	5.848651	2.459294	H	8.122969	5.612228	0.871909	H	15.064713	6.232094	1.407592
P	7.940186	5.381422	3.871434	H	7.746386	7.144293	1.140299	H	14.616806	5.81297	-0.070501
N	10.192494	3.682829	3.383636	C	5.321754	6.199148	2.501576	H	14.625448	4.72387	1.102037
O	10.253692	7.538378	3.577356	H	5.212478	7.129334	2.790065	C	11.350666	2.971632	3.099627
C	7.874979	3.593226	3.942829	H	4.86467	5.605405	3.133192	H	11.322875	2.022037	3.09983
H	7.080393	3.119489	4.159016	H	4.934377	6.086464	1.608472	P	12.460056	6.145664	2.904472
C	6.826241	7.382614	2.26732	C	7.643989	4.040878	5.708302	C	11.308529	8.459982	3.165716
H	6.345266	7.612214	1.444921	H	8.273481	3.716535	5.030844	H	11.262917	9.408155	3.202963
H	7.752076	7.697437	2.203017	H	6.789232	3.571405	5.611381	C	12.510098	7.888529	2.892995
H	6.388063	7.810589	3.032333	H	8.009907	3.872145	6.601622	H	13.298166	8.387943	2.714055
C	7.430986	5.211744	1.22045	C	7.421377	5.564522	5.519995	C	13.569048	4.235081	4.315557
H	6.895607	5.444548	0.433322	C	8.28082	6.293714	6.56451	H	12.648566	3.908925	4.397616
H	7.447518	4.237786	1.327847	H	9.22241	6.05315	6.438274	H	14.09897	3.911898	5.073938
H	8.345788	5.543009	1.10293	H	7.994357	6.031106	7.464151	H	13.95948	3.90443	3.479704
C	5.383525	5.362759	2.615862	H	8.173816	7.261932	6.457222	C	12.987861	6.229474	5.66606
H	4.889165	5.530485	1.786492	C	5.940243	5.855889	5.815847	H	13.689458	6.176528	6.348228
H	4.954576	5.84295	3.354658	H	5.751898	6.801449	5.640209	H	12.26202	5.612228	5.895362
H	5.383738	4.401647	2.807362	H	5.748908	5.653756	6.755496	H	12.638602	7.144293	5.626972
C	7.370902	6.017607	5.543789	H	5.376295	5.298089	5.240331	C	15.063235	6.199148	4.265695
C	7.601306	7.530287	5.629246	C	13.569273	5.848651	4.307977	H	15.17251	7.129334	3.977206
H	8.515551	7.738097	5.343965	P	12.444803	5.381422	2.895837	H	15.520318	5.605405	3.634079
H	7.471777	7.828753	6.553669	O	10.131297	7.538378	3.189916	H	15.450612	6.086464	5.158799
H	6.963969	7.991339	5.044771	C	12.510009	3.593226	2.824442	C	12.741	4.040878	1.05897
C	8.296225	5.336482	6.564307	H	13.304595	3.119489	2.608255	H	12.111507	3.716535	1.736428
H	8.124639	4.371621	6.567813	C	13.558747	7.382614	4.499951	H	13.595756	3.571405	1.155891
H	8.123508	5.70223	7.456937	H	14.039723	7.612214	5.322351	H	12.375082	3.872145	0.165649
H	9.23059	5.501227	6.318967	H	12.632913	7.697437	4.564254	C	12.963612	5.564522	1.247276
C	5.925473	5.665112	5.881855	H	13.996926	7.810589	3.734938	C	12.104169	6.293714	0.202761
H	5.320275	6.232094	5.359679	C	12.954003	5.211744	5.546821	H	11.162578	6.05315	0.328998
H	5.768182	5.81297	6.837773	H	13.489382	5.444548	6.333949	H	12.390632	6.031106	-0.69688
H	5.759541	4.72387	5.665235	H	12.93747	4.237786	5.439424	H	12.211173	7.261932	0.310049
C	9.034322	2.971632	3.667644	H	12.0392	5.543009	5.664341	C	14.444745	5.855889	0.951424
H	9.062114	2.022037	3.667441	C	15.001464	5.362759	4.15141	H	14.633091	6.801449	1.127062
P	7.924933	6.145664	3.862799	H	15.495823	5.530485	4.980779	H	14.636081	5.653756	0.011775
N	10.192494	7.771289	3.383636	H	15.430412	5.84295	3.412613	H	15.008694	5.298089	1.52694
O	10.192494	3.901826	3.383636	H	15.00125	4.401647	3.959909	C	9.034322	10.654932	3.667644
C	9.076459	8.459982	3.601555	C	13.014087	6.017607	1.223482	C	11.350666	10.654932	3.099627
H	9.122072	9.408155	3.564308	C	12.783682	7.530287	1.138025	H	9.062114	9.705337	3.667441
C	7.874891	7.888529	3.874276	H	11.869437	7.738097	1.423306	H	11.322875	9.705337	3.09983
H	7.086822	8.387943	4.053216	H	12.913212	7.828753	0.213602	C	9.076459	0.776682	3.601555
C	6.815941	4.235081	2.451715	H	13.42102	7.991339	1.722501	C	11.308529	0.776682	3.165716
H	7.736423	3.908925	2.369655	C	12.088764	5.336482	0.202964	H	9.122072	1.724855	3.564308
H	6.286018	3.911898	1.693334	H	12.260349	4.371621	0.199459	H	11.262917	1.724855	3.202963
H	6.425509	3.90443	3.287567	H	12.26148	5.70223	-0.689666				
C	7.397128	6.229474	1.101211	H	11.154398	5.501227	0.448305				

A.4. X-Ray Single-Crystal Analysis of **8**

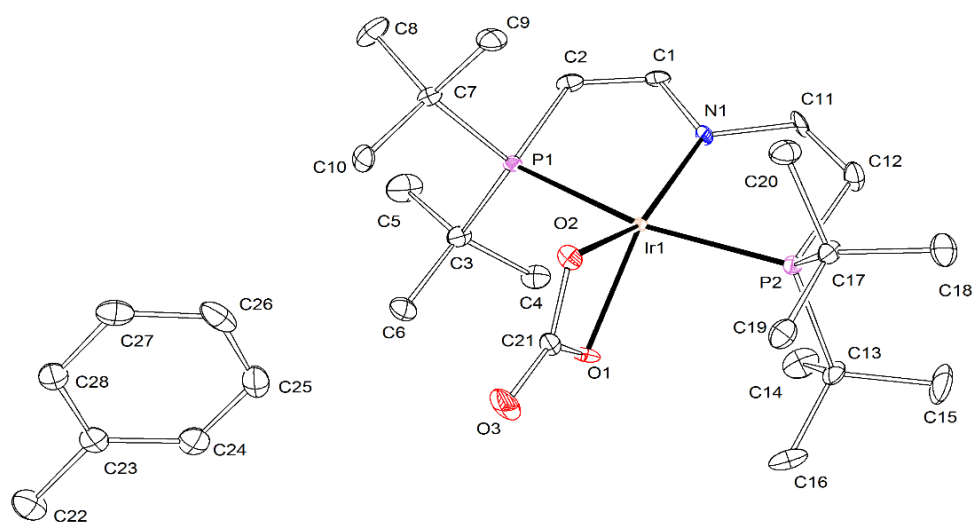


Figure A4: Thermal ellipsoid plot of **8** with the anisotropic displacement parameters drawn at the 50% probability level. The asymmetric unit contains one complex molecule and one toluene solvent molecule.

Table A7: Crystal data and structure refinement for **8**.

Crystal data and structure refinement for 8	
Identification code	SJKF_DD_081018_a (DD-266)
CCDC Identifier	1912514
Empirical formula	C ₂₈ H ₄₈ IrNO ₃ P ₂
Formula weight	700.81
Temperature	100(2) K
Wavelength	0.71073 Å
Crystal system	Triclinic
Space group	P ₁
Unit cell dimensions	a = 9.6329(3) Å α = 112.299(2)° b = 11.9945(3) Å β = 98.906(2)° c = 14.0860(4) Å γ = 91.614(2)°
Volume	1480.91(8) Å ³
Z	2
Density (calculated)	1.572 Mg/m ³
Absorption coefficient	4.644 mm ⁻¹
F(000)	708
Crystal size	0.480 x 0.373 x 0.305 mm ³
Crystal shape and color	Block, dark orange
Theta range for data collection	2.434 to 30.639°
Index ranges	-13 < h <= 13, -17 <= k <= 17, -20 <= l <= 20
Reflections collected	79020
Independent reflections	9015 [R(int) = 0.1147]
Completeness to theta	99.9 %
Refinement method	Full-matrix least-squares on F ²
Data / restraints / parameters	9015 / 0 / 329
Goodness-of-fit on F ²	1.063
Final R indices [I > 2σ(I)]	R1 = 0.0371, wR2 = 0.0542
R indices (all data)	R1 = 0.0542, wR2 = 0.0580
Largest diff. peak and hole	1.834 and -2.294 eÅ ⁻³

Table A8: Cartesian coordinates from X-Ray single-crystal analysis of **8**.

Ir	6.518685	4.345428	3.295313	C	6.340656	1.643647	1.041601
P	7.343656	6.479733	2.818108	H	6.070264	1.157195	0.23498
P	6.210528	2.066402	3.71801	H	7.299689	1.513418	1.195545
O	4.708374	4.587738	2.326465	H	6.155346	2.598828	0.92456
O	4.91276	5.001455	4.407782	C	5.761911	-0.39367	2.362752
O	2.880704	5.286188	3.467067	H	5.531826	-0.823898	1.512831
N	8.387074	3.871134	3.299557	H	5.186534	-0.745999	3.073527
C	9.398462	4.828944	3.04996	H	6.699503	-0.579042	2.579435
H	10.309566	4.560393	3.066372	C	4.069379	1.409771	2.007679
C	9.09712	6.094837	2.793553	H	3.916039	2.376506	2.05557
H	9.760393	6.749818	2.610337	H	3.535199	0.959829	2.695156
C	6.958158	7.138875	1.107648	H	3.806788	1.08081	1.122676
C	7.20422	5.953724	0.163073	C	5.456902	1.574169	5.347857
H	7.017983	6.227091	-0.759422	C	5.704367	0.114075	5.724228
H	6.613555	5.211551	0.409427	H	5.159605	-0.467228	5.15351
H	8.138187	5.666059	0.236314	H	5.459818	-0.027338	6.662623
C	7.862619	8.294823	0.680514	H	6.652404	-0.099658	5.597942
H	7.688984	8.515749	-0.258329	C	3.957799	1.862729	5.355383
H	8.800747	8.031796	0.786105	H	3.801044	2.784298	5.061203
H	7.677995	9.077985	1.239948	H	3.607098	1.745407	6.262928
C	5.484487	7.558806	0.999057	H	3.502921	1.243732	4.746828
H	5.254452	7.703026	0.057418	C	6.14743	2.482981	6.392971
H	5.343541	8.388855	1.500598	H	7.116944	2.344794	6.356287
H	4.915363	6.852415	1.369876	H	5.81915	2.258644	7.288681
C	7.162278	7.723185	4.208153	H	5.943467	3.421012	6.195752
C	8.138857	8.897606	4.093651	C	4.065376	4.985217	3.404571
H	9.057081	8.556837	4.060043	C	0.407821	11.436591	1.448117
H	8.036537	9.484586	4.871716	H	0.988906	12.152532	1.116226
H	7.947769	9.402811	3.275951	H	-0.410707	11.826316	1.820295
C	7.479242	6.933965	5.486093	H	0.176768	10.834783	0.70998
H	6.787578	6.254935	5.630702	C	1.13022	10.659628	2.524171
H	7.501082	7.546096	6.251093	C	1.673387	9.413063	2.257123
H	8.351424	6.497039	5.392337	H	1.607409	9.049211	1.382044
C	5.735831	8.252265	4.304409	C	2.312359	8.691111	3.254179
H	5.532925	8.790749	3.511137	H	2.672904	7.833419	3.062179
H	5.646654	8.806992	5.10735	C	2.424978	9.217861	4.525811
H	5.110907	7.499166	4.356596	H	2.859855	8.722869	5.210172
C	8.807047	2.558534	3.596802	C	1.901944	10.469476	4.799335
H	9.737048	2.367687	3.631268	H	1.989586	10.841659	5.66899
C	7.939504	1.583025	3.829577	C	1.249648	11.18013	3.802714
H	8.210359	0.696901	4.039182	H	0.880638	12.033277	3.998894
C	5.555843	1.115857	2.241813				

A.5. X-Ray Single-Crystal Analysis of **10**

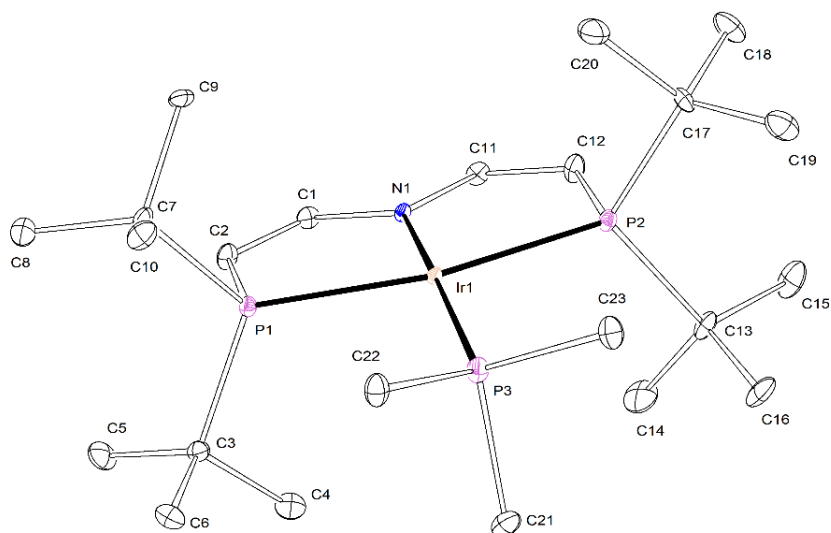


Figure A5: Thermal ellipsoid plot of **10** with the anisotropic displacement parameters drawn at the 50% probability level. The asymmetric unit contains one complex molecule.

Table A9: Crystal data and structure refinement for **10**.

Crystal data and structure refinement for 10	
Identification code	mo_CW_DD_050219_0m_a (DD-344)
CCDC Identifier	1912515
Empirical formula	C ₂₃ H ₄₉ IrNP ₃
Formula weight	624.74
Temperature	100(2) K
Wavelength	0.71073 Å
Crystal system	Monoclinic
Space group	P2 ₁ /c
Unit cell dimensions	a = 11.1109(12) Å α = 90° b = 15.9480(17) Å β = 103.160(4)° c = 15.5609(5) Å γ = 90°
Volume	2684.9(5) Å ³
Z	4
Density (calculated)	1.546 Mg/m ³
Absorption coefficient	5.161 mm ⁻¹
F(000)	1264
Crystal size	0.055 x 0.050 x 0.035 mm ³
Crystal shape and color	Block, clear lighth yellow
Theta range for data collection	2.275 to 28.377°
Index ranges	-14 ≤ h ≤ 14, -21 ≤ k ≤ 21, -20 ≤ l ≤ 20
Reflections collected	67875
Independent reflections	6662 [R(int) = 0.1756]
Completeness to theta = 25.242°	99.3 %
Refinement method	Full-matrix least-squares on F ²
Data / restraints / parameters	6662 / 0 / 268
Goodness-of-fit on F ²	1.018
Final R indices [I > 2σ(I)]	R1 = 0.0449, wR2 = 0.0561
R indices (all data)	R1 = 0.0810, wR2 = 0.0628
Largest diff. peak and hole	1.714 and -1.038 eÅ ⁻³

Table A10: Cartesian coordinates from X-Ray single-crystal analysis of **10**.

Ir	1.752199	10.321083	4.464199	C	4.838035	10.878498	6.360729
P	0.203808	8.939045	3.391935	C	4.892618	9.373022	6.198418
P	3.759011	11.474666	4.921039	H	3.984525	9.006872	6.239663
P	0.623737	10.798582	6.341486	H	5.433786	8.986283	6.918119
N	2.891847	9.707723	2.821014	H	5.294858	9.15219	5.332483
C	2.395774	8.807315	1.918471	C	6.277738	11.438719	6.289271
H	2.951412	8.516998	1.204694	H	6.835256	10.993419	6.961046
C	1.163116	8.327456	2.009536	H	6.262204	12.402776	6.464673
H	0.813433	7.702836	1.384975	H	6.648064	11.274981	5.396834
C	-0.301495	7.312477	4.23643	C	4.28053	11.210758	7.746265
C	0.934952	6.864035	5.029347	H	4.210452	12.183188	7.845588
H	1.687968	6.735909	4.415393	H	4.880968	10.854576	8.43401
H	0.740391	6.020258	5.488248	H	3.393079	10.807338	7.846633
H	1.165481	7.549799	5.690409	C	3.851456	13.375986	4.793866
C	-0.627764	6.194921	3.227033	C	5.093458	13.865399	4.060225
H	-1.350831	6.49023	2.635126	H	5.103093	13.496665	3.152287
H	-0.909317	5.390201	3.710329	H	5.894594	13.570105	4.541248
H	0.169347	5.99353	2.69369	H	5.081754	14.844287	4.015147
C	-1.479165	7.462978	5.19437	C	3.767465	14.155349	6.113914
H	-2.275222	7.737172	4.692861	H	3.736813	15.116376	5.924481
H	-1.267446	8.142427	5.868114	H	4.554865	13.955377	6.662001
H	-1.651368	6.606044	5.637528	H	2.957089	13.891792	6.597877
C	-1.271479	9.723145	2.48174	C	2.619725	13.768817	3.938295
C	-2.060051	8.756887	1.604971	H	2.62467	13.255451	3.103543
H	-2.635403	9.264353	0.995169	H	2.656487	14.726399	3.733118
H	-2.613288	8.179203	2.171195	H	1.799418	13.572944	4.43741
H	-1.438384	8.205996	1.084946	C	0.861469	9.545022	7.672004
C	-0.623257	10.788136	1.573469	H	0.360473	8.732838	7.448917
H	-0.080224	10.346026	0.887846	H	0.536106	9.906148	8.522969
H	-0.053451	11.374879	2.113329	H	1.814206	9.32966	7.751462
H	-1.324241	11.320114	1.142161	C	-1.204402	10.939244	6.465355
C	-2.252034	10.451011	3.393693	H	-1.499195	11.76358	6.024925
H	-2.934177	10.89746	2.849864	H	-1.467124	10.961252	7.409234
H	-1.769942	11.11826	3.925446	H	-1.621764	10.16795	6.027986
H	-2.682483	9.805293	3.992176	C	0.968508	12.317837	7.283773
C	4.177711	10.135066	2.660824	H	1.924776	12.362236	7.493495
H	4.677894	9.823458	1.915683	H	0.451509	12.310293	8.116283
C	4.754856	10.980708	3.523229	H	0.714818	13.09873	6.748763
H	5.641277	11.299078	3.399133				

A.6. X-Ray Single-Crystal Analysis of **14-H**

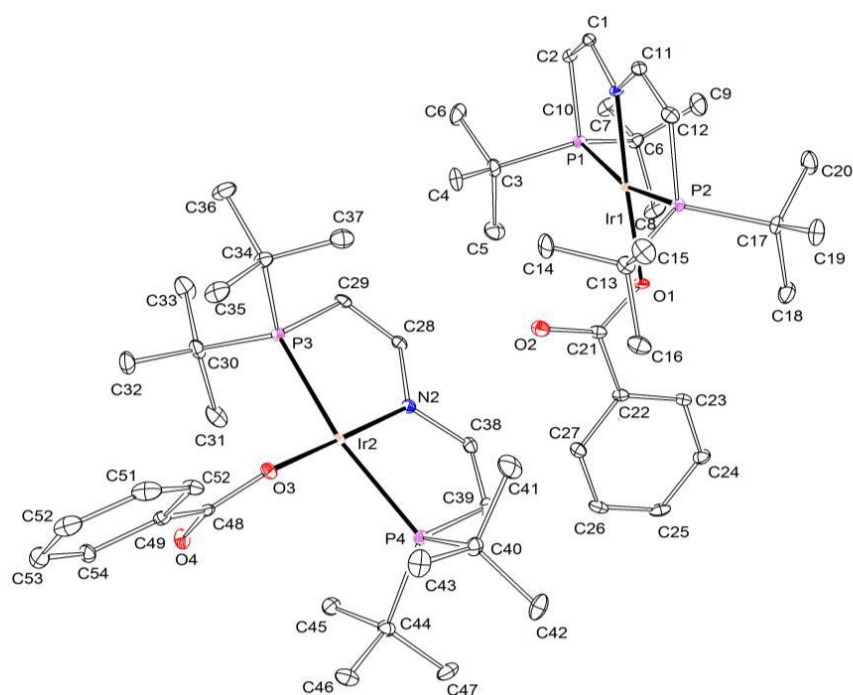


Figure A6: Thermal ellipsoid plot of **14-H** with the anisotropic displacement parameters drawn at the 50% probability level. The asymmetric unit contains two complex molecules.

Table A11: Crystal data and structure refinement for **14-H**.

Crystal data and structure refinement for 14-H	
Identification code	mo_CW_DD_280518_0m_a (NW-DD-44)
CCDC Identifier	unpublished
Empirical formula	C ₂₇ H ₄₅ IrNO ₂ P ₂
Formula weight	669.78
Temperature	103(2) K
Wavelength	0.71073 Å
Crystal system	Monoclinic
Space group	P2 ₁ /n
Unit cell dimensions	a = 12.370(2) Å α = 90° b = 18.583(3) Å β = 94.268(7)° c = 25.566(5) Å γ = 90°
Volume	5860.7(18) Å ³
Z	8
Density (calculated)	1.518 Mg/m ³
Absorption coefficient	4.688 mm ⁻¹
F(000)	2696
Crystal size	0.154 x 0.135 x 0.079 mm ³
Crystal shape and color	Block, clear intense blue
Theta range for data collection	2.182 to 28.364°
Index ranges	-16 < h <= 16, -24 < k <= 24, -34 < l <= 29
Reflections collected	76523
Independent reflections	14607 [R(int) = 0.0743]
Completeness to theta = 25.242°	99.9 %
Refinement method	Full-matrix least-squares on F ²
Data / restraints / parameters	14607 / 0 / 619
Goodness-of-fit on F ²	1.008
Final R indices [I > 2σ(I)]	R1 = 0.0308, wR2 = 0.0446
R indices (all data)	R1 = 0.0550, wR2 = 0.0492
Largest diff. peak and hole	0.649 and -0.842 eÅ ⁻³

Table A12: Cartesian coordinates from X-Ray single-crystal analysis of **14-H**

Ir	2.452817	11.13989	4.001664	C	0.931742	7.513328	6.765275	H	6.139481	10.07279	12.32370
P	0.612423	12.51779	4.280909	H	0.755394	7.558876	5.832905	C	9.236504	8.887131	12.74146
P	4.404435	10.12016	3.275164	C	0.458567	6.443866	7.504803	H	9.784036	8.194896	12.31554
O	1.892368	9.684995	5.348886	H	-0.05074	5.764527	7.078657	H	9.126847	8.677695	13.69251
O	2.857103	10.56603	7.164192	C	0.722045	6.356486	8.86207	H	9.678177	9.756876	12.64733
N	2.938458	12.47447	2.650389	H	0.402901	5.61625	9.364751	C	7.179958	7.564209	12.15010
C	2.130464	13.57580	2.386059	C	1.447548	7.347228	9.475245	H	6.269004	7.630831	11.79499
H	2.400503	14.20725	1.729669	H	1.626132	7.294674	10.40682	H	7.145609	7.271575	13.08477
C	0.973428	13.76004	3.045252	C	1.920704	8.423455	8.742448	H	7.689413	6.91401	11.62277
H	0.393659	14.49167	2.868981	H	2.425898	9.101659	9.175248	C	10.01212	12.65514	11.86242
C	0.488045	13.50165	5.872269	I	7.761746	11.85160	10.01073	C	11.47602	13.03844	11.94518
C	1.939153	13.80837	6.257036	P	7.053783	14.00300	9.520575	C	12.31533	12.89789	10.83824
H	2.409064	12.97106	6.453193	P	7.969004	9.562865	10.29505	H	11.97931	12.51976	10.03411
H	1.952154	14.38383	7.05018	O	9.641185	12.30729	10.68884	C	13.6425	13.31004	10.90935
H	2.384341	14.26642	5.513786	O	9.304564	12.71808	12.86098	H	14.21383	13.20558	10.15758
C	-0.170794	12.69940	6.99404	N	6.051285	11.37053	9.184095	C	14.12531	13.86784	12.06725
H	-1.117994	12.56121	6.783989	C	5.211448	12.32580	8.627237	H	15.02491	14.17043	12.10781
H	-0.091721	13.19175	7.837689	H	4.398262	12.05227	8.21932	C	13.30638	13.99053	13.17438
H	0.274903	11.83083	7.079703	C	5.528685	13.62473	8.655842	H	13.64866	14.36671	13.97678
C	-0.244478	14.83836	5.689981	H	4.989353	14.29355	8.250501	C	11.98897	13.56712	13.11812
H	0.2357	15.38741	5.035478	C	6.473355	15.03817	10.97255	H	11.43521	13.63956	13.88663
H	-0.281289	15.31035	6.54806	C	5.834332	14.01755	11.93123				
H	-1.155486	14.67065	5.370072	H	5.103085	13.55272	11.47342				
C	-1.013668	11.74951	3.776571	H	5.482881	14.48411	12.71813				
C	-1.300129	10.52255	4.645382	H	6.510169	13.36601	12.21257				
H	-2.076101	10.04282	4.287461	C	7.646076	15.72327	11.67554				
H	-1.488202	10.80911	5.563476	H	8.352945	15.06653	11.84705				
H	-0.519497	9.930093	4.641507	H	7.340408	16.10364	12.52541				
C	-0.817187	11.26613	2.335069	H	7.996362	16.43868	11.10466				
H	-1.614378	10.77655	2.043179	C	5.415643	16.09509	10.58676				
H	-0.03682	10.67486	2.292314	H	5.806692	16.73249	9.953349				
H	-0.674767	12.03798	1.748255	H	5.122033	16.57207	11.39092				
C	-2.199287	12.71793	3.824399	H	4.646983	15.65141	10.17115				
H	-1.982513	13.52523	3.312871	C	8.140334	14.94756	8.325991				
H	-2.385045	12.96117	4.755393	C	9.565027	15.02905	8.903269				
H	-2.988936	12.28703	3.435578	H	9.896597	14.12468	9.083747				
C	4.097421	12.34914	1.882332	H	9.550752	15.54415	9.736848				
H	4.308852	13.01987	1.243662	H	10.15473	15.47022	8.256721				
C	4.916657	11.29958	2.030177	C	7.641863	16.35370	8.00185				
H	5.707167	11.18994	1.51485	H	8.211321	16.75079	7.31015				
C	5.831877	10.07322	4.48808	H	7.675862	16.90676	8.810162				
C	5.751459	11.41190	5.234134	H	6.718446	16.30618	7.677148				
H	5.834817	12.14857	4.59322	C	8.196932	14.10950	7.054259				
H	6.478413	11.46497	5.889197	H	7.308538	14.08179	6.641498				
H	4.889786	11.47700	5.69638	H	8.482791	13.19867	7.275732				
C	7.208076	9.969657	3.815272	H	8.835875	14.50917	6.427826				
H	7.278924	9.111806	3.346779	C	5.667488	10.03503	9.068425				
H	7.910038	10.02873	4.496569	H	4.838209	9.826193	8.654695				
H	7.313685	10.70231	3.173058	C	6.431093	9.047228	9.52162				
C	5.650829	8.922793	5.481434	H	6.182132	8.133849	9.442561				
H	4.734548	8.932382	5.828902	C	9.329363	8.744726	9.305399				
H	6.282568	9.029091	6.223052	C	9.108088	9.207399	7.862317				
H	5.819456	8.070368	5.028289	H	9.843458	8.886054	7.29985				
C	4.140434	8.496265	2.36913	H	9.078978	10.18656	7.834017				
C	3.458854	7.492477	3.310118	H	8.260216	8.845653	7.52966				
H	3.207781	6.690562	2.805856	C	9.292344	7.214579	9.356898				
H	2.655779	7.900218	3.69644	H	8.38351	6.90312	9.163495				
H	4.077988	7.246004	4.028689	H	9.558474	6.911259	10.24998				
H	5.196128	7.113336	1.236625	H	9.911343	6.850213	8.690235				
H	6.007382	7.602231	2.52656	C	10.70166	9.263856	9.737663				
H	5.886537	8.557033	1.247945	H	11.38023	8.966892	9.095958				
C	3.185434	8.812537	1.21651	H	10.91792	8.913985	10.62717				
H	3.632497	9.402693	0.574449	H	10.68607	10.2433	9.766804				
H	2.38594	9.257556	1.567446	C	7.862851	8.93701	12.06837				
H	2.926132	7.979959	0.769306	C	6.991359	9.971386	12.79744				
C	2.191708	9.693228	6.606366	H	7.45723	10.83327	12.81998				
C	1.663472	8.520367	7.380873	H	6.821503	9.667787	13.71360				

A.7. X-Ray Single-Crystal Analysis of **14-F**

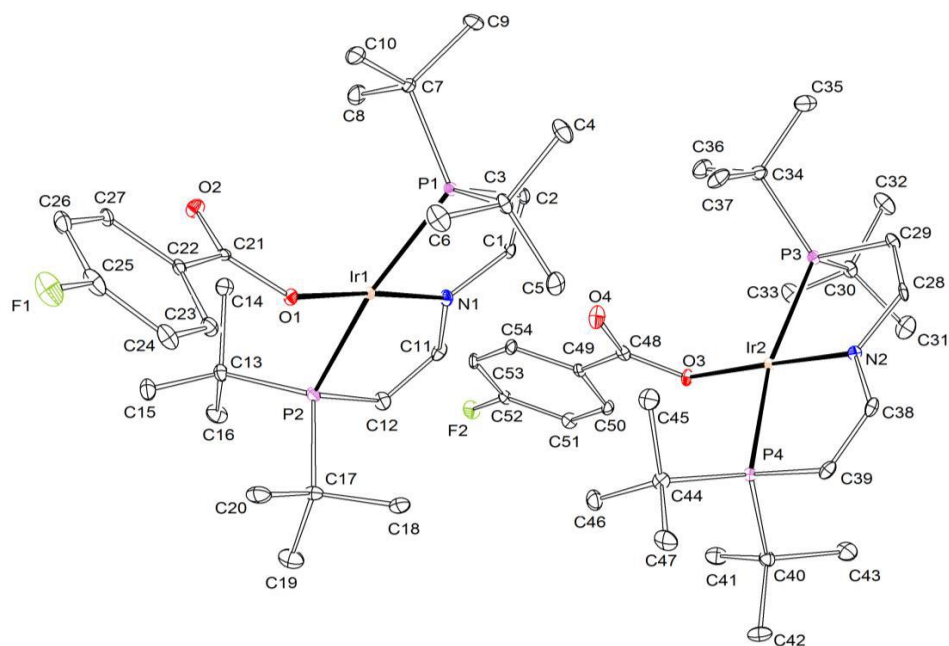


Figure A7: Thermal ellipsoid plot of **14-F** with the anisotropic displacement parameters drawn at the 50% probability level. The asymmetric unit contains two complex molecules.

Table A13: Crystal data and structure refinement for **914-F**.

Crystal data and structure refinement for 14-F	
Identification code	mo_CW_DD_250618_0m_a (NW-DD-61)
CCDC Identifier	unpublished
Empirical formula	C ₂₇ H ₄₄ IrNO ₂ P ₂
Formula weight	687.77
Temperature	100(2) K
Wavelength	0.71073 Å
Crystal system	Monoclinic
Space group	P2 ₁ /n
Unit cell dimensions	a = 12.4837(5) Å α = 90° b = 18.583(3) Å β = 94.480(2)° c = 25.5619(10) Å γ = 90°
Volume	5911.4(4) Å ³
Z	8
Density (calculated)	1.546 Mg/m ³
Absorption coefficient	4.655 mm ⁻¹
F(000)	2760
Crystal size	0.200 x 0.105 x 0.089 mm ³
Crystal shape and color	Block, clear intense blue
Theta range for data collection	2.192 to 28.343 °
Index ranges	-16 ≤ h ≤ 16, -24 ≤ k ≤ 24, -34 ≤ l ≤ 34
Reflections collected	219961
Independent reflections	14732 [R(int) = 0.1746]
Completeness to theta = 25.242°	99.9 %
Refinement method	Full-matrix least-squares on F ²
Data / restraints / parameters	14732 / 0 / 637
Goodness-of-fit on F ²	1.016
Final R indices [I > 2σ(I)]	R1 = 0.0365, wR2 = 0.0478
R indices (all data)	R1 = 0.0667, wR2 = 0.0529
Largest diff. peak and hole	0.904 and -1.093 eÅ ⁻³

Table A14: Cartesian coordinates from X-Ray single-crystal analysis of **14-F**.

Ir	2.661991	11.816838	15.51165	C	0.442023	12.60319	13.62937	H	5.509987	11.34964	19.79686
P	3.325785	13.971356	16.03715	C	-1.01419	12.98378	13.51946	H	4.603406	12.04695	20.91618
P	2.477499	9.532305	15.21477	C	-1.88451	12.88645	14.60672	H	3.916161	11.34516	19.65275
F	-4.89300	14.285311	13.21197	H	-1.57081	12.52955	15.42934	C	4.770636	8.801621	20.08179
O	0.785569	12.265528	14.82346	C	-3.19331	13.30241	14.49928	H	4.135232	8.899323	19.34212
O	1.175261	12.642326	12.64715	H	-3.79325	13.22162	15.23141	H	4.603198	7.955285	20.54664
N	4.376557	11.348043	16.34553	C	-3.60358	13.83392	13.31103	H	5.685126	8.805504	19.72955
C	5.201982	12.313153	16.89965	C	-2.80169	13.93371	12.21186	C	3.21825	9.87337	21.73900
H	6.021278	12.052119	17.30352	H	-3.13190	14.29430	11.39737	H	2.516811	9.885634	21.05474
C	4.862168	13.609257	16.87458	C	-1.49274	13.49436	12.31723	H	3.098837	10.63586	22.34294
H	5.398195	14.2852	17.27241	H	-0.91728	13.54201	11.56289	H	3.16107	9.03941	22.25051
C	2.230464	14.852124	17.26147	Ir	7.95995	11.07210	21.53628	C	8.235924	9.637756	18.91914
C	2.691907	16.260201	17.61763	P	9.791645	12.45913	21.2554	C	8.806677	8.46154	18.16569
H	2.644063	16.830637	16.82218	P	6.026397	10.03032	22.27067	C	9.579124	7.509252	18.82047
H	3.616141	16.228835	17.94199	F	10.43427	5.32426	16.09526	H	9.735063	7.588447	19.75425
H	2.112253	16.62663	18.31773	O	8.519097	9.643553	20.17269	C	10.12409	6.44304	18.11770
C	2.211838	13.984196	18.52641	O	7.557341	10.47760	18.32922	H	10.65158	5.786087	18.55664
H	1.91668	13.078362	18.29673	N	7.470629	12.39156	22.89120	C	9.877746	6.366911	16.77004
H	1.594118	14.373053	19.18033	C	8.261255	13.50780	23.13743	C	9.130718	7.276833	16.08320
H	3.11279	13.946736	18.91020	H	7.981559	14.14371	23.78540	H	8.987277	7.189834	15.14813
C	0.797794	14.906828	16.70832	C	9.408588	13.70285	22.47867	C	8.586592	8.335724	16.79858
H	0.779747	15.464499	15.90268	H	9.976079	14.44561	22.64826	H	8.056891	8.982773	16.34775
H	0.200989	15.290297	17.38448	C	11.42466	11.70105	21.77705	C	5.507203	11.20516	23.51023
H	0.498985	14.000585	16.48508	C	11.22805	11.24761	23.23166				
C	3.843354	15.057247	14.60165	H	10.45658	10.64558	23.28472				
C	4.460973	14.079315	13.59657	H	11.07100	12.03069	23.79955				
C	3.783144	13.430836	13.31299	H	12.03116	10.77727	23.53859				
H	5.209012	13.606804	14.01797	C	12.61344	12.67543	21.72820				
H	4.785777	14.57485	12.81598	H	12.77514	12.94721	20.80061				
C	4.903057	16.108426	14.98628	H	13.41286	12.23351	22.08319				
H	5.147978	16.630458	14.19389	H	12.40988	13.46653	22.26963				
H	5.698269	15.656856	15.33857	C	11.71892	10.46781	20.92472				
H	4.536663	16.706289	15.67090	H	11.91081	10.74492	20.00450				
C	2.649678	15.761173	13.95520	H	10.94015	9.872924	20.93106				
H	2.931489	16.175041	13.11276	H	12.49454	9.994485	21.29181				
H	2.310587	16.452502	14.56141	C	9.918849	13.42528	19.65369				
H	1.941935	15.10712	13.77712	C	10.64069	14.77174	19.82598				
C	4.767473	10.018901	16.46518	H	10.64961	15.24945	18.97034				
H	5.592971	9.814337	16.88852	H	11.56161	14.61325	20.12124				
C	4.008344	9.022091	15.99811	H	10.17096	15.31081	20.49618				
H	4.261461	8.109716	16.07558	C	10.58144	12.61118	18.53826				
C	2.596767	8.897112	13.45226	H	10.46427	13.07392	17.68239				
C	3.475638	9.928874	12.72085	H	10.16617	11.72482	18.48994				
H	3.671487	9.608062	11.81579	H	11.53780	12.51390	18.72880				
H	4.314384	10.050825	13.21281	C	8.457053	13.71825	19.25239				
H	3.000305	10.784278	12.66848	H	8.44507	14.30944	18.47086				
C	1.23624	8.837966	12.75953	H	7.994483	14.15377	19.99853				
H	0.772327	9.693147	12.87719	H	8.003757	12.87755	19.03300				
H	0.700025	8.118524	13.15359	C	6.321867	12.25536	23.66061				
H	1.363726	8.664303	11.80351	H	6.11104	12.92038	24.30545				
C	3.294631	7.528001	13.37451	C	5.507203	11.20516	23.51023				
H	3.334687	7.234337	12.44040	H	4.715032	11.09340	24.02255				
H	2.789877	6.873668	13.90126	C	6.305395	8.414102	23.16102				
H	4.203797	7.603962	13.73232	C	7.023207	7.429481	22.23945				
C	1.103919	8.726886	16.20499	H	6.406382	7.127103	21.54053				
C	1.296984	9.237285	17.63955	H	7.329718	6.658252	22.76065				
H	1.343103	10.216201	17.63456	H	7.793985	7.8715	21.82603				
H	2.129356	8.872918	18.0067	C	5.035853	7.780841	23.73031				
H	0.541758	8.948676	18.19339	H	4.440204	7.525511	22.99517				
C	1.16592	7.193049	16.20267	H	4.580648	8.426347	24.31042				
H	0.982116	6.860067	15.29950	H	5.272798	6.984693	24.25030				
H	0.496509	6.838122	16.82420	C	7.261754	8.736771	24.33121				
H	2.058712	6.901782	16.48284	H	8.042254	9.221974	23.99095				
C	-0.26464	9.205473	15.72370	H	7.554454	7.902271	24.75351				
H	-0.25225	10.179967	15.62067	H	6.795016	9.290726	24.9913				
H	-0.94775	8.955068	16.38027	C	4.596019	9.96626	21.06241				
H	-0.47188	8.788428	14.86143	C	4.662451	11.29859	20.28622				

A.8. X-Ray Single-Crystal Analysis of **14-OMe**

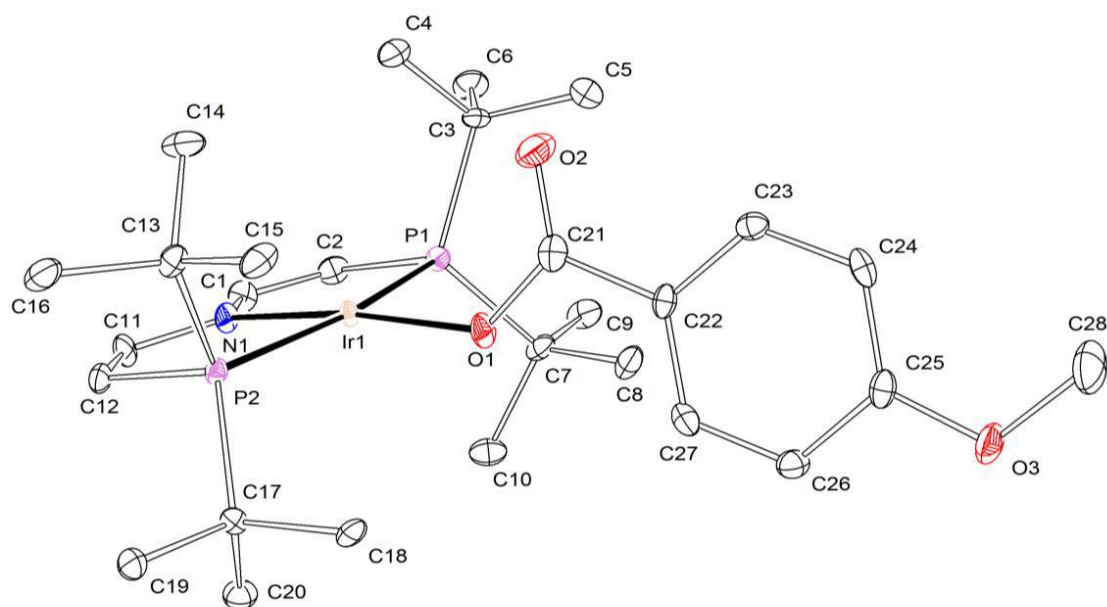


Figure A8: Thermal ellipsoid plot of **14-OMe** with the anisotropic displacement parameters drawn at the 50% probability level. The asymmetric unit contains one complex molecule.

Table A15: Crystal data and structure refinement for **14-OMe**.

Crystal data and structure refinement for 14-OMe	
Identification code	MO_DD_021219_0m_a (MH-DD-018)
CCDC Identifier	unpublished
Empirical formula	C ₂₈ H ₄₇ IrNO ₃ P ₂
Formula weight	699.80
Temperature	100(2) K
Wavelength	0.71073 Å
Crystal system	Monoclinic
Space group	P2 ₁ /c
Unit cell dimensions	a = 8.4979(2) Å α = 90° b = 11.9821(3) Å β = 94.2010(10)° c = 28.9933(7) Å γ = 90°
Volume	2944.24(12) Å ³
Z	4
Density (calculated)	1.579 Mg/m ³
Absorption coefficient	4.672 mm ⁻¹
F(000)	1412
Crystal size	0.174 x 0.107 x 0.095 mm ³
Crystal shape and color	Block, clear intense blue
Theta range for data collection	2.208 to 28.354 °
Index ranges	-11<=h<=11, -15<=k<=15, -38<=l<=38
Reflections collected	70890
Independent reflections	7330 [R(int) = 0.1037]
Completeness to theta = 25.242°	100%
Refinement method	Full-matrix least-squares on F ²
Data / restraints / parameters	7330 / 0 / 329
Goodness-of-fit on F ²	1.029
Final R indices [>2σ(I)]	R1 = 0.0290, wR2 = 0.0414
R indices (all data)	R1 = 0.0503, wR2 = 0.0453
Largest diff. peak and hole	0.648 and -0.831 eÅ ⁻³

Table A16: Cartesian coordinates from X-Ray single-crystal analysis of **14-OMe**.

Ir	4.742295	3.126549	11.380726	C	4.530399	3.493333	14.895335
P	3.799737	3.071168	9.255299	C	3.073131	3.554071	14.403484
P	5.492279	2.674441	13.524225	H	3.02189	4.116259	13.602412
O	5.548542	4.98985	11.307136	H	2.506645	3.934946	15.106649
O	3.759925	6.336494	11.415482	H	2.763037	2.649686	14.188267
O	8.448441	10.322028	9.694756	C	5.027116	4.923697	15.140624
N	4.188991	1.234576	11.423723	H	5.102183	5.394749	14.284555
C	3.610908	0.64109	10.310943	H	5.904837	4.894616	15.575541
H	3.378511	-0.279291	10.348157	H	4.391669	5.395576	15.718499
C	3.371979	1.322812	9.192235	C	4.559202	2.702587	16.212431
H	3.002656	0.916367	8.417042	H	4.206434	1.801077	16.059989
C	2.145231	3.915774	8.981673	H	4.007586	3.160578	16.880551
C	1.420242	3.828017	10.344861	H	5.481955	2.641765	16.536833
H	0.501897	4.156171	10.248167	C	7.347066	2.743853	13.789841
H	1.89547	4.37645	11.003496	C	7.870411	4.148371	13.459049
H	1.403953	2.895834	10.646795	H	7.520676	4.430573	12.588175
C	2.289163	5.392269	8.595103	H	8.849817	4.133213	13.428428
H	2.687823	5.458853	7.70234	H	7.57488	4.778066	14.149375
H	2.865943	5.845384	9.245034	C	7.785714	2.34927	15.198571
H	1.405721	5.816435	8.590823	H	7.377894	1.491328	15.439407
C	1.275007	3.206386	7.927678	H	7.498909	3.037331	15.834767
H	0.437322	3.701007	7.809153	H	8.761796	2.265995	15.225462
H	1.076476	2.29486	8.227819	C	7.942556	1.765071	12.765976
H	1.757401	3.171878	7.075338	H	7.640989	2.009937	11.866273
C	4.985787	3.376124	7.8455	H	7.64559	0.854491	12.973502
C	5.633192	4.763376	7.994848	H	8.920896	1.806505	12.805156
H	6.27884	4.902225	7.270806	C	4.951767	6.137375	11.215879
H	6.09382	4.817667	8.858146	C	5.882424	7.265682	10.833271
H	4.939389	5.454108	7.950781	C	5.378349	8.546185	10.678429
C	4.359616	3.232327	6.451113	H	4.456219	8.707069	10.840586
H	5.055082	3.335829	5.768449	C	6.196674	9.60013	10.290239
H	3.675246	3.922808	6.327557	H	5.837934	10.473494	10.185219
H	3.948835	2.346539	6.367258	C	7.539971	9.362849	10.058396
C	6.098412	2.329488	8.004419	C	8.055518	8.079662	10.194732
H	5.716077	1.431022	7.920854	H	8.974034	7.914992	10.016642
H	6.514739	2.426627	8.886252	C	7.231431	7.043761	10.589398
H	6.774407	2.462945	7.307558	H	7.591062	6.170829	10.695026
C	4.456579	0.445986	12.536012	C	7.962214	11.65554	9.542892
H	4.210673	-0.47152	12.521467	H	8.709069	12.253315	9.330132
C	5.048549	0.940715	13.622739	H	7.538943	11.945962	10.377708
H	5.222603	0.413011	14.393248	H	7.304821	11.682823	8.816624

A.9. X-Ray Single-Crystal Analysis of **11**

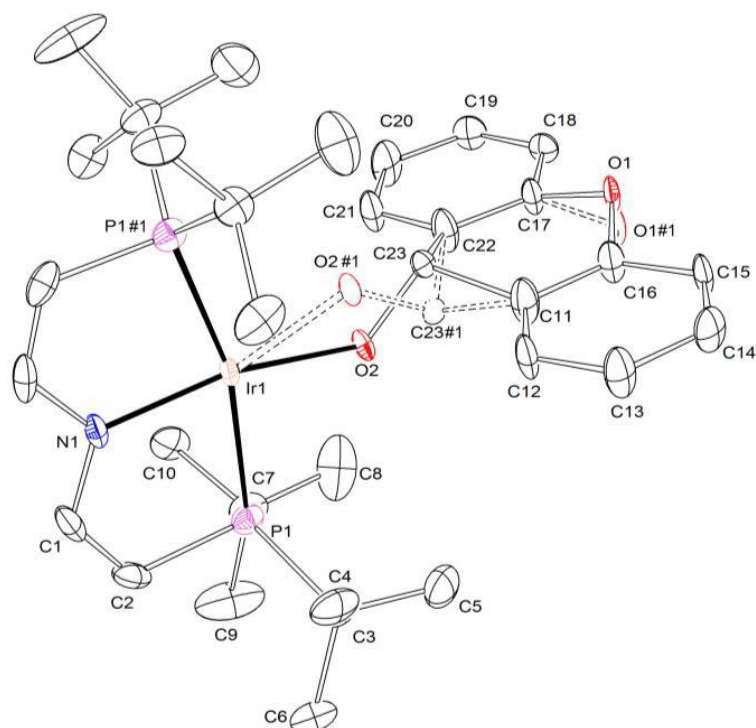


Figure A9: Thermal ellipsoid plot of **11** with the anisotropic displacement parameters drawn at the 50% probability level. The asymmetric unit contains a half complex molecule. The disorder was refined using PART -1 command.

Table A17: Crystal data and structure refinement for **11**.

Crystal data and structure refinement for 11		
Identification code	MO_DD_171219_2_0m_a (DD-MH-22)	
CCDC Identifier	unpublished	
Empirical formula	C ₃₃ H ₄₉ IrNO ₂ P ₂	
Formula weight	745.87	
Temperature	100(2) K	
Wavelength	0.71073 Å	
Crystal system	Orthorhombic	
Space group	Pnma	
Unit cell dimensions	a = 13.0432(6) Å	$\alpha = 90^\circ$
	b = 15.6336(7) Å	$\beta = 90^\circ$
	c = 15.8611(7) Å	$\gamma = 90^\circ$
Volume	3234.3(3) Å ³	
Z	4	
Density (calculated)	1.532 Mg/m ³	
Absorption coefficient	4.256 mm ⁻¹	
F(000)	1508	
Crystal size	0.190 x 0.118 x 0.098 mm ³	
Crystal shape and color	Block, clear intense blue	
Theta range for data collection	2.405 to 30.564 °	
Index ranges	-18<=h<=18, -22<=k<=22, -22<=l<=22	
Reflections collected	47456	
Independent reflections	5121 [R(int) = 0.1422]	
Completeness to theta = 25.242°	99.9%	
Refinement method	Full-matrix least-squares on F ²	
Data / restraints / parameters	5121 / 0 / 217	
Goodness-of-fit on F ²	1.012	
Final R indices [I>2sigma(I)]	R1 = 0.0393,	wR2 = 0.0534
R indices (all data)	R1 = 0.0797,	wR2 = 0.0622
Largest diff. peak and hole	0.984 and -1.722 eÅ ⁻³	

Table A18: Cartesian coordinates from X-Ray single-crystal analysis of **11**

Ir	3.350185	11.7252	6.751975	C	7.221629	11.7252	10.506377
P	3.077126	9.412834	6.611557	C	8.466941	11.7252	8.49281
N	1.620057	11.7252	5.77206	C	9.728206	11.7252	7.931565
C	1.008422	10.54552	5.422038	H	10.499711	11.7252	8.485911
H	0.184457	10.581086	4.950519	C	9.857672	11.7252	6.558263
O	8.43719	11.990752	9.86911	H	10.721184	11.7252	6.162228
O	5.009893	11.272639	7.738218	C	8.744931	11.7252	5.769269
C	5.944673	12.112241	8.320194	H	8.835085	11.7252	4.823567
H	5.726969	13.078663	8.183709	C	7.49941	11.7252	6.335542
C	1.523485	9.358492	5.716769	H	6.735495	11.7252	5.770792
H	1.101876	8.542918	5.472682	C	7.319713	11.7252	7.719597
C	2.686077	8.507836	8.214083	P	3.077126	14.037566	6.611557
C	3.945072	8.206639	9.025918	C	1.008422	12.90488	5.422038
H	4.459914	7.501533	8.580744	H	0.184457	12.869314	4.950519
H	3.690965	7.908069	9.924068	C	1.523485	14.091908	5.716769
H	4.491804	9.017132	9.093597	H	1.101876	14.907482	5.472682
C	1.791066	9.484452	8.994227	C	2.686077	14.942564	8.214083
H	2.295199	10.300588	9.194664	C	3.945072	15.243761	9.025918
H	1.50212	9.065049	9.831503	H	4.459914	15.948867	8.580744
H	1.005331	9.710279	8.453839	H	3.690965	15.542331	9.924068
C	1.895933	7.216016	7.995866	H	4.491804	14.433268	9.093597
H	1.080264	7.413531	7.489833	C	1.791066	13.965948	8.994227
H	1.656265	6.829116	8.863785	H	2.295199	13.149812	9.194664
H	2.445117	6.577947	7.494227	H	1.50212	14.385351	9.831503
C	4.2669	8.461389	5.506895	H	1.005331	13.740121	8.453839
C	5.668705	8.36754	6.106539	C	1.895933	16.234384	7.995866
H	6.296044	8.052336	5.422815	H	1.080264	16.036869	7.489833
H	5.661153	7.738366	6.85788	H	1.656265	16.621284	8.863785
H	5.948221	9.251683	6.42365	H	2.445117	16.872453	7.494227
C	3.766667	7.06448	5.13289	C	4.2669	14.989011	5.506895
H	2.860087	7.129422	4.766419	C	5.668705	15.08286	6.106539
H	3.756285	6.496558	5.93148	H	6.296044	15.398064	5.422815
H	4.363237	6.672843	4.461236	H	5.661153	15.712034	6.85788
C	4.354094	9.304165	4.22987	H	5.948221	14.198717	6.42365
H	4.944729	8.86089	3.585624	C	3.766667	16.38592	5.13289
H	4.713369	10.189746	4.446818	H	2.860087	16.320978	4.766419
H	3.459944	9.400796	3.840559	H	3.756285	16.953842	5.93148
C	6.024354	11.7252	9.837974	H	4.363237	16.777557	4.461236
C	4.860692	11.7252	10.57063	C	4.354094	14.146235	4.22987
H	4.023097	11.7252	10.122348	H	4.944729	14.58951	3.585624
C	4.896652	11.7252	11.949832	H	4.713369	13.260654	4.446818
H	4.087335	11.7252	12.447347	H	3.459944	14.049604	3.840559
C	6.113674	11.7252	12.606069	O	8.43719	11.459648	9.86911
H	6.141717	11.7252	13.555657	O	5.009893	12.177761	7.738218
C	7.27821	11.7252	11.886372	C	5.944673	11.338159	8.320194
H	8.117266	11.7252	12.331894	H	5.726969	10.371737	8.183709

A.10. X-Ray Single-Crystal Analysis of **12**

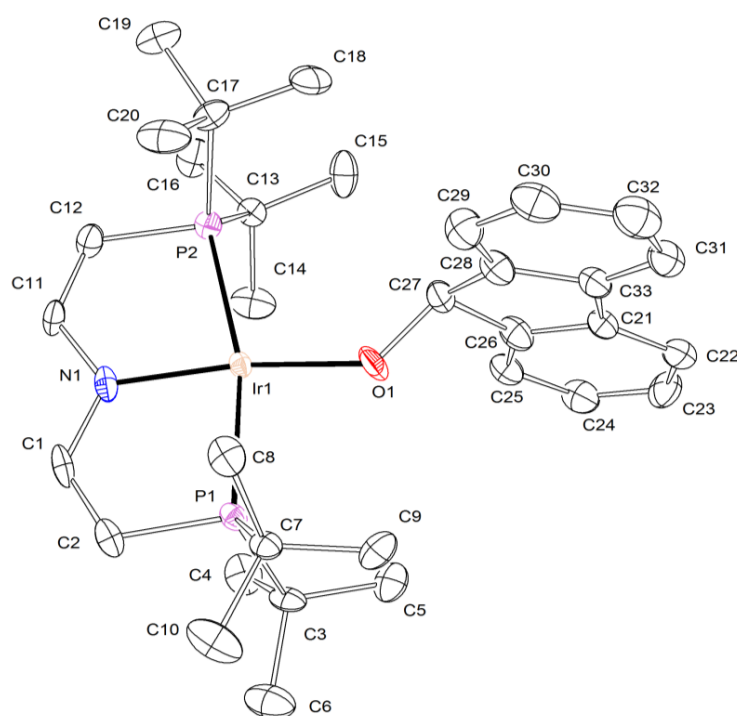


Figure A10: Thermal ellipsoid plot of **12** with the anisotropic displacement parameters drawn at the 50% probability level. The asymmetric unit one complex molecule.

Table A19: Crystal data and structure refinement for **12**.

Crystal data and structure refinement for 12	
Identification code	MO_DD_181219_0m_a (MH-DD-21)
CCDC Identifier	unpublished
Empirical formula	C ₃₃ H ₄₉ IrNOP ₂
Formula weight	729.87
Temperature	100(2) K
Wavelength	0.71073 Å
Crystal system	Triclinic
Space group	P1
Unit cell dimensions	a = 8.7365(16) Å b = 12.087(3) Å c = 15.565(3) Å
Volume	1606.9(6) Å ³
Z	2
Density (calculated)	1.508 Mg/m ³
Absorption coefficient	4.279 mm ⁻¹
F(000)	738
Crystal size	0.249 x 0.118 x 0.092 mm ³
Crystal shape and color	Plate, clear intense blue
Theta range for data collection	2.325 to 28.484°
Index ranges	-11 ≤ h ≤ 11, -16 ≤ k ≤ 16, -20 ≤ l ≤ 20
Reflections collected	25068
Independent reflections	7991 [R(int) = 0.0978]
Completeness to theta = 25.242°	99.8%
Refinement method	Full-matrix least-squares on F ²
Data / restraints / parameters	7991 / 0 / 355
Goodness-of-fit on F ²	1.027
Final R indices [I > 2σ(I)]	R1 = 0.0472, wR2 = 0.0746
R indices (all data)	R1 = 0.0800, wR2 = 0.0846
Largest diff. peak and hole	1.742 and -1.988 eÅ ⁻³

Table A20: Cartesian coordinates from X-Ray single-crystal analysis of **12**.

Ir	4.26921	2.642109	12.249178	C	1.315497	4.984311	10.074406
P	4.955528	0.663459	13.221627	H	1.673634	5.744378	9.570001
P	3.565832	4.8506	11.842245	H	0.338465	4.973412	9.998943
O	4.160095	1.692399	10.537625	H	1.680479	4.150331	9.711536
N	4.559171	3.349301	14.084169	C	1.219116	6.473865	12.056518
C	5.080344	2.52314	15.074365	H	1.628351	7.187947	11.524533
H	5.245789	2.892027	15.934046	H	1.467329	6.584761	12.998069
C	5.35886	1.229383	14.867124	H	0.24412	6.518569	11.968285
H	5.735489	0.665798	15.532729	C	4.648375	5.96257	10.784638
C	3.572034	-0.5973	13.454561	C	4.544146	5.670444	9.283948
C	2.458595	0.18465	14.177136	H	3.633292	5.860879	8.976572
H	2.139009	0.908017	13.598348	H	4.753998	4.727428	9.11937
H	2.812498	0.563762	15.008659	H	5.178493	6.236214	8.796179
H	1.715984	-0.420427	14.384073	C	4.372847	7.46234	10.979764
C	3.016752	-1.069224	12.102499	H	5.073394	7.983739	10.535038
H	2.830565	-0.291274	11.536329	H	4.367799	7.671693	11.937129
H	2.188992	-1.573429	12.247337	H	3.501704	7.687653	10.591505
H	3.67641	-1.644059	11.661122	C	6.081068	5.650871	11.230688
C	3.975467	-1.807494	14.298093	H	6.260595	4.695214	11.108635
H	4.638295	-2.339451	13.810156	H	6.187002	5.884983	12.176394
H	3.184826	-2.357347	14.479611	H	6.711754	6.173105	10.69225
H	4.361793	-1.501186	15.145049	C	2.922965	0.701091	7.531163
C	6.54088	-0.131212	12.580436	C	2.012341	-0.124361	6.869881
C	7.453578	1.048601	12.241994	H	2.237332	-0.525078	6.038419
H	8.329952	0.713102	11.959473	C	0.784269	-0.346264	7.444528
H	7.560798	1.616255	13.033624	H	0.15929	-0.910149	7.00414
H	7.054769	1.572365	11.516025	C	0.43522	0.242492	8.667171
C	6.287639	-0.918494	11.3023	H	-0.423825	0.093791	9.044546
H	5.715688	-0.394225	10.703604	C	1.363464	1.048727	9.322669
H	5.842783	-1.763641	11.521915	H	1.147872	1.443332	10.159519
H	7.14142	-1.104409	10.858563	C	2.592517	1.268883	8.750228
C	7.250963	-0.998587	13.637084	C	3.760262	2.112651	9.27786
H	6.693645	-1.776187	13.849546	H	3.504157	3.079009	9.301908
H	7.397174	-0.469809	14.449125	C	4.797237	1.877288	8.214134
H	8.113797	-1.301559	13.284777	C	6.098087	2.339884	8.169508
C	4.279082	4.672852	14.397299	H	6.447021	2.872809	8.874305
H	4.434276	4.981408	15.282292	C	6.897764	2.005664	7.057579
C	3.799914	5.519002	13.492292	H	7.793776	2.317905	7.011096
H	3.593879	6.421707	13.704861	C	5.071117	0.754184	6.087748
C	1.714378	5.117521	11.555416	H	4.714115	0.226034	5.383407
C	1.03918	4.014075	12.369922	C	6.391621	1.230979	6.038875
H	0.0662	4.119987	12.319953	H	6.941323	1.016287	5.294413
H	1.326874	4.075487	13.304731	C	4.318652	1.073804	7.178277
H	1.291611	3.139339	12.00725				

A.11. X-Ray Single-Crystal Analysis of **15**

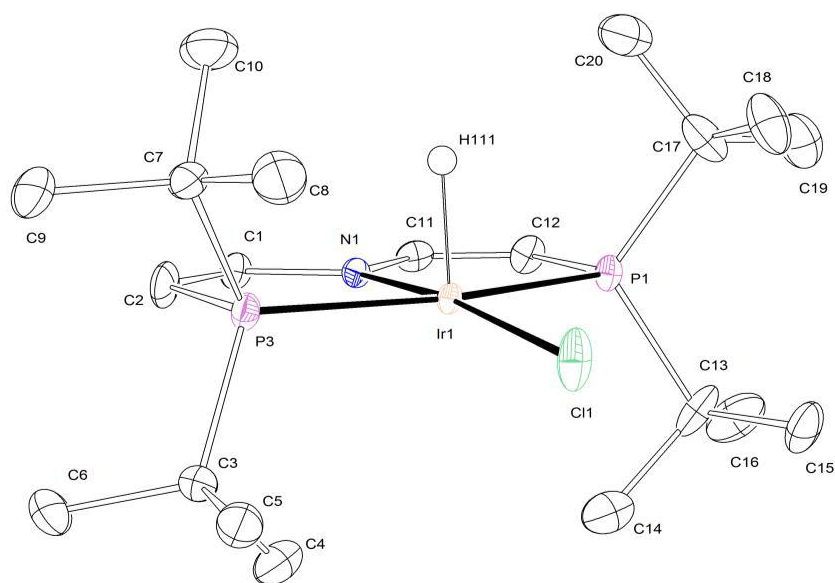


Figure A11: Thermal ellipsoid plot of **15** with the anisotropic displacement parameters drawn at the 50% probability level. The asymmetric unit contains one complex molecule. The structure was refined as twin using the twin law $-100\ 0\ -10\ 001$ (BASF: 0.0898(4)). The Ir-H hydrogen atom was found from the residual density map and isotropically refined.

Table A21: Crystal data and structure refinement for **15**

Crystal data and structure refinement for 15	
Identification code	mo_CW_DD_030220_0m_a (DD-286)
CCDC Identifier	unpublished
Empirical formula	C ₂₀ H ₄₁ ClIrNP ₂
Formula weight	585.13
Temperature	100(2) K
Wavelength	0.71073 Å
Crystal system	Orthorhombic
Space group	P2 ₁ /c
Unit cell dimensions	a = 8.5923(3) Å $\alpha = 90^\circ$ b = 11.5184(4) Å $\beta = 90.047(2)^\circ$ c = 24.0866(9) Å $\gamma = 90^\circ$
Volume	2383.84(15) Å ³
Z	4
Density (calculated)	1.630 Mg/m ³
Absorption coefficient	5.852 mm ⁻¹
F(000)	1168
Crystal size	0.130 x 0.042 x 0.032 mm ³
Crystal shape and color	Block, clear intense brown
Theta range for data collection	2.370 to 28.367°
Index ranges	-11 < h <= 11, -15 < k <= 15, -32 < l <= 32
Reflections collected	99645
Independent reflections	5975 [R(int) = 0.0609]
Completeness to theta = 25.242°	100%
Refinement method	Full-matrix least-squares on F ²
Data / restraints / parameters	5975 / 0 / 243
Goodness-of-fit on F ²	1.055
Final R indices [I > 2sigma(I)]	R1 = 0.0198, wR2 = 0.0387
R indices (all data)	R1 = 0.0242, wR2 = 0.0398
Largest diff. peak and hole	1.123 and -0.569 eÅ ⁻³

Table A22: Cartesian coordinates from X-Ray single-crystal analysis of **15**.

Ir	2.251553	4.509361	15.133991	H	2.440326	5.527254	12.022822
Cl	-0.104047	4.414623	15.328033	H	2.337575	5.164206	10.467623
P	2.625706	6.02797	16.84055	C	4.991518	5.16621	16.013055
P	2.464391	3.012833	13.377452	H	5.939839	5.112419	15.995689
N	4.274138	4.416132	15.123658	C	4.405223	5.978637	16.913123
C	4.912726	3.628146	14.202563	H	4.904067	6.488165	17.540844
H	5.86191	3.589755	14.210824	C	2.031276	5.413199	18.524251
C	4.240983	2.906783	13.286598	C	2.174008	3.870528	18.423136
H	4.684236	2.376338	12.634959	H	1.507176	3.521209	17.795656
C	1.885312	1.278646	13.81867	H	2.032223	3.470736	19.30656
C	2.212219	1.15806	15.32059	H	3.072707	3.645885	18.103314
H	2.028329	0.244063	15.622564	H	2.387103	5.601329	14.131555
H	1.657446	1.787322	15.827203	C	0.557629	5.735691	18.742066
H	3.15867	1.366151	15.466627	H	0.041504	5.449562	17.959686
C	0.378828	1.117803	13.635058	H	0.449898	6.701428	18.869147
H	0.165862	1.104914	12.678556	H	0.233983	5.263448	19.537454
H	-0.08433	1.8681	14.062764	C	2.883162	5.881595	19.683804
H	0.087582	0.277121	14.045927	H	3.807243	5.583222	19.551737
C	2.635454	0.180793	13.05409	H	2.534377	5.504805	20.518549
H	2.474484	0.283802	12.092914	H	2.859588	6.860117	19.732146
H	2.315305	-0.698038	13.346597	C	2.158637	7.802553	16.526509
H	3.595873	0.255167	13.234282	C	0.691035	7.913325	16.120602
C	1.858517	3.558368	11.697509	H	0.493697	8.836456	15.85736
C	0.358806	3.898195	11.752354	H	0.122669	7.661015	16.878029
H	0.10543	4.38972	10.943285	H	0.514696	7.31362	15.365849
H	0.177824	4.451378	12.540805	C	2.406737	8.696853	17.775784
H	-0.16201	3.069895	11.807922	H	2.257356	9.636236	17.539928
C	2.12034	2.525847	10.599546	H	3.329968	8.58001	18.083009
H	1.91662	2.919603	9.725564	H	1.78912	8.437435	18.491084
H	1.550447	1.742077	10.745559	C	3.039493	8.287696	15.417442
H	3.061683	2.254416	10.624138	H	2.858895	7.768677	14.606013
C	2.625048	4.841771	11.347266	H	3.97879	8.176659	15.67394
H	3.586499	4.653019	11.327804	H	2.857399	9.235315	15.246379

A.12. X-Ray Single-Crystal Analysis of 25

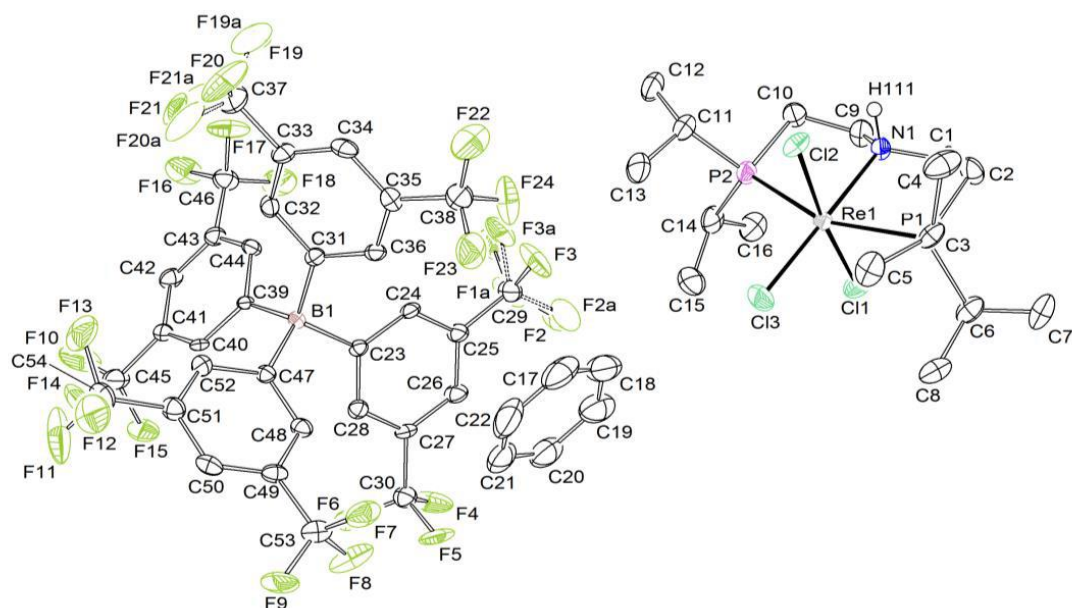


Figure A12: Thermal ellipsoid plot of **25** with the anisotropic displacement parameters drawn at the 50% probability level. The asymmetric unit contains one complex molecule, one benzene solvent molecule and one BARF_{24} anion with two disordered CF_3 groups. The disordered CF_3 groups were refined in two different positions with population of 0.829(5) on their main domains using PART commands and some restraints and constrains (SADI, RIGU, SIMU, EADP). The N-H hydrogen atom was refined isotropically on a calculated position using AFIX 13 command.

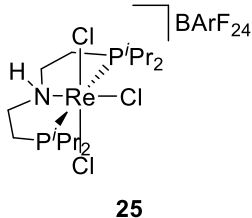
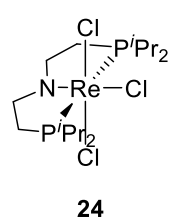
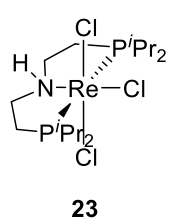
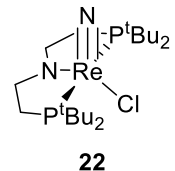
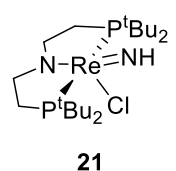
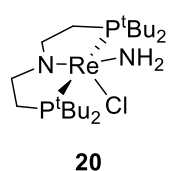
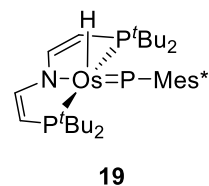
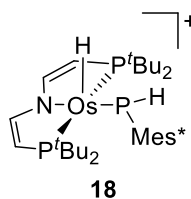
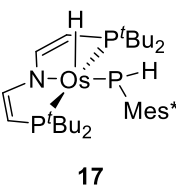
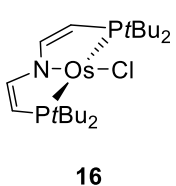
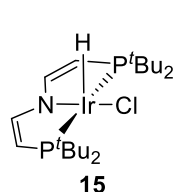
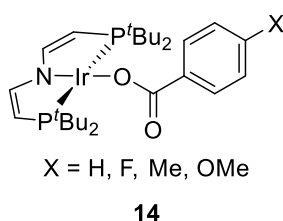
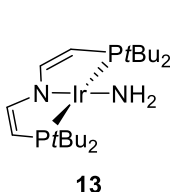
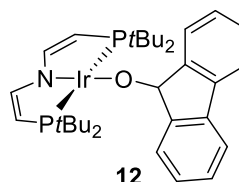
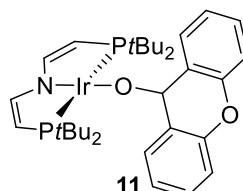
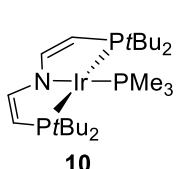
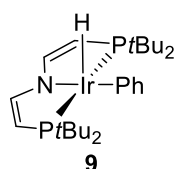
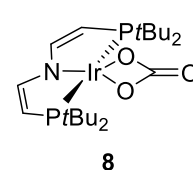
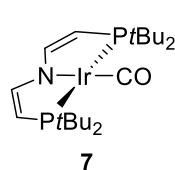
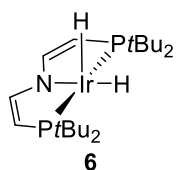
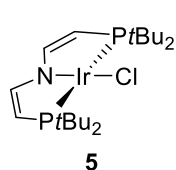
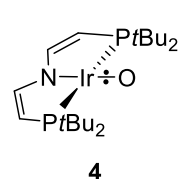
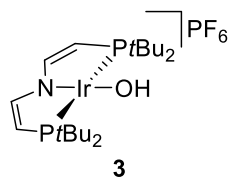
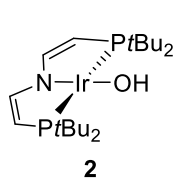
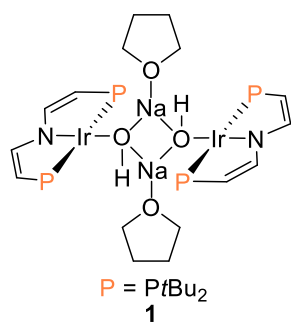
Table A23: Crystal data and structure refinement for **25**.

Crystal data and structure refinement for 25	
Identification code	mo_CW_DD_22719_0m_a (DD-380)
CCDC Identifier	unpublished
Empirical formula	$\text{C}_{54}\text{H}_{55}\text{BCl}_3\text{F}_{24}\text{N}_2\text{P}_2\text{Re}$
Formula weight	1539.29
Temperature	100(2) K
Wavelength	0.71073 Å
Crystal system	Orthorhombic
Space group	$P2_1/c$
Unit cell dimensions	$a = 14.0923(10)$ Å $\alpha = 90^\circ$ $b = 11.5184(4)$ Å $\beta = 103.942(4)^\circ$ $c = 29.199(2)$ Å $\gamma = 90^\circ$
Volume	6200.2(8) Å ³
Z	4
Density (calculated)	1.649 Mg/m ³
Absorption coefficient	2.250 mm ⁻¹
F(000)	3052
Crystal size	0.297 x 0.206 x 0.118 mm ³
Crystal shape and color	Block, clear intense orange
Theta range for data collection	2.229 to 26.585 °
Index ranges	-17<=h<=17, -19<=k<=19, -36<=l<=36
Reflections collected	65141
Independent reflections	12767 [R(int) = 0.1000]
Completeness to theta = 25.242°	99.4%
Refinement method	Full-matrix least-squares on F ²
Data / restraints / parameters	12767 / 120 / 834
Goodness-of-fit on F ²	1.023
Final R indices [I>2sigma(I)]	R1 = 0.0422, wR2 = 0.0946
R indices (all data)	R1 = 0.0693, wR2 = 0.1059
Largest diff. peak and hole	1.206 and -1.072 eÅ ⁻³

Table A24: Cartesian coordinates from X-Ray single-crystal analysis of **25**.

R	13.977905	3.432378	4.700529	F	3.66329	3.125454	17.761542	H	10.911576	2.241975	11.84683
C	13.693873	1.899033	2.983707	F	-1.197985	4.436256	10.921916	C	10.680521	1.565545	9.974294
C	14.436847	5.095423	6.263187	F	-0.288329	3.523854	12.609406	H	11.441757	2.011965	9.622582
C	12.798105	2.169394	6.195259	F	-0.14853	2.579329	10.741341	C	9.900325	0.778868	9.144053
P	16.277448	2.557764	5.091916	F	1.189865	7.948109	8.756605	H	10.124637	0.677766	8.226471
P	12.161827	4.882894	3.799893	F	3.090425	8.468679	9.580612	C	8.780748	0.136826	9.672656
N	15.103317	4.664745	3.261513	F	2.985966	7.185667	7.887142	H	8.240078	-0.409547	9.114382
H	15.360081	5.493015	3.759567	F	10.619353	6.512342	13.143961	C	8.455015	0.294193	11.01121
C	16.393179	4.04933	2.810132	F	10.169536	4.455787	13.351004	H	7.683466	-0.128831	11.36932
H	16.885927	4.686776	2.234826	F	10.223827	5.304799	11.437398	C	9.25839	1.067984	11.81631
H	16.208584	3.233046	2.281245	C	5.516414	3.174701	10.54671	H	9.051801	1.165872	12.73840
C	17.231661	3.697398	4.022183	C	6.408359	3.684807	9.600307				
H	17.459988	4.519411	4.524431	H	6.786914	4.543646	9.747244				
H	18.07422	3.264143	3.735026	C	6.763901	2.987634	8.453946				
C	17.024584	2.590569	6.798847	C	6.222156	1.734586	8.194221				
H	17.724545	1.876955	6.827639	H	6.461268	1.249663	7.41309				
C	17.719857	3.916385	7.113379	C	5.321055	1.214203	9.111775				
H	18.469625	4.046597	6.495877	C	4.972097	1.924106	10.247792				
H	18.054349	3.8994	8.034362	H	4.338562	1.546262	10.846449				
H	17.081028	4.652511	7.011359	C	7.736151	3.596327	7.508875				
C	15.968991	2.230129	7.850528	C	4.774995	-0.164477	8.880955				
H	15.2951	2.940359	7.893716	C	6.076914	5.179773	12.312784				
H	16.399257	2.134415	8.7258	C	5.679094	6.386135	12.911413				
H	15.537791	1.385216	7.604349	H	4.751959	6.582983	12.975969				
C	16.580949	0.876352	4.404898	C	6.594286	7.299065	13.411196				
H	16.229083	0.88056	3.468868	C	7.954624	7.061603	13.3393				
C	18.060169	0.496785	4.316821	H	8.577624	7.69863	13.668796				
H	18.145415	-0.395528	3.920701	C	8.389222	5.867226	12.772751				
H	18.450747	0.493882	5.215615	C	7.466426	4.950787	12.286231				
H	18.531989	1.14884	3.757697	H	7.78589	4.13458	11.919838				
C	15.79134	-0.176137	5.163245	C	6.132775	8.569222	14.04318				
H	14.853367	0.100916	5.225307	C	9.846614	5.562414	12.683597				
H	16.162605	-0.276571	6.064617	C	3.571914	4.67271	11.342237				
H	15.848491	-1.031933	4.689165	C	2.340087	4.053848	11.565121				
C	14.311826	5.132451	2.084971	H	2.313271	3.2806	12.116368				
H	14.02886	4.356424	1.53925	C	1.150752	4.520249	11.015235				
H	14.86764	5.724609	1.518846	C	1.139982	5.6397	10.203952				
C	13.091983	5.887673	2.580701	H	0.332689	5.9601	9.819083				
H	12.504144	6.105977	1.814618	C	2.349948	6.279242	9.971376				
H	13.377226	6.737384	3.001107	C	3.526055	5.806723	10.514432				
C	11.499647	6.13116	4.972609	H	4.335456	6.26516	10.321558				
H	12.293018	6.583417	5.380065	C	-0.131676	3.792585	11.305595				
C	10.692647	7.219699	4.286045	C	2.392229	7.467812	9.070258				
H	11.203087	7.576817	3.529513	C	4.793719	3.099557	13.169863				
H	10.506833	7.940129	4.923895	C	5.433686	1.869503	13.353867				
H	9.847427	6.844432	3.961764	H	5.980056	1.526948	12.656279				
C	10.735238	5.491804	6.120416	C	5.295613	1.128021	14.530267				
H	9.915025	5.079664	5.777205	C	4.528358	1.611547	15.568402				
H	10.504401	6.177612	6.781305	H	4.413073	1.104111	16.36322				
H	11.29347	4.805919	6.542721	C	3.925188	2.86017	15.42804				
C	10.724121	4.09305	2.93658	C	4.043264	3.567667	14.250903				
H	9.982511	4.763829	2.929382	H	3.598417	4.403373	14.172093				
C	10.216832	2.870432	3.714877	C	6.003733	-0.170377	14.647901				
H	9.372482	2.562018	3.324538	C	3.11896	3.406916	16.573834				
H	10.072579	3.116806	4.652381	B	5.000389	4.038183	11.839243				
H	10.881659	2.152191	3.664434	F	7.274588	4.675489	6.912712				
C	11.015357	3.736988	1.489714	F	8.218206	2.789839	6.614701				
H	10.259584	3.235871	1.118136	F	8.849772	4.079574	8.178465				
H	11.825358	3.187152	1.445307	F	7.075188	3.594355	6.308359				
H	11.149118	4.558132	0.971794	F	8.705975	2.810209	7.140726				
F	4.625077	-0.459384	7.596074	F	7.897015	4.876544	7.599588				
F	5.588651	-1.107822	9.377904	F	6.902363	9.607769	14.061146				
F	3.579885	-0.358329	9.450763	F	5.724441	8.278926	15.311823				
F	7.30549	-0.017761	14.924658	F	4.887428	8.782139	13.596532				
F	5.952602	-0.903336	13.542915	F	6.4901	9.646925	13.278315				
F	5.519832	-0.936669	15.631144	F	6.758523	8.816388	15.192771				
F	3.009584	4.729223	16.560005	F	4.857795	8.694559	14.204484				
F	1.917837	2.888348	16.609173	C	10.365544	1.703272	11.286324				

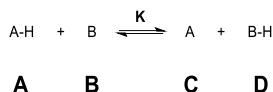
B. List of Chemical Compounds



C. Independent PCET Model

C.1. Derivation of the fitting function

For a general HAT reaction (Scheme C1) the equilibrium constant is derived via eq. c1.



Scheme C1: General HAT reaction

$$K = \frac{[\text{C}][\text{D}]}{[\text{A}][\text{B}]} \quad \text{eq. C1}$$

For the calorimetric titration reactant **A** will be the sample cell concentration and **B** the syringe concentration. The products **C** and **D** are always simultaneously formed, therefore eq. C2 holds true.

$$[\text{C}] = [\text{D}] \quad \text{eq. C2}$$

Only the starting concentrations of **A** and **B** are known, but not the concentrations within the experiment. Therefore, the total concentrations must be defined following eq. C3.

$$[\text{A}_T] = [\text{A}] + [\text{C}] \text{ and } [\text{B}_T] = [\text{B}] + [\text{C}] \quad \text{eq. C3}$$

Inserting eq. C2 and C3 in eq. C1 leads to eq. 4.

$$K = \frac{[\text{C}]^2}{[\text{A}_T - [\text{C}]][\text{B}_T - [\text{C}]]} \quad \text{eq. C4}$$

To analyse the calorimetric process eq. C4 has to be solved for the product formation. Therefore follows:

$$[\text{C}] = -\frac{\sqrt{K} \sqrt{\text{A}_T^2 K - 2\text{A}_T \text{B}_T (K - 2) + \text{B}_T^2 K} + K(\text{A}_T + \text{B}_T)}{2(K - 1)} \quad \text{eq. C5}$$

Which can be simplified to eq. C6.

$$[\text{C}] = \frac{K(\text{A}_T + \text{B}_T) - \sqrt{K[K(\text{A}_T - \text{B}_T)^2 + 4\text{A}_T \text{B}_T]}}{2(K - 1)} \quad \text{eq. C6}$$

The heat is proportional to the formed products and for integration plotted as a function of the added titrant **B**. It follows:

$$\frac{d[\text{C}]}{d[\text{B}_T]} = \frac{\sqrt{K}(\text{A}_T(K - 2) - \text{B}_T K)}{\sqrt{K(\text{A}_T - \text{B}_T)^2 + 4\text{A}_T \text{B}_T}} + K \quad \text{eq. C7}$$

The observable in calorimetry is the heat of reaction dQ , which is directly connected to the reaction enthalpy via eq. C8 with the reaction volume for normalisation.

$$d[\text{C}] = \frac{1}{\Delta H^0 V_0} \frac{dQ}{dB_T} \quad \text{eq. 8}$$

This yield the final product function for the calorimetric fitting process in Isothermal Titration Calorimetry with only ΔH^0 and K as unknown variables.

$$\frac{1}{V_0} \frac{d[Q]}{d[B_T]} = \frac{\Delta H^0}{2(K-1)} \left(\frac{\sqrt{K}(A_T(K-2) - B_T K)}{\sqrt{K(A_T - B_T)^2 + 4A_T B_T}} + K \right)$$

eq. 9

C.2. Incooperation into Visual Basics

The following figure shows the translation of the results in Section C.1. into visual basic directly within the NANOANALYZE Program by TAINSTRUMENTS.

The screenshot displays the 'Script Components' window in the NANOANALYZE software. It is divided into two main sections: 'Script Components' (left) and 'Script Components' (right, top to bottom).

Left Section (Main Function):

```

Main Function InFunction Aux Functions Global Variables/Constants Provided Constants
Insert calculations for one model point here.
' quadratic constants a, b, and c
Dim a As Double = 1/(4*(K-1)*(TotalCellVolume))
Dim b As Double = MolarWeight*(iteration)/(1+(K-1)*TotalCellVolume)
' calculate the root using quadratic formula
Bound = (K*(A*B)-Sqr(K*(A*B)^2+(K-1)*TotalCellVolume))/(2*(K-1))
If OverfillMode Then
' Take note of solution from overflow into account
OldBound = Oldbound + (TotalCellVolume - InjectionVolume(iteration)) / TotalCellVolume
End If
' calculate heat
Heat = log * (bound-Oldbound) * TotalCellVolume*1e-6 + dh
' save value of bound for the next iteration of modeldatapoint()
Oldbound = Bound
Return Heat

```

Right Section (Top):

```

Script Components
Main Function InFunction Aux Functions Global Variables/Constants Provided Constants
'Place global variable initialization code here.
OverfillMode = (CellVolume(1) = CellVolume(0))
TotalCellVolume = CellVolume(0)
OldBound = 0
End Function

```

Right Section (Bottom):

```

Script Components
Main Function InFunction Aux Functions Global Variables/Constants Provided Constants
Public Function ds1() As Double
Return (dh * 1000 + R * (Temperature + 273.15) * Log(Rs(1))) / (Temperature + 273.15)
End Function
Public Function Ra1() As Double
Return R * (Temperature + 273.15) * Log(Rs) / 1000
End Function
Public Function manufds1() As Double
Return -(Temperature + 273.15) * ds1() / 1000
End Function

```

Variables Table:

Name	Script Name	Units	Value	Min	Max	Var	Std	Median	Precision	Visible	Calculated	Temperature	Default Min
dh	dh	kJ/mol	20	1000	1000	<input checked="" type="checkbox"/>	<input type="checkbox"/>	<input type="checkbox"/>	4	<input checked="" type="checkbox"/>	<input type="checkbox"/>	<input type="checkbox"/>	-100
K	K		20	0.001	1000E10	<input checked="" type="checkbox"/>	<input type="checkbox"/>	<input type="checkbox"/>	4	<input checked="" type="checkbox"/>	<input type="checkbox"/>	<input type="checkbox"/>	100
n	n		1	0.100		<input checked="" type="checkbox"/>	<input type="checkbox"/>	<input type="checkbox"/>	4	<input checked="" type="checkbox"/>	<input type="checkbox"/>	<input type="checkbox"/>	Default Max
ds	ds	1/Kmol				<input type="checkbox"/>	<input type="checkbox"/>	<input type="checkbox"/>	4	<input checked="" type="checkbox"/>	<input type="checkbox"/>	<input type="checkbox"/>	100

Scheme C2: Main function of the independent PCET model (left) and the initial function, auxiliary functions, global variables and provided constants (Right top to bottom) of the independent PCET model.

D. Cartesian Coordinates of Computed Structures

Table D1: xyz data of **4**^{3A'}(Cs)
65

E(B3LYP(V)-D3/def2TZVP)=-1703.03451629705592

Ir	0.02322186	-0.14047041	0.00000000
P	0.00831253	0.22776427	2.33116093
P	0.00831253	0.22776427	-2.33116093
N	0.06831915	1.95655412	0.00000000
O	0.01677776	-1.94355902	0.00000000
C	0.08491872	2.63988700	1.18561360
H	0.11502875	3.72764850	1.12704192
C	0.08491872	2.63988700	-1.18561360
H	0.11502875	3.72764850	-1.12704192
C	0.06473572	2.01724657	2.38754281
H	0.07067232	2.58819506	3.30486097
C	0.06473572	2.01724657	-2.38754281
H	0.07067232	2.58819506	-3.30486097
C	1.55115456	-0.37586696	-3.24622368
C	-1.60754443	-0.31352409	-3.16069497
C	1.55115456	-0.37586696	3.24622368
C	-1.60754443	-0.31352409	3.16069497
C	2.73935234	-0.02277196	-2.32978671
H	3.67065113	-0.28685244	-2.83979431
H	2.69350150	-0.56995160	-1.38849788
C	2.76805124	1.04407131	-2.10133173
H	1.76181177	0.32150679	-4.59895065
H	1.83811081	1.40373568	-4.48376980
H	0.97095436	0.10684366	-5.31447724
H	2.70200660	-0.02908994	-5.03542956
C	1.50056862	-1.89918863	-3.42649950
H	2.48305928	-2.25444701	-3.75105169
H	0.78002115	-2.19539341	-4.18923339
H	1.24913897	-2.40474650	-2.49196280
C	-2.71861641	0.50802275	-2.47855872
H	-2.61431685	1.57554014	-2.67389061
H	-2.71583584	0.35811169	-1.39767321
H	-3.68753471	0.18083312	-2.86639107
C	-1.86810104	-1.80324814	-2.87903314
H	-1.17183906	-2.45468549	-3.40381503
H	-2.87585298	-2.05592556	-3.22250273
H	-1.79832369	-2.02722502	-1.81447919
C	-1.64121314	-0.04550641	-4.67044254
H	-1.39498552	0.99107582	-4.90971416
H	-2.64968063	-0.24068721	-5.04766802
H	-0.96018475	-0.69844906	-5.21587235
C	1.76181177	0.32150679	4.59895065
H	2.70200660	-0.02908994	5.03542956
H	0.97095436	0.10684366	5.31447724
H	1.83811081	1.40373568	4.48376980
C	2.73935234	-0.02277196	2.32978671
H	2.76805124	1.04407131	2.10133173
H	2.69350150	-0.56995160	1.38849788
H	3.67065113	-0.28685244	2.83979431
C	1.50056862	-1.89918863	3.42649950
H	1.24913897	-2.40474650	2.49196280
H	0.78002115	-2.19539341	4.18923339
H	2.48305928	-2.25444701	3.75105169
C	-2.71861641	0.50802275	2.47855872
H	-2.61431685	1.57554014	2.67389061
H	-3.68753471	0.18083312	2.86639107
H	-2.71583584	0.35811169	1.39767321
C	-1.64121314	-0.04550641	4.67044254
H	-0.96018475	-0.69844906	5.21587235
H	-2.64968063	-0.24068721	5.04766802
H	-1.39498552	0.99107582	4.90971416
C	-1.86810104	-1.80324814	2.87903314
H	-1.79832369	-2.02722502	1.81447919
H	-2.87585298	-2.05592556	3.22250273
H	-1.17183906	-2.45468549	3.40381503

Table D2: xyz data of **4me**^{3A'}(Cs) ^tBu:Me
29

E(B3LYP(V)-D3/def2TZVP) = -1231.40496563

Ir	0.02322186	-0.14047041	0.00000000
P	0.00831253	0.22776427	2.33116093
P	0.00831253	0.22776427	-2.33116093
N	0.06831915	1.95655412	0.00000000
O	0.01677776	-1.94355902	0.00000000
C	0.08491872	2.63988700	1.18561360
H	0.11502875	3.72764850	1.12704192
C	0.08491872	2.63988700	-1.18561360
H	0.11502875	3.72764850	-1.12704192
C	0.06473572	2.01724657	2.38754281
H	0.07067232	2.58819506	3.30486097
C	0.06473572	2.01724657	-2.38754281
H	0.07067232	2.58819506	-3.30486097
C	1.55115456	-0.37586696	-3.24622368
C	-1.60754443	-0.31352409	-3.16069497
C	1.55115456	-0.37586696	3.24622368
C	-1.60754443	-0.31352409	3.16069497
C	2.73935234	-0.02277196	-2.32978671
H	3.67065113	-0.28685244	-2.83979431
H	2.69350150	-0.56995160	-1.38849788
C	2.76805124	1.04407131	-2.10133173
H	1.76181177	0.32150679	-4.59895065
H	1.83811081	1.40373568	-4.48376980
H	0.97095436	0.10684366	-5.31447724
H	2.70200660	-0.02908994	-5.03542956
C	1.50056862	-1.89918863	-3.42649950
H	2.48305928	-2.25444701	-3.75105169
H	0.78002115	-2.19539341	-4.18923339
H	1.24913897	-2.40474650	-2.49196280
C	-2.71861641	0.50802275	-2.47855872
H	-2.61431685	1.57554014	-2.67389061
H	-2.71583584	0.35811169	-1.39767321
H	-3.68753471	0.18083312	-2.86639107
C	-1.86810104	-1.80324814	-2.87903314
H	-1.17183906	-2.45468549	-3.40381503
H	-2.87585298	-2.05592556	-3.22250273
H	-1.79832369	-2.02722502	-1.81447919
C	-1.64121314	-0.04550641	-4.67044254
H	-1.39498552	0.99107582	-4.90971416
H	-2.64968063	-0.24068721	-5.04766802
H	-0.96018475	-0.69844906	-5.21587235
C	1.76181177	0.32150679	4.59895065
H	2.70200660	-0.02908994	5.03542956
H	0.97095436	0.10684366	5.31447724
H	1.83811081	1.40373568	4.48376980
C	2.73935234	-0.02277196	2.32978671
H	2.76805124	1.04407131	2.10133173
H	2.69350150	-0.56995160	1.38849788
H	3.67065113	-0.28685244	2.83979431
C	1.50056862	-1.89918863	3.42649950
H	1.24913897	-2.40474650	2.49196280
H	0.78002115	-2.19539341	4.18923339
H	2.48305928	-2.25444701	3.75105169
C	-2.71861641	0.50802275	2.47855872
H	-2.61431685	1.57554014	2.67389061
H	-3.68753471	0.18083312	2.86639107
H	-2.71583584	0.35811169	1.39767321
C	-1.64121314	-0.04550641	4.67044254
H	-0.96018475	-0.69844906	5.21587235
H	-2.64968063	-0.24068721	5.04766802
H	-1.39498552	0.99107582	4.90971416
C	-1.86810104	-1.80324814	2.87903314
H	-1.79832369	-2.02722502	1.81447919
H	-2.87585298	-2.05592556	3.22250273
H	-1.17183906	-2.45468549	3.40381503

Table D3: xyz data of **4h**^{3A'}(Cs) ^tBu:H
17

E(B3LYP(V)-D3/def2TZVP) = -1074.14708225

Ir	0.02322186	-0.14047041	0.00000000
P	0.00831253	0.22776427	2.33116093
P	0.00831253	0.22776427	-2.33116093
N	0.06831915	1.95655412	0.00000000
O	0.01677776	-1.94355902	0.00000000
C	0.08491872	2.63988700	1.18561360
H	0.11502875	3.72764850	1.12704192
C	0.08491872	2.63988700	-1.18561360
H	0.11502875	3.72764850	-1.12704192
C	0.06473572	2.01724657	2.38754281
H	0.07067232	2.58819506	3.30486097
C	0.06473572	2.01724657	-2.38754281
H	0.07067232	2.58819506	-3.30486097
C	1.55115456	-0.37586696	-3.24622368
C	-1.60754443	-0.31352409	-3.16069497
C	1.55115456	-0.37586696	3.24622368
C	-1.60754443	-0.31352409	3.16069497
C	2.73935234	-0.02277196	-2.32978671
H	3.67065113	-0.28685244	-2.83979431
H	2.69350150	-0.56995160	-1.38849788
C	2.76805124	1.04407131	-2.10133173
H	1.76181177	0.32150679	-4.59895065
H	1.83811081	1.40373568	-4.48376980
H	0.97095436	0.10684366	-5.31447724
H	2.70200660	-0.02908994	-5.03542956
C	1.50056862	-1.89918863	-3.42649950
H	2.48305928	-2.25444701	-3.75105169
H	0.78002115	-2.19539341	-4.18923339
H	1.24913897	-2.40474650	-2.49196280
C	-2.71861641	0.50802275	-2.47855872
H	-2.61431685	1.57554014	-2.67389061
H	-2.71583584	0.35811169	-1.39767321
H	-3.68753471	0.18083312	-2.86639107
C	-1.86810104	-1.80324814	-2.87903314
H	-1.17183906	-2.45468549	-3.40381503
H	-2.87585298	-2.05592556	-3.22250273
H	-1.79832369	-2.02722502	-1.81447919
C	-1.64121314	-0.04550641	-4.67044254
H	-1.39498552	0.99107582	-4.90971416
H	-2.64968063	-0.24068721	-5.04766802
H	-0.96018475	-0.69844906	-5.21587235
C	1.76181177	0.32150679	4.59895065
H	2.70200660	-0.02908994	5.03542956
H	0.97095436	0.10684366	5.31447724
H	1.83811081	1.40373568	4.48376980
C	2.73935234	-0.02277196	2.32978671
H	2.76805124	1.04407131	2.10133173
H	2.69350150	-0.56995160	1.38849788
H	3.67065113	-0.28685244	2.83979431
C	1.50056862	-1.89918863	3.42649950
H	1.24913897	-2.40474650	2.49196280
H	0.78002115	-2.19539341	4.18923339
H	2.48305928	-2.25444701	3.75105169
C	-2.71861641	0.50802275	2.47855872
H	-2.61431685	1.57554014	2.67389061
H	-3.68753471	0.18083312	2.86639107
H	-2.71583584	0.35811169	1.39767321
C	-1.64121314	-0.04550641	4.67044254
H	-0.96018475	-0.69844906	5.21587235
H	-2.64968063	-0.24068721	5.04766802
H	-1.39498552	0.99107582	4.90971416
C	-1.86810104	-1.80324814	2.87903314
H	-1.79832369	-2.02722502	1.81447919
H	-2.87585298	-2.05592556	3.22250273
H	-1.17183906	-2.45468549	3.40381503

Table D4: xyz data of 4 ¹A'(Cs)

65

E(B3LYP(V)-D3/def2TZVP)=-1703.00633285815093

Ir	-0.0298281579	-0.0973829171	0.0000000000
P	-0.0186695120	0.1846628807	2.3325446875
P	-0.0186695120	0.1846628807	-2.3325446875
N	-0.2471987979	1.9030873015	-0.0000000000
O	0.8567711343	-1.6835949596	-0.0000000000
C	-0.2273192968	2.6027725485	1.1992341983
H	-0.2978954486	3.6871576584	1.1309505548
C	-0.2273192968	2.6027725485	-1.1992341983
H	-0.2978954486	3.6871576584	-1.1309505548
C	-0.1277468141	1.9881392673	2.3934301135
H	-0.1297821396	2.5663808244	3.3067711449
C	-0.1277468141	1.9881392673	-2.3934301135
H	-0.1297821396	2.5663808244	-3.3067711449
C	1.5924389747	-0.2622678441	-3.2117418542
C	-1.5624645946	-0.4670333280	-3.2157995472
C	1.5924389747	-0.2622678441	3.2117418542
C	-1.5624645946	-0.4670333280	3.2157995472
C	2.7180892418	0.1921319386	-2.2598704591
H	3.6818353101	0.0226371493	-2.7495032255
H	2.6983547965	-0.3746845813	-1.3303722001
H	2.6437800918	1.2552045367	-2.0228378268
C	1.7790918059	0.4456089533	-4.5613892425
H	1.7610186226	1.5314647830	-4.4526969233
H	1.0298879803	0.1619267018	-5.2975246025
H	2.7576536724	0.1742994820	-4.9695797005
C	1.6784076346	-1.7870805036	-3.3743636870
H	2.6919082134	-2.0542987077	-3.6889901767
H	0.9941440339	-2.1556656602	-4.1395326832
H	1.4697629140	-2.2894200183	-2.4273274461
C	-2.7553779613	0.2798676378	-2.5880522719
H	-2.7351956980	1.3461065157	-2.8140366308
H	-2.7750312504	0.1604807860	-1.5029709590
H	-3.6843425089	-0.1362979749	-2.9882955693
C	-1.7197402767	-1.9662028139	-2.9058876729
H	-0.9396701401	-2.5714806121	-3.3633083042
H	-2.6808743867	-2.3118891910	-3.2987947359
H	-1.6982992421	-2.1506675404	-1.8314401561
C	-1.5685525621	-0.2356854903	-4.7313238094
H	-1.3926034510	0.8109718440	-4.9877669084
H	-2.5467222719	-0.5147701138	-5.1353558248
H	-0.8223479912	-0.8460846932	-5.2392636422
C	1.7790918059	0.4456089533	4.5613892425
H	2.7576536724	0.1742994820	4.9695797005
H	1.0298879803	0.1619267018	5.2975246025
H	1.7610186226	1.5314647830	4.4526969233
C	2.7180892418	0.1921319386	2.2598704591
H	2.6437800918	1.2552045367	2.0228378268
H	2.6983547965	-0.3746845813	1.3303722001
H	3.6818353101	0.0226371493	2.7495032255
C	1.6784076346	-1.7870805036	3.3743636870
H	1.4697629140	-2.2894200183	2.4273274461
H	0.9941440339	-2.1556656602	4.1395326832
H	2.6919082134	-2.0542987077	3.6889901767
C	-2.7553779613	0.2798676378	2.5880522719
H	-2.7351956980	1.3461065157	2.8140366308
H	-3.6843425089	-0.1362979749	2.9882955693
H	-2.7750312504	0.1604807860	1.5029709590
C	-1.5685525621	-0.2356854903	4.7313238094
H	-0.8223479912	-0.8460846932	5.2392636422
H	-2.5467222719	-0.5147701138	5.1353558248
H	-1.3926034510	0.8109718440	4.9877669084
C	-1.7197402767	-1.9662028139	2.9058876729
H	-1.6982992421	-2.1506675404	1.8314401561
H	-2.6808743867	-2.3118891910	3.2987947359
H	-0.9396701401	-2.5714806121	3.3633083042

Table D5: xyz data of 4me ¹A'(Cs) ^tBu:Me

29

E(B3LYP(V)-D3/def2TZVP) = -1231.40496563

I	-0.02982816	-0.09738292	0.00000000
P	-0.01866951	0.18466288	2.33254469
P	-0.01866951	0.18466288	-2.33254469
N	-0.24719880	1.90308730	0.00000000
O	0.85677113	-1.68359496	0.00000000
C	-0.22731930	2.60277255	1.19923420
H	-0.29789545	3.68715766	1.13095056
C	-0.22731930	2.60277255	-1.19923420
H	-0.29789545	3.68715766	-1.13095056
C	-0.12774681	1.98813927	2.39343011
H	-0.12978214	2.56638082	3.30677115
C	-0.12774681	1.98813927	-2.39343011
H	-0.12978214	2.56638082	-3.30677115
C	1.59243898	-0.26226784	-3.21174185
C	-1.56246460	-0.46703333	-3.21579955
C	1.59243898	-0.26226784	3.21174185
C	-1.56246460	-0.46703333	3.21579955
H	2.38724762	0.05857859	-2.53963646
H	1.72499478	0.24044717	-4.17022503
H	1.65342771	-1.34401540	-3.32711063
H	-2.40608766	0.06117174	-2.77185945
H	-1.67379460	-1.52824343	-2.99642368
H	-1.56679785	-0.30236591	-4.29451059
H	1.72499478	0.24044717	4.17022503
H	2.38724762	0.05857859	2.53963646
H	1.65342771	-1.34401540	3.32711063
H	-2.40608766	0.06117174	2.77185945
H	-1.56679785	-0.30236591	4.29451059
H	-1.67379460	-1.52824343	2.99642368

Table D6: xyz data of 4h ¹A'(Cs) ^tBu:H

17

E(B3LYP(V)-D3/def2TZVP) = -1074.11808336

Ir	-0.02982816	-0.09738292	0.00000000
P	-0.01866951	0.18466288	2.33254469
P	-0.01866951	0.18466288	-2.33254469
N	-0.24719880	1.90308730	0.00000000
O	0.85677113	-1.68359496	0.00000000
C	-0.22731930	2.60277255	1.19923420
H	-0.29789545	3.68715766	1.13095056
C	-0.22731930	2.60277255	-1.19923420
H	-0.29789545	3.68715766	-1.13095056
C	-0.12774681	1.98813927	2.39343011
H	-0.12978214	2.56638082	3.30677115
C	-0.12774681	1.98813927	-2.39343011
H	-0.12978214	2.56638082	-3.30677115
H	1.18152063	-0.14827674	-2.98749982
H	-1.16602787	-0.29968190	-2.98898534
H	1.18152063	-0.14827674	2.98749982
H	-1.16602787	-0.29968190	2.98898534

Table D7: xyz data of 2²A(C1)

66

E(B3LYP(V)-D3/def2TZVP)=-1703.66592875412994

Ir	0.0050958848	-0.0156777177	-0.0882343990
P	-2.3124919190	-0.0023251148	0.2028011184
P	2.3243994711	-0.0141122055	0.2134758945
N	-0.0017481669	-0.0543978270	1.9312039329
O	0.1472304536	-0.0255323898	-2.0622208719
H	-0.7026424592	-0.0245540780	-2.5115971839
C	-1.1919566468	-0.0603323501	2.6234292271
H	-1.1254519701	-0.0822505932	3.7099385235
C	1.1887359932	-0.0858461070	2.6276294720
H	1.1156417377	-0.1165700739	3.7135721441
C	-2.3898016333	-0.0390265573	2.0008413680
H	-3.3073033307	-0.0328197877	2.5717051577
C	2.3898295740	-0.0786063806	2.0120729664
H	3.3029031461	-0.0952036685	2.5902553202
C	3.2386485545	-1.5593207391	-0.3854775126
C	3.1876083130	1.5944795914	-0.2980978610
C	-3.2705549530	-1.5465776493	-0.3506172359
C	-3.1723670696	1.6033523041	-0.3339373118
C	2.3159075649	-2.7430408202	-0.0325160000
H	2.8164750092	-3.6772505567	-0.3051141328
H	1.3714679948	-2.6865338340	-0.5732738996
H	2.0936289730	-2.7762841036	1.0356788813
C	4.5933796531	-1.7843379437	0.3016100866
H	4.4860017573	-1.8597340832	1.3849638763
H	5.3148182757	-1.0002188357	0.0824421749
H	5.0192351836	-2.7286018496	-0.0520153182
C	3.4057483122	-1.5038369124	-1.9111699929
H	3.7125355610	-2.4892855774	-2.2749953239
H	4.1779266579	-0.7937343776	-2.2086731951
H	2.4699766884	-1.2312864958	-2.4037958700
C	2.5026906513	2.7075452708	0.5191456688
H	2.6787212312	2.5949720193	1.5893851581
H	1.4243931595	2.7159568926	0.3515082189
H	2.9052539409	3.6752011507	0.2057254678
C	2.9262117827	1.8650484407	-1.7903304587
H	3.4759456499	1.1837625167	-2.4372479707
H	3.2558965740	2.8812054378	-2.0285424526
H	1.8680426358	1.7722226746	-2.0348995321
C	4.6933022486	1.6190667060	-0.0103772707
H	4.9185561140	1.3640646378	1.0273374740
H	5.0794686606	2.6266404914	-0.1940588016
H	5.2430632153	0.9392481916	-0.6608863413
C	-4.5999716637	-1.7492486789	0.3930052742
H	-5.0505385628	-2.6915366111	0.0658407031
H	-5.3213368183	-0.9588605053	0.1976195371
H	-4.4481317211	-1.8179839925	1.4707398486
C	-2.3475813728	-2.7359953764	-0.0195464197
H	-2.0921499057	-2.7602006624	1.0411988426
H	-1.4179955912	-2.6924365813	-0.5870272595
H	-2.8632577394	-3.6690958443	-0.2667560156
C	-3.5160748362	-1.5222594973	-1.8652107891
H	-2.5914833962	-1.3536239307	-2.4210265166
H	-4.2410079698	-0.7616549938	-2.1551880122
H	-3.9141678833	-2.4907313012	-2.1824041044
C	-2.5384287577	2.7225515551	0.5143564023
H	-2.7924333425	2.6244865844	1.5698952992
H	-2.9083958822	3.6895861455	0.1608598466
H	-1.4506010617	2.7200858593	0.4258675514
C	-4.6901234262	1.6143332817	-0.1197319133
H	-5.2052304428	0.9266394911	-0.7903479188
H	-5.0768283636	2.6176527063	-0.3241203157
H	-4.9591160014	1.3619051994	0.9077514410
C	-2.8430187354	1.8845474615	-1.8103614247
H	-1.7648524327	1.9356820940	-1.9679293234
H	-3.2711176045	2.8500733175	-2.0965550073
H	-3.2556138754	1.1348813063	-2.4848956458

Table D8: xyz data of 2me²A(C1)¹Bu:Me

30

E(B3LYP(V)-D3/def2TZVP) = -1232.03745741

Ir	0.0050958848	-0.0156777177	-0.0882343990
P	-2.3124919190	-0.0023251148	0.2028011184
P	2.3243994711	-0.0141122055	0.2134758945
N	-0.0017481669	-0.0543978270	1.9312039329
O	0.1472304536	-0.0255323898	-2.0622208719
H	-0.7026424592	-0.0245540780	-2.5115971839
C	-1.1919566468	-0.0603323501	2.6234292271
H	-1.1254519701	-0.0822505932	3.7099385235
C	1.1887359932	-0.0858461070	2.6276294720
H	1.1156417377	-0.1165700739	3.7135721441
C	-2.3898016333	-0.0390265573	2.0008413680
H	-3.3073033307	-0.0328197877	2.5717051577
C	2.3898295740	-0.0786063806	2.0120729664
H	3.3029031461	-0.0952036685	2.5902553202
C	3.2386485545	-1.5593207391	-0.3854775126
C	3.1876083130	1.5944795914	-0.2980978610
C	-3.2705549530	-1.5465776493	-0.3506172359
C	-3.1723670696	1.6033523041	-0.3339373118
H	2.5867727657	-2.3955667391	-0.1361257801
H	4.2011395354	-1.7191879114	0.1026751680
H	3.3572504733	-1.5199401416	-1.4683639161
H	2.7034809351	2.3812392253	0.2795627679
H	3.0025009675	1.7860822933	-1.3548189076
H	4.2594987768	1.6119829452	-0.0932720663
H	-4.2143361794	-1.6904581281	0.1772962158
H	-2.6183288502	-2.3870884780	-0.1166635965
H	-3.4450898908	-1.5292903848	-1.4273100404
H	-2.7241461093	2.3946730899	0.2658419034
H	-4.2529692398	1.6111704682	-0.1814287636
H	-2.9390142620	1.8025871951	-1.3800264405

Table D9: xyz data of 2h²A((C1)¹Bu:H

18

E(B3LYP(V)-D3/def2TZVP) = -1074.78244850

Ir	0.0050958848	-0.0156777177	-0.0882343990
P	-2.3124919190	-0.0023251148	0.2028011184
P	2.3243994711	-0.0141122055	0.2134758945
N	-0.0017481669	-0.0543978270	1.9312039329
O	0.1472304536	-0.0255323898	-2.0622208719
H	-0.7026424592	-0.0245540780	-2.5115971839
C	-1.1919566468	-0.0603323501	2.6234292271
H	-1.1254519701	-0.0822505932	3.7099385235
C	1.1887359932	-0.0858461070	2.6276294720
H	1.1156417377	-0.1165700739	3.7135721441
C	-2.3898016333	-0.0390265573	2.0008413680
H	-3.3073033307	-0.0328197877	2.5717051577
C	2.3898295740	-0.0786063806	2.0120729664
H	3.3029031461	-0.0952036685	2.5902553202
H	-3.0234805337	-1.1483310991	-0.2078964403
H	-2.9509967012	1.1899790353	-0.1957568051
H	3.0043142266	-1.1632630238	-0.2319577042
H	2.9654541046	1.1804946785	-0.1664399618

Table D10: xyz data of 4+ ²A''(Cs)

65

E(UPBE1PBE-D3(BJ)/def2TZVP) = -1702.18117658 <S2> = 0.9298

N	-0.04402339	0.00000000	1.85406003
C	-0.04499775	1.18409063	2.59510905
C	-0.04499775	-1.18409063	2.59510905
C	-0.02671447	-2.37904680	1.99645369
P	0.01446540	-2.34282627	0.20194402
C	-1.57704960	-3.11286682	-0.38800661
C	1.57550258	-3.23673873	-0.28659437
C	-0.02671447	2.37904680	1.99645369
P	0.01446540	2.34282627	0.20194402
C	1.57550258	3.23673873	-0.28659437
C	-1.57704960	3.11286682	-0.38800661
C	1.73309837	-4.56042978	0.45777010
C	2.72861344	-2.30982109	0.10403497
C	1.59051143	-3.45661222	-1.79594879
C	2.72861344	2.30982109	0.10403497
C	1.73309837	4.56042978	0.45777010
C	1.59051143	3.45661222	-1.79594879
C	-1.61854121	-4.62248667	-0.18277398
C	-1.77714236	-2.76574472	-1.86280256
C	-2.69016715	-2.45204841	0.42717433
C	-2.69016715	2.45204841	0.42717433
C	-1.77714236	2.76574472	-1.86280256
C	-1.61854121	4.62248667	-0.18277398
Ir	0.08237422	0.00000000	-0.10305373
O	0.50626869	0.00000000	-1.79877184
H	2.70427796	2.05090805	1.16523660
H	3.67129414	2.82870026	-0.08975388
H	2.72151780	1.38900242	-0.48034963
H	1.39676236	2.53246414	-2.34523130
H	2.58275910	3.81353159	-2.08477991
H	0.86907893	4.21236716	-2.10849421
H	-1.42218064	4.90849233	0.85268265
H	-2.62050419	4.98006281	-0.43588800
H	-0.91486175	5.14509492	-0.83097387
H	-2.65786415	1.36256493	0.34474564
H	-3.65335471	2.78725447	0.03393327
H	-2.64501243	2.72231069	1.48297183
H	-1.77274893	1.68655195	-2.02390651
H	-1.01946210	3.20882170	-2.50738303
H	-2.74946632	3.15267758	-2.17946196
H	-2.64501243	-2.72231069	1.48297183
H	-3.65335471	-2.78725447	0.03393327
H	-2.65786415	-1.36256493	0.34474564
H	-0.91486175	-5.14509492	-0.83097387
H	-2.62050419	-4.98006281	-0.43588800
H	-1.42218064	-4.90849233	0.85268265
H	-1.01946210	-3.20882170	-2.50738303
H	-1.77274893	-1.68655195	-2.02390651
H	-2.74946632	-3.15267758	-2.17946196
H	2.70427796	-2.05090805	1.16523660
H	2.72151780	-1.38900242	-0.48034963
H	3.67129414	-2.82870026	-0.08975388
H	0.86907893	-4.21236716	-2.10849421
H	2.58275910	-3.81353159	-2.08477991
H	1.39676236	-2.53246414	-2.34523130
H	1.80526492	-4.41290601	1.53674209
H	2.66620496	-5.02782950	0.13152856
H	0.92716844	-5.26339419	0.25485995
H	1.80526492	4.41290601	1.53674209
H	0.92716844	5.26339419	0.25485995
H	2.66620496	5.02782950	0.13152856
H	-0.06831680	-1.07899195	3.67646059
H	-0.03791943	-3.28983941	2.58035035
H	-0.06831680	1.07899195	3.67646059
H	-0.03791943	3.28983941	2.58035035

Table D11: xyz data of 4+ ⁴A''(Cs)

65

E(UPBE1PBE-D3(BJ)/def2TZVP) = -1702.16317837 <S2> = 3.7863

N	0.03800444	0.00000000	1.92148364
C	0.01810707	1.17597021	2.62125454
C	0.01810707	-1.17597021	2.62125454
C	-0.04067448	-2.36830445	1.99096263
P	-0.01054829	-2.33221609	0.19674380
C	-1.58524123	-3.12983278	-0.39351135
C	1.56865296	-3.19782748	-0.28615254
C	-0.04067448	2.36830445	1.99096263
P	-0.01054829	2.33221609	0.19674380
C	1.56865296	3.19782748	-0.28615254
C	-1.58524123	3.12983278	-0.39351135
C	1.75208905	-4.50964277	0.47235267
C	2.70067964	-2.24059685	0.09361274
C	1.58918535	-3.43312422	-1.79275092
C	2.70067964	2.24059685	0.09361274
C	1.75208905	4.50964277	0.47235267
C	1.58918535	3.43312422	-1.79275092
C	-1.63737194	-4.63011106	-0.13367850
C	-1.76291709	-2.83147008	-1.88143051
C	-2.70227534	-2.42942764	0.38222351
C	-2.70227534	2.42942764	0.38222351
C	-1.76291709	2.83147008	-1.88143051
C	-1.63737194	4.63011106	-0.13367850
Ir	0.01549097	0.00000000	-0.12969436
O	0.51623709	0.00000000	-1.84638212
H	2.65985227	1.95428959	1.14753498
H	3.65538783	2.74629548	-0.07480305
H	2.68405698	1.33787190	-0.51840058
H	1.36524731	2.52151720	-2.35157074
H	2.59240019	3.76063375	-2.07879220
H	0.89295128	4.21627157	-2.09480051
H	-1.45631623	4.87791217	0.91446622
H	-2.63566283	4.99674195	-0.38832388
H	-0.92425492	5.17685340	-0.75100609
H	-2.67182419	1.34396993	0.24211705
H	-3.66573772	2.78354638	0.00690946
H	-2.65619445	2.63556576	1.45289667
H	-1.69391862	1.76148332	-2.09026125
H	-1.03066102	3.34421584	-2.50270868
H	-2.75562193	3.17152373	-2.18849808
H	-2.65619445	-2.63556576	1.45289667
H	-3.66573772	-2.78354638	0.00690946
H	-2.67182419	-1.34396993	0.24211705
H	-0.92425492	-5.17685340	-0.75100609
H	-2.63566283	-4.99674195	-0.38832388
H	-1.45631623	-4.87791217	0.91446622
H	-1.03066102	-3.34421584	-2.50270868
H	-1.69391862	-1.76148332	-2.09026125
H	-2.75562193	-3.17152373	-2.18849808
H	2.65985227	-1.95428959	1.14753498
H	2.68405698	-1.33787190	-0.51840058
H	3.65538783	-2.74629548	-0.07480305
H	0.89295128	-4.21627157	-2.09480051
H	2.59240019	-3.76063375	-2.07879220
H	1.36524731	-2.52151720	-2.35157074
H	1.82909613	-4.34763795	1.54896380
H	2.68888155	-4.96847657	0.14454470
H	0.95399106	-5.22607428	0.28414954
H	1.82909613	4.34763795	1.54896380
H	0.95399106	5.22607428	0.28414954
H	2.68888155	4.96847657	0.14454470
H	0.04061579	-1.10617031	3.70668937
H	-0.08448584	-3.28512176	2.56470279
H	0.04061579	1.10617031	3.70668937
H	-0.08448584	3.28512176	2.56470279

Table D12: xyz data of Mes*OH¹A' (Cs)

49

E(B3LYP(V)-D3/def2TZVP) = -779.03307004271915

C	0.40442879	1.18230327	0.00000000
C	-0.47890621	-1.47666010	0.00000000
C	1.35508336	0.14577914	0.00000000
C	-0.98246635	0.92342527	0.00000000
C	-1.37669709	-0.40951321	0.00000000
C	0.87360170	-1.16720701	0.00000000
H	-2.43148325	-0.63306780	0.00000000
H	1.58715691	-1.97232425	0.00000000
O	0.77372584	2.50675302	0.00000000
H	1.72930373	2.58561535	0.00000000
C	-1.00820434	-2.91797490	0.00000000
C	-2.02525536	2.05980519	0.00000000
C	2.87613810	0.41884766	0.00000000
C	0.12216822	-3.95775724	0.00000000
H	0.75516695	-3.86733241	0.88544228
H	0.75516695	-3.86733241	-0.88544228
H	-0.30337380	-4.96346252	0.00000000
C	-1.87083642	-3.15003432	1.25794262
H	-1.28153274	-2.99484739	2.16429581
H	-2.25862597	-4.17213696	1.27243201
H	-2.72310404	-2.46995548	1.29371219
C	-1.87083642	-3.15003432	-1.25794262
H	-2.72310404	-2.46995548	-1.29371219
H	-2.25862597	-4.17213696	-1.27243201
H	-1.28153274	-2.99484739	-2.16429581
C	-1.87083642	2.92946601	-1.26725216
H	-0.89319689	3.40121976	-1.31932464
H	-2.63115302	3.71503916	-1.27323219
H	-2.00807119	2.32141395	-2.16468428
C	-1.87083642	2.92946601	1.26725216
H	-0.89319689	3.40121976	1.31932464
H	-2.00807119	2.32141395	2.16468428
H	-2.63115302	3.71503916	1.27323219
C	-3.46567748	1.51724646	0.00000000
H	-3.67770527	0.91548282	0.88630282
H	-3.67770527	0.91548282	-0.88630282
H	-4.16265727	2.35753922	0.00000000
C	3.29481238	1.18890276	1.27595121
H	3.05517724	0.59914695	2.16250509
H	2.80221415	2.15410638	1.40282409
H	4.37177883	1.37286730	1.26840033
C	3.29481238	1.18890276	-1.27595121
H	2.80221415	2.15410638	-1.40282409
H	3.05517724	0.59914695	-2.16250509
H	4.37177883	1.37286730	-1.26840033
C	3.69962789	-0.88253905	0.00000000
H	3.50285395	-1.48922200	0.88535989
H	4.76292099	-0.63443460	0.00000000
H	3.50285395	-1.48922200	-0.88535989

Table D13: xyz data of Mes*OH^{Me} ¹A' (Cs) ^tBu:Me

22

E(B3LYP(V)-D3/def2TZVP) = -425.325964546

C	0.404428790	1.182303275	0.000000000
C	-0.478906207	-1.476660103	0.000000000
C	1.355083361	0.145779137	0.000000000
C	-0.982466347	0.923425269	0.000000000
C	-1.376697092	-0.409513205	0.000000000
C	0.873601700	-1.167207011	0.000000000
H	-2.431483251	-0.633067800	0.000000000
H	1.587156912	-1.972324247	0.000000000
O	0.773725839	2.506753017	0.000000000
H	1.729303734	2.585615350	0.000000000
C	-1.008204339	-2.917974904	0.000000000
H	-0.205682842	-3.656180789	0.000000000
H	-1.618831584	-3.082241690	0.890453829
H	-1.618831584	-3.082241690	-0.890453829
C	-2.025255356	2.059805187	0.000000000
H	-1.916151730	2.674257980	-0.895368178
H	-1.916151730	2.674257980	0.895368178
H	-3.045862512	1.675376681	0.000000000
C	2.876138096	0.418847662	0.000000000
H	3.172084764	0.963173525	0.901926686
H	3.172084764	0.963173525	-0.901926686
H	3.458820774	-0.501984031	0.000000000

Table D14: xyz data of Mes*OH^H ¹A' (Cs) ^tBu:Me

13

E(B3LYP(V)-D3/def2TZVP) = -307.412570837

C	0.40442879	1.18230328	0.00000000
C	-0.47890621	-1.47666010	0.00000000
C	1.35508336	0.14577914	0.00000000
C	-0.98246635	0.92342527	0.00000000
C	-1.37669709	-0.40951321	0.00000000
C	0.87360170	-1.16720701	0.00000000
H	-2.43148325	-0.63306780	0.00000000
H	1.58715691	-1.97232425	0.00000000
O	0.77372584	2.50675302	0.00000000
H	1.72930373	2.58561535	0.00000000
H	-0.85141752	-2.49103374	0.00000000
H	-1.71263515	1.71912714	0.00000000
H	2.42057903	0.33706307	0.00000000

Table D15: xyz data of Mes*O^{2A} (Cs)

48

E(B3LYP(V)-D3/def2TZVP) = -778.40576486694818

C	0.42887515	1.23904273	0.00000000
C	-0.45989312	-1.45264666	0.00000000
C	1.38723894	0.13308698	0.00000000
C	-1.00283896	0.92563434	0.00000000
C	-1.38078327	-0.38865632	0.00000000
C	0.90719205	-1.15475784	0.00000000
H	-2.43455432	-0.63128204	0.00000000
H	1.61060641	-1.97338915	0.00000000
O	0.82057433	2.41930657	0.00000000
C	-0.98219231	-2.87873524	0.00000000
C	-2.02047147	2.05465003	0.00000000
C	2.87779205	0.42917507	0.00000000
C	0.13751951	-3.91404963	0.00000000
H	0.77073551	-3.82750843	0.88613283
H	0.77073551	-3.82750843	-0.88613283
H	-0.29581615	-4.91663524	0.00000000
C	-1.84188218	-3.09717364	1.25117212
H	-1.25291409	-2.94710932	2.15892549
H	-2.23204013	-4.11835951	1.26138579
H	-2.69175459	-2.41338445	1.28453084
C	-1.84188218	-3.09717364	-1.25117212
H	-2.69175459	-2.41338445	-1.28453084
H	-2.23204013	-4.11835951	-1.26138579
H	-1.25291409	-2.94710932	-2.15892549
C	-1.84033589	2.91811772	-1.25613531
H	-0.85254335	3.37331535	-1.28222294
H	-2.59308423	3.71125015	-1.26426270
H	-1.97485302	2.31732067	-2.15963970
C	-1.84033589	2.91811772	1.25613531
H	-0.85254335	3.37331535	1.28222294
H	-1.97485302	2.31732067	2.15963970
H	-2.59308423	3.71125015	1.26426270
C	-3.45308061	1.52711245	0.00000000
H	-3.66944472	0.92674794	0.88763635
H	-3.66944472	0.92674794	-0.88763635
H	-4.14268216	2.37392620	0.00000000
C	3.24995152	1.22928437	1.25620079
H	2.99829626	0.66759814	2.15982530
H	2.73106366	2.18510199	1.28197617
H	4.32774642	1.41380803	1.26406519
C	3.24995152	1.22928437	-1.25620079
H	2.73106366	2.18510199	-1.28197617
H	2.99829626	0.66759814	-2.15982530
H	4.32774642	1.41380803	-1.26406519
C	3.71214012	-0.84958819	0.00000000
H	3.52761195	-1.46071242	0.88738275
H	4.77074592	-0.58122904	0.00000000
H	3.52761195	-1.46071242	-0.88738275

Table D16: xyz data of Mes*O^{Me} 2A (Cs) tBu:Me

21

E(B3LYP(V)-D3/def2TZVP) = -424.694213273

C	0.4308158593	1.2440794891	0.0000000000
C	-0.4611465907	-1.4568441096	0.0000000000
C	1.3945046177	0.1333174589	0.0000000000
C	-1.0080569431	0.9302754976	0.0000000000
C	-1.3834579905	-0.3881976167	0.0000000000
C	0.9098863314	-1.1564480544	0.0000000000
H	-2.4338848979	-0.6342056593	0.0000000000
H	1.6104913531	-1.9739497447	0.0000000000
O	0.8240289343	2.4286391599	0.0000000000
C	-0.9879795502	-2.8928557501	0.0000000000
H	-0.1905108562	-3.6353892886	0.0000000000
H	-1.5999065480	-3.0507260807	0.8914051236
H	-1.5999065480	-3.0507260807	-0.8914051236
C	-2.0332965572	2.0676503195	0.0000000000
H	-1.9061594053	2.6816106033	-0.8930034687
H	-1.9061594053	2.6816106033	0.8930034687
H	-3.0579685857	1.6938669500	0.0000000000
C	2.8961436521	0.4316053298	0.0000000000
H	3.1614554855	0.9998915439	0.8929773445
H	3.1614554855	0.9998915439	-0.8929773445
H	3.4950225405	-0.4799722393	0.0000000000

Table D17: xyz data of Mes*O^H 2A (Cs) tBu:Me

12

E(B3LYP(V)-D3/def2TZVP) = -306.770251191

C	0.4308158593	1.2440794891	0.0000000000
C	-0.4611465907	-1.4568441096	0.0000000000
C	1.3945046177	0.1333174589	0.0000000000
C	-1.0080569431	0.9302754976	0.0000000000
C	-1.3834579905	-0.3881976167	0.0000000000
C	0.9098863314	-1.1564480544	0.0000000000
H	-2.4338848979	-0.6342056593	0.0000000000
H	1.6104913531	-1.9739497447	0.0000000000
O	0.8240289343	2.4286391599	0.0000000000
H	-0.8335078280	-2.4718054205	0.0000000000
H	-1.7315181965	1.7328650610	0.0000000000
H	2.4542896221	0.3438347706	0.0000000000

Table D18: xyz data of **23** ³A'' (Cs)

60

E(UPBE1PBE-D3/def2TZVP) = -2827.42785609

Re	0.1518433799	0.0661960579	0.0000000000
N	-0.2532309345	-2.0907674786	0.0000000000
H	0.7085356660	-2.4348286738	0.0000000000
P	0.0204876528	-0.2595350252	2.3954180254
P	0.0204876528	-0.2595350252	-2.3954180254
Cl	2.4397617653	-0.6259757032	0.0000000000
Cl	0.6905150586	2.3648247163	0.0000000000
Cl	-2.2291542895	0.3138010227	0.0000000000
C	-0.9248724832	-2.5726185276	1.2216829378
H	-0.9828237827	-3.6676813150	1.2039378150
H	-1.9435002468	-2.1793545500	1.1968305700
C	-0.1899552105	-2.0932903392	2.4584788139
H	0.8169720808	-2.5224182575	2.4809344625
H	-0.7079515426	-2.4284321927	3.3594013698
C	-0.9248724832	-2.5726185276	-1.2216829378
H	-1.9435002468	-2.1793545500	-1.1968305700
H	-0.9828237827	-3.6676813150	-1.2039378150
C	-0.1899552105	-2.0932903392	-2.4584788139
H	-0.7079515426	-2.4284321927	-3.3594013698
H	0.8169720808	-2.5224182575	-2.4809344625
C	-1.4482542269	0.4069807733	-3.2883055553
H	-2.2610375332	-0.0605231178	-2.7185909534
C	-1.5759072085	1.9130043245	-3.0878461140
H	-1.4413977511	2.1915310957	-2.0426970291
H	-2.5690863183	2.2405942764	-3.4066025132
H	-0.8407788999	2.4576066869	-3.6826372038
C	-1.5890014223	0.0210563375	-4.7528214392
H	-0.8865003936	0.5763265203	-5.3768427360
H	-2.5957089540	0.2695171600	-5.1009344122
H	-1.4325422026	-1.0444155374	-4.9344608128
C	1.5855088940	0.0278416648	-3.3272489450
H	2.3104545402	-0.3879225797	-2.6170226434
C	1.7290957429	-0.7089269108	-4.6517209361
H	2.7620381179	-0.6187705541	-5.0001609820
H	1.0869667761	-0.2879346602	-5.4255857573
H	1.5058182079	-1.7745781906	-4.5701938028
C	1.8842094489	1.5146133116	-3.4666836826
H	1.7432500128	2.0460123832	-2.5233800269
H	1.2482604834	1.9774398294	-4.2247157124
H	2.9218645108	1.6496443580	-3.7829981438
C	1.5855088940	0.0278416648	3.3272489450
H	2.3104545402	-0.3879225797	2.6170226434
C	1.7290957429	-0.7089269108	4.6517209361
H	2.7620381179	-0.6187705541	5.0001609820
H	1.5058182080	-1.7745781906	4.5701938028
H	1.0869667761	-0.2879346602	5.4255857573
C	1.8842094489	1.5146133116	3.4666836826
H	1.2482604834	1.9774398294	4.2247157124
H	1.7432500128	2.0460123832	2.5233800269
H	2.9218645109	1.6496443580	3.7829981437
C	-1.4482542269	0.4069807733	3.2883055553
H	-2.2610375332	-0.0605231178	2.7185909534
C	-1.5759072085	1.9130043245	3.0878461140
H	-1.4413977510	2.1915310957	2.0426970291
H	-0.8407788999	2.4576066869	3.6826372038
H	-2.5690863183	2.2405942764	3.4066025132
C	-1.5890014223	0.0210563375	4.7528214392
H	-1.4325422026	-1.0444155374	4.9344608128
H	-2.5957089540	0.2695171600	5.1009344122
H	-0.8865003936	0.5763265203	5.3768427360

Table D20: xyz data of **23me** ³A''(Cs) 'Pr:Me

36

E(UPBE1PBE-D3/def2TZVP) = -2513.1750413

Ree	-0.1061115559	-0.0700213799	0.0000000000
N	0.0000000000	1.9908532315	0.0000000000
H	-0.2435638982	2.4885207565	0.0000000000
P	0.0770653000	0.2296472689	2.3954180254
P	0.0770653162	0.2296472689	-2.3954180250
Cl	-2.2489011998	0.9892825555	0.0000000000
Cl	-1.0157716943	-2.2486400521	0.0000000000
Cl	2.2016598989	-0.7061416772	0.0000000000
C	1.3902465602	2.3555861430	1.2216829370
H	1.6276456457	3.4261759503	1.2039378150
H	2.3302541294	1.8000280029	1.1968305700
C	0.5864588408	2.0037563375	2.4584788139
H	-0.3361049259	2.0000000000	2.4809344625
H	1.1525521707	2.2490696146	3.3594013698
C	1.3000000000	2.3555861430	-1.2216829378
H	2.3302541294	1.8000280029	-1.1960000000
H	1.6276456457	3.4261759503	-1.2039378150
C	0.5864588408	2.0037560000	-2.4584788139
H	1.1525521707	2.2490696146	-3.3594013698
H	-0.3361000000	2.5927634992	-2.4809344625
C	1.4160733015	-0.6695210325	-3.2883000000
H	2.2947189221	-0.3421703575	-2.7185909534
H	1.3289711378	-1.7400000000	-3.1451481490
H	1.5611144884	-0.4132711410	-4.3380592718
C	-1.5000000000	0.2037792305	-3.3272489450
H	-2.1605390369	0.7331931644	-2.6100000000
H	-1.5284934840	0.7411124032	-4.2757121312
H	-1.8995829235	0.0000000000	-3.4269565103
C	-1.5139116452	0.2037792305	3.3272489450
H	-2.0000000000	0.7331931644	2.6170226434
H	-1.5284934840	0.7411124032	4.2700000000
H	-1.8995829235	-0.8097317603	3.4269565103
C	1.4160733015	0.0000000000	3.2883055553
H	2.2947189221	-0.3421703575	2.7185909534
H	1.0000000000	-1.7453789437	3.1451481490
H	1.5611144884	-0.4132711410	4.3380000000

Table D21: xyz data of **23H** ³A''(Cs) 'Pr:H

24

E(UPBE1PBE-D3/def2TZVP) = -2355.98895176

Re	-0.10611156	-0.07002138	0.00000000
N	0.64845636	1.99085323	0.00000000
H	-0.24356390	2.48852076	0.00000000
P	0.07706532	0.22964727	2.39541803
P	0.07706532	0.22964727	-2.39541803
Cl	-2.24890120	0.98928256	0.00000000
Cl	-1.01577169	-2.24864005	0.00000000
Cl	2.20165990	-0.70614168	0.00000000
C	1.39024656	2.35558614	1.22168294
H	1.62764565	3.42617595	1.20393782
H	2.33025413	1.80002800	1.19683057
C	0.58645884	2.00375634	2.45847881
H	-0.33610493	2.59276350	2.48093446
H	1.15255217	2.24906961	3.35940137
C	1.39024656	2.35558614	-1.22168294
H	2.33025413	1.80002800	-1.19683057
H	1.62764565	3.42617595	-1.20393782
C	0.58645884	2.00375634	-2.45847881
H	1.15255217	2.24906961	-3.35940137
H	-0.33610493	2.59276350	-2.48093446
H	1.10095661	-0.45791442	-3.07817703
H	-1.13560430	0.20993021	-3.10567535
H	-1.13560430	0.20993021	3.10567535
H	1.10095661	-0.45791442	3.07817703

Table D22: xyz data of 2²A(C1)
66
E(UPBE1PBE-D3(BJ)/def2TZVP) = -1703.03656783 <S2> = 0.7561

Ir	0.0048245	-0.01354098	-0.08555563
P	-2.28958551	0.00101498	0.19570832
P	2.30190885	-0.01265728	0.20200033
N	-0.00077528	-0.04869755	1.90868597
O	0.1383322	-0.04012764	-2.04115916
H	-0.71786906	-0.03420379	-2.47173432
C	-1.18192243	-0.05448759	2.60266814
H	-1.10789281	-0.07600755	3.68984564
C	1.1817513	-0.08181722	2.60467578
H	1.10313426	-0.11197948	3.69140481
C	-2.37816961	-0.03373065	1.9832946
H	-3.29605906	-0.02749024	2.55566329
C	2.38015028	-0.07645888	1.99033533
H	3.2942501	-0.09389551	2.56891265
C	3.20187613	-1.54227214	-0.38913126
C	3.15526334	1.57651306	-0.3029798
C	-3.2310043	-1.52839625	-0.34899129
C	-3.14151498	1.58564246	-0.33548809
C	2.26314167	-2.703042	-0.05296301
H	2.748788	-3.64494312	-0.32902176
H	1.32240456	-2.61840565	-0.59919631
H	2.03360242	-2.73638387	1.01478285
C	4.5328471	-1.77980685	0.31545218
H	4.40115604	-1.86352802	1.39613958
H	5.26315152	-0.99650835	0.11724235
H	4.95821864	-2.72483625	-0.03843447
C	3.38852945	-1.4838125	-1.90195031
H	3.68821981	-2.47283159	-2.26379808
H	4.17316619	-0.78098064	-2.18716025
H	2.4607094	-1.20010509	-2.4053355
C	2.46208716	2.67028072	0.51202016
H	2.64260967	2.55576558	1.5820399
H	1.38189852	2.65518021	0.34625908
H	2.84780992	3.64475961	0.19646889
C	2.89314383	1.84766855	-1.78383225
H	3.45648378	1.17847009	-2.4332839
H	3.20276092	2.87211757	-2.01559734
H	1.83513956	1.73418307	-2.02711898
C	4.64967913	1.60586699	-0.01225923
H	4.87250064	1.34821182	1.02599563
H	5.03031185	2.61720116	-0.19047022
H	5.20507573	0.93113496	-0.66515283
C	-4.54507268	-1.73431252	0.39780705
H	-4.9911963	-2.68132722	0.07641443
H	-5.27189583	-0.9465812	0.20512349
H	-4.38181594	-1.79819696	1.47492839
C	-2.300821	-2.69683384	-0.016499
H	-2.05107379	-2.71497387	1.04680144
H	-1.36752567	-2.63385085	-0.57856035
H	-2.80282745	-3.63728467	-0.26703091
C	-3.47771456	-1.51021356	-1.85288135
H	-2.55311202	-1.34034532	-2.41017822
H	-4.20731175	-0.75328264	-2.1445847
H	-3.87107837	-2.48302031	-2.16481985
C	-2.50255151	2.68766549	0.51101759
H	-2.76205019	2.58879199	1.56584332
H	-2.85648719	3.66043003	0.15498919
H	-1.41301848	2.66384636	0.42591109
C	-4.6487102	1.5986994	-0.12078616
H	-5.16691135	0.91705366	-0.79702967
H	-5.03104839	2.60585765	-0.31768584
H	-4.91734035	1.34005834	0.90594921
C	-2.81004266	1.86764623	-1.79980911
H	-1.72926769	1.91631752	-1.94920308
H	-3.23452528	2.83596579	-2.08410865
H	-3.22176964	1.11909104	-2.4779125

Table D23: xyz data of 4³A'' (Cs)
65
E(UPBE1PBE-D3(BJ)/def2TZVP) = -1702.40237812 <S2> = 2.0163

Ir	0.02633205	-0.13117178	0.00000000
P	0.00711979	0.21834134	2.30776158
P	0.00711978	0.21834134	-2.30776158
N	0.06152214	1.93385832	0.00000000
O	0.04840650	-1.92176986	0.00000000
C	0.07869579	2.61848419	1.17753100
H	0.10714185	3.70688614	1.11154177
C	0.07869579	2.61848419	-1.17753100
H	0.10714185	3.70688614	-1.11154177
C	0.06088827	1.99839362	2.37724022
H	0.06645750	2.57056079	3.29510959
C	0.06088827	1.99839362	-2.37724022
H	0.06645750	2.57056079	-3.29510959
C	1.53382645	-0.37630266	-3.20971778
C	-1.58964223	-0.31661762	-3.12621707
C	1.53382646	-0.37630266	3.20971778
C	-1.58964223	-0.31661762	3.12621707
C	2.70111592	-0.03099016	-2.28275917
H	3.63950392	-0.29788287	-2.77971093
H	2.63288571	-0.57846451	-1.34149980
H	2.72689414	1.03680522	-2.05325920
C	1.75140731	0.33226195	-4.54286929
H	1.82939099	1.41297188	-4.40947496
H	0.96182569	0.12948958	-5.26511887
H	2.69416610	-0.01494437	-4.97794622
C	1.48425612	-1.88790418	-3.40111353
H	2.47070968	-2.23989327	-3.71923596
H	0.76966282	-2.17806838	-4.17307850
H	1.22527863	-2.40009520	-2.47113324
C	-2.68125844	0.50579025	-2.43925859
H	-2.57603566	1.57205919	-2.64461094
H	-2.65403032	0.36336402	-1.35604568
H	-3.65700724	0.17417979	-2.80744396
C	-1.85229122	-1.79361766	-2.83931720
H	-1.16001080	-2.45034421	-3.36480584
H	-2.86430781	-2.04286699	-3.17433747
H	-1.77527790	-2.00904384	-1.77219247
C	-1.62758370	-0.05053581	-4.62564705
H	-1.37583513	0.98512601	-4.86613419
H	-2.64039143	-0.23875863	-4.99657525
H	-0.95349928	-0.70961327	-5.17452696
C	1.75140731	0.33226195	4.54286928
H	2.69416610	-0.01494437	4.97794622
H	0.96182570	0.12948958	5.26511887
H	1.82939099	1.41297188	4.40947496
C	2.70111592	-0.03099016	2.28275917
H	2.72689414	1.03680522	2.05325919
H	2.63288571	-0.57846451	1.34149980
H	3.63950392	-0.29788287	2.77971092
C	1.48425612	-1.88790418	3.40111352
H	1.22527863	-2.40009520	2.47113324
H	0.76966283	-2.17806838	4.17307850
H	2.47070968	-2.23989327	3.71923596
C	-2.68125844	0.50579025	2.43925859
H	-2.57603566	1.57205919	2.64461095
H	-3.65700724	0.17417979	2.80744397
H	-2.65403032	0.36336402	1.35604568
C	-1.62758370	-0.05053581	4.62564705
H	-0.95349927	-0.70961327	5.17452697
H	-2.64039142	-0.23875863	4.99657525
H	-1.37583513	0.98512601	4.86613419
C	-1.85229122	-1.79361766	2.83931720
H	-1.77527790	-2.00904384	1.77219248
H	-2.86430781	-2.04286699	3.17433747
H	-1.16001080	-2.45034421	3.36480584

Table D24: xyz data of $2^{Rh} \text{ } ^2A(C1)$
66
E(UPBE1PBE-D3(BJ)/def2TZVP) = -1709.22482819 <S2> = 0.7565

Rh	0.01066531	-0.00734290	-0.08429858
P	-2.29792350	0.00264047	0.19142356
P	2.31295934	-0.00827354	0.20588853
N	0.00274389	-0.04154497	1.91346215
O	0.14781297	-0.05855629	-2.02644840
H	-0.71033575	-0.05556378	-2.45368214
C	-1.17829159	-0.05218371	2.59816098
H	-1.11267499	-0.07415581	3.68723849
C	1.18274642	-0.07467451	2.60555075
H	1.10802327	-0.10509022	3.69384974
C	-2.37617918	-0.03630517	1.97784526
H	-3.29309611	-0.03449620	2.55251100
C	2.38397129	-0.07004200	1.99346935
H	3.29630148	-0.08905556	2.57546442
C	3.20110137	-1.54317406	-0.38458149
C	3.16434072	1.57842224	-0.30385442
C	-3.23131895	-1.52863888	-0.35677434
C	-3.14933796	1.58761022	-0.33418096
C	2.24299466	-2.69087891	-0.05779703
H	2.71754221	-3.64039056	-0.32677095
H	1.31159608	-2.59419820	-0.61845649
H	1.99992610	-2.71964268	1.00714802
C	4.52431168	-1.79599013	0.32879029
H	4.38376188	-1.88291944	1.40810466
H	5.26141018	-1.01641173	0.13946895
H	4.94565851	-2.74238290	-0.02643772
C	3.39793452	-1.48450548	-1.89600319
H	3.68808957	-2.47663920	-2.25719492
H	4.19307116	-0.79098194	-2.17478764
H	2.47627444	-1.18895386	-2.40380774
C	2.45405816	2.67370013	0.49410915
H	2.61235795	2.56219200	1.56794385
H	1.37725053	2.65901092	0.30648235
H	2.84392330	3.64810010	0.18365669
C	2.91630378	1.83499157	-1.79000317
H	3.50529863	1.17576524	-2.42668123
H	3.20459431	2.86505052	-0.20438400
H	1.86466140	1.69337357	-2.04759999
C	4.65480428	1.61682073	0.00530796
H	4.86377874	1.37586219	1.05044239
H	5.03682525	2.62560786	-0.18443178
H	5.21913165	0.93177876	-0.62900648
C	-4.53073384	-1.75471646	0.40923646
H	-4.97806403	-2.69886624	0.08106562
H	-5.26398584	-0.96690190	0.24085888
H	-4.34821371	-1.83317123	1.48224241
C	-2.27910723	-2.68648756	-0.05011588
H	-2.00549340	-2.70600836	1.00736870
H	-1.36050196	-2.60942956	-0.63480288
H	-2.77258095	-3.63315484	-0.29376894
C	-3.50322716	-1.50034745	-1.85606959
H	-2.59152057	-1.31127616	-2.42794665
H	-4.24881522	-0.75166292	-2.12789190
H	-3.88809844	-2.47597413	-2.16976589
C	-2.49379893	2.68719823	0.50263331
H	-2.73519372	2.58758396	1.56159665
H	-2.85016118	3.66145022	0.15343086
H	-1.40554823	2.66315614	0.40011320
C	-4.65349366	1.60544206	-0.09890098
H	-5.18135790	0.91883515	-0.76260238
H	-5.03817123	2.61137343	-0.29776361
H	-4.90743022	1.35395565	0.93336630
C	-2.83483251	1.86533270	-1.80312325
H	-1.75572238	1.89619133	-1.96978839
H	-3.24816442	2.84033095	-2.08095856
H	-3.26788516	1.12347782	-2.47487209

Table D25: xyz data of $4^{Rh} \text{ } ^1A'(Cs)$
65
E(RPBE1PBE-D3(BJ)/def2TZVP) = -1708.54535146

Rh	-0.01703227	-0.08947148	0.00000000
P	-0.00764073	0.17240218	2.32490995
P	-0.00764073	0.17240218	-2.32490995
N	-0.21012262	1.87961986	0.00000000
O	1.05652181	-1.50891653	0.00000000
C	-0.19252410	2.57070464	1.18716642
H	-0.25417345	3.65726099	1.11332862
C	-0.19252410	2.57070464	-1.18716642
H	-0.25417345	3.65726099	-1.11332862
C	-0.10967381	1.96172322	2.38499758
H	-0.10917465	2.54859652	3.29454071
C	-0.10967381	1.96172322	-2.38499758
H	-0.10917465	2.54859652	-3.29454071
C	1.57170542	-0.26931554	-3.21411563
C	-1.55153083	-0.46885813	-3.16683529
C	1.57170542	-0.26931554	3.21411563
C	-1.55153083	-0.46885813	3.16683529
C	2.68678747	0.19398984	-2.27221037
H	3.65230391	0.01857166	-2.75789608
H	2.65518504	-0.36514775	-1.33644133
C	2.60819702	1.26135336	-2.05183159
H	1.73629535	0.43601767	-4.55538743
H	1.70609531	1.52184792	-4.44303077
H	0.98233479	0.14358271	-5.28527000
H	2.71590697	0.17683191	-4.97052001
C	1.66626628	-1.78300951	-3.37407109
H	2.67899735	-2.04244054	-3.69933391
H	0.97485760	-2.15919035	-4.13047242
H	1.47526447	-2.28218415	-2.42090168
C	-2.70973663	0.27029426	-2.49459025
H	-2.69037350	1.33948189	-2.70925418
H	-2.68560768	0.13987223	-1.40872741
C	-3.65538673	-0.14095316	-2.86107764
H	-1.70075161	-1.95908118	-2.86432203
H	-0.93430704	-2.56243806	-3.34891869
H	-2.67545767	-2.30162625	-3.22691931
H	-1.64460634	-2.14721047	-1.79010839
C	-1.60261155	-0.22344015	-4.66883297
H	-1.42830152	0.82567813	-4.91871344
H	-2.59497829	-0.49324943	-5.04557425
H	-0.87443449	-0.83334133	-5.20505122
C	1.73629535	0.43601767	4.55538743
H	2.71590697	0.17683191	4.97052001
H	0.98233479	0.14358271	5.28527000
H	1.70609531	1.52184792	4.44303077
C	2.68678747	0.19398984	2.27221037
H	2.60819702	1.26135336	2.05183159
H	2.65518504	-0.36514775	1.33644133
H	3.65230391	0.01857166	2.75789608
C	1.66626628	-1.78300951	3.37407109
H	1.47526447	-2.28218415	2.42090168
H	0.97485760	-2.15919035	4.13047242
H	2.67899735	-2.04244054	3.69933391
C	-2.70973663	0.27029426	2.49459025
H	-2.69037350	1.33948189	2.70925418
H	-2.68560768	-0.14095316	2.86107764
H	-1.70075161	-1.95908118	2.86432203
H	-0.93430704	-2.56243806	3.34891869

Table D26: xyz data of 4^{Rh} 3A'(Cs)

65

E(UPBE1PBE-D3(BJ)/def2TZVP) = -1708.58244994 <S2> = 2.0173

Rh	0.02314609	-0.12941801	0.00000000
P	0.00437260	0.21457979	2.31442203
P	0.00437260	0.21457979	-2.31442203
N	0.06065934	1.93299156	0.00000000
O	0.04395996	-1.90111941	0.00000000
C	0.07777974	2.61381779	1.17687560
H	0.10717228	3.70359891	1.11504975
C	0.07777974	2.61381779	-1.17687560
H	0.10717228	3.70359891	-1.11504975
C	0.05912497	1.99524269	2.37870189
H	0.06572700	2.57113249	3.29474268
C	0.05912497	1.99524269	-2.37870189
H	0.06572700	2.57113249	-3.29474268
C	1.53424085	-0.37661951	-3.21126819
C	-1.59070167	-0.31697914	-3.13552024
C	1.53424085	-0.37661951	3.21126819
C	-1.59070167	-0.31697914	3.13552024
C	2.69080898	-0.04594221	-2.26553939
H	3.63603316	-0.30590837	-2.75306033
H	2.61122273	-0.60962678	-1.33434077
H	2.71417926	1.01828587	-2.01951572
C	1.76734164	0.34529213	-4.53434997
H	1.85051707	1.42386707	-4.38788570
H	0.98032351	0.15578621	-5.26339852
H	2.71052751	-0.00303788	-4.96781100
C	1.48272887	-1.88569858	-3.41972135
H	2.47090535	-2.23699993	-3.73338773
H	0.77386360	-2.16549674	-4.20074371
H	1.21457903	-2.40709937	-2.49754354
C	-2.68155670	0.49464491	-2.43481364
H	-2.57713423	1.56384786	-2.62441587
H	-2.65361365	0.33717657	-1.35344699
H	-3.65841337	0.16785391	-2.80429729
C	-1.84749774	-1.79751742	-2.86147639
H	-1.15905458	-2.44697339	-3.40080295
H	-2.86224618	-2.04660255	-3.18834225
H	-1.75860808	-2.02361839	-1.79719612
C	-1.63407740	-0.03500669	-4.63183424
H	-1.39187321	1.00568284	-4.86001668
H	-2.64509453	-0.22876961	-5.00507686
H	-0.95327594	-0.68093065	-5.18819293
C	1.76734164	0.34529213	4.53434997
H	2.71052751	-0.00303788	4.96781100
H	0.98032351	0.15578621	5.26339852
H	1.85051707	1.42386707	4.38788570
C	2.69080898	-0.04594221	2.26553939
H	2.71417926	1.01828587	2.01951572
H	2.61122273	-0.60962678	1.33434077
H	3.63603316	-0.30590837	2.75306033
C	1.48272887	-1.88569858	3.41972135
H	1.21457903	-2.40709937	2.49754354
H	0.77386360	-2.16549674	4.20074371
H	2.47090535	-2.23699993	3.73338773
C	-2.68155670	0.49464491	2.43481364
H	-2.57713423	1.56384786	2.62441587
H	-3.65841337	0.16785391	2.80429729
H	-2.65361365	0.33717657	1.35344699
C	-1.63407740	-0.03500669	4.63183424
H	-0.95327594	-0.68093065	5.18819293
H	-2.64509453	-0.22876961	5.00507686
H	-1.39187321	1.00568284	4.86001668
C	-1.84749774	-1.79751742	2.86147639
H	-1.75860808	-2.02361839	1.79719612
H	-2.86224618	-2.04660255	3.18834225
H	-1.15905458	-2.44697339	3.40080295

Table D27: xyz data of 23^{1A'} (Cs)

60

E(RPBE1PBE-D3/def2TZVP) = -2827.41310991

Re	0.0712099339	0.0993327626	0.0000000000
N	-0.4835944919	-2.0345140444	0.0000000000
H	0.4546104888	-2.4324177636	0.0000000000
P	-0.0081740653	-0.2040317720	2.3556383962
P	-0.0081740650	-0.2040317720	-2.3556383962
Cl	2.2472752190	-0.8835734151	0.0000000001
Cl	0.7157954063	2.3274540658	0.0000000000
Cl	-2.2736883148	0.3526098012	-0.0000000001
C	-1.1538318070	-2.4730308099	1.2372963843
H	-1.2686422175	-3.5636545064	1.2272087523
H	-2.1504860613	-2.0280046091	1.2391510049
C	-0.3517171037	-2.0249634660	2.4458991827
H	0.6210762168	-2.5274699021	2.4478958381
H	-0.8650809148	-2.3106702014	3.3662790600
C	-1.1538318069	-2.4730308099	-1.2372963845
H	-2.1504860612	-2.0280046091	-1.2391510051
H	-1.2686422174	-3.5636545064	-1.2272087524
C	-0.3517171034	-2.0249634660	-2.4458991827
H	-0.8650809144	-2.3106702014	-3.3662790601
H	0.6210762171	-2.5274699021	-2.4478958380
C	-1.4298311667	0.5394540725	-3.2751480389
H	-2.2764915156	0.0948826268	-2.7371846125
C	-1.5101049312	2.0457140323	-3.0552043706
H	-1.4261742824	2.3020615089	-1.9995762144
H	-2.4688534184	2.4202841494	-3.4247798361
H	-0.7197850388	2.5719579563	-3.5932025939
C	-1.5512588003	0.1884680125	-4.7499554095
H	-0.8059985905	0.7201987101	-5.3445347296
H	-2.5350916257	0.4914220083	-5.1204229591
H	-1.4403531298	-0.8796693612	-4.9478239943
C	1.5562623364	-0.0331336541	-3.3217599514
H	2.2692276374	-0.4590531637	-2.6050067895
C	1.6719934493	-0.8137357654	-4.6235401875
H	2.7079443785	-0.7792645060	-4.9741706011
H	1.0483476546	-0.3921853598	-5.4120999845
H	1.4039538465	-1.8658203207	-4.5088209481
C	1.9190287146	1.4350368530	-3.5068796048
H	1.8053252365	1.9992625987	-2.5790058803
H	1.2966494284	1.9036044627	-4.2730235420
H	2.9589525450	1.5215994387	-3.8334961317
C	1.5562623361	-0.0331336541	3.3217599516
H	2.2692276371	-0.4590531637	2.6050067897
C	1.6719934488	-0.8137357654	4.6235401877
H	2.7079443780	-0.7792645060	4.9741706014
H	1.4039538461	-1.8658203207	4.5088209482
H	1.0483476540	-0.3921853598	5.4120999846
C	1.9190287142	1.4350368530	3.5068796050
H	1.2966494280	1.9036044627	4.2730235421
H	1.8053252362	1.9992625987	2.5790058805
H	2.9589525446	1.5215994387	3.8334961320
C	-1.4298311671	0.5394540725	3.2751480387
H	-2.2764915159	0.0948826268	2.7371846123
C	-1.5101049315	2.0457140323	3.0552043705
H	-1.4261742826	2.3020615089	1.9995762143
H	-0.7197850392	2.5719579563	3.5932025938
H	-2.4688534187	2.4202841494	3.4247798359
C	-1.5512588008	0.1884680125	4.7499554094
H	-1.4403531303	-0.8796693612	4.9478239941
H	-2.5350916262	0.4914220083	5.1204229589
H	-0.8059985911	0.7201987101	5.3445347295

Table D28: xyz data of **23me** ¹A' (Cs) /Pr:Me

36

E(RPBE1PBE-D3/def2TZVP) = -2513.16332935

Re	-0.0712099339	-0.0993327626	0.0000000000
N	0.4835000000	2.0345140444	0.0000000000
H	-0.4546104889	2.4324177636	0.0000000000
P	0.0081740651	0.2040317720	2.3556383962
P	0.0081740651	0.2040317720	-2.3556383962
Cl	0.0000000000	0.8835734150	0.0000000000
Cl	-0.7157954062	-2.3274540659	0.0000000000
Cl	2.2730000000	-0.3526098011	0.0000000000
C	1.1538318068	2.4730308099	1.2372963844
H	1.0000000000	3.5636545064	1.2272087524
H	2.1504860612	2.0280046093	1.2390000000
C	0.3517171035	2.0249634660	2.4458991827
H	-0.6210762171	2.5274600000	2.4478958381
H	0.8650809145	2.3106702014	3.3662790601
C	1.1538310000	2.4730308099	-1.2372963844
H	2.1504860612	2.0280046093	-1.2391510000
H	1.2686422173	3.5636545064	-1.2272087524
C	0.3517171035	2.0249634660	-2.4458991827
H	0.8650809145	2.3106702014	-3.3662790601
H	-0.6210762000	2.5274699021	-2.4478958381
C	1.4298311669	-0.5394540724	-3.2751480000
H	2.2764915158	-0.0948826266	-2.7371846124
H	1.4871795380	-1.6155410000	-3.1180181075
H	1.5168955349	-0.2877948861	-4.3325940890
C	-1.5562000000	0.0331336541	-3.3217599515
H	-2.2692276373	0.4590531636	-2.6050000000
H	-1.6391550982	0.5922422929	-4.2541640090
H	-1.8156575466	-1.0100000000	-3.4541293063
C	-1.5562623363	0.0331336541	3.3217599515
H	-2.0000000000	0.4590531636	2.6050067896
H	-1.6391550982	0.5922422929	4.2500000000
H	-1.8156575466	-1.0166780719	3.4541293063
C	1.4298311669	-0.5000000000	3.2751480388
H	2.2764915158	-0.0948826266	2.7371846124
H	1.4000000000	-1.6155410809	3.1180181075
H	1.5168955349	-0.2877948861	4.3320000000

Table D29: xyz data of **23h** ¹A' (Cs) /Pr:H

24

E(RPBE1PBE-D3/def2TZVP) = -2355.98342861

Re	-0.0712099339	-0.0993327626	0.0000000000
N	0.4835944918	2.0345140444	0.0000000000
H	-0.4546104889	2.4324177636	0.0000000000
P	0.0081740651	0.2040317720	2.3556383962
P	0.0081740651	0.2040317720	-2.3556383962
Cl	-2.2472752191	0.8835734150	0.0000000000
Cl	-0.7157954062	-2.3274540659	0.0000000000
Cl	2.2736883148	-0.3526098011	0.0000000000
C	1.1538318068	2.4730308099	1.2372963844
H	1.2686422173	3.5636545064	1.2272087524
H	2.1504860612	2.0280046093	1.2391510050
C	0.3517171035	2.0249634660	2.4458991827
H	-0.6210762171	2.5274699021	2.4478958381
H	0.8650809145	2.3106702014	3.3662790601
C	1.1538318068	2.4730308099	-1.2372963844
H	2.1504860612	2.0280046093	-1.2391510050
H	1.2686422173	3.5636545064	-1.2272087524
C	0.3517171035	2.0249634660	-2.4458991827
H	0.8650809145	2.3106702014	-3.3662790601
H	-0.6210762171	2.5274699021	-2.4478958381
H	1.0935208897	-0.3635734539	-3.0576268500
H	-1.1867332670	0.0735007936	-3.0935563641
H	-1.1867332670	0.0735007936	3.0935563641
H	1.0935208897	-0.3635734539	3.0576268500

Table D30: xyz data of **24** ²A'' (Cs)

59

E(UPBE1PBE-D3/def2TZVP) = -2826.81473043

Re	0.0693461503	-0.0293170956	0.0000000000
N	-0.9160798892	-1.6770430334	0.0000000000
P	-0.0710102583	-0.2674440395	2.4128075904
P	-0.0710102584	-0.2674440395	-2.4128075904
Cl	2.2164075338	-0.9132762085	0.0000000000
Cl	1.0388343672	2.2007696546	0.0000000000
Cl	-2.0480505281	1.0418173021	0.0000000000
C	-1.5439642112	-2.2197861965	1.1991777525
H	-1.7260928306	-3.2925256097	1.0644324505
H	-2.5317840998	-1.7442934728	1.3103698529
C	-0.7017541916	-1.9897007298	2.4398115614
H	0.1801029203	-2.6358410937	2.4035102925
H	-1.2628921822	-2.2348950823	3.3433484474
C	-1.5439642113	-2.2197861965	-1.1991777524
H	-2.5317840998	-1.7442934728	-1.3103698528
H	-1.7260928307	-3.2925256097	-1.0644324505
C	-0.7017541917	-1.9897007298	-2.4398115614
H	-1.2628921823	-2.2348950823	-3.3433484474
H	0.1801029202	-2.6358410937	-2.4035102925
C	-1.3412185901	0.7443975252	-3.2806278059
H	-2.2181438057	0.5421052407	-2.6532903474
C	-1.0400967016	2.2345107666	-3.1635607742
H	-0.7461220966	2.5118339062	-2.1508119586
H	-1.9309668413	2.8078654293	-3.4329281140
H	-0.2397160945	2.5296654302	-3.8443041681
C	-1.6642129340	0.3467482308	-4.7131513772
H	-0.8767814895	0.6600208925	-5.4001326686
H	-2.5847270318	0.8465292864	-5.0278977057
H	-1.8153318590	-0.7272428820	-4.8381067459
C	1.5197945631	-0.3518173764	-3.3352178649
H	2.0964668163	-0.9962458705	-2.6608967759
C	1.4604793953	-1.0194740551	-4.7015230365
H	2.4782080555	-1.2167444884	-5.0503241070
H	0.9808200096	-0.3813923998	-5.4441372179
H	0.9300931023	-1.9738274297	-4.6810065302
C	2.2201599054	0.9996357684	-3.3800948037
H	2.2104615327	1.4927867634	-2.4059664185
H	1.7507290972	1.6655789683	-4.1069149080
H	3.2603795665	0.8610997469	-3.6863452472
C	1.5197945632	-0.3518173764	3.3352178649
H	2.0964668164	-0.9962458705	2.6608967758
C	1.4604793955	-1.0194740551	4.7015230365
H	2.4782080556	-1.2167444884	5.0503241069
H	0.9300931024	-1.9738274297	4.6810065302
H	0.9808200097	-0.3813923998	5.4441372178
C	2.2201599055	0.9996357684	3.3800948036
H	1.7507290973	1.6655789683	4.1069149079
H	2.2104615328	1.4927867634	2.4059664184
H	3.2603795666	0.8610997469	3.6863452471
C	-1.3412185900	0.7443975252	3.2806278059
H	-2.2181438057	0.5421052407	2.6532903474
C	-1.0400967015	2.2345107666	3.1635607742
H	-0.7461220965	2.5118339062	2.1508119586
H	-0.2397160944	2.5296654302	3.8443041682
H	-1.9309668412	2.8078654293	3.4329281140
C	-1.6642129339	0.3467482308	4.7131513772
H	-1.8153318589	-0.7272428820	4.8381067459
H	-2.5847270316	0.8465292864	5.0278977058
H	-0.8767814893	0.6600208925	5.4001326687

Table D31: xyz data of **24me** ²A'' (Cs) ⁱPr:Me

35

E(UPBE1PBE-D3/def2TZVP) = -2512.56087673

Re	0.0693461503	-0.0293170956	0.0000000000
N	-0.9000000000	-1.6770430334	0.0000000000
P	-0.0710102583	-0.2674440395	2.4128075904
P	-0.0710102583	-0.2674440395	-2.4128075904
Cl	2.2164075338	-0.9132762000	0.0000000000
Cl	1.0388343672	2.2007696546	0.0000000000
Cl	-2.0480505282	1.0418173021	0.0000000000
C	-1.5439642112	-2.2197861965	1.1991777524
H	-1.7260928306	-3.2925250000	1.0644324505
H	-2.5317840998	-1.7442934728	1.3103698528
C	-0.7017000000	-1.9897007298	2.4398115614
H	0.1801029203	-2.6358410936	2.4035102925
H	-1.2628921822	-2.2348950824	3.3433484474
C	-1.5439642112	-2.2100000000	-1.1991777524
H	-2.5317840998	-1.7442934728	-1.3103698528
H	0.0000000000	-3.2925256097	-1.0644324505
C	-0.7017541916	-1.9897007298	-2.4398115614
H	-1.2628921822	-2.2348950824	-3.3433484474
H	0.1801029000	-2.6358410936	-2.4035102925
C	-1.3412185901	0.7443975252	-3.2806270000
H	-2.2181438057	0.5421052407	-2.6532903474
H	-1.1261767633	1.8085000000	-3.1970260841
H	-1.5726407636	0.4594858364	-4.3070164245
C	1.5100000000	-0.3518173764	-3.3352178649
H	2.0964668163	-0.9962458705	-2.6000000000
H	1.4773117532	-0.8300075737	-4.3137952693
C	2.0205297026	0.0000000000	-3.3673032050
H	1.5197945631	-0.3518173764	3.3352178649
H	2.0000000000	-0.9962458705	2.6608967758
H	1.4773117532	-0.8300075737	4.3000000000
H	2.0205297026	0.6144212967	3.3673032050
C	-1.3412185901	0.7400000000	3.2806278059
H	-2.2181438057	0.5421052407	2.6532903474
H	-1.1000000000	1.8085402722	3.1970260841
H	-1.5726407636	0.4594858364	4.3070000000

Table D32: xyz data of **24h** ²A'' (Cs) ⁱPr:H

23

E(UPBE1PBE-D3/def2TZVP) = -2355.37397073

Re	0.06934615	-0.029317096	0.0000000001
N	-0.916079889	-1.677043033	-0.0000000007
P	-0.071010258	-0.26744404	2.4128075904
P	-0.071010257	-0.267444038	-2.4128075903
Cl	2.216407534	-0.913276208	0.0000000003
Cl	1.038834367	2.200769655	0.0000000001
Cl	-2.048050528	1.041817302	0.0000000001
C	-1.543964211	-2.219786197	1.1991777524
H	-1.726092831	-3.29252561	1.0644324505
H	-2.5317841	-1.744293473	1.3103698528
C	-0.701754192	-1.98970073	2.4398115614
H	0.18010292	-2.635841094	2.4035102925
H	-1.262892182	-2.234895082	3.3433484474
C	-1.543964211	-2.219786196	-1.1991777546
H	-2.531784099	-1.744293472	-1.3103698551
H	-1.72609283	-3.292525609	-1.0644324536
C	-0.701754191	-1.989700728	-2.4398115630
H	-1.262892181	-2.23489508	-3.3433484495
H	0.180102921	-2.635841092	-2.4035102942
H	-1.0415911	0.505715772	-3.0759190296
H	1.143053293	-0.331835717	-3.1167686783
H	1.143053292	-0.331835719	3.1167686789
H	-1.041591102	0.50571577	3.0759190298

Table D33: xyz data of **24** ⁴A' (Cs)

59

2 E(UPBE1PBE-D3/def2TZVP) = -2826.80890737

Re	-0.053732088	-0.0712042708	0.000000
N	0.814242484	1.7804058554	0.000000
P	0.048660198	0.3187911341	2.449927392
P	0.048660198	0.3187911341	-2.449927392
Cl	-2.235360674	0.8328209074	0.000000
Cl	-0.961389261	-2.2549093001	0.000000
Cl	2.130707878	-0.9734141439	0.000000
C	1.488489849	2.2393779783	1.189813455
H	1.733086415	3.3060103638	1.085863501
H	2.451378687	1.7168451069	1.340331503
C	0.606556101	2.0539349347	2.41338002
H	-0.29390501	2.6650461208	2.305295213
H	1.118168811	2.3460261308	3.332463499
C	1.488489849	2.2393779783	-1.189813455
H	2.451378687	1.7168451069	-1.340331503
H	1.733086415	3.3060103638	-1.085863501
C	0.606556101	2.0539349347	-2.41338002
H	1.118168811	2.3460261308	-3.332463499
H	-0.29390501	2.6650461208	-2.305295213
C	1.362443061	-0.6307107397	-3.320344343
H	2.233304655	-0.3728456877	-2.704843431
C	1.155069953	-2.1361815815	-3.204676914
H	0.94197959	-2.4406659916	-2.180089127
H	2.06282785	-2.6506673058	-3.530205112
H	0.336887842	-2.4751514185	-3.842139791
C	1.632427492	-0.2106859711	-4.757957224
H	0.848539827	-0.5652392070	-5.429037635
H	2.572160987	-0.6582524752	-5.092924837
H	1.721463566	0.8703759897	-4.879277524
C	-1.559859727	0.3299917651	-3.337270122
H	-2.160581822	0.9135765633	-2.629361175
C	-1.552559783	1.0533720093	-4.676902059
H	-2.583806199	1.1983403824	-5.010552042
H	-1.038618198	0.4782189877	-5.447648584
H	-1.085203449	2.0383068306	-4.618597231
C	-2.18283122	-1.0556983530	-3.429755076
H	-2.159580715	-1.5745629736	-2.469947024
H	-1.673432071	-1.6740356286	-4.171614252
H	-3.226525982	-0.9630818314	-3.740736355
C	-1.559859727	0.3299917651	3.337270122
H	-2.160581822	0.9135765633	2.629361175
C	-1.552559783	1.0533720093	4.676902059
H	-2.583806199	1.1983403824	5.010552042
H	-1.085203449	2.0383068306	4.618597231
H	-1.038618198	0.4782189877	5.447648584
C	-2.18283122	-1.0556983530	3.429755076
H	-1.673432071	-1.6740356286	4.171614252
H	-2.159580715	-1.5745629736	2.469947024
H	-3.226525982	-0.9630818314	3.740736355
C	1.362443061	-0.6307107397	3.320344343
H	2.233304655	-0.3728456877	2.704843431
C	1.155069953	-2.1361815815	3.204676914
H	0.94197959	-2.4406659916	2.180089127
H	2.06282785	-2.4751514185	3.842139791
H	0.336887842	-2.6506673058	3.530205112
C	1.632427492	-0.2106859711	4.757957224
H	1.721463566	0.8703759897	4.879277524
H	2.572160987	-0.6582524752	5.092924837
H	0.848539827	-0.5652392070	5.429037635

Table D34: xyz data of **24me** ⁴A' (Cs) ¹Pr:Me

35

E(UPBE1PBE-D3(BJ)/def2TZVP) = -2512.55509575

Re	-0.053732088	-0.071204271	0.000000000
N	0.800000000	1.780405855	0.000000000
P	0.048660198	0.318791134	2.4499273922
P	0.000000000	0.318791134	-2.4499273922
Cl	-2.235360674	0.832820907	0.000000000
Cl	-0.961389261	-2.2549093	0.000000000
Cl	2.130707878	-0.973414144	0.000000000
C	1.488489849	2.239377978	1.1898134551
H	1.733086415	3.306010364	1.000000000
H	2.451378687	1.716845107	1.3403315033
C	0.606556101	2.000000000	2.4133800202
H	-0.29390501	2.665046121	2.3052952126
H	1.100000000	2.346026131	3.3324634993
C	1.488489849	2.239377978	-1.1890000000
H	2.451378687	1.716845107	-1.3403315033
H	1.733086415	3.306000000	-1.0858635009
C	0.606556101	2.053934935	-2.4133800202
H	1.110000000	2.346026131	-3.3324634993
H	-0.29390501	2.665046121	-2.3000000000
C	1.362443061	-0.63071074	-3.3203443431
H	2.233304655	0.000000000	-2.7048434313
H	1.214332674	-1.705950778	-3.2377321477
H	1.555822219	-0.329863629	-4.3500495272
C	-1.559859727	0.329991765	-3.3372701223
H	-2.160581822	0.913576563	-2.6293611747
H	-1.554633973	0.847832323	-4.2962619589
H	-2.005389918	-0.661011499	-3.4034125300
C	-1.559859727	0.329991765	3.3372701223
H	-2.160581822	0.91357656	2.6293611747
H	-1.554633973	0.847832323	4.2962619589
H	-2.0053899	-0.661011499	3.4034125374
C	1.362443061	-0.63071074	3.3203443400
H	2.233304655	-0.372845688	2.7048434313
H	1.214332674	-1.7059507	3.2377321477
H	1.555822219	-0.329863629	4.3500495272

Table D35: xyz data of **24h** ⁴A' (Cs) ¹Pr:H

23

E(UPBE1PBE-D3/def2TZVP) = -2355.36392902

Re	-0.053732088	-0.071204271	0.000000000
N	0.814242484	1.780405855	0.000000000
P	0.048660198	0.318791134	2.4499273922
P	0.048660198	0.318791134	-2.4499273922
Cl	-2.235360674	0.832820907	0.000000000
Cl	-0.961389261	-2.2549093	0.000000000
Cl	2.130707878	-0.973414144	0.000000000
C	1.488489849	2.239377978	1.1898134551
H	1.733086415	3.306010364	1.0858635009
H	2.451378687	1.716845107	1.3403315033
C	0.606556101	2.053934935	2.4133800202
H	-0.29390501	2.665046121	2.3052952126
H	1.118168811	2.346026131	3.3324634993
C	1.488489849	2.239377978	-1.1898134551
H	2.451378687	1.716845107	-1.3403315033
H	1.733086415	3.306010364	-1.0858635009
C	0.606556101	2.053934935	-2.4133800202
H	1.118168811	2.346026131	-3.3324634993
H	-0.29390501	2.665046121	-2.3052952126
H	1.051853461	-0.406240307	-3.1145702682
H	-1.180001271	0.327346691	-3.1277205643
H	-1.180001271	0.327346691	3.1277205643
H	1.051853461	-0.406240307	3.1145702682

Table D36: xyz data of **25** ²A'' (Cs)

60

E(UPBE1PBE-D3(BJ)/def2TZVP) = -2827.20275985 <S2> = 0.7561

Re	0.18584665	-0.08508213	0.000000000
Cl	-1.51019687	1.47589730	0.000000000
Cl	1.30483117	-2.12602689	0.000000000
Cl	2.05692248	1.15245699	0.000000000
P	-0.17700374	-0.24907186	2.42350039
P	-0.17700374	-0.24907186	-2.42350039
N	-1.57453606	-1.46201071	0.000000000
H	-1.09462209	-2.36044101	0.000000000
C	-2.39477084	-1.40365121	1.22965459
H	-3.13103535	-2.21324922	1.20824442
H	-2.93945928	-0.45850273	1.21534955
C	-1.51185065	-1.51567008	2.45594203
H	-1.02018490	-2.49301576	2.47350518
H	-2.11331500	-1.44254516	3.36367692
C	1.21537321	-1.01692782	3.35793478
H	1.56365444	-1.76703256	2.63881215
C	2.35046337	-0.02942960	3.59621834
H	2.62376691	0.51825631	2.69326570
H	3.23367828	-0.57368756	3.93702833
H	2.09285445	0.69120753	4.37415673
C	0.81666090	-1.73605395	4.64129782
H	0.50876761	-1.04208490	5.42231446
H	1.68378045	-2.28574276	5.01559168
H	0.01539391	-2.46136471	4.49334622
C	-0.87449375	1.22177698	3.27934666
H	-1.82048098	1.36190864	2.74218586
C	-1.18431168	1.02057949	4.75675111
H	-1.78580276	1.85979701	5.11365032
H	-0.27159017	1.00037962	5.35365563
H	-1.74536215	0.10673271	4.95990202
C	-0.02797250	2.46952339	3.05036531
H	0.19410048	2.62804610	1.99543121
H	0.91596538	2.41979285	3.59340445
H	-0.57121452	3.34420397	3.41451650
C	-2.39477084	-1.40365121	-1.22965459
H	-2.93945928	-0.45850273	-1.21534955
H	-3.13103535	-2.21324922	-1.20824442
C	-1.51185065	-1.51567008	-2.45594203
H	-2.11331500	-1.44254516	-3.36367692
H	-1.02018490	-2.49301576	-2.47350518
C	1.21537321	-1.01692782	-3.35793478
H	1.56365444	-1.76703256	-2.63881215
C	0.81666090	-1.73605395	-4.64129782
H	0.01539391	-2.46136471	-4.49334622
H	1.68378045	-2.28574276	-5.01559168
H	0.50876761	-1.04208490	-5.42231446
C	2.35046337	-0.02942960	-3.59621834
H	2.09285445	0.69120753	-4.37415673
H	3.23367828	-0.57368756	-3.93702833
H	2.62376691	0.51825631	-2.69326570
C	-0.87449375	1.22177698	-3.27934666
H	-1.82048098	1.36190864	-2.74218586
C	-1.18431168	1.02057949	-4.75675111
H	-1.78580276	1.85979701	-5.11365032
H	-0.27159017	1.00037962	-4.95990202
H	-1.74536215	0.10673271	-5.35365563
C	-0.02797250	2.46952339	-3.05036531
H	-0.57121452	3.34420397	-3.41451650
H	0.91596538	2.41979285	-3.59340445
H	0.19410048	2.62804610	-1.99543121

Table D37: xyz data of 25 'A' (Cs)

60

E(UPBE1PBE-D3(BJ)/def2TZVP) = -2827.23051893 <S2> = 3.7703

Re	0.12657891	0.02482185	0.00000000
Cl	-1.49596587	1.69286923	0.00000000
Cl	1.45985395	-1.89645793	0.00000000
Cl	1.88759281	1.46641479	0.00000000
P	-0.18461113	-0.26361071	2.46657692
P	-0.18461113	-0.26361071	-2.46657692
N	-1.56159607	-1.41565764	0.00000000
H	-1.06105706	-2.30589646	0.00000000
C	-2.38756079	-1.36651916	1.22514238
H	-3.14409235	-2.15651420	1.18317985
H	-2.90501811	-0.40564854	1.22772344
C	-1.51475934	-1.52867208	2.45271914
H	-1.02845401	-2.50913472	2.44547749
H	-2.12051287	-1.47686532	3.35889307
C	1.21901696	-1.04330184	3.35933543
H	1.51231979	-1.81909842	2.64241011
C	2.39364311	-0.08665797	3.51832966
H	2.64630849	0.41833339	2.58478234
H	3.27100296	-0.64980702	3.84280501
H	2.19177159	0.66881513	4.27930813
C	0.84601481	-1.71898102	4.67331597
H	0.61673322	-0.99587639	5.45496349
H	1.69893522	-2.31013686	5.01496373
H	-0.00149226	-2.39992632	4.57793841
C	-0.8905514	1.20360815	3.32192310
H	-1.81501521	1.35827577	2.75153163
C	-1.24579721	0.97184717	4.78471378
H	-1.86499952	1.80156085	5.13326136
H	-0.35254014	0.95079510	5.40985287
H	-1.80614627	0.05129103	4.95712895
C	-0.02770836	2.44829827	3.14712264
H	0.22013214	2.63770135	2.10358091
H	0.90110268	2.37476910	3.71312524
H	-0.57569156	3.31397984	3.52513801
C	-2.38756079	-1.36651916	-1.22514238
H	-2.90501811	-0.40564854	-1.22772344
H	-3.14409235	-2.15651420	-1.18317985
C	-1.51475934	-1.52867208	-2.45271914
H	-2.12051287	-1.47686532	-3.35889307
H	-1.02845401	-2.50913472	-2.44547749
C	1.21901696	-1.04330184	-3.35933543
H	1.51231979	-1.81909842	-2.64241011
C	0.84601481	-1.71898102	-4.67331597
H	-0.00149226	-2.39992632	-4.57793841
H	1.69893522	-2.31013686	-5.01496373
H	0.61673322	-0.99587639	-5.45496349
C	2.39364311	-0.08665797	-3.51832966
H	2.19177159	0.66881513	-4.27930813
H	3.27100296	-0.64980702	-3.84280501
H	2.64630849	0.41833339	-2.58478234
C	-0.8905514	1.20360815	-3.32192310
H	-1.81501521	1.35827577	-2.75153163
C	-1.24579721	0.97184717	-4.78471378
H	-1.86499952	1.80156085	-5.13326136
H	-1.80614627	0.05129103	-4.95712895
H	-0.35254014	0.95079510	-5.40985287
C	-0.02770836	2.44829827	-3.14712264
H	-0.57569156	3.31397984	-3.52513801
H	0.90110268	2.37476910	-3.71312524
H	0.22013214	2.63770135	-2.10358091

Table D38: xyz data of Mes*OH 'A'

49

E(RPBE1PBE-D3(BJ)/def2TZVP) = -778.610534501

C	0.400141343	1.179146088	0.000000000
C	-0.479041371	-1.472189579	0.000000000
C	1.346321971	0.145607972	0.000000000
C	-0.981242207	0.919160338	0.000000000
C	-1.375696921	-0.409493935	0.000000000
C	0.869921685	-1.164360287	0.000000000
H	-2.43379699	-0.630371379	0.000000000
H	1.585876745	-1.971129708	0.000000000
O	0.776456973	2.489925836	0.000000000
H	1.733502267	2.540362506	0.000000000
C	-1.002531314	-2.903740563	0.000000000
C	-2.014268089	2.047660817	0.000000000
C	2.854840941	0.422291827	0.000000000
C	0.12471686	-3.930794234	0.000000000
H	0.757464507	-3.836922237	0.8861648427
H	0.757464507	-3.836922237	-0.8861648427
H	-0.297866518	-4.938418234	0.000000000
C	-1.859431541	-3.132883953	1.2489793930
H	-1.269740553	-2.980780461	2.1561873738
H	-2.251085034	-4.154124349	1.2611462515
H	-2.708862505	-2.447912926	1.2841632459
C	-1.859431541	-3.132883953	-1.2489793930
H	-2.708862505	-2.447912926	-1.2841632459
H	-2.251085034	-4.154124349	-1.2611462515
H	-1.269740553	-2.980780461	-2.1561873738
C	-1.859380187	2.910952052	-1.2583540554
H	-0.87877795	3.379292939	-1.3110643798
H	-2.617977528	3.698941357	-1.2610180659
H	-2.000947028	2.303837997	-2.1562557636
C	-1.859380187	2.910952052	1.2583540554
H	-0.87877795	3.379292939	1.3110643798
H	-2.000947028	2.303837997	2.1562557636
H	-2.617977528	3.698941357	1.2610180659
C	-3.443025872	1.50669775	0.000000000
H	-3.653812098	0.90438773	0.8871960443
H	-3.653812098	0.90438773	-0.8871960443
H	-4.139387254	2.348373926	0.000000000
C	3.273883959	1.183435262	1.2688256594
H	3.037225744	0.58804765	2.1531052569
H	2.785871714	2.150611525	1.4079785828
H	4.352175496	1.363020039	1.2567342207
C	3.273883959	1.183435262	-1.2688256594
H	2.785871714	2.150611525	-1.4079785828
H	3.037225744	0.58804765	-2.1531052569
H	4.352175496	1.363020039	-1.2567342207
C	3.669766159	-0.871239181	0.000000000
H	3.470964543	-1.477246193	0.8863288491
H	4.733485993	-0.622195841	0.000000000
H	3.470964543	-1.477246193	-0.8863288491

Table D39: xyz data of Mes*OH^{Me} tBu:Me 1A'

22

E(RPBE1PBE-D3(BJ)/def2TZVP) = -425.088872333

C	0.40068800	1.179294	0.0000000000
C	-0.47847200	-1.472049	0.0000000000
C	1.34687700	0.145764	0.0000000000
C	-0.98069400	0.919297	0.0000000000
C	-1.37513700	-0.409361	0.0000000000
C	0.87048800	-1.164208	0.0000000000
H	-2.43323500	-0.630247	0.0000000000
H	1.58645000	-1.970971	0.0000000000
O	0.77699200	2.490077	0.0000000000
H	1.73403700	2.540522	0.0000000000
C	-1.00195000	-2.903604	0.0000000000
H	-0.195829105	-3.638060853	0.0000000000
H	-1.613024011	-3.067016939	0.8906761453
H	-1.613024011	-3.067016939	-0.8906761453
C	-2.013729	2.047789	0.0000000000
H	-1.903469516	2.662364901	-0.8958197733
H	-1.903469516	2.662364901	0.8958197732
H	-3.033853625	1.661534036	0.0000000000
C	2.855394	0.422461	0.0000000000
H	3.153737598	0.964379437	0.9033737279
H	3.153737598	0.964379437	-0.9033737280
H	3.436482823	-0.499884237	0.0000000000

Table D42: xyz data of Mes*O^{Me} tBu:Me 2A''

21

E(UPBE1PBE-D3(BJ)/def2TZVP) = -424.453274740

C	0.428747	1.239799	0.0000000000
C	-0.459329	-1.452119	0.0000000000
C	1.387395	0.13409	0.0000000000
C	-1.002886	0.926023	0.0000000000
C	-1.380493	-0.388365	0.0000000000
C	0.90768	-1.153879	0.0000000000
H	-2.434201	-0.631262	0.0000000000
H	1.611304	-1.972329	0.0000000000
O	0.820143	2.420163	0.0000000000
C	-0.981262	-2.878342	0.0000000000
H	-0.18089098	-3.618003686	0.0000000000
H	-1.593880144	-3.034169511	0.8916487249
H	-1.593880144	-3.034169511	-0.8916487249
C	-2.020809	2.054777	0.0000000000
H	-1.892848701	2.668934372	-0.8934013470
H	-1.892848701	2.668934372	0.8934013469
H	-3.044373549	1.677565097	0.0000000000
C	2.877872	0.430561	0.0000000000
H	3.142390406	0.999633924	0.8933585474
H	3.142390406	0.999633924	-0.8933585475
H	3.474183245	-0.482861973	0.0000000000

Table D40: xyz data of Mes*OH^H tBu:H

13

! 1-A' (CS): E(RPBE1PBE-D3(BJ)/def2TZVP) = -307.235852150

C	0.400688	1.179294	0.0000000000
C	-0.478472	-1.472049	0.0000000000
H	-0.849882414	-2.487744854	0.0000000000
C	1.346877	0.145764	0.0000000000
H	2.412955759	0.341307567	0.0000000000
C	-0.980694	0.919297	0.0000000000
H	-1.710673789	1.716730149	0.0000000000
C	-1.375137	-0.409361	0.0000000000
C	0.870488	-1.164208	0.0000000000
H	-2.433235	-0.630247	0.0000000000
H	1.58645	-1.970971	0.0000000000
O	0.776992	2.490077	0.0000000000
H	1.734037	2.540522	0.0000000000

Table D41: xyz data of pyridinium 1A'

12

E(RPBE1PBE-D3(BJ)/def2TZVP) = -248.454161612

C	2.11612442	-2.46169864	0.00000000
C	3.30150603	-1.73726782	0.00000000
C	0.89510164	-1.79910311	0.00000000
C	0.88348091	-0.42452649	0.00000000
C	3.24251545	-0.36390844	0.00000000
N	2.04664589	0.24215332	0.00000000
H	-0.02022982	0.1702531	0.00000000
H	4.26506435	-2.22886627	0.00000000
H	4.11448661	0.27649934	0.00000000
H	2.14396135	-3.54500974	0.00000000
H	-0.0419374	-2.33953953	0.00000000
H	2.02061057	1.25535427	0.00000000

Table D43: xyz data of Mes*O²A''

48

E(UPBE1PBE-D3(BJ)/def2TZVP) = -777.978971168

C	0.42887515	1.23904273	0.00000000
C	-0.45989312	-1.45264666	0.00000000
C	1.38723894	0.13308698	0.00000000
C	-1.00283896	0.92563434	0.00000000
C	-1.38078327	-0.38865632	0.00000000
C	0.90719205	-1.15475784	0.00000000
H	-2.43455432	-0.63128204	0.00000000
H	1.61060641	-1.97338915	0.00000000
O	0.82057433	2.41930657	0.00000000
C	-0.98219231	-2.87873524	0.00000000
C	-2.02047147	2.05465003	0.00000000
C	2.87779205	0.42917507	0.00000000
C	0.13751951	-3.91404963	0.00000000
H	0.77073551	-3.82750843	0.88613283
H	0.77073551	-3.82750843	-0.88613283
H	-0.29581615	-4.91663524	0.00000000
C	-1.84188218	-3.09717364	1.25117212
H	-1.25291409	-2.94710932	2.15892549
H	-2.23204013	-4.11835950	1.26138579
H	-2.69175459	-2.41338445	1.28453084
C	-1.84188218	-3.09717364	-1.25117212
H	-2.69175459	-2.41338445	-1.28453084
H	-2.23204013	-4.11835950	-1.26138579
H	-1.25291409	-2.94710932	-2.15892549
C	-1.84033589	2.91811772	-1.25613531
H	-0.85254335	3.37331535	-1.28222294
H	-2.59308423	3.71125015	-1.26426270
H	-1.97485302	2.31732067	-2.15963970
C	-1.84033589	2.91811772	1.25613531
H	-0.85254335	3.37331535	1.28222294
H	-1.97485302	2.31732067	2.15963970
H	-2.59308423	3.71125015	1.26426270
C	-3.45308061	1.52711245	0.00000000
H	-3.66944472	0.92674794	0.88763635
H	-3.66944472	0.92674794	-0.88763635
H	-4.14268216	2.37392620	0.00000000
C	3.24995152	1.22928436	1.25620079
H	2.99829626	0.66759814	2.15982530
H	2.73106366	2.18510199	1.28197617
H	4.32774642	1.41380803	1.26406519
C	3.24995152	1.22928436	-1.25620079
H	2.73106366	2.18510199	-1.28197617
H	2.99829626	0.66759814	-2.15982530
H	4.32774642	1.41380803	-1.26406519
C	3.71214012	-0.84958819	0.00000000
H	3.52761195	-1.46071242	0.88738275
H	4.77074592	-0.58122904	0.00000000
H	3.52761195	-1.46071242	-0.88738275

Table D44: xyz data of Mes*O^{Me} tBu:Me 2A''

21

E(UPBE1PBE-D3(BJ)/def2TZVP) = -424.453274740

C	0.428747	1.239799	0.0000000000
C	-0.459329	-1.452119	0.0000000000
C	1.387395	0.13409	0.0000000000
C	-1.002886	0.926023	0.0000000000
C	-1.380493	-0.388365	0.0000000000
C	0.90768	-1.153879	0.0000000000
H	-2.434201	-0.631262	0.0000000000
H	1.611304	-1.972329	0.0000000000
O	0.820143	2.420163	0.0000000000
C	-0.981262	-2.878342	0.0000000000
H	-0.18089098	-3.618003686	0.0000000000
H	-1.593880144	-3.034169511	0.8916487249
H	-1.593880144	-3.034169511	-0.8916487249
C	-2.020809	2.054777	0.0000000000
H	-1.892848701	2.668934372	-0.8934013470
H	-1.892848701	2.668934372	0.8934013469
H	-3.044373549	1.677565097	0.0000000000
C	2.877872	0.430561	0.0000000000
H	3.142390406	0.999633924	0.8933585474
H	3.142390406	0.999633924	-0.8933585475
H	3.474183245	-0.482861973	0.0000000000

Table D45: xyz data of Mes*O^H tBu:H 2A''

12

E(UPBE1PBE-D3(BJ)/def2TZVP) = -306.590089742

C	0.428747	1.239799	0.0000000000
C	0.90768	-1.153879	0.0000000000
C	-0.459329	-1.452119	0.0000000000
H	-0.80304663	-2.47806005	0.0000000000
C	1.387395	0.13409	0.0000000000
H	2.4417846	0.37632374	0.0000000000
C	-1.002886	0.926023	0.0000000000
H	-1.7042911	1.74962255	0.0000000000
C	-1.380493	-0.388365	0.0000000000
H	-2.434201	-0.631262	0.0000000000
H	1.611304	-1.972329	0.0000000000
O	0.820143	2.420163	0.0000000000

Table D46: xyz data of 17 ²A

114

E(UPBE-PBE-D3(BJ)/def2SVP) = -2656.56726064 <S2> = 0.7544

N	5.2453802	9.37972619	14.4794318
Os	5.13619555	7.70643968	15.7588866
P	5.17038953	9.43646522	17.3892599
P	5.17560649	6.59293147	13.6300561
P	5.24064514	6.06867156	17.3319205
C	5.19774122	9.23424838	13.1087582
H	5.20690079	10.1679962	12.5135237
C	5.13857679	8.01264491	12.5052471
H	5.09963627	7.92763444	11.4105892
C	6.8653321	5.7838459	13.1972003
C	7.19396879	5.79526719	11.6965411
H	6.49828516	5.17697311	11.0998867
H	8.21530357	5.38242559	11.5471451
H	7.1863691	6.82375227	11.2861685
C	7.87915672	6.69174257	13.9202007
H	8.91275463	6.32051328	13.7492462
H	7.70129206	6.70460445	15.0139729
H	7.82021023	7.73411398	13.5471042
C	6.93509556	4.35333715	13.7457931
H	6.34013547	3.64935706	13.131517
H	6.57395302	4.28390615	14.789471
H	7.98696453	3.99427467	13.7252668
C	3.71218434	5.51480427	13.0298621
C	3.83861092	5.08669337	11.5608635
H	3.99874143	5.94602781	10.8797372
H	2.8965458	4.58739229	11.2466111
H	4.65820243	4.35828497	11.4079521
C	2.47038794	6.41146809	13.1958215
H	2.52993893	7.3155997	12.5580879
H	2.35496761	6.74482903	14.2454309
H	1.56302451	5.83765782	12.9095941
C	3.57215285	4.28509189	13.9327891
H	2.6002511	3.78177261	13.7393882
H	3.60230528	4.56778631	14.9984172
H	4.36829032	3.53698667	13.7679558
C	5.26135937	10.656809	14.995783
H	5.28942209	11.4851358	14.2614563
C	5.23910314	10.9067847	16.3378689
H	5.24023185	11.9371017	16.7191619
C	3.62230322	9.7527502	18.4864219
C	6.79828815	9.57585593	18.4169477
C	7.8832024	9.04427307	17.459996
H	7.73526111	7.96760147	17.2436043
H	8.88587766	9.16539348	17.9240336
H	7.88198766	9.59752691	16.4983917
H	4.99921664	6.37628012	18.7077226
C	7.14769564	11.0269111	18.7867263
H	8.12377991	11.0384916	19.3183599
H	6.40196361	11.4932893	19.4561973
H	7.25135088	11.6605221	17.8847426
C	6.75731351	8.70581871	19.6807512
H	6.49228319	7.65613267	19.4486856
H	6.04162636	9.09150467	20.4330944
H	7.76207804	8.69766913	20.1557945
C	5.08523808	4.20793669	17.3414017
C	6.27270476	3.40687652	17.2579645
C	6.15823443	2.09814394	16.7438818
H	7.06961581	1.50713984	16.6115406
C	4.92856704	1.52304186	16.3994981
C	3.77364959	2.24059472	16.7529776
H	2.80059482	1.75306682	16.6194325
C	3.80576853	3.5552205	17.2508428
C	2.48135193	4.15902892	17.8106573
C	1.93910778	5.35890143	17.0045922
H	1.60034361	5.03780649	16.0004281
H	2.69572406	6.1517896	16.8642017
H	1.06651227	5.79817679	17.5311145
C	2.73674922	4.56981854	19.2810355

H	3.50715248	5.35783386	19.366194
H	3.0776952	3.69835317	19.8758137
H	1.80331947	4.95922648	19.7378163
C	1.34718582	3.11183232	17.8456906
H	1.04188392	2.78756589	16.8305163
H	0.45595834	3.56625417	18.3231519
H	1.62145646	2.21284508	18.4333282
C	7.64879094	3.83660471	17.8558871
C	8.393078	4.89821842	17.0234447
H	8.65053769	4.51219907	16.0191474
H	9.33577645	5.18685081	17.5332508
H	7.77630954	5.80775192	16.8991777
C	8.60516465	2.63149523	17.9934644
H	8.91850638	2.22563955	17.0107526
H	8.1585891	1.80780059	18.5856153
H	9.52560287	2.96233309	18.5151436
C	7.4090645	4.37360588	19.2867699
H	6.80301381	5.29925002	19.2807734
H	8.37802129	4.60901558	19.7738545
H	6.87920427	3.62330192	19.9075005
C	4.80609957	0.14734474	15.7239236
C	4.07655432	0.32645028	14.3725721
H	4.65112017	0.99506476	13.6997255
H	3.07098765	0.77233877	14.5066943
H	3.95184559	-0.65178643	13.8631763
C	6.17960712	-0.49011692	15.4527433
H	6.04835379	-1.46565155	14.9424891
H	6.74078123	-0.67747189	16.3904252
H	6.80617036	0.14907674	14.7983842
C	3.99326053	-0.80794752	16.6264479
H	2.9709452	-0.42572731	16.8173142
H	4.49166834	-0.9437722	17.6075563
H	3.89483429	-1.80445975	16.1478698
H	3.55129876	7.79706536	15.6977041
C	3.26435772	8.50273306	19.3034064
H	3.06710368	7.63999579	18.6405575
H	2.34016719	8.69999324	19.8882461
H	4.05555329	8.21444527	20.0214492
H	4.09098055	11.8773822	18.8645148
H	2.82832494	11.1784099	19.9185045
C	2.47374172	10.0306637	17.4984347
H	2.64830007	10.9536017	16.9121902
H	1.5250938	10.146914	18.0648538
H	2.35065613	9.19313868	16.78315
C	3.79616844	10.9625835	19.4161986

Table D47: xyz data of 19 ¹A

113

E(RPBE-PBE-D3(BJ)/def2SVP) = -2655.96534768

N	5.53174285	9.33924349	14.5435534
Os	5.19295584	7.63525275	15.8094306
P	5.03900605	9.43148113	17.4277058
P	5.29447078	6.58128408	13.6571548
P	5.70563667	6.07987033	17.3056903
C	5.49563831	9.21929774	13.1690901
H	5.57822913	10.1571161	12.5849332
C	5.35303939	8.01512561	12.5498844
H	5.33021817	7.94130467	11.454218
C	6.92783879	5.68414535	13.1654138
C	7.21634488	5.70498905	11.6551222
H	6.47650419	5.13536556	11.0640517
H	8.20992015	5.23932385	11.4776979
H	7.26049822	6.73831046	11.260219
C	8.01294643	6.52592232	13.8643746
H	9.01579304	6.09167859	13.6632555
H	7.86345487	6.55641576	14.960039
H	8.00835625	7.56879277	13.4878638
C	6.93432683	4.24083003	13.6794176
H	6.26503618	3.59005228	13.0826302
H	6.62291849	4.166676	14.7374382
H	7.95844838	3.8165152	13.5966953
C	3.76100996	5.60165169	13.0694708
C	3.87726976	5.11649885	11.6172757
H	4.09883523	5.94022616	10.9097225
H	2.90773644	4.66843072	11.3097835
H	4.64911129	4.3320721	11.499012
C	2.57299358	6.5763089	13.1798037
H	2.70056829	7.45428954	12.516184
H	2.45071579	6.94896703	14.2153686
H	1.64015867	6.04773157	12.8886826
C	3.53981122	4.4148564	14.0134856
H	2.55837567	3.93883336	13.8010669
H	3.54581856	4.74382359	15.0657113
H	4.31588959	3.63484251	13.911047
C	5.58558164	10.6111654	15.073697
H	5.76049122	11.4368332	14.3552997
C	5.39196109	10.8741054	16.3985089
H	5.40944442	11.9052343	16.7767969
C	3.31533749	9.81457372	18.1767009
C	6.44165425	9.50000191	18.7430897
C	7.70825851	9.04245398	17.9905394
H	7.64954538	7.9728515	17.7117502
H	8.59345556	9.18039675	18.6477963
H	7.86931065	9.64173811	17.07073
C	6.68179576	10.9261472	19.2669093
H	7.5342955	10.9021997	19.9793308
H	5.81296858	11.3429121	19.8073038
H	6.9529837	11.620541	18.4481688
C	6.14962482	8.54662286	19.9078967
H	5.91567526	7.5235899	19.5436148
H	5.31724537	8.90744235	20.5437224
H	7.05118804	8.46712404	20.552385
C	5.32768179	4.24212566	17.2698002
C	6.44270406	3.34354552	17.1010038
C	6.18038054	2.0655048	16.5633653
H	7.02744734	1.40899684	16.3407955
C	4.88336319	1.5904659	16.321248
C	3.82523209	2.37323793	16.8195446
H	2.80995871	1.95439994	16.8070802
C	4.01222793	3.6657859	17.3304793
C	2.82742796	4.34945346	18.0680091
C	2.00627304	5.27432802	17.1472817
H	1.547136	4.69897866	16.3193531
H	2.6400066	6.06552866	16.7052185
H	1.18929834	5.76056496	17.7198729
C	3.37365707	5.13319807	19.2790898
H	4.05694685	5.9550227	18.9738947

H	3.94456881	4.46616649	19.9559012
H	2.54398513	5.59604417	19.8514756
C	1.86038135	3.28778262	18.6409469
H	1.29730975	2.75436392	17.8496935
H	1.11000814	3.78904582	19.2855577
H	2.39393636	2.53416034	19.2545275
C	7.87755695	3.63458237	17.6411324
C	8.6595369	4.70777901	16.8589637
H	8.80781202	4.41217328	15.8036017
H	9.65940556	4.8548909	17.3181494
H	8.13233012	5.682202	16.880058
C	8.75070393	2.36092142	17.629002
H	8.97082129	2.00942209	16.6006462
H	8.28423967	1.52737251	18.1910264
H	9.72295662	2.58854949	18.1101705
C	7.74178087	4.07549001	19.1198392
H	7.19091808	5.03365225	19.2002951
H	8.74702127	4.21565336	19.5691061
H	7.19979138	3.30977965	19.7108082
C	4.59689856	0.24179024	15.6425069
C	3.69959865	0.48784597	14.4079678
H	4.21132759	1.13933098	13.6709082
H	2.74767141	0.9825618	14.6856162
H	3.45238776	-0.47172652	13.9079075
C	5.88517734	-0.45593298	15.1731937
H	5.63389491	-1.40353343	14.6552592
H	6.55231381	-0.70822174	16.0219522
H	6.45626218	0.17535132	14.4626561
C	3.86572178	-0.69346629	16.6323236
H	2.90225107	-0.26308636	16.9703754
H	4.48697401	-0.87806645	17.5319895
H	3.64852381	-1.67178555	16.1550939
H	3.63959273	7.30606258	15.8256535
C	2.7911638	8.57739567	18.9157422
H	2.78498746	7.69853359	18.2473053
H	1.7487752	8.76105616	19.2543166
H	3.3939553	8.32530558	19.8081505
H	3.74091298	11.9360003	18.619619
H	2.24839976	11.2874995	19.3593852
C	2.41325259	10.0814953	16.9559454
H	2.71312716	11.0010383	16.4169711
H	1.36268522	10.2003015	17.296812
H	2.45142615	9.23746545	16.2373102
C	3.3006618	11.0398156	19.1006706
H	3.83414612	10.8520689	20.0525323

Table D48: xyz data of Mes*P ³A

48

E(UPBE-PBE-D3(BJ)/def2SVP) = -1043.00517060 <S2> = 2.0095

C	-4.29229334	1.42606636	0.22200909
C	-2.99198846	0.81085245	0.07847518
C	-5.47486304	0.60068952	0.07929523
C	-5.31104726	-0.76354046	-0.19266727
C	-4.05454603	-1.37931613	-0.3355638
C	-2.92108818	-0.56598655	-0.19439347
C	-1.6637529	1.60118599	0.21179058
C	-1.58864046	2.70372974	-0.869759
C	-0.42301689	0.70510659	0.01385345
C	-1.54609878	2.21091953	1.62790395
C	-6.91587345	1.15855329	0.21390892
C	-7.17429031	2.23307866	-0.86755954
C	-3.97032955	-2.88478971	-0.63403464
C	-2.51714459	-3.3749683	-0.75551203
C	-4.69760363	-3.17816175	-1.96658947
C	-4.65539365	-3.66687531	0.51039908
H	-6.47431541	3.09071684	-0.77555828
H	-8.20590536	2.63149422	-0.7771844
H	-7.05189899	1.80478922	-1.88291956
C	-7.13174992	1.74023986	1.6302411
C	-7.98949851	0.06798657	0.01701514
H	-7.94186088	-0.39087581	-0.99090978
H	-8.9930087	0.52586208	0.12444555
H	-7.91182279	-0.73891945	0.77306131
H	-6.42963527	2.57308369	1.8479073
H	-6.97891535	0.95927322	2.40231633
H	-8.163175	2.13645006	1.73178939
H	-1.63974143	2.26118863	-1.88509648
H	-0.63721113	3.26764747	-0.78073231
H	-2.42105941	3.43334091	-0.77649744
H	-0.39393565	0.24462296	-0.99397529
H	-0.36389552	-0.10338734	0.76979788
H	0.48973182	1.3246013	0.12054038
H	-2.376391	2.91589633	1.84601841
H	-0.59447127	2.77254546	1.72854243
H	-1.5667517	1.41565603	2.40023392
H	-4.15212568	-3.47238716	1.47898985
H	-4.61429199	-4.7580558	0.31233085
H	-5.72118735	-3.38481323	0.62138712
H	-1.97733823	-2.86621758	-1.57946068
H	-2.50451964	-4.46245384	-0.97029298
H	-1.94732624	-3.21370857	0.18172425
H	-6.20442734	-1.38941083	-0.30094042
P	-4.44205099	3.19864575	0.57430733
H	-1.93509525	-1.02676825	-0.30210388
H	-4.2251241	-2.62720371	-2.8047307
H	-5.76461699	-2.88198573	-1.92714665
H	-4.65708945	-4.26253652	-2.19915142

Table D49: xyz data of Mes*PH ²A

49

E(UPBE-PBE-D3(BJ)/def2SVP) = -1043.61560710 <S2> = 0.7541

C	-4.30275837	1.44510214	0.23520462
C	-3.00461847	0.83793583	0.10132009
C	-5.47982558	0.62842654	0.05528223
C	-5.31375994	-0.74329807	-0.1919054
C	-4.05925832	-1.36522783	-0.28568588
C	-2.93247959	-0.54736221	-0.14543651
C	-1.65205738	1.60143083	0.2054077
C	-1.65611572	2.88710663	-0.64926016
C	-0.46597086	0.76451307	-0.32982155
C	-1.33287767	1.90258412	1.68955888
C	-6.93418814	1.17357867	0.14291345
C	-7.18179940	2.2206555	-0.96931411
C	-3.96887993	-2.87822072	-0.54519874
C	-2.51321537	-3.37057261	-0.61830655
C	-4.66311253	-3.20599493	-1.88693217
C	-4.68168386	-3.63085849	0.60169619
H	-6.51521925	3.10088666	-0.88820039
H	-8.22631414	2.59185895	-0.91705588
H	-7.02656077	1.76552575	-1.96833192
C	-7.20692615	1.76832976	1.5441546
C	-7.99039991	0.06627449	-0.06460375
H	-7.91124622	-0.40951784	-1.06253895
H	-9.00032749	0.51711377	0.00586057
H	-7.92800398	-0.72619407	0.70783013
H	-6.53262516	2.62271719	1.76891839
H	-7.05785843	1.00170836	2.33131609
H	-8.25013622	2.1408825	1.60951758
H	-1.80502216	2.64353538	-1.72071042
H	-0.69112290	3.42370539	-0.54265855
H	-2.46192078	3.60037992	-0.36737044
H	-0.62797555	0.4363945	-1.37610036
H	-0.25919521	-0.1304451	0.28959103
H	0.45061584	1.38736928	-0.30945486
H	-2.10595172	2.52421456	2.17868544
H	-0.36517686	2.43949486	1.77478808
H	-1.25409304	0.95676046	2.2621461
H	-4.20159495	-3.41189926	1.57685028
H	-4.63765631	-4.72688832	0.43294747
H	-5.74932682	-3.34467525	0.67989842
H	-1.95390605	-2.88482815	-1.443183
H	-2.49496395	-4.46373784	-0.80179366
H	-1.96606450	-3.18199894	0.32738165
H	-6.20586573	-1.36777829	-0.31293872
P	-4.53733615	3.2520471	0.56803194
H	-1.94532794	-1.00822932	-0.23771776
H	-4.17067016	-2.67559438	-2.7268799
H	-5.73079431	-2.90956218	-1.88081716
H	-4.61710714	-4.29581471	-2.09157962
H	-3.61604477	3.3502193	1.67223545

Table D50: xyz data of Mes*PH 4A

49

E(UPBE-PBE-D3(BJ)/def2SVP) = -1043.51315469 <S2> = 3.7640

C	-4.27144164	1.18478336	0.75666526
C	-2.96422795	0.75254911	0.19232865
C	-5.48580925	0.53280405	0.19630713
C	-5.32897116	-0.82320305	-0.02384777
C	-4.03615846	-1.45836202	-0.0044699
C	-2.87909333	-0.61562378	-0.02737433
C	-1.83635498	1.7527852	-0.05705776
C	-2.4297574	3.00406147	-0.74055906
C	-0.74328404	1.15577466	-0.96159978
C	-1.19009598	2.16967173	1.28625123
C	-6.74264972	1.33822501	-0.12906373
C	-6.35935945	2.36938482	-1.21791533
C	-3.94957981	-2.98212195	-0.13126548
C	-2.49560951	-3.48620685	-0.13642461
C	-4.63095345	-3.45081727	-1.43961833
C	-4.67978378	-3.61243329	1.0792886
H	-5.53916293	3.02701121	-0.86670507
H	-7.23020615	3.00848723	-1.47351752
H	-6.01605143	1.86121873	-2.14148792
C	-7.25657543	2.09574899	1.11489447
C	-7.8721381	0.44049952	-0.66033752
H	-7.56985656	-0.09777315	-1.58091618
H	-8.75987769	1.05704181	-0.9076579
H	-8.18429563	-0.31054148	0.0934087
H	-6.49525829	2.799762	1.50714277
H	-7.52367331	1.39458044	1.93141381
H	-8.16015467	2.68657751	0.85643184
H	-2.89249308	2.74516873	-1.71425942
H	-1.63944968	3.76165429	-0.92020484
H	-3.21335294	3.46600171	-0.10615817
H	-1.16205846	0.80815355	-1.92727693
H	-0.2306669	0.29920364	-0.47966977
H	0.02931377	1.92182663	-1.17658909
H	-1.93508819	2.62312642	1.97315662
H	-0.38723339	2.91736673	1.11398001
H	-0.74718085	1.29318702	1.80054539
H	-4.20193919	-3.30506852	2.03160659
H	-4.65069338	-4.72076686	1.01910398
H	-5.74227584	-3.30012185	1.12049797
H	-1.93447366	-3.12339299	-1.02105606
H	-2.48060757	-4.59444207	-0.16748417
H	-1.94911653	-3.1657976	0.77335136
H	-6.19783417	-1.4265074	-0.32866574
P	-4.3008938	1.47398986	2.5826926
H	-1.91597137	-1.05302599	-0.32542257
H	-4.13280265	-3.00613684	-2.32469494
H	-5.70175438	-3.16834903	-1.47557585
H	-4.57516963	-4.55566453	-1.52996295
H	-4.142598	0.08779111	2.9955117

E. List of abbreviations

AO	Atomic Orbital
BA-CPET	Basic Asynchronous Concerted Proton Electron Transfer
BArF ₂₄	Tetrakis[3,5-bis(trifluoromethyl)phenyl]borate
BD(F)E	Bond Dissociation (Free) Energy
CASPT2	Complete Active Space Perturbation Theory of Second Order
CASSCF	Complete Active Space Self Consistent Field
CBS	Complete Basis Set (limit)
CC	Coupled Cluster
CCSD(T)	Coupled Cluster Singles, Doubles and perturbative Triples
CI	Configuration Interaction
CISDT	Configuration Interaction (with) Singles, Doubles and Triples
CPET	Concerted Proton Electron Transfer
CV	Cyclic Voltammetry
<i>D</i>	Zero-Field Splitting Parameter
DCM	Dichloromethane
DLPNO	Domain-Based Local Pair Natural Orbital
DF	Dirac-Fock (method)
DFT	Density Functional Theory
DZ	Double Zeta
ECP	Electron Core Potential
ET	Electron Transfer
Fc/Fc ⁺	Ferrocene/Ferrocenium
FCI	Full Configuration Interaction
Fullsystem	see ONIOM referring to the full, untruncated system
GOE	Great Oxygenation Event
HAT	Hydrogen Atom Transfer
HF	Hartree-Fock (method)
HMDSO	Hexamethyldisiloxane
HOMO	Highest Occupied Molecular Orbital
IR	Infra-Red (spectroscopy)
ITC	Isothermal Titration Calorimetry
LCAO	Linear Combination of Atomic Orbitals
Mes*O(H)	2,4,6-Tris- <i>tert</i> -butylphenoxy/phenol
MM	Molecular Mechanics
MO	Molecular Orbital
M-O	Metal-Oxygen Bond
MS-CPET	Multi-Centre Concerted Proton Electron Transfer
Na/Hg	Sodium-Mercury Alloy
NBO/NPA	Natural Bond Orbitals/Natural Population Analysis

NEVPT2	n-Electron Valence Perturbation Theory of Second Order
NIR	Near-Infra-Red (spectroscopy)
NMR	Nuclear Magnetic Resonance (technique)
OA-CPET	Oxidative Asynchronous Concerted Proton Electron Transfer
OAT	Oxygen Atom Transfer
OEC	Oxygen Evolving Reaction
ONIOM	Our Own n-layered integrated molecular orbital and molecular mechanics
PAO	Projected Atomic Orbitals
PCET	Proton Coupled Electron Transfer
PNO	Pair of Natural Orbitals
PNP	Bis(di- <i>tert</i> -butylphosphinoethylene)amide (Chapter II-III)
P ^H NP	Bis(di-isopropylphosphinoethyl)amine
PSII	Photosystem II
PT	Proton Transfer
QDPT	Quasi-Degenerate Perturbation Theory
SARC	All-Electron Relativistic Contracted (basis set)
SMD	Solvation Model Bases Density
SOC	Spin-Orbit Coupling
SOMF	Spin-Orbit Mean Field (operator)
SOMO	Singly Occupied Molecular Orbital
SORCI	Spectroscopy Oriented Configuration Interaction
SQUID	Superconducting Quantum Interference Device (technique)
SZ	Single Zeta
TD-DFT	Time-Dependent Density Functional Theory
THF	Tetrahydrofuran
TIP	Temperature Independent Paramagnetism
Truncation	See ONIOM Referring to truncated model system
UV-VIS	Ultra-Violet-Visual (spectroscopy)
WFT	Wavefunction Theory
XRD	X-Ray Diffraction
ZORA	Zeorth Order Regular Approximation

F. Curriculum Vitae

Daniel Delony



* 02. August 1992 in Celle

2017 – 2020 **Dissertation**

“Proton Coupled Electron Transfer at Heavy Metal Sites”

Georg-August Universität Göttingen, Working Group Prof. S. Schneider

2014 – 2016 **Master of Science (Chemie)**

„Amin Aktivierung durch PNP-Komplexe der Gruppe 9“

Georg-August Universität Göttingen, Working Group Prof. S. Schneider

2011 – 2014 **Bachelor of Science (Chemie)**

„Mechanistische Untersuchung zur selenkatalysierten C-H Acyloxylierung“

Georg-August Universität Göttingen, Working Group Dr. A. Breder

2006 – 2011 **Abitur**

Christian-Gymnasium Hermannsburg